GKSS
FORSCHUNGSZENTRUM
in der HELMHOLTZ-GEMEINSCHAFT

Residual strength analysis of laser beam and friction stir welded aluminium panels for aerospace applications

(Vom Promotionsausschuss der Technischen Universität Hamburg-Harburg als Dissertation angenommene Arbeit)

Author:
E. Seib

ISSN 0344-9629

HELMHOLTZ
GEMEINSCHAFT
GKSS is member of the Helmholtz-Gemeinschaft
Deutscher Forschungszentren e.V.

GKSS 2006/3

GKSS 2006/3

Residual strength analysis of laser beam and friction stir welded aluminium panels for aerospace applications

(Vom Promotionsausschuss der Technischen Universität Hamburg-Harburg als Dissertation angenommene Arbeit)

Author:
E. Seib
(Institute for Materials Research)

GKSS-Forschungszentrum Geesthacht GmbH • Geesthacht • 2006

Die Berichte der GKSS werden kostenlos abgegeben.
The delivery of the GKSS reports is free of charge.

Anforderungen/Requests:

GKSS-Forschungszentrum Geesthacht GmbH
Bibliothek/Library
Postfach 11 60
D-21494 Geesthacht
Germany
Fax.: (49) 04152/871717

ISSN 0344-9629

GKSS-Forschungszentrum Geesthacht GmbH · Telefon (04152)87-0
Max-Planck-Straße 1 · D-21502 Geesthacht / Postfach 11 60 · D-21494 Geesthacht

GKSS 2006/3

Residual strength analysis of laser beam and friction stir welded aluminium panels for aerospace applications

(Vom Promotionsausschuss der Technischen Universität Hamburg-Harburg als Dissertation angenommene Arbeit)

Eduard Seib

212 pages with 147 figures and 18 tables

Abstract

The thesis deals with the residual strength analysis of cracked laser beam and friction stir welded thin-walled panels for aircraft fuselage applications made of the Al 6013 T6 alloy. Detailed experimental work has been carried out in order to improve the understranding of the fracture and deformation behaviour of these components containing highly strength undermatched weld joints. Moreover, the experimental results have been used to verify the proposed analysis route for the residual strength prediction of cracked unstiffened as well as stiffened welded fuselage panels. The results have shown a good agreement of the predicted maximum load levels with the experimental values.

Restfestigkeitsanalyse von laserstrahl- und reibrührgeschweißten Aluminiumblechen für flugzeugtechnische Anwendungen

Zusammenfassung

In dieser Arbeit wurde die Restfertigkeit von laserstrahl- und reibrührgeschweißten dünnwandigen Flugzeugrumpfkomponenten mit einem Anfangsriss anaylisiert. Der untersuchte Werkstoff ist eine Al-Legierung (AL 6013 T6). Es wurden umfangreiche Versuche durchgeführt, die zum einen zum besseren Verständnis des Bruch- und Deformationsverhaltens dieser Schweißnähte mit Undermatch einen Beitrag leisten. Zum anderen wurden die experimentellen Ergebnisse zur Verifizierung der vorgeschlagenen Methode zur Vorhersage der Restfestigkeit von geschweißten Rumpfblechen mit und ohne Versteifungen herangezogen. Die Ergebnisse zeigen eine gute Übereinstimmung der vorhergesagten Maximallasten mit den Messwerten.

Manuscript received / Manuskripteingang in TDB: 15. März 2006

Acknowledgment

This work was conducted at the GKSS Research Center in cooperation with AIRBUS Deutschland GmbH Hamburg and I would like to thank AIRBUS for the financial support and provision of the material investigated within this study.

I would like to express my sincere gratitude to Professor K.-H. Schwalbe for his invaluable advice and guidance during this work as well as for his comments and reviews on the manuscript.

I am also grateful to Professor W. Fricke for his interest in this topic and taking over the co-referee of this thesis.

I wish to thank my supervisors Dr. M. Koçak and Dr. A. Motarjemi from GKSS as well as the AIRBUS colleagues Dr. H. Assler, Dr. H.-J. Schmidt, Mr. M. Pacchione, Dr. S. Werner, and N. Ohrloff for their input and encouragement to complete this thesis.

Furthermore, I wish to thank Professor S. T. Ariaratnam from the University of Waterloo/Canada for the review of this manuscript.

My deep appreciation is addressed to my lovely wife Elena and my sweet son Jonas who gave me strength throughout the entire time of this work.

Eduard Seib, December 2005

Contents

Nomenclature

a	half skin crack length
a_0	initial half skin crack length
a_{eff}	effective half crack length
a_{str}	stringer crack length
A_{net}	net section area of stiffened panel
$A_{\mathrm{net,sk}}$	skin net section area in stiffened panel
$A_{\mathrm{net,str}}$	stringer net section area in stiffened panel
A_{sk}	skin cross-sectional area in stiffened panel
A_{str}	stringer cross-sectional area in stiffened panel
B	thickness
B_{eq}	equivalent thickness
B_{str}	thickness of stringer foot
B^*	skin thickness of weld location
d	eccentricity, offset due to stringers
E	Young's modulus
E'	$= E$ (plane stress); $=E/(1-\nu^2)$ (plane strain)
F	applied load (general)
F_{sk}	skin load in stiffened panel
F_{str}	stringer load in cracked stiffened panel
F^*_{str}	stringer load in un-cracked stiffened panel
F_{TS}	maximum tensile load carrying capacity
F_{Y}	yield load (general)
F_{YB}	yield load of base material M(T) panel
F_{YM}	mismatch yield load
G_{I}	strain energy release rate
H	half weld width
I_{n}	integration constant in HRR field
J	J-integral
K	linear elastic stress intensity factor
K_{c}	fracture toughness of thin sheets
K_{c0}	apparent fracture toughness of thin sheets
K_{i}	stress intensity factor at initiation of stable crack growth in thin sheets
K_{I}	linear elastic stress intensity factor of Mode I
$K_{\mathrm{I\,sk}}$	K-factor for skin crack
$K_{\mathrm{I\,str}}$	K-factor for stringer crack
K_{J}	$= \sqrt{JE}$
L_0	gauge length
L_{s}	$= \frac{F_{\mathrm{str}}}{F^*_{\mathrm{str}}}$, stringer load concentration factor
m	constraint parameter
M	weld strength mismatch factor $M = R_{\mathrm{p0.2W}}/R_{\mathrm{p0.2B}}$
M_{res}	$= F\,d$, out-of-plane bending moment in stiffened panels

n	strain hardening exponent in Ramberg-Osgood equation $(1 \leq n < \infty)$
N	strain hardening exponent in piece wise power stress-strain relationship $(0 < N < 1)$ (general)
N_{B}	strain hardening exponent of base material
N_{M}	strain hardening exponent of mismatch material
N_{W}	strain hardening exponent of weld material
r	polar coordinate
r_{p}	plastic zone correction
r_{Y}	Irwin's plastic zone radius
R_{m}	uniaxial tensile strength of material (general)
R_{mB}	uniaxial tensile strength of base material
R_{mW}	uniaxial tensile strength of weld material
$R_{\mathrm{p0.2}}$	uniaxial yield strength of (base) material
$R_{\mathrm{p0.2B}}$	uniaxial yield strength of base material
$R_{\mathrm{p0.2W}}$	uniaxial yield strength of weld material
u, v, w	displacement components in direction of x, y, z coordinate axes, respectively
v_{LL}	load line displacement or total elongation of specimen/panel measured at gauge length L_0
$\mathcal{W}$	strain energy density
W	half panel width

α	constant in Ramberg-Osgood equation
β	general correction function of K_{I}
β_{sk}	correction function of $K_{\mathrm{I\,sk}}$
β_{str}	correction function of $K_{\mathrm{I\,str}}$
δ	CTOD
δ_5	CTOD measured across the fatigue crack tip at a gauge length of 5 mm
ε	engineering strain
ε^*	engineering strain defining the contour of plastic zone in weld
$\varepsilon_{0.2}$	total engineering strain at $R_{\mathrm{p0.2}}$
$\varepsilon_{\mathrm{ref}}$	reference (true) strain corresponding to σ_{ref}
$\varepsilon_{\mathrm{true}}$	$= \ln(1+\varepsilon)$, true strain
$\tilde{\varepsilon}_{ij}(n, \theta)$	dimensionless function in strain equation of HRR field
κ	$= 3 - 4\nu$ for plane strain and $\kappa = (3-\nu)/(1+\nu)$ for plane stress
λ	unit elongation of a one-dimensional infinitesimally small element
μ	shear modulus
ν	Poisson's ratio
ω	experimentally measured plastic zone length in the weld
θ	polar coordinate
σ	engineering stress
σ_{ref}	$= L_{\mathrm{r}} R_{\mathrm{p0.2}}$, reference (true) stress
σ_{true}	$= \sigma(1+\varepsilon)$, true stress

$\tilde{\sigma}_{ij}(n,\theta)$	dimensionless function in stress equation of HRR field
$\sigma_{\mathrm{xx}}, \sigma_{\mathrm{yy}}, \sigma_{\mathrm{zz}}$	stress components in direction of x, y, z coordinate axes, respectively
τ_{xy}	shear stress component
ψ	$= (W-a)/H$
ψ_1	$= \left(1 + 0.43\, e^{-5(M-1)}\right) e^{-(M-1)/5}$

BM	base material
CDF	Crack Driving Force
CTOD	Crack Tip Opening Displacement
C(T)	compact specimen, eg. C(T)50 → $W = 50$ mm
DE(T)	double edge notched tension specimen
EDM	Electrical Discharge Machining
EPFM	Elastic Plastic Fracture Mechanics
ETM	Engineering Treatment Model
FE	Finite Element
FEA	Finite Element Analysis
FAD	Failure Assessment Diagram
FITNET	FITness-for-Service NETwork
FSW	Friction Stir Welding
GLS	$= v_{\mathrm{LL}}/L_0 * 100\%$, Gauge Length Strain
HAZ	Heat Affected Zone
HRR	singular stress and strain fields at crack tip in Ramberg-Osgood material
LEFM	Linear Elastic Fracture Mechanics
LBW	Laser Beam Welding
M(T)	middle cracked tension specimen, eg. M(T)760 → $2W = 760$ mm
OM	overmatching ($M > 1$)
SEM	Scanning Electron Microscope
SE(B)	single edge notched bend specimen
SE(T)	single edge notched tension specimen
SIF	Stress Intensity Factor
SINTAP	Structural INTegrity Assessment Procedure
TMAZ	Thermo-Mechanically Affected Zone
UM	undermatching ($M < 1$)
WM	weld material

differential structure	riveted structure
integral structure	welded structure
bay	distance between two stiffeners (stringer or frame)
one-bay crack	crack extending over one bay
two-bay crack	crack extending over two bays, here over broken central stringer

1 Introduction

Driven by the demand for lighter and cost-effective airplanes as well as by the close competition with the non-metallic composite materials, the design of metallic structures in the aerospace industry has experienced revolutionary changes in the last decade. The well established joining technique by rivets is currently being replaced by welding using novel welding technologies like laser beam welding (LBW) and friction stir welding (FSW). The adoption of these welding processes provides weight and cost savings of about 15%, respectively [1]. The most widely used metallic material in aircraft structures is aluminium and was deemed to be unweldable [2]. However, newly developed aluminium alloys with silicon (Si) and magnesium (Mg) as the main alloying elements allow the use of welding while maintaining the properties of the conventional base material alloy. Stringer-to-skin joints in some of the AIRBUS airplanes are already being produced using LBW with 12%Si wire addition, whereas for the skin-to-skin joints, LBW and FSW techniques are currently under consideration in order to replace riveted lap joints.

Today's airplanes are designed to satisfy the damage tolerance requirements of fatigue and residual strength. The residual strength of a structure is defined as the remaining load carrying capacity in the presence of a single or multiple cracks. Conventional analysis tools for the residual strength prediction of riveted structures are well established. However, the change from the differential (riveted) to integral (welded) design introduces new aspects which potentially need to be considered in the analysis route for cracked welded components made of thin sheets. The material is no longer homogeneous since joining of aluminium alloys by LBW and FSW usually produces a weld joint area having significantly lower strength (undermatching) than the base material. In such welded structures, a lower strength weld zone leads to a localization of the plastic strain if the component experiences a high level of external loads. In particular, for cracks located in the weld material, the plastic zone at the crack tip is entirely confined to the softer weld material leading to an increase of the crack tip constraint which in turn influences the fracture performance.

Unlike in the differential structure where a skin crack grows underneath a stringer, the skin crack in an integral structure also propagates into the stringer adding a new crack to the structure, **Fig. 1.1**. Failure may then occur due to instability of the skin crack as well as the stringer crack. Thus, stringer failure criterion should also be based on the fracture mechanics approach. This crack branching effect is not covered in the conventional residual strength prediction tool for riveted structures and its significance for the failure prediction of integrally stiffened welded panels needs to be analyzed.

1.1 Objectives

The aim of this study is to improve the understanding of the fracture behaviour of LBW and FSW butt joints in thin Al-alloy sheets with a long crack under static loading as well

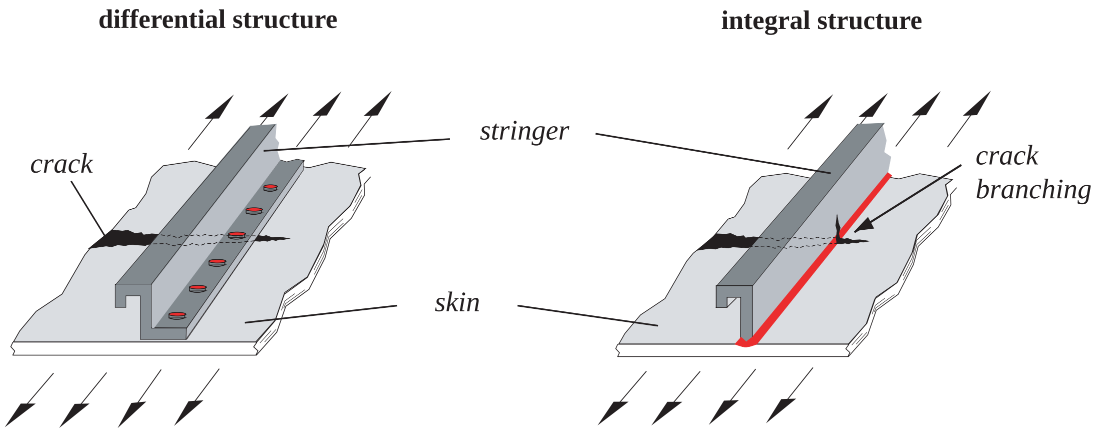

Figure 1.1: Differential (riveted) versus integral (welded) structure.

as the residual strength behaviour of integrally stiffened LB welded panels and to propose a verified engineering methodology for the residual strength prediction of thin-walled welded structures.

The objectives of the work conducted are:

- to investigate the deformation and ductile fracture behaviour of LBW and FSW joints under static loading and identify the crack growth mechanisms,
- to identify the fracture toughness criteria for thin welded components and the weakest zones of the LBW and FSW joints with respect to ductile crack growth,
- to determine the strain distribution (plastic zone development) in and around both kind of weld joints (and at the crack tip) using a remote digital image analysis technique, and hence to improve the understanding of the plastic zone development, deformation and fracture process for strength mismatched welds,
- to conduct residual strength tests on LBW and FSW M(T) panels to generate the data on the deformation and fracture properties of these weld joints,
- to conduct residual strength tests on LB welded stiffened panels with a one-bay and two-bay (over the broken central stringer) cracks to determine the deformation and failure loads of these panels,
- to identify the specific features of LBW and FSW joints for the application of the defect assessment procedure SINTAP to predict the residual strength of LBW and FSW M(T) panels as well as of the LB welded stiffened panels,
- to develop a basis for engineering tools to assess the residual strength of welded airframe panels containing cracks with different crack lengths up to the two-bay crack.

1.2 Structure of the thesis

The thesis starts with the state-of-the-art given in Section 2 including the theoretical background to the fracture mechanics parameters in elastic and elastic-plastic materials. The current approach to the residual strength predictions of aerospace structures has been reviewed highlighting the drawbacks when applied to welded structural components. Specific features of weldments have also been reviewed, including the effects of weld strength mismatch on the crack driving force as well as the resistance to crack propagation. Existing defect assessment procedures, including their modifications for weld defects, have been presented and their potential of application to thin-walled welded aerospace structures is discussed.

In Section 3, the Structural Integrity Assessment Procedure SINTAP is introduced which is used as a residual strength prediction methodology in this study. The background to the derivation of the underlying set of equations is also presented.

The results of the experimental program including the mechanical characterization of base and weld materials, and results of the residual strength and fracture behaviour of cracked LBW and FSW unstiffened as well as stiffened LB welded panels are presented in Section 4. All material data required for the residual strength analysis of all welded panels investigated in this study are given in this section.

The application of the SINTAP procedure needs the stress intensity factor and the yield load solutions of the cracked component to be assessed. For homogeneous and butt welded middle cracked tension loaded panels, these solutions can be found in the open literature. However, the yield load and stress intensity factor solutions of cracked integrally stiffened welded panels are not available in the literature so that there is a need to generate this input information in order to predict the residual strength of stiffened welded panels using the SINTAP procedure. In Section 5, these input parameters have been numerically derived by means of the finite element method for one-bay and two-bay crack scenarios, respectively.

In Section 6, the SINTAP predictions of the residual strength are compared with the experimental results giving recommendations for the use of the SINTAP procedure as a prediction tool for welded panels.

2 State-of-the-Art

2.1 Theoretical background to fracture mechanics

2.1.1 K-factor

The two generally accepted approaches to linear elastic fracture mechanics (LEFM) are based on the singular nature of the stress distribution at a crack tip and on the energy balance.

In 1957 Irwin [3] developed a series of linear elastic crack stress field solutions using Westergaard's [4] equations. Taking the notation and coordinate system illustrated in **Fig. 2.1**, these singular solutions for mode I are [5]:

$$\sigma_{\mathrm{xx}} = \frac{K_{\mathrm{I}}}{\sqrt{2\pi r}} \cos\frac{\theta}{2}\left(1 - \sin\frac{\theta}{2}\sin\frac{3\theta}{2}\right) \tag{2.1}$$

$$\sigma_{\mathrm{yy}} = \frac{K_{\mathrm{I}}}{\sqrt{2\pi r}} \cos\frac{\theta}{2}\left(1 + \sin\frac{\theta}{2}\sin\frac{3\theta}{2}\right) \tag{2.2}$$

$$\tau_{\mathrm{xy}} = \frac{K_{\mathrm{I}}}{\sqrt{2\pi r}} \cos\frac{\theta}{2}\sin\frac{\theta}{2}\cos\frac{3\theta}{2} \tag{2.3}$$

and

$$\sigma_{\mathrm{zz}} = \nu(\sigma_{\mathrm{xx}} + \sigma_{\mathrm{yy}}) \qquad \text{for plane strain} \tag{2.4}$$

$$\sigma_{\mathrm{zz}} = 0 \qquad \text{for plane stress} \tag{2.5}$$

where ν is Poisson's ratio.

The respective displacement fields are [5]:

$$u = \frac{K_{\mathrm{I}}}{8\mu}\sqrt{\frac{2r}{\pi}}\left[(2\kappa - 1)\cos\frac{\theta}{2} - \cos\frac{3\theta}{2}\right] \tag{2.6}$$

$$v = \frac{K_{\mathrm{I}}}{8\mu}\sqrt{\frac{2r}{\pi}}\left[(2\kappa + 1)\sin\frac{\theta}{2} - \sin\frac{3\theta}{2}\right] \tag{2.7}$$

and

$$w = 0 \qquad \text{for plane strain} \tag{2.8}$$

$$w = -\frac{\nu}{E}\int(\sigma_{\mathrm{xx}} + \sigma_{\mathrm{yy}})dz \qquad \text{for plane stress} \tag{2.9}$$

where μ is the shear modulus, $\kappa = 3 - 4\nu$ for plane strain and $\kappa = (3 - \nu)/(1 + \nu)$ for plane stress.

In analogy, singular stress and associated displacement fields are defined for mode II and mode III, see eg. [5]. The omission of higher order terms in r from the above equations

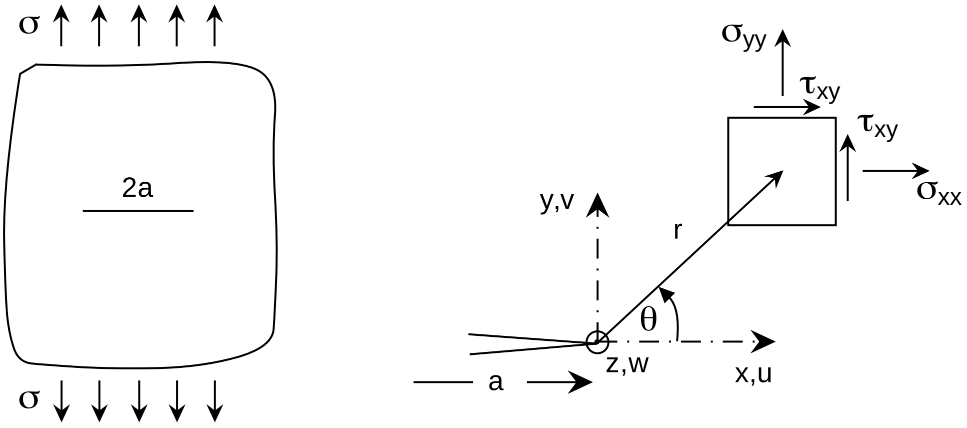

Figure 2.1: Coordinates, stress and displacement components in the crack tip stress field.

gives acceptable approximations to the stress and displacement fields provided that r is small compared to other dimensions in the x-y plane, eg. crack length.

The parameter

$$K_\mathrm{I} = \sigma\sqrt{\pi a}\,\beta \tag{2.10}$$

is the stress intensity factor and may be described as the amplitude of the inverse square root stress singularity at the crack tip and is independent of r and θ. σ is the uniform stress normal to the crack plane at infinity, a is the half length of the through-thickness crack, and β is the geometry correction function.

For linear elastic material, K_I is related to the elastic strain energy release rate, G_I, through the following equation:

$$G_\mathrm{I} = \frac{K_\mathrm{I}^2}{E'} \tag{2.11}$$

where $E' = E$ for plane stress and $E' = E/(1-\nu^2)$ for plane strain condition. E and ν are Young's modulus and Poisson's ratio, respectively.

The above observations are valid for linear elastic materials. In ductile materials a plastic zone is present at the crack tip. The estimation of its size can be obtained by considering the distance from the crack tip, r_Y, at which the local stress, σ_yy, is equal to the yield strength, $R_\mathrm{p0.2}$. Thus, substituting $R_\mathrm{p0.2}$ for σ_yy in Eq. (2.2) gives for $\theta = 0$ the Irwin's plastic zone correction [6]:

$$r_\mathrm{Y} = \frac{1}{2\pi}\left(\frac{K_\mathrm{I}}{R_\mathrm{p0.2}}\right)^2 \tag{2.12}$$

which is the first approximation of the plane stress plastic zone. Taking into account the stress redistribution of the stress truncated above the yield strength value, the plane stress plastic zone is then $2r_\mathrm{Y}$ which is considered the second approximation [6]. In this way the allowance for small crack tip plasticity can be made if the real crack is virtually extended by the distance r_Y as shown in **Fig. 2.2**.

If the plastic zone at the crack tip becomes large compared to the crack length or other geometrical dimensions of the cracked structure, the stress and strain fields are no longer

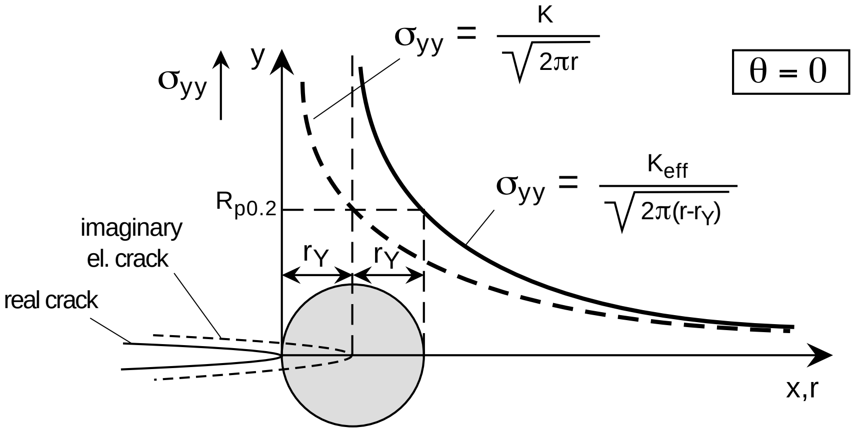

Figure 2.2: Irwin's plastic zone correction and the resulting imaginary elastic crack.

characterized by the linear elastic stress intensity factor K. In elastic-plastic fracture mechanics (EPFM), two additional fracture controlling parameters are introduced: the crack tip opening displacement and the J-integral.

2.1.2 Crack tip opening displacement (CTOD)

Wells [7] performed an approximate analysis that related the crack tip opening displacement (CTOD) to the K-factor under small scale yielding conditions. Solving for the displacement at the physical crack length, a, by assuming an effective crack length of $a + r_\mathrm{Y}$, Eq. (2.7) gives a displacement of the crack flanks, **Fig. 2.2**, at a distance r_Y behind the crack tip:

$$v = \frac{\kappa + 1}{2\mu} K_\mathrm{I} \sqrt{\frac{r_\mathrm{Y}}{2\pi}}. \tag{2.13}$$

Substituting Irwin's plastic zone correction for plane stress as given in Eq. (2.12) into Eq. (2.13) gives:

$$\delta = 2v = \frac{4}{\pi} \frac{K_\mathrm{I}^2}{R_\mathrm{p0.2} E} \tag{2.14}$$

where δ is CTOD, **Fig. 2.3**.

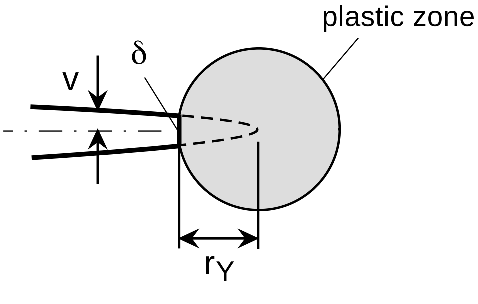

Figure 2.3: Definition of the Crack Tip Opening Displacement (CTOD).

Alternatively, CTOD can be derived using Dugdale's strip yield model which assumes plane stress conditions and a perfectly plastic material (see eg. [6]):

$$\delta = \frac{K_\mathrm{I}^2}{R_\mathrm{p0.2} E}. \tag{2.15}$$

The above expression differs from Eq. (2.14) by the factor $4/\pi$. Generally, CTOD depends on the stress state. For the case of an ideally plastic material, the relationship between CTOD and K_I can be written as:

$$\delta = \frac{K_\mathrm{I}^2}{m R_\mathrm{p0.2} E'} \tag{2.16}$$

where m is a dimensionless constant ($m = 1.0$ for plane stress and $m = 2.0$ for plane strain), $E' = E$ for plane stress and $E' = E/(1-\nu^2)$ for plane strain.

2.1.3 J-integral

The path independent J-integral was first introduced into fracture mechanics by Cherepanov [8] and Rice [9]. Its formal expression is given by:

$$J = \int_\Gamma \left(\mathcal{W}\, dy - T_i \frac{\partial u_i}{\partial x}\, ds \right) \tag{2.17}$$

where Γ is the integration path running counter-clockwise, i.e. mathematically positive, around the crack tip, T_i are the components of the traction vector, u_i are the displacement vector components, and ds is the length increment along the contour Γ, **Fig. 2.4**. The strain energy density, $\mathcal{W}$, per unit volume is:

$$\mathcal{W} = \int_0^{\varepsilon_{ij}} \sigma_{ij}\, d\varepsilon_{ij} \tag{2.18}$$

where σ_{ij} and ε_{ij} are stress and strain tensors, respectively. The components of the traction vector are defined as:

$$T_i = \sigma_{ij} n_j \tag{2.19}$$

where n_j are components of the unit vector normal to Γ.

Rice [9] also showed the equivalence of the J-integral with the strain energy release rate:

$$J = -\frac{1}{B}\frac{\partial U}{\partial a} \tag{2.20}$$

where B is the thickness and U is the potential energy which is equal to the work of external forces in equilibrium. For a specific case of a linear elastic material, J is equal to the linear elastic strain energy release rate, G:

$$J = G. \tag{2.21}$$

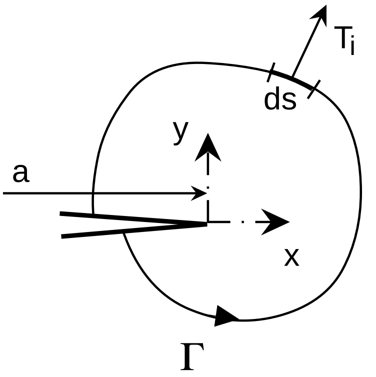

Figure 2.4: Path Γ for the evaluation of the J-integral.

Hutchinson [10] and Rice and Rosengren [11] independently showed that J characterizes the intensity of the stress and strain fields near the crack tip (also called the HRR field) in a nonlinear elastic material with a relationship for uniaxial deformation given by the Ramberg-Osgood equation:

$$\frac{\varepsilon}{\varepsilon_0} = \frac{\sigma}{\sigma_0} + \alpha \left(\frac{\sigma}{\sigma_0} \right)^n \tag{2.22}$$

where σ_0 is a reference stress which is usually equal to the yield strength, $\varepsilon_0 = \sigma_0 / E$ (E is Young's modulus), α is a dimensionless constant, and n is the strain hardening exponent (note $1 \leq n < \infty$). The stress and strain distributions in front of the crack tip in a such material are then:

$$\sigma_{ij} = \sigma_0 \left(\frac{EJ}{\alpha \sigma_0^2 I_{\mathrm{n}} r} \right)^{\frac{1}{1+n}} \tilde{\sigma}_{ij}(n, \theta) \tag{2.23}$$

and

$$\varepsilon_{ij} = \frac{\alpha \sigma_0}{E} \left(\frac{EJ}{\alpha \sigma_0^2 I_{\mathrm{n}} r} \right)^{\frac{n}{1+n}} \tilde{\varepsilon}_{ij}(n, \theta) \tag{2.24}$$

where I_{n} is an integration constant depending on n, and $\tilde{\sigma}_{ij}$ and $\tilde{\varepsilon}_{ij}$ are dimensionless functions of n and θ. All of these parameters are dependent on the stress state (i.e. plane stress or plane strain).

2.2 Current state of residual strength analysis of riveted structures

2.2.1 Damage tolerance philosophy

Historically, there are three different approaches for ensuring the safety of an aircraft structure. They can be briefly summarized as follows:

1. *Safe-life* approach predicts the replacement time for an aircraft component in terms of a number of service cycles usually specified as a number of landings or flight hours. The replacement time or the safe-life is obtained from component fatigue tests and is based upon the time period for failure. Once a component has reached its safe-life, it is replaced, whether or not any fatigue cracks are present. However, this approach involves two significant problems: (a) the presence of manufacturing or accidental defects which drastically reduce the life time of a component is not accounted for and (b) to ensure a reasonable service life, the components tend to be over-designed and the selected safety factors are conservative which may lead to a premature replacement of potentially serviceable components.

2. In a *fail-safe* philosophy a structure is capable of sustaining a certain amount of damage without catastrophic failure of the entire structure. This design approach usually includes additional load path elements to enhance the residual strength of the structure and crack arrest features to prevent cracks from propagating to failure. In a fail-safe design, an aircraft remains airworthy until the damage is detected and repaired. The specification of necessary inspection intervals is based on the service experience and does not consider the initiation and growth of cracks.

3. *Damage tolerance* approach assumes that the structure contains an initial flaw or defect that will grow under the service usage. The objective of this design philosophy is to detect cracks in the structural elements before they propagate to failure. The damage tolerance approach requires a fracture mechanics based engineering evaluation of crack growth and residual strength characteristics to establish the inspection intervals. The crack propagation is investigated to determine the time the crack will require to reach the critical size which is specified by the residual strength of the structural element.

In addition to requirements such as strength, stiffness, and aeroelastic response, it is necessary to design and maintain both metallic and composite aircraft structures to withstand the effects of damage. To ensure that aircraft structures are designed and maintained to withstand the effects of damage, the Federal Aviation Administration (FAA) and United States Air Force (USAF) have established specific guidelines which must be followed. The FAA requires commercial transport aircraft certified under Part 25 of the Federal Aviation Regulations (FAR) to meet certain damage tolerance requirements which essentially state that:

- the residual strength of an airframe structural component shall not drop below that required to sustain some load level (in most cases limit load, which is the maximum load to be expected in service, or some multiple thereof),

- that inspections must be scheduled to ensure that the required level of residual strength is maintained.

An important step in the satisfaction of the damage tolerance requirements by commercial and military airframe manufacturers and maintenance organizations is through the performance of a damage tolerance assessment. The damage tolerance assessment involves the development of damage growth curves and residual strength diagrams for individual structural components of an airframe. This allows the residual strength as a function of aircraft usage to be determined. Further, with this information appropriate inspection intervals can be specified which ensure that the structural integrity of the aircraft will be maintained throughout its life.

2.2.2 Residual strength approach to (riveted) stiffened panels

The current approach to the residual strength analysis of airframe structures is based on linear elastic fracture mechanics where the stress intensity factor, K, is the crack tip parameter. The extension to the effective stress intensity factor, K_{eff}, takes into account the plasticity effect at the crack tip. This approach is legitimate as long as the plastic zone size in front of the crack tip is much smaller than other geometrical dimensions like the crack length. For high strength materials used in aircraft design, the above condition is generally fulfilled, justifying the use of linear elastic fracture mechanics.

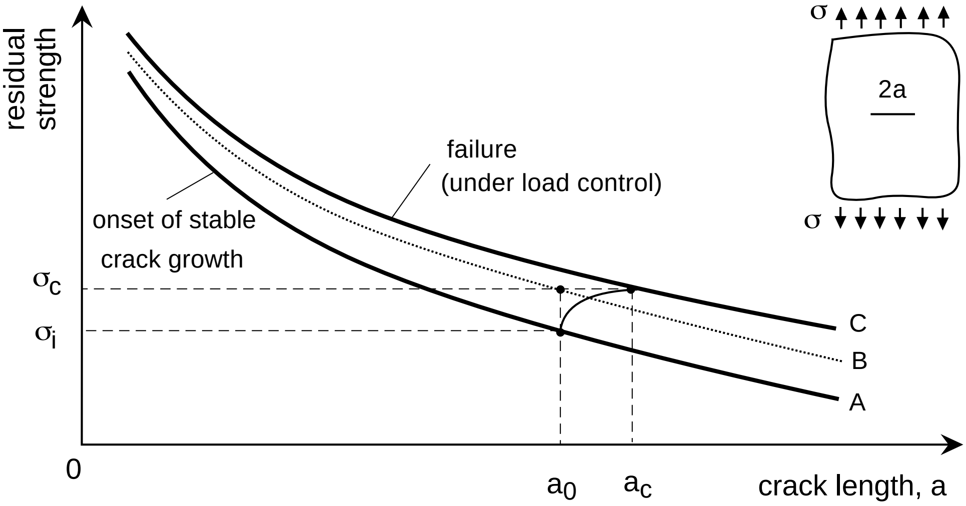

Figure 2.5: Residual strength diagram of a thin sheet of infinite width, after [12].

Fig. 2.5 schematically shows a residual strength diagram of an infinitely wide thin sheet. At the applied stress σ_{i} the crack of initial length a_0 starts to grow in a stable manner. If the loading is increased to σ_{c} the crack will extend to a_c at which time the failure occurs.

The lowest curve (curve A) in this diagram defines the onset of the stable crack extension:

$$\sigma_{\text{i}} = \frac{K_{\text{i}}}{\sqrt{\pi a_0}} \frac{1}{\beta} \tag{2.25}$$

where K_{i} is the stress intensity at crack initiation.

The upper curve (curve C) represents the residual strength as a function of the critical crack length, a_{c}:

$$\sigma_{\mathrm{c}} = \frac{K_{\mathrm{c}}}{\sqrt{\pi a_c}} \frac{1}{\beta} \tag{2.26}$$

where K_{c} is known as plane stress fracture toughness. If the stable crack extension is not monitored, the residual strength diagram can be based on the initial crack length (curve B):

$$\sigma_{\mathrm{c}} = \frac{K_{\mathrm{c0}}}{\sqrt{\pi a_0}} \frac{1}{\beta} \tag{2.27}$$

where K_{c0} is often referred to as apparent fracture toughness and is based on the maximum applied stress and initial crack length.

The principle of a residual strength diagram of a stiffened structure is shown in **Fig. 2.6**. For short skin cracks, the skin failure line is close to that of unstiffened panels. The effect of the stringer comes into play for longer cracks. The closer the skin crack approaches the stringer, the more load is transferred from the skin to the stringer. Thus, the stress intensity at the skin crack tip reduces leading to an increase of the skin failure stress. On the other hand, with increasing skin crack, the stringer carries more load; thus, the residual strength of the stringer decreases. The stringer failure line (which corresponds to the residual strength of the stringer) sharply drops in the case where the skin crack is close to the stringer.

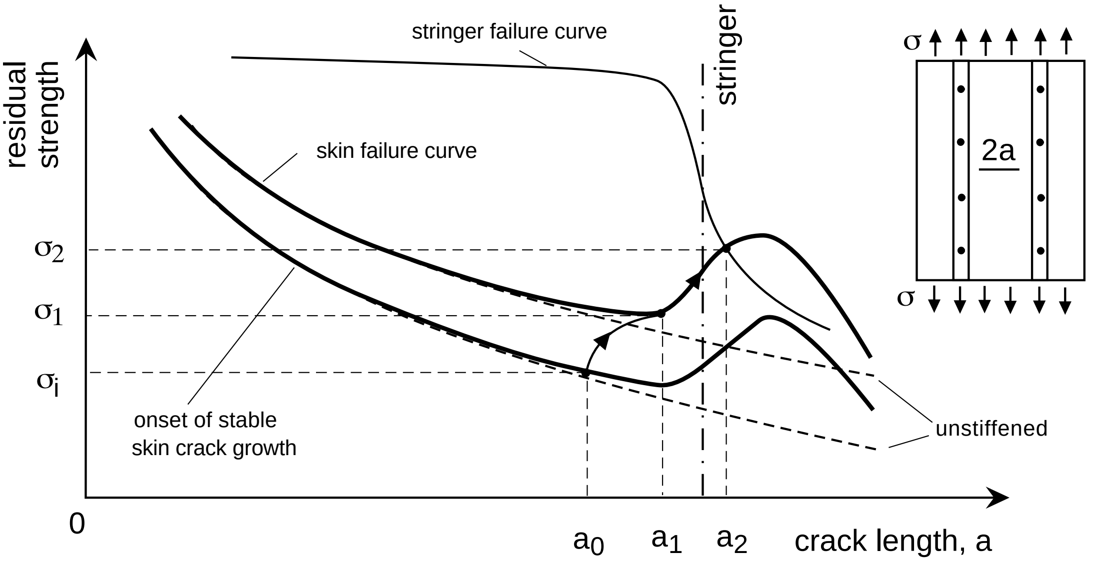

Figure 2.6: Residual strength diagram of a stiffened riveted panel with a one-bay crack, after [12].

Consider a particular crack scenario in a stiffened structure with an initial half crack length a_0, **Fig. 2.6**. The initiation of stable crack growth takes place at the applied stress σ_{i}. With further load increase up to σ_1 the skin crack stably extends to a_1 reaching the failure curve of the skin. However, due to the stringer effect the skin failure line rises. The skin does not fail at this stage but is able to sustain higher loads. The stringer, however, carries more and more load until the skin crack grows to a_2. At this point, the stringer failure curve intersects the skin failure line. Any load increase above σ_2 will cause a stringer failure whereas the skin is stable.

The residual strength of a stiffened riveted structure is defined by the individual failure of the three structural elements:

- skin failure
- stringer (general: stiffener) failure
- rivet failure.

The skin failure criterion is defined in terms of applied gross stress, σ, as [13]:

$$\sigma = \frac{K_\mathrm{c}}{\sqrt{\pi a_c}} \frac{1}{\beta} \tag{2.28}$$

where β is the geometry (due to stiffener) correction function.

The stringer failure criterion in terms of applied gross stress is given as [13]:

$$\sigma = \frac{R_\mathrm{m}^\mathrm{str}}{L_\mathrm{s}} \tag{2.29}$$

where $R_\mathrm{m}^\mathrm{str}$ is the ultimate tensile strength of the stringer material and

$$L_\mathrm{s} = \frac{F_\mathrm{max}}{F_\infty} \tag{2.30}$$

is the stringer load concentration factor defining the ratio between the maximum load in the stringer in the cracked region, F_max, and the remote stringer load unaffected by the crack, F_∞. L_s as well as β are functions of the skin crack length.

The rivet failure occurs if the maximum shear stress resulting from the rivet forces exceeds the shear strength of the rivet material.

The construction of such residual strength diagrams presented above is based on the assumption that the fracture toughness values K_i, K_c0, and K_c are material constants, i.e. they are size and geometry independent. The assumption for the initiation toughness K_i may be true (see eg. [14]) but the critical fracture toughness is generally size and geometry dependent.

2.2.3 Effect of size and geometry on fracture toughness K_c

It is well known that the fracture toughness of a material is thickness dependent. Moreover, for a given thickness in thin sheets, K_c is influenced by the initial crack length and specimen width, **Fig. 2.7**. For a fixed panel width, there is an intermediate range of

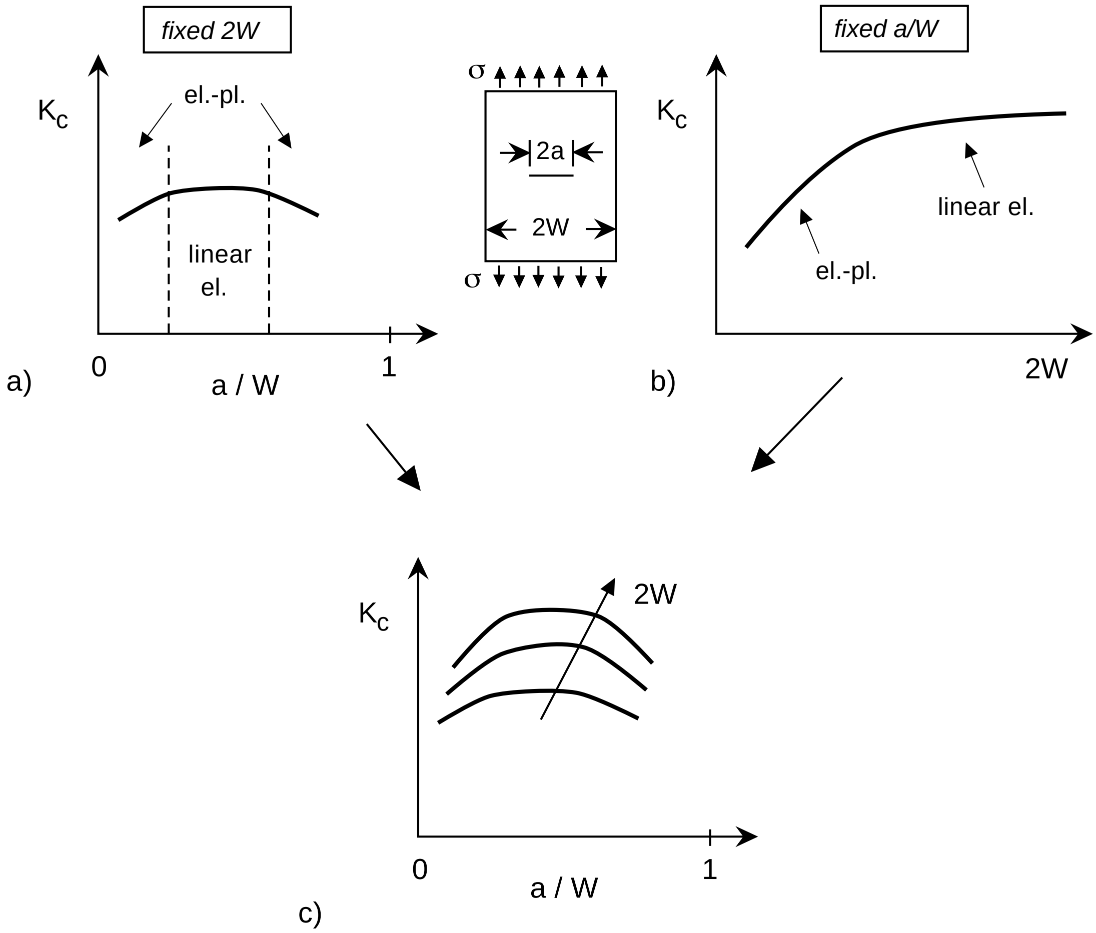

Figure 2.7: Variation of K_c with a) crack length and b) panel width. In c) the combination of a) and b) is shown; after [15].

crack length to width ratios, a/W, where the linear elastic fracture mechanics approach is applicable, i.e. net section stress is below the yield stress of the material. Outside this range - for short and long cracks - the fracture behaviour of the test panel is affected by net section yielding. On the other hand, for a fixed a/W, the critical stress intensity factor, K_c, increases with increasing panel width. Narrow panels suffer from the net section yielding resulting in lower (formally determined) K_c-values. These effects were first addressed by Srawley and Brown [15]. Further investigations on thin sheets of different aerospace aluminium alloys were conducted by Schwalbe and Setz [14] concluding identical trends.

This variation of K_c can be predicted by the R-curve approach presented in the subsequent section.

2.2.4 R-curve approach

During residual strength tests of cracked panels, the applied load is steadily increased. This load increase is generally accompanied by stable crack extension until the crack length and the applied stress result in a critical stress intensity factor at the crack tip. This phenomenon is handled by the fracture resistance curve (R-curve) approach.

The R-curve represents the rate of energy absorption in the creation of new surfaces and in plastic deformation at the crack tip. The R-curve is obtained experimentally by continuously increasing the applied load and simultaneously measuring the stable crack extension. The R-curve is then a plot of a crack tip loading parameter versus the corresponding stable crack extension.

ASTM E561 [16] is a standard for R-curve determination which is widely used in the aerospace industry. It is currently the only standard for the fracture toughness determination of thin sheet materials. To account for crack tip plasticity, the standard is based on the effective crack length, a_{eff}. It has been shown for different materials that within the validity range, i.e. net section stress of the specimen is below the yield strength of the material, the K_{eff} R-curves are independent of specimen size (width) and geometry (initial crack to width ratio).

The tangency point between the R-curve and the crack driving force defines the critical stress intensity factor, K_{c}. **Fig. 2.8** shows that for different initial crack lengths the tangency condition is met at different points on the R-curve which is assumed to be a material property. From this observation it can be concluded that the critical stress intensity factor cannot be a material constant.

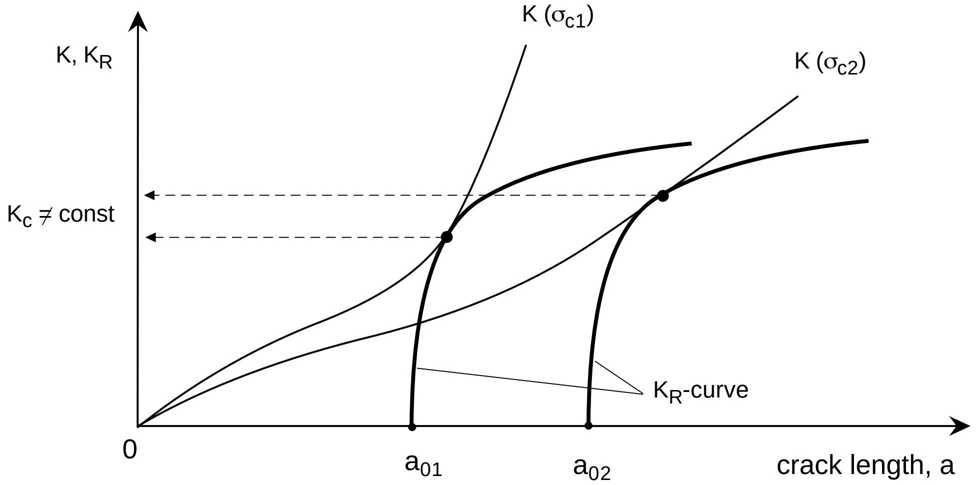

Figure 2.8: K_{R}-curve as a material property for different initial crack lengths. The tangency condition gives the critical stress intensity factor, K_{c}, which is not a constant.

The R-curve approach to stiffened riveted panels is depicted in **Fig. 2.9**. The R-curve as obtained from the ASTM E561 standard is plotted into the diagram starting from the initial crack length, a_0. For the applied stress σ_{c1} the crack driving force is tangent to the R-curve predicting instability of the skin crack. However, the crack is arrested since the crack driving force falls below the R-curve due to the stringer effect which reduces the crack tip stress. An increase in the applied stress to the value σ_{c2} leads to the second

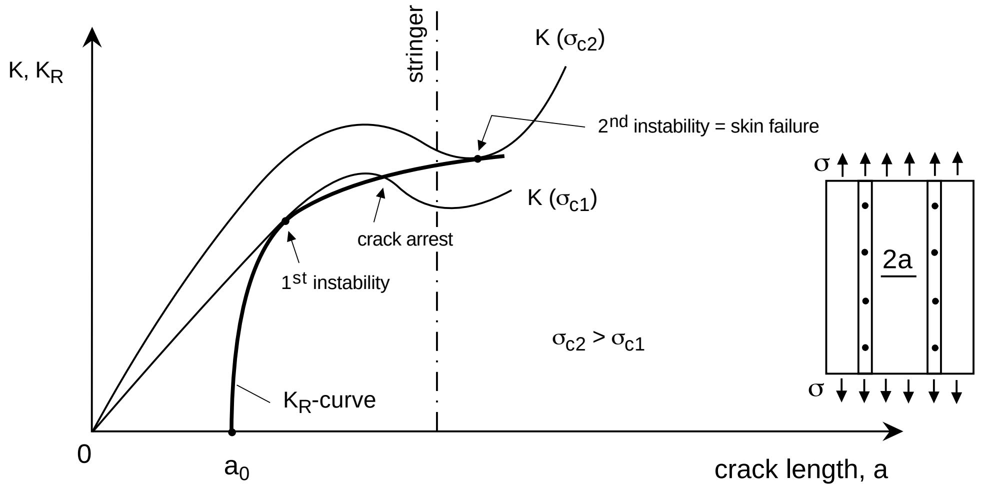

Figure 2.9: R-curve approach to stiffened panels with a one-bay crack.

instability of the arrested skin crack. It should be noted that the crack driving force is calculated for a constant stress, thus being a function of the crack length only:

$$K = \sigma\sqrt{\pi a}\,\beta. \tag{2.31}$$

Any attempt to correct for plasticity effects at the crack tip (eg. Irwin correction) resulting in any effective crack length will not change the shape of the crack driving force determined in Eq. (2.31). This is due to the fact that a is an independent variable. Therefore, the tangency points will remain. The geometry correction function β in Eq. (2.31) for riveted structures can be determined analytically by means of the displacement compatibility method [13,17].

2.3 Strength mismatched welds

A large amount of research effort has been undertaken worldwide regarding the experimental and numerical aspects of the strength mismatch in welded joints. This issue has been a topic at two international conferences [18,19]. This section briefly describes the general features of strength mismatched welds with regard to their fracture and deformation behaviour.

2.3.1 Strength mismatch phenomenon

Welded joints may exhibit substantial mechanical heterogeneity with respect to deformation and fracture properties. The heterogeneity in deformation properties may have an effect on the crack driving force. The measure of the heterogeneity is defined as the weld strength mismatch ratio, M:

$$M = \frac{R_{\mathrm{p0.2W}}}{R_{\mathrm{p0.2B}}} \tag{2.32}$$

where $R_{\mathrm{p0.2W}}$ and $R_{\mathrm{p0.2B}}$ are the uniaxial yield strengths of the weld and base materials, respectively. $M > 1$ is referred to as *overmatching* and $M < 1$ as *undermatching.*

Assuming that the elastic properties such as Young's modulus and Poisson's ratio are identical for both weld and base materials, the heterogeneity of the deformation properties should not play any role as long as the external loading causes elastic strains in all constituents of the joint. As soon as one of the joint materials is loaded beyond its yield strength, strength mismatch becomes significant. **Fig. 2.10** demonstrates the strength mismatch on a transversely welded panel loaded in tension. All three configurations (under-, even, and overmatch) are externally loaded to the same stress level, σ, which causes different amounts of the local strain due to the different uniaxial stress-strain relationships of each material. In the undermatched weld, the strain is higher than in the base material. For relatively high degree of undermatching, the plastic strain may be entirely confined to the weld material while the base material remains elastic. In such a configuration the local ductility of the weld metal may be exhausted at a low global deformation of the panel. In the case of overmatching, the stronger weld metal reduces the strain in the weld material compared to that in the base plate, shifting the potential failure location to the base metal.

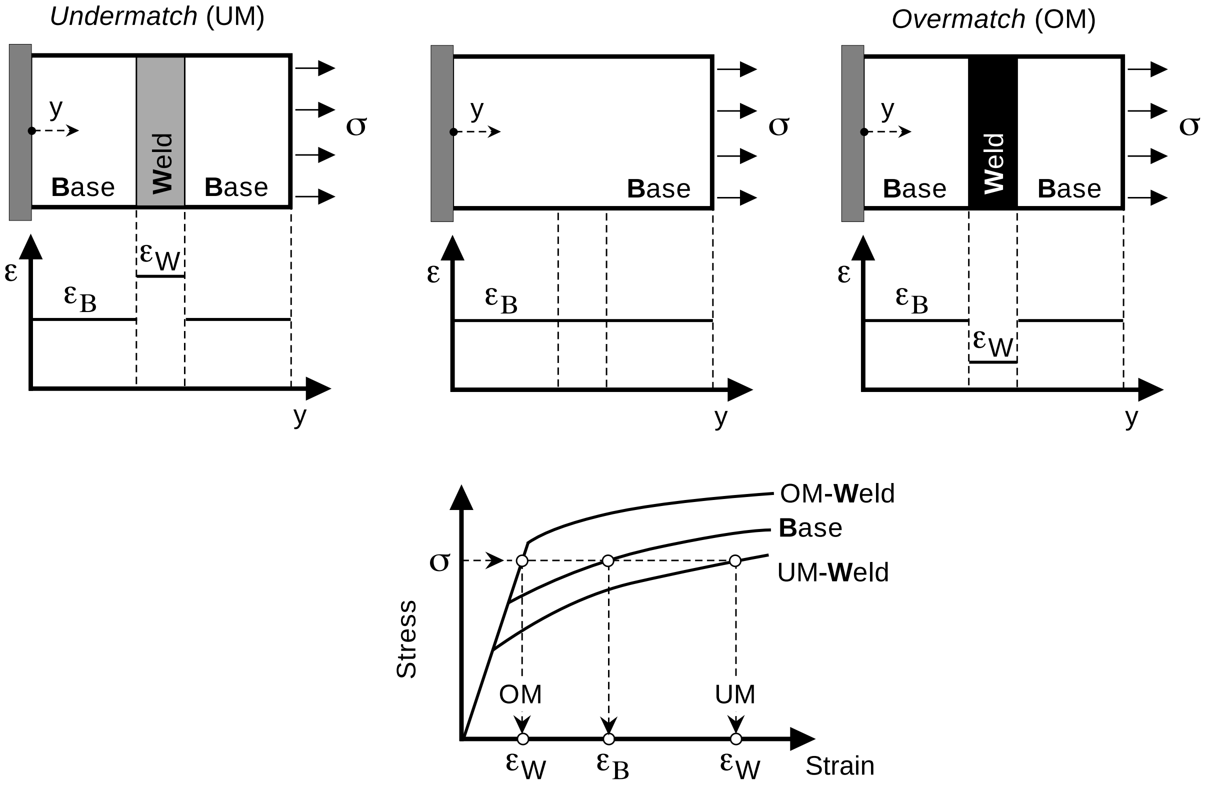

Figure 2.10: Strength mismatch phenomenon for a welded panel loaded transverse to the weld direction. ε_{B} and ε_{W} denote the strain in the base and weld materials, respectively.

In the presence of cracks in the weld, plastic strain localization occurs at the crack tips even at nominally elastic applied loads, i.e. loads below the yield strength of the weakest material. Depending on the mismatch ratio, M, the spread of the plastic zone can obtain different patterns which in turn highly influences the crack tip loading as shown in **Fig. 2.11**. The same applied load causes different plastic zone shapes and sizes ahead of the crack tip. For a given applied load, the crack driving force in the undermatched weld is higher than a crack would have in the plain base material. In the overmatched weld, the stronger weld metal shields the crack from extensive plastic deformations leading to a lower crack driving force than a crack would experience in the base material.

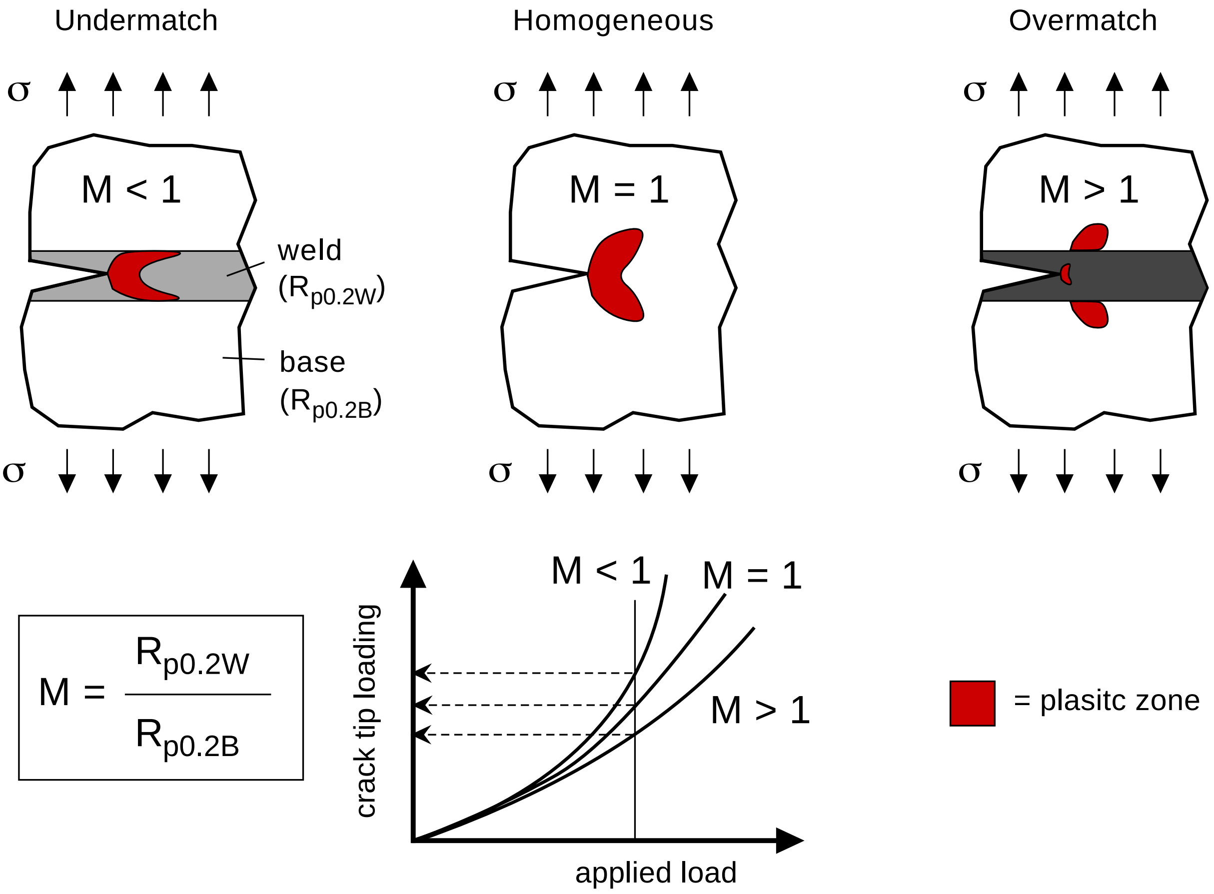

Figure 2.11: Plastic zone patterns for different strength mismatch levels.

2.3.2 Constraint effect on fracture

In the following sections, the influence of constraint on the crack driving force and fracture resistance will be given in terms of qualitative trend diagrams gathered from the published literature. First, it should be noted that the term *constraint* lacks a unique definition. For the general discussion, however, it can be understood literally as a structural obstacle against plastic deformation. The overall structural condition determines the local stress triaxiality, commonly defined as the ratio of hydrostatic and yield stress (which is a function of the equivalent plastic strain in a hardening material), $\sigma_\mathrm{h}/\sigma_\mathrm{e}$. In this sense, the stress triaxiality may be interpreted as the local constraint effect.

It is well known that the resistance to crack initiation and propagation of ductile crack growth depends on the geometry and loading configuration (bending or tension) of the specimen or structural component. The difference is related to the fundamental mechanism of ductile fracture which is governed by the void growth and coalescence and is sensitive to the triaxial stress state. High stress triaxiality promotes this ductile fracture process resulting in a lower fracture toughness.

Crack tip constraint and the resulting triaxiality of the stress state is the reason for the transferability problem of fracture data obtained from small laboratory specimens to be used in the prediction of fracture behaviour of large and complex components. Geometrical differences between cracked bodies of the same material affect the stress distribution around the crack tip and, consequently, preclude the definition of a single material fracture toughness parameter. When analyzing strength mismatched welds, it is important to consider constraint effects not only due to the specimen geometry and loading but also those induced by the material heterogeneity: mismatch of material properties and joint dimensions. Overmatching results in a reduction in constraint, whereas undermatching in an increase in constraint at the crack tip for a crack in the center of the weld metal.

Various approaches have been proposed to quantify these constraint effects in homogeneous as well as heterogeneous materials. The basic ideas of these approaches have been discussed by Brocks and Schmitt [20]. All of these approaches like the elastic T-stress [21–23], the Q-stress [24] and the A_2-stress [25, 26] address the in-plane constraint, which is influenced by the specimen dimension in the direction of the growing crack, and do not cover the out-of-plane constraint, which is affected by the specimen dimension parallel to the crack front. For a given in-plane configuration, the plane strain condition gives the highest possible out-of-plane constraint resulting in the highest stress triaxiality, whereas the plane stress condition yields the lower limit. In a three-dimensional cracked body, the out-of-plane constraint lies between these two limiting cases.

The Q_M-approach [27, 28] is the same as the Q-stress approach but addresses the effect of the material mismatch on the crack tip stress field. The parameter Q_M represents the Q-stress quantifying the difference between the crack tip stress distributions due to the material mismatching measured at a distance $r/(J/\sigma_\mathrm{Y}) = 2$ and $\theta = 0$ from the crack tip (r is the radial coordinate in a polar coordinate system, J is the J-integral value, and σ_Y is the yield strength of the material where the crack is located). Whereas in overmatching the change of the stress distribution due to material mismatch could be approximated by Q_M, no elevation in the stress field at $r/(J/\sigma_\mathrm{Y}) = 2$ has been observed in undermatching [29]. However, at distances from the crack tip greater than this, the stress distribution can be elevated significantly above that in homogeneous specimens [30] (see Section 2.3.6). Thus, the Q_M-approach may work for overmatching but appears to fail for undermatching. To be able to capture any effect with this method, the distance at which Q_M is determined must be increased. This will not be consistent with the overall Q-stress approach for which numerous compendia already exist.

2.3.3 Effect of geometry on fracture resistance in homogeneous materials

Fig. 2.12 summarizes the effect of the geometry (crack ratio, a/W) and loading type (bending or tension) on the crack tip triaxiality in homogeneous specimens [31,32]. The results schematically shown in this diagram were derived from the analysis based on the slip line theory. If the plane strain condition prevails, the in-plane constraint of a bend specimen is higher than that of a tension specimen, leading to a lower R-curve for a bend specimen than for a tension specimen. Moreover, the fracture resistance of a shallow-cracked bend specimen is higher than that of a deeply-cracked specimen due to the geometry effect (a/W). On the other hand, under the plane stress condition, the effect of the geometry and loading mode on the crack tip stress triaxiality is very small implying that the fracture resistance obtained from a bend or tension specimen may be considered unique. Indeed, Hellmann and Schwalbe [33] found in their tests on a high strength aluminium alloy that all data points from M(T), C(T) and SE(B) specimens form a common R-curve. Similar results were obtained for an austenitic steel [34].

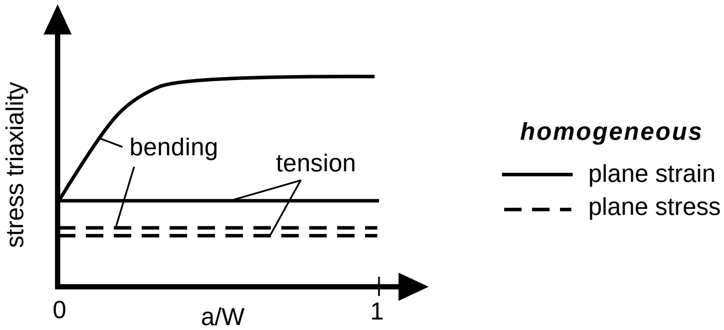

Figure 2.12: Schematic showing the effect of geometry and loading type on the stress triaxiality in homogeneous specimens, after [31,32].

Liu and Zhuang [35] analyzed different homogeneous specimen types (SE(B), DE(T), SE(T), and M(T)) under both plane stress and plane strain conditions using the finite element method. They observed that the opening stress component is almost independent of the specimen type under plane stress conditions, whereas the analysis did show a specimen type effect under plane strain conditions. Hence, this numerical result concludes a geometry independence of the crack characterization under plane stress condition and confirms the experimental findings mentioned above.

2.3.4 Effect of strength mismatch on crack driving force

Lei et al. [36] analyzed the effect of mismatch on the crack driving force using a 2D plane stress elastic-plastic finite element analysis of an M(T) specimen. Different mismatch levels were attained by varying the base material properties while keeping the weld material properties constant. The results are schematically shown in **Fig. 2.13a**. For a given applied load level, the stress intensity at the crack tip in terms of the J-integral of an undermatched weld ($M < 1$) is higher than for a homogeneous case ($M = 1$), whereas overmatching ($M > 1$) decreases the crack tip loading. Similar findings were reported by Hao et al. [37] for an SE(B) specimen under plane strain conditions.

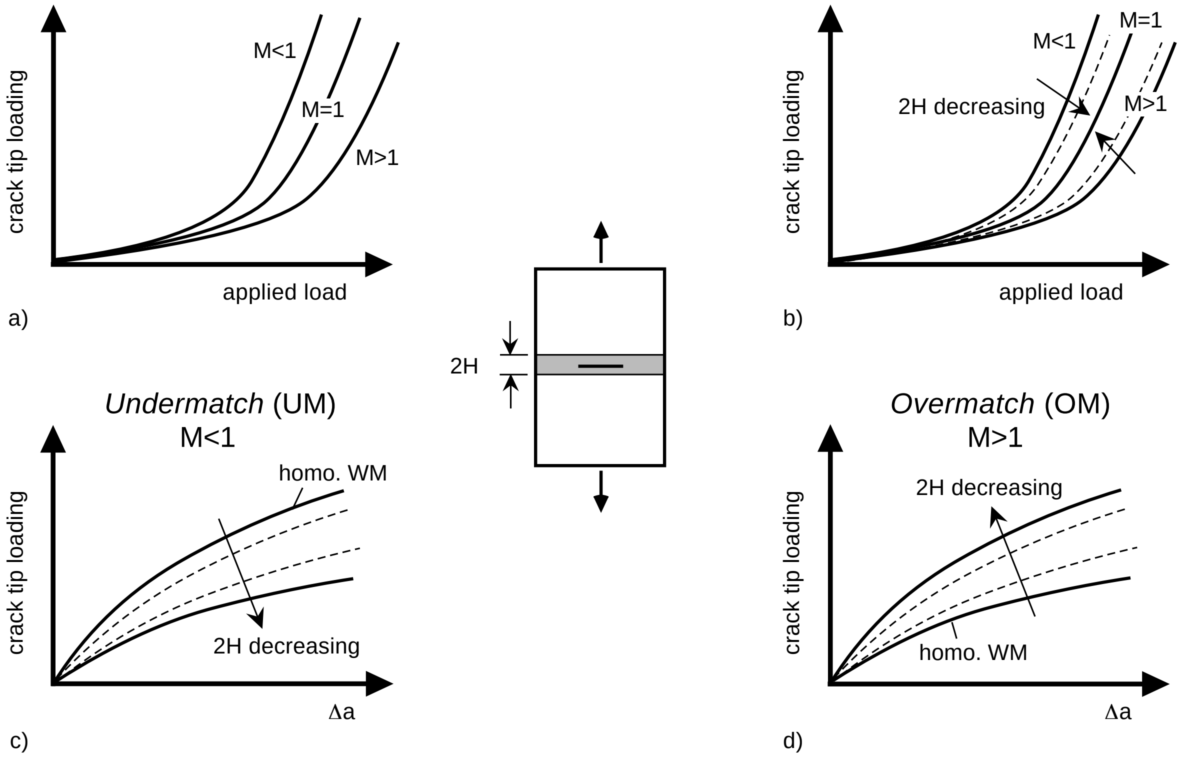

Figure 2.13: Strength mismatch constraint effects on the crack driving force a), b) and crack resistance curve c), d).

Dong and Gordon [38] conducted a 2D plane strain elastic-plastic finite element analysis for a welded M(T) panel to establish the relationship between the crack driving force and the applied stress for under- and overmatching welds. Base material was kept constant while the weld material yield strength was varied in order to obtain different mismatch ratios. The effect of the variation of the weld width, $2H$, on the crack driving force is schematically shown in **Fig. 2.13b**. At low applied loads, i.e. under nominally elastic loading, the crack driving force is independent of the weld width. At higher loads, the crack driving force in the overmatching weld increases more rapidly as the weld width becomes smaller, approaching the curve for the base material as $2H \rightarrow 0$. In the case of an undermatching weld, the crack tip loading decreases with decreasing weld width. Similar numerical results were reported by Kirk and Dodds [39] who demonstrated on M(T) panels that cracks of length greater than twice the weld width ($2H$) negate any mismatch effect on the crack driving force. The authors also concluded that such long cracks can be modelled accurately by ignoring the weld and assuming the entire component is made from the base material. However, it should be noted that the cases analyzed in Refs. [38] and [39] did not address highly undermatched welds but only 20% undermatching.

2.3.5 Effect of strength mismatch on crack resistance curve

Koçak et al. [40] experimentally analyzed the effect of the weld width, $2H$, on the ductile fracture resistance behaviour. They carried out fracture toughness tests on diffusion bonded titanium alloys using single edge notch bend specimens. In the overmatching weld, a smaller weld width increases the R-curve (in terms of CTOD δ_5), whereas in the undermatching weld, the opposite trend is true, **Fig. 2.13c-d**. A similar tendency was demonstrated by Burstow and Howard [41] who used the Rousselier ductile damage model [42] in their detailed 2D plane strain finite element analysis and showed that weld strength overmatching significantly raises the R-curve (in terms of the J-integral) with decreasing weld width, whereas in the undermatching weld, the R-curve is lowered as the weld width decreases.

The trends described above can be explained by considering the development of the plastic zone at the crack tip. For a large weld width, the interaction of the plastic zone in the weld with the base material is negligible, so that the R-curve behaviour is similar to that of the homogeneous weld material. As the weld width decreases, this interaction becomes more pronounced leading to a highly constrained plastic deformation at the crack tip within the undermatched weld which in turn lowers the R-curve. Therefore, crack growth resistance curves of undermatched weld joints can be much lower than those obtained from the most highly constrained (eg. bend) specimen of homogeneous weld material.

In the overmatching weld, the interaction of the crack tip with the interface causes the weaker base material to yield first resulting in a relaxation of the crack tip stress field. This leads to a reduction of the crack tip constraint which in turn raises the R-curve. For the overmatched weld, a highly constrained (eg. bend) specimen of a homogeneous weld material may yield a conservative R-curve. However, when analyzing an overmatched weld joint, consideration should also be given to the base material properties since a reduction in constraint may lead to a crack path deviation from this low constraint region into the base material, eg. [43].

The different constraint levels in bend and tension specimens can be quantified by the T-stress acting parallel to the crack with positive values in the direction of crack growth. As homogeneous tensile specimens show negative T-stresses and homogeneous bend specimens have T-stress values equal or greater than zero for the plane strain condition [44], the effect of specimen geometry and loading type can be captured by varying the T-stress level in the power series expansion after Williams [21]. This idea was incorporated in the modified boundary layer formulation by Larsson and Carlsson [22].

An interesting outcome specific to highly undermatched welds was found by Burstow et al. [29] in their numerical analysis. In such welds, they observed a uniform constraint level irrespective of the geometrical constraint that was simulated by applying different T-stresses in the modified boundary layer formulation using a 2D plane strain finite element analysis. This observation suggests that for a highly undermatched weld, the R-curve for a given sheet thickness and weld width should be geometry (in-plane dimensions) and loading type independent.

Based on the results of the review presented above, the following conclusions can be drawn for the configurations analyzed in the present work, namely homogeneous thin sheet material and highly undermatched LBW and FSW welds introduced in such thin sheets:

- Since in homogeneous thin sheets a plane stress condition can be assumed, the R-curve should be geometry and loading mode independent. It might be expected, then, that an R-curve obtained from a bend-type (eg. compact) specimen would yield the same R-curve as that from a tension-type (eg. middle-cracked tension) specimen.
- If a narrow highly undermatched weld is introduced in a thin sheet as is the case in the laser beam weld, a similar constraint level may be attained in front of the weld crack irrespective of the loading type. It might be expected that the R-curves of a C(T) and M(T) specimens are similar for a given thickness.

2.3.6 Local stresses in strength mismatched welds

The distribution of the crack tip stresses will be discussed in this section with particular focus on the strength undermatched joints. The knowledge of the stress profiles at the weld crack tip as well as along the ligament will provide helpful information when interpreting the fracture behaviour of such undermatched welds observed during testing of LBW and FSW welds in this study. As in the previous section, the diagrams, found in the open literature, will be given in the form of qualitative plots representing the relevant trends rather than absolute values. If available and important, these values will also be given.

Fig. 2.14 shows the variation of the crack tip triaxiality with the strength mismatch factor, M, and the weld slenderness, $\psi = (W-a)/H$ ($W-a$ is the uncracked ligament, H is the half weld width) for a mismatched M(T) panel, obtained from a 2D plane strain FE analysis based on a perfectly plastic material [32]. The general trend that overmatching decreases the crack tip triaxiality, whereas undermatching strongly increases it as compared to the homogeneous ($M = 1$) material is clearly visible. For short ligaments (small ψ) in undermatched welds, the stress triaxiality rapidly increases reaching a plateau at a degree of slenderness around $\psi = 4$. Beyond this ψ value, the crack tip stress triaxiality remains almost constant.

There is an interesting feature specific to the undermatched joints that the highest stress can occur at some distance ahead of the crack tip. This effect is particularly pronounced for highly undermatched joints where the yield strength of the base material is high enough to remain elastic so that the plastic deformation at the crack tip is entirely confined to the weld metal.

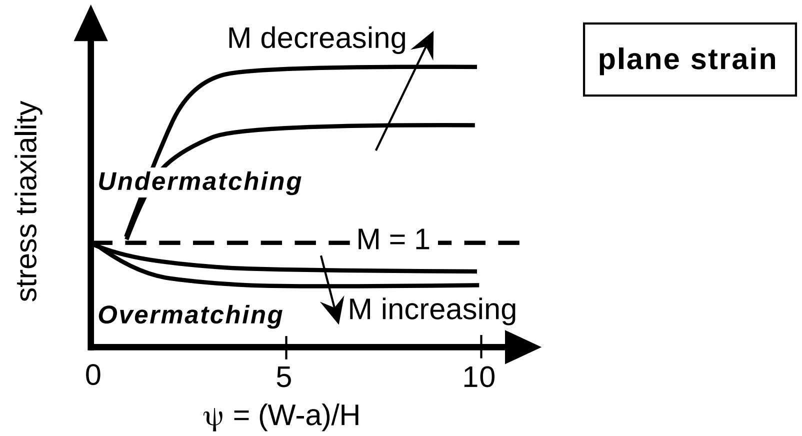

Figure 2.14: Variation of the crack tip stress triaxiality with the mismatch ratio, M, and weld slenderness, ψ, for a plane strain M(T) specimen [31,32]. Results of an FE analysis based on a perfectly plastic material.

Experimental studies on ceramic plates sandwiching thin soft metal layers showed that secondary cracks were observed to nucleate and grow at a distance several metal layer thicknesses ahead of the crack tip [45, 46]. A similar failure mechanism was observed in diffusion bonded bi-material (titanium bonded by a thin aluminium layer) joints [47] where a crack initiated within the soft aluminium layer close to the interface rather than at the tip of the machined notch. Furthermore, a brittle fracture was detected along the interface as the aluminium layer thickness was drastically reduced.

Such extreme cases, where a thin elastic-plastic ductile layer embedded in an elastic environment, were analyzed analytically by means of slip line fields [48] as well as numerically using FE analysis [30,49,50] in order to provide an insight into the stress distribution for a better understanding of the fracture mechanism. These analyses revealed that the local stresses in the constrained layer are much higher than in the homogeneous material for a given geometry and applied load. The hydrostatic stress can exceed up to five times the layer yield stress and the location of this stress elevation is not at the crack tip but some distance in front of it [30]. Such high stresses enhance ductile and cleavage fracture at locations far ahead of the crack tip but possibly adjacent to the interface [45, 47] where the constraint imposed by the stronger base material is expected to be highest.

Fig. 2.15 shows the distribution of the stress triaxiality along the crack ligament [30]. For higher loading levels, a second peak stress develops several layer thicknesses ahead of the crack tip. This second maximum stress and also its distance to the crack tip increases almost linearly with the normalized applied load, $K_\mathrm{I}/(R_{\mathrm{p0.2W}}\sqrt{2H})$. An increase of the normalized load is obtained by increasing the externally applied load (K_I) and/or decreasing the weld width ($2H$). These trends of the distribution of the stress triaxiality are also representative of the individual stress components. Not only the opening stress but also the stress acting in the ligament direction exceeds several times the yield stress of the weld material [48].

In a thin undermatched weld the location of the crack relative to the weld/base material

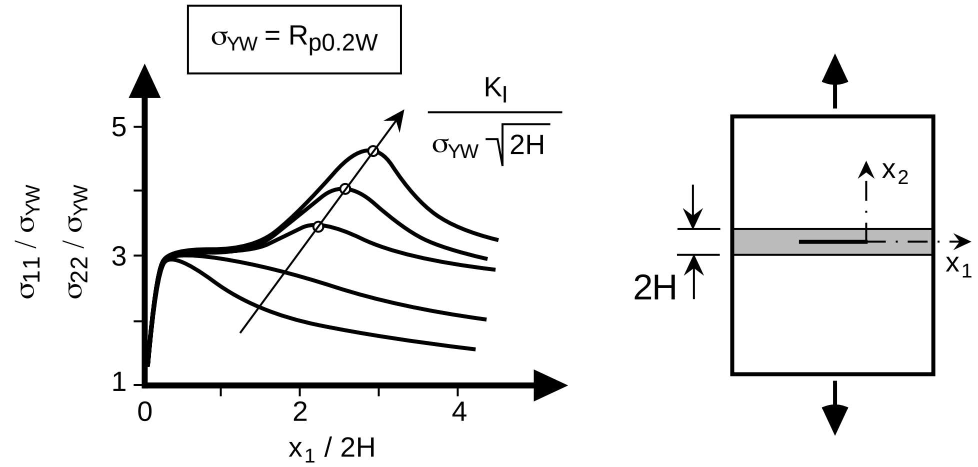

Figure 2.15: Stress distribution along the ligament for different loading levels [30]. Results of an FE large deformation analysis based on an elastic base and elastic-plastic weld material model with strain hardening. σ_YW denotes the yield strength of the weld material.

interface may not be clearly defined due to the very small weld dimensions. Kim et al. [51] studied the problem with a crack at the interface and at the weld centerline in a constrained ductile, perfectly plastic layer under plane strain conditions using small strain FE analysis. The authors found that at low normalized load levels, $K_\mathrm{I}/(R_\mathrm{p0.2W}\sqrt{2H})$, the maximum stresses (including the second peak stresses several layer thicknesses ahead of the crack tip) of the interfacial crack were slightly higher than those of the centerline crack. However, at load levels beyond $K_\mathrm{I}/(R_\mathrm{p0.2W}\sqrt{2H}) \approx 10$, the maximum stresses are not affected by the crack location. Varias et al. [30] reported that at this normalized load level, the second triaxiality maximum develops ahead of the crack tip. For slightly lower normalized load levels, the stress distribution in front of the crack is very flat up to the location where the second peak stress starts developing (see **Fig. 2.15**).

The high stress levels developing ahead of a crack in a constrained layer make it susceptible to failure mechanisms associated with high normal stresses. Three competing mechanisms can lead to failure of a cracked layer joining two stronger materials [30]:

1. near-tip void growth and coalescence with the main crack,
2. high-triaxiality cavitations, i.e. void nucleation and growth at highly stressed sites at distances several layer thicknesses from the main crack tip,
3. interfacial debonding.

The mechanism requiring the lowest fracture energy will become active. Crack propagation by growth and coalescence of near-tip microvoids with the main crack is a typical ductile fracture mechanism. Voids may nucleate around the second phase particles or residual pores formed in the processing.

At the sites with high triaxial stresses ahead of the crack tip secondary cracks or cavitations are likely to occur in the constrained layer. The nucleated cavity may grow to a new crack without connecting with the main crack which itself causes the formation of a new crack with further increased loading [50]. A rupture of one or many ligaments bridging the adjacent cavitations leads to a sudden coalescence with the main crack and potentially to an unstable final fracture of the joint.

Interfacial debonding is operative when the tensile traction across the interface reaches a critical value of the adhesion forces.

2.4 Defect assessment procedures

Generally, the flaw assessment procedures can be classified according to their methodology: Failure Assessment Diagram (FAD) and Crack Driving Force (CDF).

In the FAD concept, a normalized toughness and a normalized load are plotted in one diagram. The failure assessment line represents the failure locus interpolating between the fracture failure and plastic collapse. If the assessment point lies within the area bounded by the failure assessment line and the diagram axes, the component to be assessed is considered safe. Failure of the component must be assumed if the assessment point lies on the failure assessment line or outside the safe region. This graphical representation of the structural integrity analysis is simple; however, it complicates its physical interpretation since the applied parameter is not directly compared with the corresponding critical material resistance as in the case of the CDF approach. In the CDF methodology, the crack tip loading is estimated and compared with the material toughness value. The plastic collapse is determined in a separate step.

2.4.1 Design curve approach

Historically, design curve approaches were the first attempts to give an analytical fracture mechanics approach to an engineering assessment method. Based on the experimental observations that the CTOD is a quadratic function of the local strain, ε, in the linear elastic regime and a linear function under the net section yielding condition, Wells [52] formulated the following expression:

$$\delta = \begin{cases} C_1(\varepsilon/\varepsilon_{\mathrm{Y}})^2 & \text{for} \quad (\varepsilon/\varepsilon_{\mathrm{Y}}) < k \\ C_2(\varepsilon/\varepsilon_{\mathrm{Y}}) + C_3 & \text{for} \quad (\varepsilon/\varepsilon_{\mathrm{Y}}) \geq k \end{cases} \tag{2.33}$$

where ε_{Y} is the yield strain, C_1, C_2, C_3 are empirical constants depending in particular on the component geometry and loading type (bending or tension), and k is a constant ranging from 0.5 to 1. Similarly, the above equation can be expressed in terms of the J-integral as proposed by Turner [53]. Failure of the cracked component is assumed when the applied CTOD (or J) in Eq. (2.33) exceeds the characteristic material value. A widely used approach of this type is the TWI Design Curve [54] which has become a part of some procedures like WES 2805 [55] developed by the Japan Welding Engineering

Society or the Chinese structural integrity assessment procedure SAPV-95 [56] with an overview given in [57].

The advantage of the design curve approach is that there is no need for the stress intensity factor solution of the component to be assessed. However, the difficulty is the lack of a unique definition of the local strain, ε, particularly in complex geometries.

2.4.2 R6 and BS7910

In the UK, the R6 procedure [58] of British Energy Generation Ltd. for assessing the integrity of cracked structures has been continually developed since 1976. This was followed by the British Standard (BS) PD6493 document [59] which is a guide to methods for assessing the acceptability of flaws in fusion welded structures. Since their initial developments, R6 and BS approaches have converged such that the latest issue of the BS procedure BS7910 [60] contains substantial parts of the R6 routine. However, for consistency with PD6493, the approach based on the crack opening displacement (which has its roots in the TWI design curve method) has been retained in BS7910. Unlike the design curve approach being a strain-based approach, the R6 method is stress-based.

Both R6 and BS7910 enable a prediction of critical loads and critical crack sizes for linear elastic and elastic-plastic material behaviour including plastic collapse as a second failure mode. All analyses within these procedures are based on the FAD route. Both R6 and BS7910 procedures have strongly contributed to the development of the SINTAP procedure [61] along with the Engineering Treatment Model (ETM) [62] which will be presented in the following section.

2.4.3 The ETM procedure

The Engineering Flaw Assessment Method (EFAM) [63] developed at GKSS is a comprehensive method for the flaw assessment consisting of two sets of documents. One refers to the determination of the crack resistance of the material (EFAM GTP02 [64]), the other to the determination of the crack tip loading in a cracked component (EFAM ETM 97 [62]). The ETM procedure allows the prediction of critical loads and critical crack sizes. A special feature of the ETM procedure is its use of CTOD δ_5 as a special definition of CTOD which is particularly suited for thin sheets. The procedure also provides an option for assessing cracks in weldments giving guidance to the determination of CDF in welded configurations with strength mismatch. The analysis philosophy follows the CDF route and has been incorporated in the SINTAP procedure [61] (see Section 3), particularly the treatment of cracked strength mismatched configurations.

2.4.4 Other methods

Numbers of developments and updates of guidelines for flaw evaluation have been undertaken worldwide in recent years. An overview of recent developments is given in the special issue on flaw assessment methods in the International Journal of Pressure Vessels and Piping (Issue 77, 2000) [57, 65–71].

SAQ [72] (overview in [65]) is a Swedish procedure for failure assessment of structures containing defects. First developed in 1989 and revised in 1996, it was intended for use in the Swedish nuclear power industry. The underlying method is mainly based on the R6 route and, therefore, follows the FAD philosophy. The document also contains information on sub-critical crack growth due to stress corrosion and fatigue, defect characterization, weld residual stress profiles, K-factor and yield load solutions, and fracture toughness data. Most of the developed solutions have been included in the SINTAP procedure [61].

The French flaw evaluation procedure RSE-M [73] (overview in [69]) specifies the requirements for in-service inspection of French pressurized water reactors. This procedure uses a J estimation scheme based on the reference stress method [74], thus having a close relationship to the R6 method.

A handbook edited by the High Pressure Institute of Japan provides a flaw evaluation procedure for engineers evaluating flaws in nuclear power components [70]. The document is intended to be self-contained. Thus, it includes all necessary input data such as J-integral, stress intensity factor, and yield load solutions as well as a large amount of material data in order to perform a flaw evaluation according to this Japanese fitness-for-service code.

Important developments are taking place in the United States. The American Petroleum Institute (API) has recently published a revised issue of the API 579 procedure [75] (overview in [71]) mainly targeted at the assessment of ageing plants and pressurized components in the refinery and petrochemical industry. The document is a modification of the R6 routine and BS7910, rather then an independent document.

After the completion of the SINTAP procedure [61], the German FKM-Richtlinie [76] has adopted the SINTAP methodology for the assessment of flaws in general engineering applications.

Procedures and codes presented above were initially designed and are used in specific industrial sectors. These industries are mainly nuclear power plants, pressure vessels, and oil and gas producers, all of them being subject to strict structural safety regulations. The underlying theory of incorporated methods is based on the fracture mechanics approach which is general and not limited to any specific application field. The task is basically to estimate the crack tip loading in a cracked structure and to compare that with the material fracture toughness determined in an appropriate test. In principle, these methods are applicable to any structural components such as thin-walled structures in the aerospace industry.

Most of the reviewed procedures and codes incorporate either the R6 procedure or its modification. Currently, an European Thematic Network on the Fitness-for-Service (FITNET) [77, 78] develops a comprehensive flaw assessment procedure by updating the SINTAP procedure and combining with other failure modes of fatigue, creep and corrosion in one document. However, currently the SINTAP procedure contains most advanced guidelines for assessing cracks in metallic structural components with and without welds including recent developments and advances in fracture mechanics and can be regarded as the most current defect assessment procedure.

Therefore, in this thesis a systematic investigation has been made to adopt the SINTAP procedure for the first time as an analysis tool for the residual strength prediction of cracked thin-walled aerospace structural components in both welded and base material conditions. The structural components under consideration are highly undermatched butt-welded wide plates joined by LBW and FSW processes as well as stiffened panels where the stiffeners are attached to the skin by a LBW T-joint. The details of the SINTAP procedure are given in Section 3.

3 Methodology and approach

3.1 The SINTAP procedure

In 1996 a European Commission part-funded three-years project **S**tructural **INT**egrity **A**ssessment **P**rocedure (SINTAP) was launched with the aim of developing a unified procedure for the assessment of structures containing flaws that is applicable within a wide range of industrial sectors. Furthermore, the project aimed at resolving national differences in fracture assessment methods and at arriving at a consensus approach. The consortium of seventeen institutions from different industries and nine European countries reviewed existing flaw assessments methods and incorporated relevant parts into a new unified procedure (called SINTAP procedure) for the evaluation of structural integrity addressing brittle fracture, ductile tearing, and plastic collapse. The core of the SINTAP procedure consists of elements from the R6 method [58] and ETM [79] with some slight modifications in order to obtain a consistent set of equations.

The underlying principles of the SINTAP procedure are [80]:

- a hierarchical structure of the analysis levels based on the quality of the input data;
- decreasing conservatism with increasing data quality;
- the choice of representation of results in terms of FAD or CDF;
- specific methods for treating weld strength mismatch problems.

The SINTAP procedure basically provides an estimation of the crack tip loading in a cracked structural component. This crack tip loading can then be compared with the material toughness value to assess the structural integrity. The SINTAP procedure is organized in various analysis levels (in total six levels). The higher the analysis level the lower the conservatism of the predicted critical condition of the cracked structural component. The most basic analysis level 0 (called default level) requires the yield strength as the only material tensile property. The fracture toughness can be estimated from the Charpy impact energy [61]. This analysis level allows an assessment of the structural integrity with a very limited information on the material data.

The next three analysis levels (levels 1-3) are analytical levels and do not need any numerical analysis provided the required input data like the K-factor and the yield load solutions are available for the structure to be assessed, **Fig. 3.1**.

Analysis level 4 allows for the account of constraint effects. It uses the estimates of fracture toughness data for the crack tip conditions relevant to those of the cracked structure to be assessed. The fracture toughness data requirements are increased compared to the lower analysis levels. The tensile data, however, are unchanged.

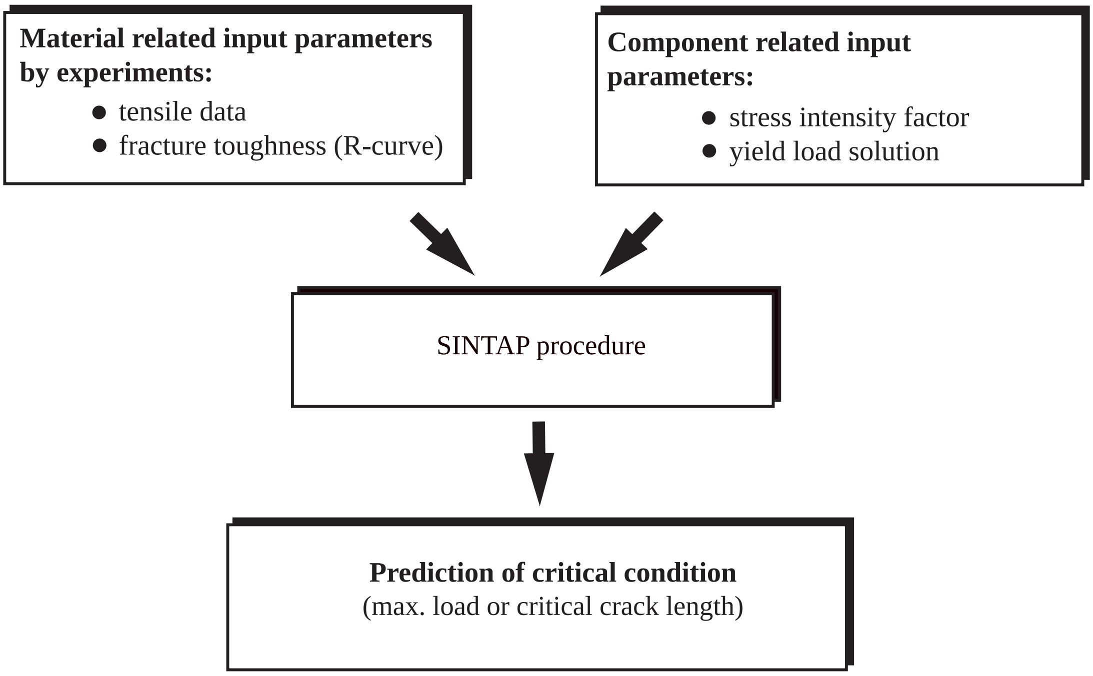

Figure 3.1: Input data for the SINTAP procedure.

The highest analysis level 5 is purely numerical and requires a full stress-strain curve for the J-integral calculation of the cracked structure.

The fracture toughness of thin sheets in aerospace applications is generally known, so that the SINTAP default level will not be used in this study. Since the aim is to provide an analytical methodology for the residual strength assessment of thin-walled structures, only SINTAP analysis levels 1-3 will be applied throughout this thesis, thus excluding the application of the SINTAP analysis levels 4 and 5.

The hierarchy of the analytical analysis levels is based on the availability of the material tensile data which is coupled with the accuracy of the crack tip loading estimation, **Tab. 3.1**. The full stress-strain curve in level 3 results in a more accurate estimation of the crack tip loading. Level 1 tends to overestimate the crack tip loading, thus yielding conservative predictions of the critical condition. Level 2 is intended for the assessment of joints with strength mismatch exceeding 10% and is basically a modification of the analysis level 1.

In the SINTAP procedure [61], the assessment of the cracked component can be achieved by using two complementary approaches: CDF and FAD. Both of the approaches lead to the same results since the failure assessment lines are based on the same plasticity correction function.

The elastic-plastic crack tip loading K_{J} with the units of a linear elastic stress intensity factor, in terms of the SINTAP-CDF expression is:

$$K_{\mathrm{J}} = K_{\mathrm{I}} \times [f(L_{\mathrm{r}})]^{-1} \tag{3.1}$$

Table 3.1: The three analytical analysis levels of the SINTAP procedure and required input information on the material side for stable tearing analysis (R-curve analysis).

	Analysis level applied to	Fracture toughness	Tensile properties
Level 1	homogeneous material	R-curve	Young's modulus E; yield strength $R_{\mathrm{p0.2}}$; tensile strength R_{m}
Level 2	heterogeneous material (eg. mismatched joints)	R-curve of material where crack is located	tensile properties of BM *and* WM: Young's modulus E; yield strength $R_{\mathrm{p0.2}}$; tensile strength R_{m};
Level 3	homogeneous material	R-curve	full *true* stress-strain curve

where K_{I} is the elastic stress intensity factor of Mode I and

$$L_{\mathrm{r}} = \frac{F}{F_{\mathrm{Y}}(a)} \tag{3.2}$$

is the ratio of applied load, F, to the yield load, $F_{\mathrm{Y}}(a)$, as a function of the crack length, a, of the cracked component. The parameter L_{r} is not only a measure of proximity to the plastic collapse but also a key parameter in estimating the elastic-plastic crack tip loading via Eq. (3.1) using linear elastic stress intensity factor. The plasticity correction function $f(L_{\mathrm{r}})$ is defined in the following subsection and is structured in various levels depending on the availability of the material tensile data.

The corresponding SINTAP-CDF expression in terms of the crack tip opening displacement (CTOD), δ, is:

$$\delta = \delta_{\mathrm{e}} \times [f(L_{\mathrm{r}})]^{-2} \tag{3.3}$$

with

$$\delta_{\mathrm{e}} = \frac{{K_{\mathrm{I}}}^2}{m\, E'\, R_{\mathrm{p0.2}}} \tag{3.4}$$

where m is considered a constraint parameter ($m = 1$ for plane stress and $m = 2$ for plane strain), $R_{\mathrm{p0.2}}$ is the yield strength of the material. $E' = E$ for plane stress and $E' = E/(1-\nu^2)$ for plane strain. E is Young's modulus and ν is Poisson's ratio.

The basic equation of the SINTAP-FAD route is:

$$K_{\mathrm{r}} = \frac{K_{\mathrm{I}}}{K_{\mathrm{mat}}} = f(L_{\mathrm{r}}) \tag{3.5}$$

where K_{mat} is the material fracture toughness. The function $f(L_{\mathrm{r}})$ is identical to the one used in the CDF route.

3.1.1 Analytical analysis levels

This section provides the definition of the plasticity correction function, $f(L_\mathrm{r})$, for the analytical SINTAP analysis levels 1-3.

Analysis level 1, homogeneous material: The required material input parameters are the yield strength, $R_{\mathrm{p}0.2}$, and the tensile strength, R_m. For materials showing continuous yielding, the function $f(L_\mathrm{r})$ is given by:

$$f(L_\mathrm{r}) = \begin{cases} \left[1+\frac{1}{2}L_\mathrm{r}^2\right]^{-\frac{1}{2}} \times \left[0.3 + 0.7\exp\left(-\mu L_\mathrm{r}^6\right)\right] & \text{for} \quad 0 \le L_\mathrm{r} \le 1 \\ f(L_\mathrm{r}=1) \times L_\mathrm{r}^{(N-1)/2N} & \text{for} \quad 1 < L_\mathrm{r} < L_\mathrm{r}^\mathrm{max} \\ 0 & \text{for} \quad L_\mathrm{r} \ge L_\mathrm{r}^\mathrm{max} \end{cases} \tag{3.6}$$

where

$$\mu = \min \begin{cases} 0.001\dfrac{E}{R_{\mathrm{p}0.2}} \\ 0.6 \end{cases} . \tag{3.7}$$

The strain hardening exponent, N, and the plastic collapse limit, $L_\mathrm{r}^\mathrm{max}$, are defined as:

$$N = 0.3\left[1 - \frac{R_{\mathrm{p}0.2}}{R_\mathrm{m}}\right] , \qquad L_\mathrm{r}^\mathrm{max} = \frac{1}{2}\left[\frac{R_{\mathrm{p}0.2}+R_\mathrm{m}}{R_{\mathrm{p}0.2}}\right] . \tag{3.8}$$

Analysis level 2, mis-match material: The required material input parameters for this level are the yield strength, $R_{\mathrm{p}0.2}$, and the tensile strength, R_m, of base (subscript B) and weld (subscript W) materials:

$$f(L_\mathrm{r}) = \begin{cases} \left[1+\frac{1}{2}L_\mathrm{r}^2\right]^{-\frac{1}{2}} \times \left[0.3 + 0.7\exp\left(-\mu_\mathrm{m} L_\mathrm{r}^6\right)\right] & \text{for} \quad 0 \le L_\mathrm{r} \le 1 \\ f(L_\mathrm{r}=1) \times L_\mathrm{r}^{(N_\mathrm{M}-1)/2N_\mathrm{M}} & \text{for} \quad 1 < L_\mathrm{r} < L_\mathrm{r}^\mathrm{max} \\ 0 & \text{for} \quad L_\mathrm{r} \ge L_\mathrm{r}^\mathrm{max} \end{cases} \tag{3.9}$$

where

$$\mu_\mathrm{M} = \frac{M-1}{(F_\mathrm{YM}/F_\mathrm{YB}-1)/\mu_\mathrm{W} + (M - F_\mathrm{YM}/F_\mathrm{YB})/\mu_\mathrm{B}} < 0.6 \ , \quad \text{else} \quad \mu_\mathrm{M} = 0.6 \ , \tag{3.10}$$

$$\mu_\mathrm{B} = 0.001\frac{E}{R_{\mathrm{p}0.2\mathrm{B}}} < 0.6 \ , \quad \text{else} \quad \mu_\mathrm{B} = 0.6 \ , \tag{3.11}$$

$$\mu_\mathrm{B} = 0.001\frac{E}{R_{\mathrm{p}0.2\mathrm{W}}} < 0.6 \ , \quad \text{else} \quad \mu_\mathrm{W} = 0.6 \ , \tag{3.12}$$

$$L_\mathrm{r}^\mathrm{max} = \frac{1}{2}\left(1 + \frac{0.3}{0.3 - N_\mathrm{M}}\right) \tag{3.13}$$

and strain hardening exponents for mismatch, N_{M}, base, N_{B}, and weld material, N_{W}, are defined as:

$$N_{\mathrm{M}} = \frac{M-1}{(F_{\mathrm{YM}}/F_{\mathrm{YB}}-1)/N_{\mathrm{W}} + (M - F_{\mathrm{YM}}/F_{\mathrm{YB}})/N_{\mathrm{B}}} \,, \tag{3.14}$$

$$N_{\mathrm{B}} = 0.3\left(1 - \frac{R_{\mathrm{p0.2B}}}{R_{\mathrm{mB}}}\right) \,, \tag{3.15}$$

$$N_{\mathrm{W}} = 0.3\left(1 - \frac{R_{\mathrm{p0.2W}}}{R_{\mathrm{mW}}}\right) \,. \tag{3.16}$$

F_{YB} is the yield load of the cracked component wholly made of the base material and F_{YM} is the mismatch corrected yield load.

Analysis level 3, homogeneous material: The required material input parameter is the complete stress-strain curve. Note that both the stress, σ_{ref}, and strain, $\varepsilon_{\mathrm{ref}}$, values are true values:

$$f(L_{\mathrm{r}}) = \begin{cases} \left[\dfrac{E\varepsilon_{\mathrm{ref}}}{\sigma_{\mathrm{ref}}} + \dfrac{1}{2}\dfrac{L_{\mathrm{r}}^2}{E\varepsilon_{\mathrm{ref}}/\sigma_{\mathrm{ref}}}\right]^{-\frac{1}{2}} & \text{for} \quad 0 \le L_{\mathrm{r}} < L_{\mathrm{r}}^{\max} \\ 0 & \text{for} \quad L_{\mathrm{r}} \ge L_{\mathrm{r}}^{\max} \end{cases} \tag{3.17}$$

where

$$\sigma_{\mathrm{ref}} = L_{\mathrm{r}} R_{\mathrm{p0.2}} \tag{3.18}$$

and $\varepsilon_{\mathrm{ref}}$ is the true strain value corresponding to the true stress value σ_{ref}. The plastic collapse limit, $L_{\mathrm{r}}^{\max}$, is defined as:

$$L_{\mathrm{r}}^{\max} = \frac{1}{2}\left(\frac{R_{\mathrm{p0.2}} + R_{\mathrm{m}}}{R_{\mathrm{p0.2}}}\right) \,. \tag{3.19}$$

3.1.2 Background to SINTAP analysis levels

To give the background to the development of the analytical SINTAP analysis levels, it is convenient to start with the plasticity correction function of level 3. The derivation of this function is based on the reference stress method [74] developed by Ainsworth [81] for steady-state creep in the early 1980s. After some modifications [82], this plasticity correction function was introduced in the R6 procedure [58] in its final version, as given in Eq. (3.17). Level 3 is a material dependent function allowing an exact description of any material by a pointwise consideration of the true stress-strain curve.

In practical applications, the availability of the full stress-strain curve is not always guaranteed so that the material properties are only given in terms of the yield and tensile strengths. For this case, the SINTAP level 1 was developed which distinguishes between materials with Lüders plateau and those exhibiting continuous yielding. Since Al-alloys show a continuous yielding, the emphasis will be placed on this case. For more information on the case with materials showing a Lüders plateau, the reader is referred to Ref. [61].

In order to obtain a material independent plasticity correction function, Eq. (3.17) was applied to a range of materials with different strain hardening behaviour [82].

Then, an empirical fit to the lower bound was found in a way that at low L_r values, i.e. elastic behaviour at low stresses, this empirical fit reproduced Eq. (3.17). In the fully plastic region, i.e. $L_\mathrm{r} > 1$, the equation of the plasticity correction function was taken from the ETM procedure [79]. There, it is assumed that the plastic deformation of the ligament ahead of the crack tip is equivalent to the plastic deformation behaviour of a material in the uniaxial tensile test. For the analytical treatment, the material's engineering stress-strain curve is described by a piece-wise power law:

$$\sigma = E\,\varepsilon \qquad \text{for} \quad \sigma < R_{\mathrm{p}0.2}, \tag{3.20}$$

$$\frac{\sigma}{R_{\mathrm{p}0.2}} = \left[\frac{\varepsilon}{\varepsilon_{0.2}}\right]^N \qquad \text{for} \quad \sigma \geq R_{\mathrm{p}0.2} \tag{3.21}$$

where $\varepsilon_{0.2}$ is the total strain value corresponding to the yield stress, $R_{\mathrm{p}0.2}$:

$$\varepsilon_{0.2} = \frac{R_{\mathrm{p}0.2}}{E} + 0.002 \tag{3.22}$$

with E being Young's modulus.

Different approaches have been proposed in the literature for the determination of the strain hardening exponent, N. A common method is the linear regression fit of the plastic part of the stress-strain curve plotted on double logarithmic scales where N is the slope of this regression line. Another method is based on the determination of N as the slope of the line going through the yield point $(\varepsilon_{\mathrm{p}0.2}, R_{\mathrm{p}0.2})$ and the point of the tensile strength $(\varepsilon_\mathrm{m}, R_\mathrm{m})$, **Fig. 3.2** [79]. Regardless of the methods used, the strain hardening exponent will be affected by whether the stress-strain curve is engineering or true. Generally, the true stress-strain curve lies above the engineering curve resulting in a higher strain hardening exponent. In the defect assessment, the use of N from the engineering stress-strain curve will result in an overestimation of the crack driving force, leading to a conservative prediction of the critical condition of the cracked structural component. Throughout this thesis, N is obtained from the engineering stress-strain curve.

The mismatch level 2 of the SINTAP procedure is intended to be applied to strength mismatched configurations having a difference in base and weld metal yield strengths of more than 10%. This level is similar to level 1 in terms of the availability of tensile and fracture toughness data. However, this analysis level also requires yield and tensile strengths of the weld material. Moreover, the mismatch corrected yield load, F_YM, is needed which takes into account different plasticity development patterns in the crack tip region of the cracked component. This is an essential improvement since the accuracy of the estimation of the crack tip loading is highly affected by the yield load definition.

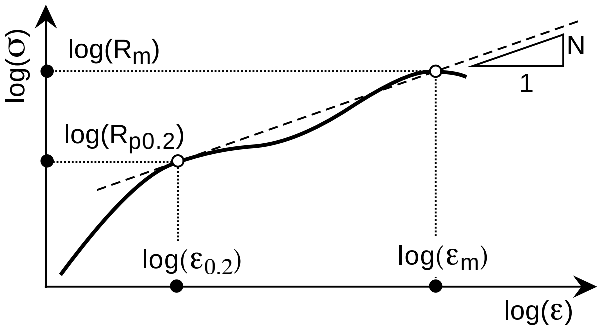

Figure 3.2: Definition of the strain hardening exponent, N, (see Eq. (3.21)) of the engineering stress-strain curve with continuous strain hardening [79].

3.2 Procedures for R-curve determination

Three different approaches to the R-curve determination will be presented in this section. The first approach is based on the ASTM E561 standard [16] and gives an R-curve in terms of K_{eff} vs. Δa_{eff}. The effective crack extension, Δa_{eff}, is obtained from an effective crack length corrected for plasticity at the crack tip. This type of the R-curve is the current approach to the residual strength analysis of cracked structures in the aerospace industry. The other two approaches are based on the elastic-plastic crack tip parameters J and CTOD plotted versus physical crack extension [64].

In defect assessment procedures, it is very important to treat the crack driving force (applied side) and the R-curve (material side) consistently. Therefore, the R-curve determined in terms of K_{eff} according to the ASTM E561 standard is only useful in combination with the K-concept on the applied side. Defect assessment procedures like the SINTAP procedure require R-curves of the cracked material in terms of the physical crack length. Therefore, only J and CTOD R-curves will be used in the SINTAP procedure in Section 6.

3.2.1 K_{eff} R-curve

The ASTM E561 [16] standard outlines a procedure for determining the R-curve in terms of K_{eff} vs. Δa_{eff}. This method is applicable to materials exhibiting predominantly linear elastic fracture behaviour such as high strength aluminium alloys used in the aerospace industry. Since this standard does not contain a minimum thickness requirement, it can be applied to thin sheets. The R-curve is valid as long as the net section stress of the specimen remains below the material's yield strength.

The standard offers two different methods to calculate the effective crack length, a_{eff}, where the choice is left to the user: the compliance method and the Irwin correction.

Using the compliance method, the effective crack length is inferred from the experimental load-CMOD curve. The ASTM E561 standard [16] embodies an analytical expression for the compliance of an M(T) panel which was originally derived by Eftis and Liebowitz [83] on the basis of the theory of elasticity:

$$EB\frac{v}{F} = 2\left(\frac{\pi a/(2W)}{\sin \pi a/(2W)}\right)^{\frac{1}{2}} \times \frac{Y}{2W}$$
$$\times \left\{ \frac{4W}{\pi Y}\cosh^{-1}\left(\frac{\cosh \pi Y/(2W)}{\cos \pi a/(2W)}\right) - \frac{1+\nu}{\left[1+\left(\frac{\sin \pi a/(2W)}{\sinh \pi Y/(2W)}\right)^2\right]^{\frac{1}{2}}} + \nu \right\} \tag{3.23}$$

where

E = Young's modulus
B = specimen thickness
v = CMOD (Crack Mouth Opening Displacement)
F = applied load
$2W$ = total specimen width
Y = half span of CMOD gauge (2.5 mm in present investigation)
a = a_{eff} = effective half crack length
ν = Poisson's ratio.

The flow chart in **Fig. A.4** illustrates the steps to follow in order to obtain the effective crack length, a_{eff}, according to the compliance method. The effective stress intensity factor, K_{eff}, is then calculated as follows [16]:

$$K_{\text{eff}} = \frac{F}{2WB}\sqrt{\pi a_{\text{eff}}} \times \sqrt{\frac{1}{\cos\frac{\pi a_{\text{eff}}}{2W}}}. \tag{3.24}$$

The K_{eff} R-curve characterizes the material resistance to fracture during stable crack growth and is plotted versus the effective crack extension, Δa_{eff}:

$$\Delta a_{\text{eff}} = a_{\text{eff}} - a_0 \tag{3.25}$$

where a_0 is the initial half crack length of the M(T) panel.

The alternative method uses the Irwin correction where the effective crack length is calculated from the experimentally measured physical crack length, a, plus the radius of the theoretical plastic zone at the crack tip:

$$a_{\text{eff}} = a + \frac{1}{2\pi}\left(\frac{K_{\text{I}}}{R_{\text{p0.2}}}\right)^2 \tag{3.26}$$

where K_{I} is the linear elastic stress intensity factor [84]:

$$K_{\text{I}} = \frac{F}{2WB}\sqrt{\pi a} \times \sqrt{\frac{1}{\cos\frac{\pi a}{2W}}} \tag{3.27}$$

and $R_{\mathrm{p0.2}}$ the yield strength of the material. The R-curve is constructed in the same way as with the compliance method using Eqs. (3.24) and (3.25).

The critical stress intensity factor, K_{c}, can be defined at the instability point where the crack driving force is tangent to the K_{eff} R-curve [85]. However, the point of instability depends on the shape of the crack driving force. Therefore, one should be careful when taking this single value as a material property.

3.2.2 K_{J} R-curve

The procedure for the determination of an R-curve in terms of the J-integral is described in the following. The important difference to the preceding procedure (K_{eff} R-curve) is that the crack resistance is plotted versus the physical crack extension, Δa. Hence, the measurement of physical crack extension in the test is essential for this procedure.

As in the ASTM E561 procedure, an experimental load-CMOD record is required. The J-integral is calculated from the area under the load-CMOD curve. Generally, up to the crack initiation, the J-integral is calculated according to [86]:

$$J_0 = \frac{K^2}{E} + \frac{\eta A^*}{B(W - a_0)} \qquad \text{with} \qquad \eta = 1 \tag{3.28}$$

where K is the stress intensity factor, E is Young's modulus, A^* is defined in **Fig. 3.3**, B is the specimen thickness, W is half width of the specimen, and a_0 is the initial half crack length. The effect of mismatch is captured by the correction factor, η, for which numbers of correction functions (eg. [87,88]) have been proposed depending on specimen geometry, mismatch ratio, and weld dimensions. However, for a long uncracked ligament and/or narrow weld width, η approaches unity for both strength under- and overmatched weld joints [89].

It should be noted that Eq. (3.28) is only valid for a stationary crack. If the specimen exhibits a considerable amount of crack extension during testing, the estimation of J should account for stable crack growth. An approximation formula is given in [64]:

$$J_j = J_{j-1} + \frac{2\Delta A^*}{B(b_{j-1} + b_j)} + \frac{2}{E(b_{j-1} + b_j)}\left[K_j^2 b_j - K_{j-1}^2 b_{j-1}\right] \tag{3.29}$$

where $j-1$ and j are two consecutive data points on the load-CMOD record, ΔA^* is defined in **Fig. 3.3**, and $b = W - a$ is the current ligament.

Both Eqs. (3.29) and (3.28) will be used to obtain R-curves in terms of the J-integral to establish their validity range in thin sheets.

The J-integral is then converted to the units of the stress intensity factor, K_{J}:

$$K_{\mathrm{J}} = \sqrt{JE} \qquad \text{plane stress.} \tag{3.30}$$

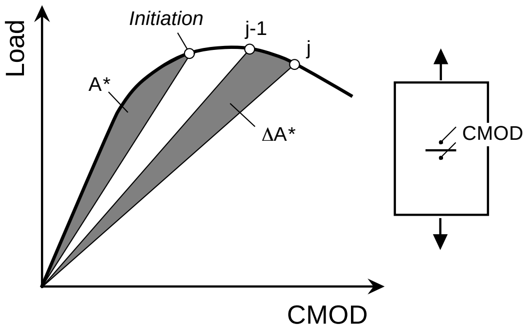

Figure 3.3: Definition of the deformation energy contributions to the J-integral calculation from the load-CMOD record, see Eq. (3.28) and Eq. (3.29).

3.2.3 CTOD R-curve

Throughout this thesis the special definition of CTOD in terms of CTOD δ_5 will be used. The fracture parameter CTOD δ_5 does not need to be inferred from the load or any other displacement parameters, but is directly accessible in the test. CTOD δ_5 is directly measured with a special clip [33] across the fatigue crack tip over a gauge length of 5 mm, **Fig. 3.4**. For the construction of the R-curve, the measured CTOD δ_5 values are plotted versus physical crack extension, Δa. This technique is not limited to standard specimen geometries but can be applied to any cracked structural component, enabling an easy verification of the transferability of R-curves from small laboratory specimens to real structures. The determination of the fracture resistance of heterogeneous materials like welded joints is performed in the same way as for homogeneous materials.

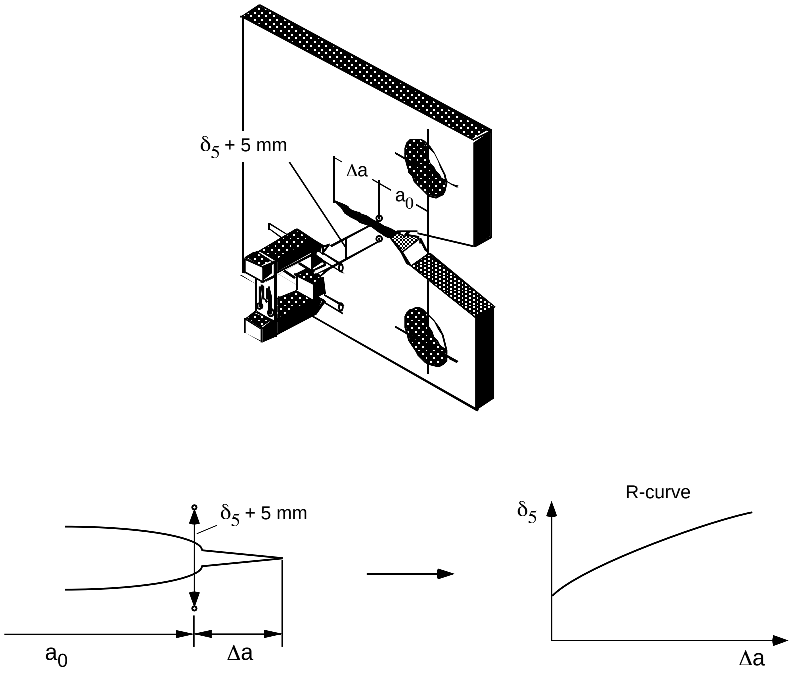

Figure 3.4: Principle of the CTOD δ_5 measurement and construction of CTOD δ_5 R-curve [90].

4 Experimental program

This section presents the experimental results of small laboratory specimens as well as the residual strength tests on large welded panels and provides the required input information to the SINTAP procedure on the material side. Section 4.1 gives an overview of the material and welds investigated within this work. Section 4.2 addresses the base and weld material characterization in terms of micro-hardness, tensile and fracture resistance properties. The results of the residual strength tests on cracked LBW and FSW panels as well as on LBW welded stiffened panels are given in Section 4.3. Finally, the plastic zone measurement within the undermatched LBW and FSW joints in cracked panels is presented in Section 4.4.

4.1 Material and welds

A high damage tolerance (HDT) and weldable aluminium alloy Al 6013 was delivered in the T4 heat treatment condition. The chemical composition of the material is given in **Tab. 4.1**. The original thickness of 3.2 mm was reduced to the desired thicknesses of 2.0 mm and 2.6 mm by chemically milling one side of the sheet material.

The material for all unstiffened panels (base and welded) was heat treated to a T6 condition prior to butt-welding them using the CO_2 LBW and FSW processes by Airbus. In the LBW process AlSi12 filler wire with a chemical composition given in **Tab. 4.1** was used. After welding no post weld heat treatment was applied to welded unstiffened panels.

In stiffened panels, the stringers, extruded from Al 6013 and delivered in T4 condition, were welded to the skin using two CO_2 laser beam sources with AlSi12 filler wire applied simultaneously from each stringer side. In contrast to the unstiffened panels, the stringers and the skin were welded in T4 and post weld heat treated to the T6 condition.

Optical macrosections of weld joints investigated in this study (LBW and FSW butt-joints, and LBW T-joint in stiffened panels) are shown in **Fig. 4.1**.

Table 4.1: Nominal chemical composition of Al 6013 sheet material and AlSi12 filler wire in wt % as specified by the supplier Alcoa.

material	Si	Fe	Mg	Cu	Mn	Cr	Zn	Ti	Be
Al 6013	0.6-1.0	–	0.8-1.2	0.6-1.1	0.2-0.8	0.1	0.25	0.1	–
AlSi12	11.0-13.0	≤ 0.5	≤ 0.05	≤ 0.05	≤ 0.15	–	≤ 0.1	≤ 0.05	≤ 0.008

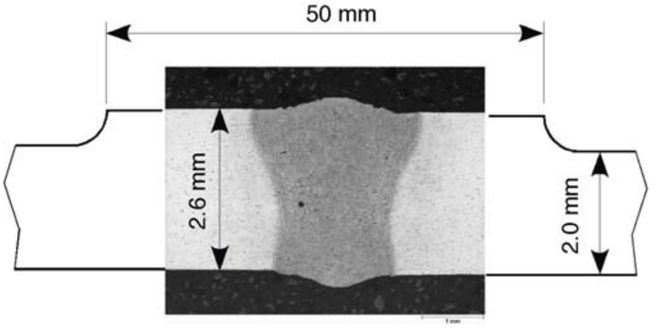
LBW butt-joint

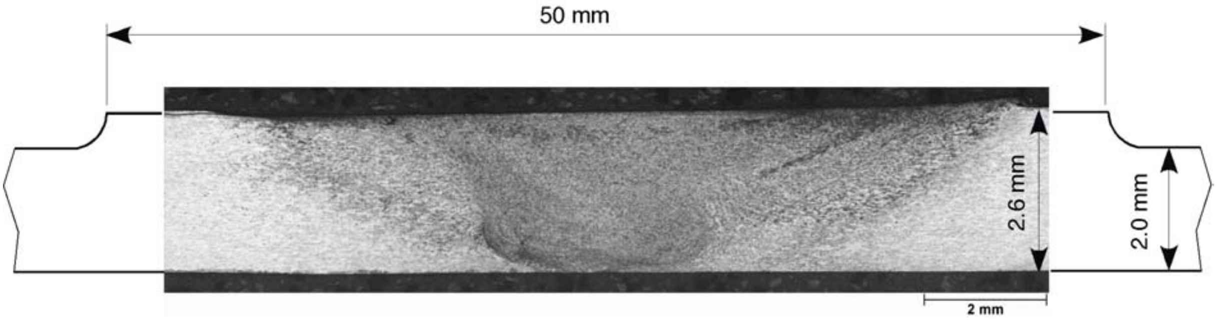
FSW butt-joint

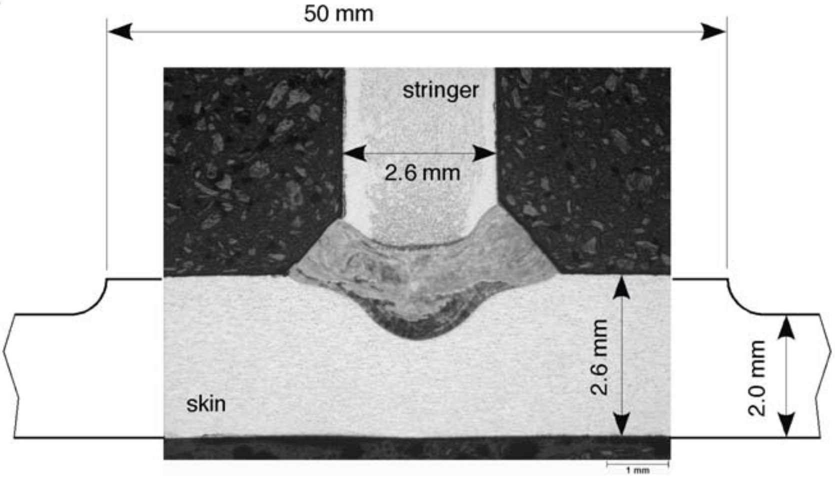
LBW T-joint

Figure 4.1: Optical macrosections of weld joints investigated in this study: LBW butt-joint, FSW butt-joint, and LBW T-joint in stiffened panels.

4.2 Mechanical properties of base and weld materials

4.2.1 Micro-hardness and microstructure

Micro-hardness measurements were conducted using the Vickers hardness technique. The diamond pyramid was impressed by a weight of 1.0 N ($HV_{0.1}$) and was held for 10 seconds to create an indentation on the specimen's surface. Two samples of each welding process were cut from different locations of the weld joints showing a very good reproduction of the hardness profiles which in turn indicates a constant weld quality along the welds. The hardness profiles of the LBW and FSW joints are shown in **Fig. 4.2**. The averaged value of the base metal hardness is 145 $HV_{0.1}$. Both joints exhibit a hardness decrease in the fusion zone, clearly demonstrating the nature of the undermatched weld joints.

In the LBW joint, the hardness drops to 80 $HV_{0.1}$ in the fusion zone. Also a 2 mm wide HAZ is detectable, possessing a hardness plateau at 110 $HV_{0.1}$.

The high strength of the material is reached by specific heat treatment where precipitation strengthening takes place during an ageing process. Only coherent precipitates are responsible for the strengthening of the alloy [91]. The other class of participates are non-coherent and do not contribute to the strengthening effect. During welding, different microstructural changes are likely to occur in the HAZ, such as recrystallization, grain growth, and modifications of the precipitates. With respect to strength, grain growth plays an important role in the case of non-heat-treatable Al-alloys, but is of minor importance in the case of heat-treatable Al-alloys where the strength is mainly affected by the modification of precipitates [92]. The observed hardness drop in the HAZ of the present LBW joint can therefore be provoked by two transformation reactions. The first one is the dissolution of strengthening (coherent) precipitates. The second is the growth or transformation of coherent precipitates to incoherent forms, often referred to as overageing [93]. Dissolved strengthening precipitates can be reformed by reconducting an appropriate heat-treatment, whereas hardness loss due to overageing (growth of precipitates) is not recoverable by a heat treatment process.

The micro-hardness profile of the LBW T-joint has also shown a hardness loss within the weld material [94]; however, due to the post weld heat treatment, this hardness drop is smaller compared to that of the LBW butt-joint.

Due to the nature of the FSW welding process, one distinguishes between the *advancing* side of the weld joint (where the direction of the tangent velocity of the rotating tool coincides with the direction of the travel velocity of the tool) and the *retreating* side (which is the opposite side of the advancing side). Despite this asymmetry, the hardness profile of the FSW joint is symmetrical with respect to the weld centerline. It may be attributed to the high rotational speed of the tool causing a homogeneous material flow and a temperature field around the tool. The hardness minimum of 90 $HV_{0.1}$ is observed in the thermomechanically affected zone (TMAZ). The weld nugget shows a slight increase of hardness (110 $HV_{0.1}$). A similar hardness profile of an FSW welded Al 6013 T6 alloy has been reported in [95].

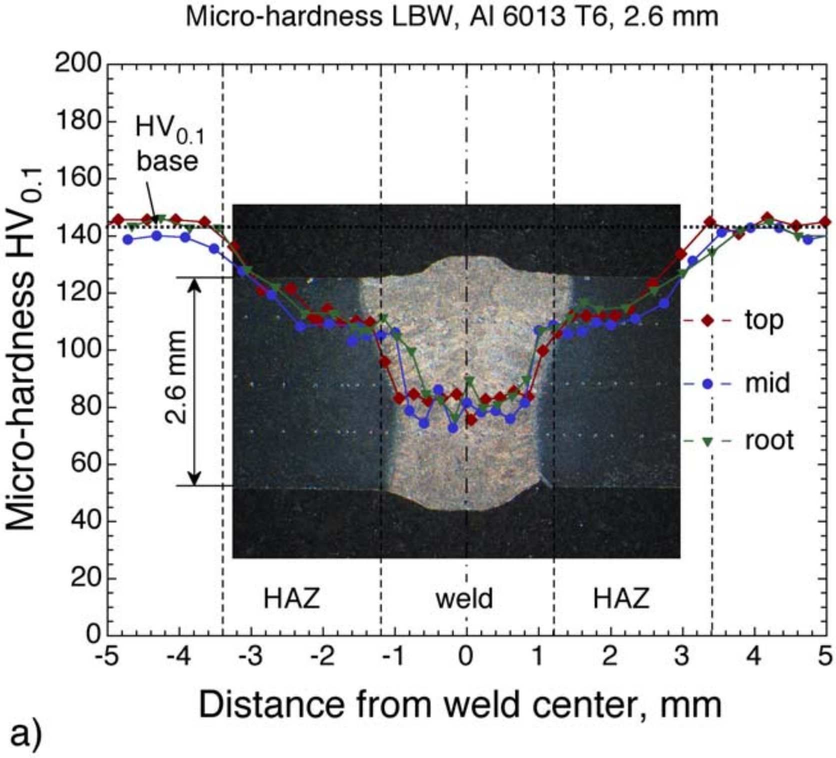

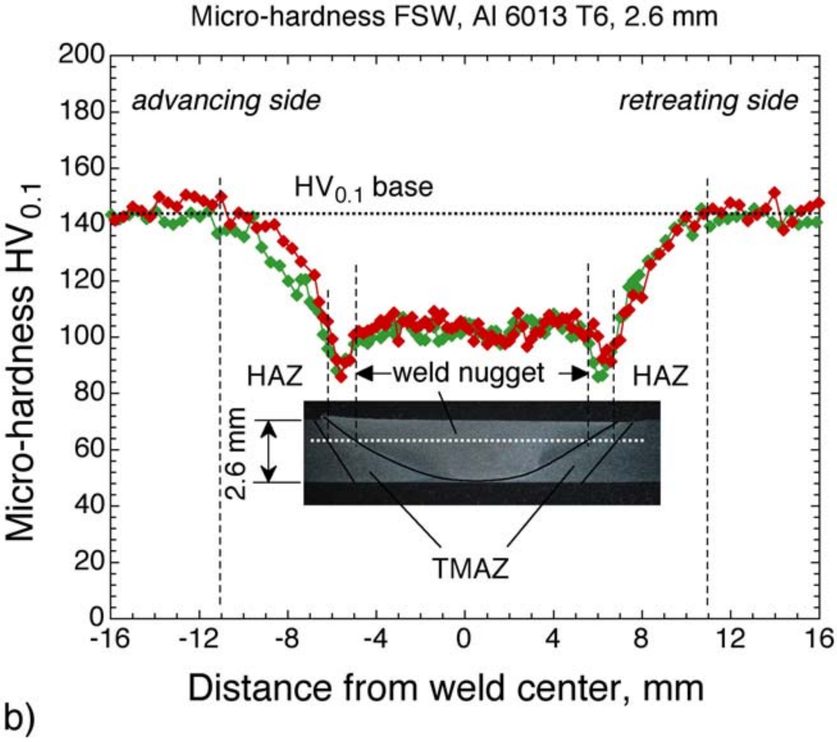

Figure 4.2: Micro-hardness profiles of the a) LBW butt-joint showing three different locations (top, mid section, and root) of the joint and b) FSW butt-joint showing two measurements at the same position (indicated by the dotted line) but two different samples.

4.2.2 Tensile properties

Global tensile properties of LBW and FSW joints were determined by testing standard flat tensile specimens with transverse welds at room temperature in as-welded condition. The geometry and dimensions of these specimens according to the standard DIN EN 895 are shown in **Fig. 4.3**. In order to make a comparison of the tensile properties between welded joints and the base material excluding any geometry and size effects, specimens of the same geometry were prepared from the base material. The elongation was measured at a gauge length of $L_0 = 50$ mm.

Micro-flat tensile specimens [96] enable the determination of local material tensile properties. These small specimens, shown with dimensions in **Fig. 4.3**, were extracted using electrical discharge machining (EDM) from different locations of the LBW and FSW joints. This technique yields local full stress-strain curves obtained from the bulk material of the region of interest. The elongation was measured at a gauge length of $L_0 = 7$ mm. It should be noted that in the case of welds, micro-flat tensile specimens are made of all-weld material.

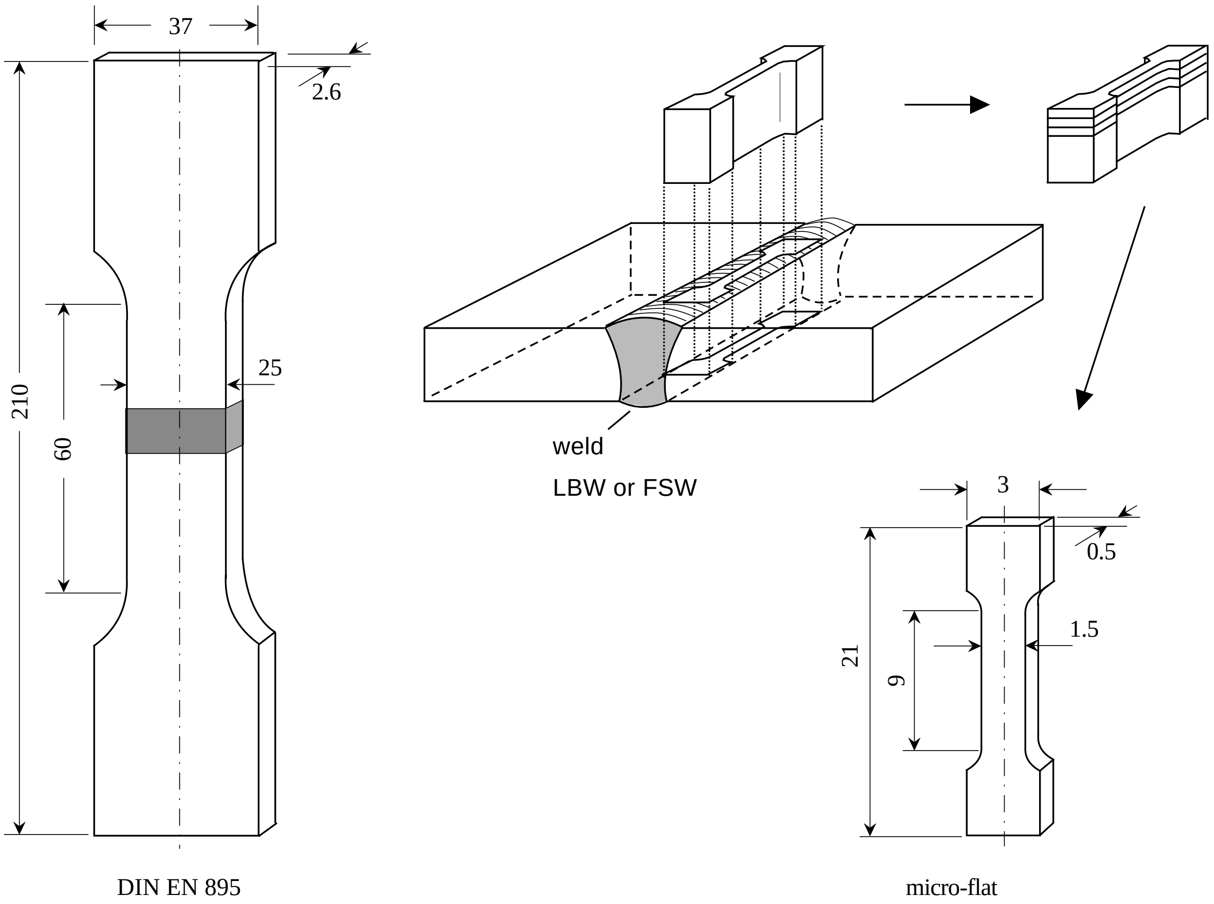

DIN EN 895

micro-flat

Figure 4.3: Dimensions of flat tensile specimens. Transverse flat tensile specimen according to DIN EN 895 for testing welds as well as the base material; micro-flat tensile specimens for determination of local tensile properties.

Table 4.2: Results of transverse tensile tests on specimens according to DIN EN 895. Elongation was measured at a gauge length $L_0 = 50$ mm (values are averages of at least 3 specimens).

Material	$R_{\mathrm{p0.2}}$ yield strength (MPa)	R_{m} tensile strength (MPa)	A elongation (%)	Joint Efficiency in terms of $\mathrm{R_m}$ (%)	Joint Efficiency in terms of A (%)
base (L)	385	400	13.0		
base (LT)	360	395	12.6		
stringer (L)	405	425	12.0		
LBW (LT)	240	290	0.9	73.4	7.1
FSW (LT)	210	285	2.6	72.2	20.6

Table 4.3: Results of micro-flat tensile tests (values are averages of at least 3 specimens)

Material	$R_{\mathrm{p0.2}}$ yield strength (MPa)	R_{m} tensile strength (MPa)	A elong. at fract. (%)	N^* strain harden. (–)	N^{**}_{SINTAP} (–)	$M = \frac{R_{\mathrm{p0.2W}}}{R_{\mathrm{p0.2B}}}$ Mismatch factor (–)
Base skin (L)	350	365	10.5	0.014	0.012	
Base skin (LT)	330	365	11.5	0.037	0.028	
Base stringer (L)	370	395	8.5	0.022	0.019	
LBW (FZ)	145	165	2.0	0.100	0.036	0.4
LBW (HAZ)	212	310	19.5	0.110	0.095	
FSW (nugget)	185	295	28.5	0.125	0.112	0.6
FSW (TMAZ / HAZ)	200	285	13.0	0.125	0.089	

*) Eq. (4.3)

**) $= 0.3(1 - R_{\mathrm{p0.2}}/R_{\mathrm{m}})$, see Eq. (3.8)

The stress-strain curves obtained from the standard flat tensile specimens are given in **Fig. 4.4** showing the strength undermatched nature of the welds. The curve for the stringer material was obtained from the stringer foot part. It should be noted that the stringer geometry only allowed an extraction of a 8 mm wide flat tensile specimen which was in accordance with the DIN 50125 standard. The respective tensile property values are summarized in **Tab. 4.2**.

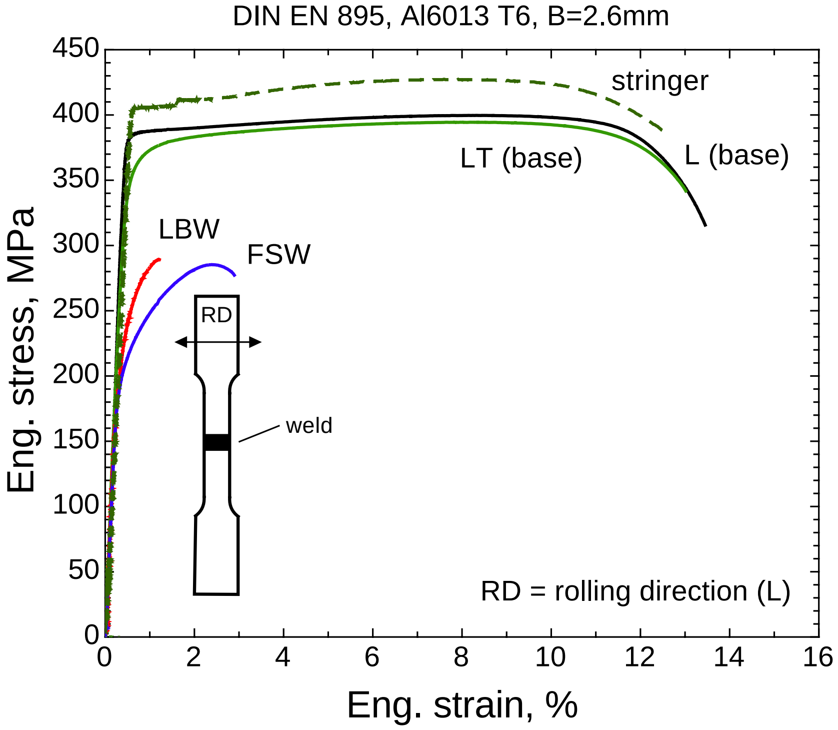

Figure 4.4: Tensile properties of base material (L and LT direction), FSW and LBW joints obtained from transverse standard tensile specimens (DIN EN 895). Due to the stringer geometry, the stringer stress-strain curve was obtained from a narrower specimen according to DIN 50125 standard. Welded joints are loaded in tension perpendicular to the welding direction, which is the L direction.

The failure locations of the LBW and FSW joints are depicted in **Fig. 4.5**. Weld strength undermatching causes a strain localization in the softer weld material which promotes the fracture in the weld metal. It should be noted that the failure location of the LBW joints was within the weld metal somewhere close to the interface but not exactly along the interface in the sense of an interfacial debonding. Moreover, the observed failure location shows a slightly lower thickness compared to the weld centerline region.

The as-welded FSW joints failed in the TMAZ on the retreating side which has a slightly lower thickness than the advancing side. This is generally true for FSW joints because the FSW process operates without filler metal and, therefore, any material gain on the advancing side leads to a material loss on the retreating side. However, if the surface of the FSW joint was machined, i.e. FSW joint had the same thickness over the entire weld width, the fracture location may equally occur either on the advancing or retreating side (given a symmetric hardness profile). The hardness profile revealed a low hardness band in the TMAZ which is inclined with respect to the loading axis providing a favourable slip orientation [97,98].

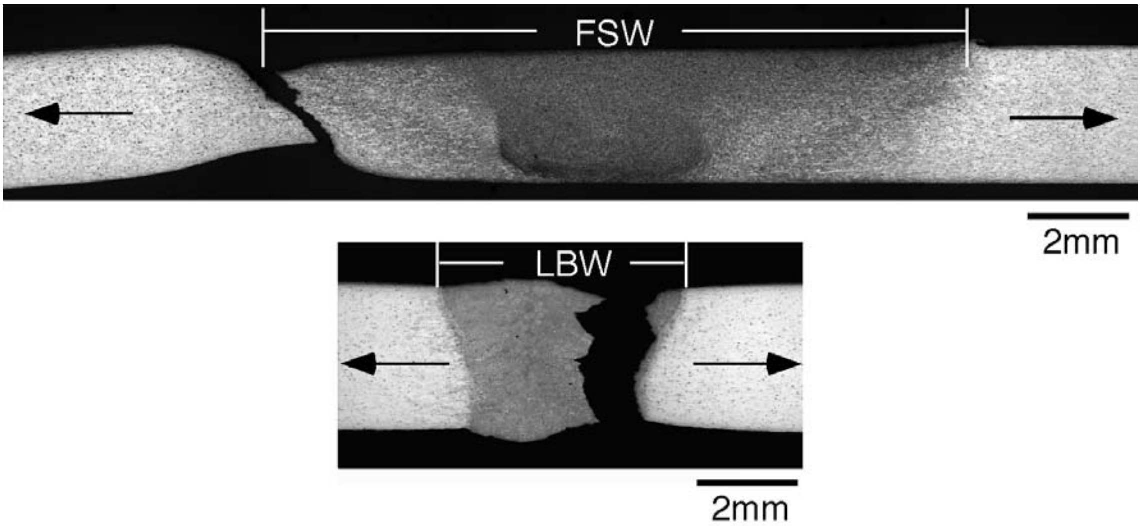

Figure 4.5: Optical macrographs of FSW and LBW joints showing the fracture locations (where minimum hardness values were measured in **Fig. 4.2**) of transverse flat tensile specimens.

The joint efficiency in terms of the tensile strength, R_m, is relatively high reaching about 73% of the base metal strength.

The joint efficiency in terms of the total elongation, A, is very poor, reaching a value of 7.1% in the LBW joint and 20.6% in the FSW joint. However, when comparing the welds only, the ductility of FSW joints is significantly higher than the ductility of LBW joints. For strength undermatched welded joints, the plastic deformation is confined to the weaker weld metal, whereas the base metal may remain elastic (in extreme undermatching) for the entire range of applied strain. In the present case of LBW and FSW joints, the base material, indeed, remained elastic, since the tensile strength of both welded joints is lower than the yield strength of the base material. The elastic base metal prevents the spread of plasticity, thus leading to an increase of the stress triaxiality. The increase of the stress triaxiality generally decreases the material toughness and reduces the fracture strain capacity.

The stress-strain curves obtained from the micro-flat tensile specimens are depicted in **Fig. 4.6**. The respective tensile properties are summarized in **Tab. 4.3**. For the base material, specimens in both directions (L and LT) were tested as was done with standard tensile specimens. No variation of tensile properties in thickness direction was found for the base and for both weld materials.

As expected from the hardness profile, the strengths of LBW and FSW weld materials are significantly lower than that of the base material. The base material elongation is about 10-11%. The FSW weld material with a fine grained dynamically recrystallized microstructure shows an elongation up to 29% and a remarkable strain hardening capacity. The LBW weld material with a coarse, as-cast microstructure with possibly fine pores

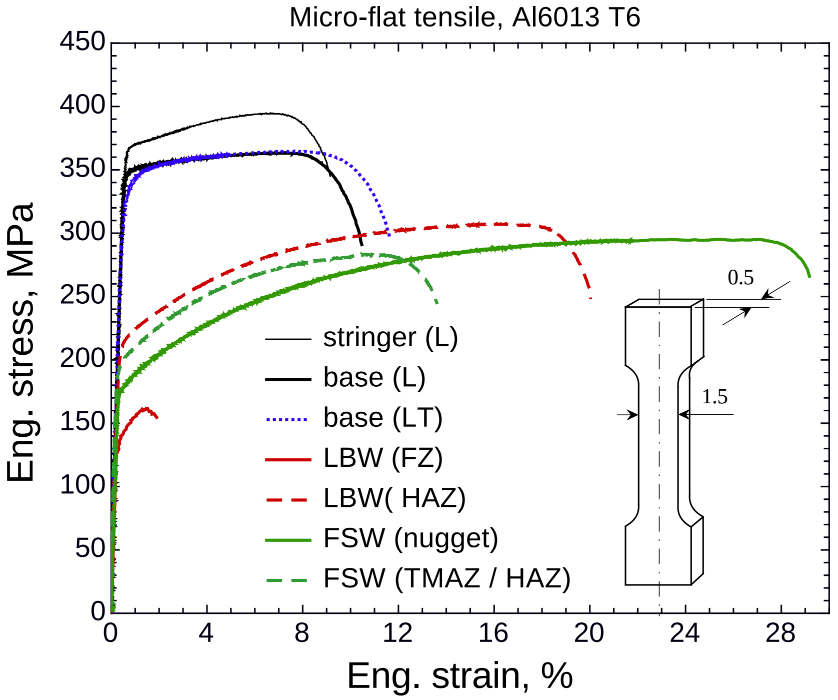

Figure 4.6: Tensile properties of base and weld (LBW and FSW) materials obtained from micro-flat tensile specimens.

displays a very small elongation of (maximum) 2%, whereas the elongation of the LBW HAZ specimen is even higher than that of the base material.

Moreover, the tensile strength of 165 MPa attained in the LBW micro-flat tensile specimen is much lower than the value of 290 MPa for the standard specimen. It should be noted that due to the constraint effect in the narrow LBW weld imposed by the stronger base material, the yield and tensile strengths of the LBW joint obtained from standard specimens are expected to be higher than in a micro-flat specimen made of the same bulk material. The fracture mechanisms in the LBW micro-flat and standard flat tensile specimens must be assumed to be different.

The clarification is provided in **Fig. 4.7** showing the fracture path of the LBW standard flat tensile specimen. It is clearly visible that the final fracture was preceded by the formation of small cracks being oriented in the loading direction and the failure then occurred in the form of their coalescence. The preferred fracture path of these small cracks is related to the dendritic grain structure (more details will be provided by the electron microscopy presented in a later section). While the small cracks did not lead to an immediate fracture of the standard specimen, they might cause the final fracture of a micro-flat tensile specimen. **Fig. 4.7** also depicts the orientation of a micro-flat tensile specimen extracted from the LBW weld material. These small cracks are perpendicularly oriented to the loading axis of the micro-flat tensile specimen and provide a potential failure location resulting in much lower strength values than in a respective LBW standard specimen.

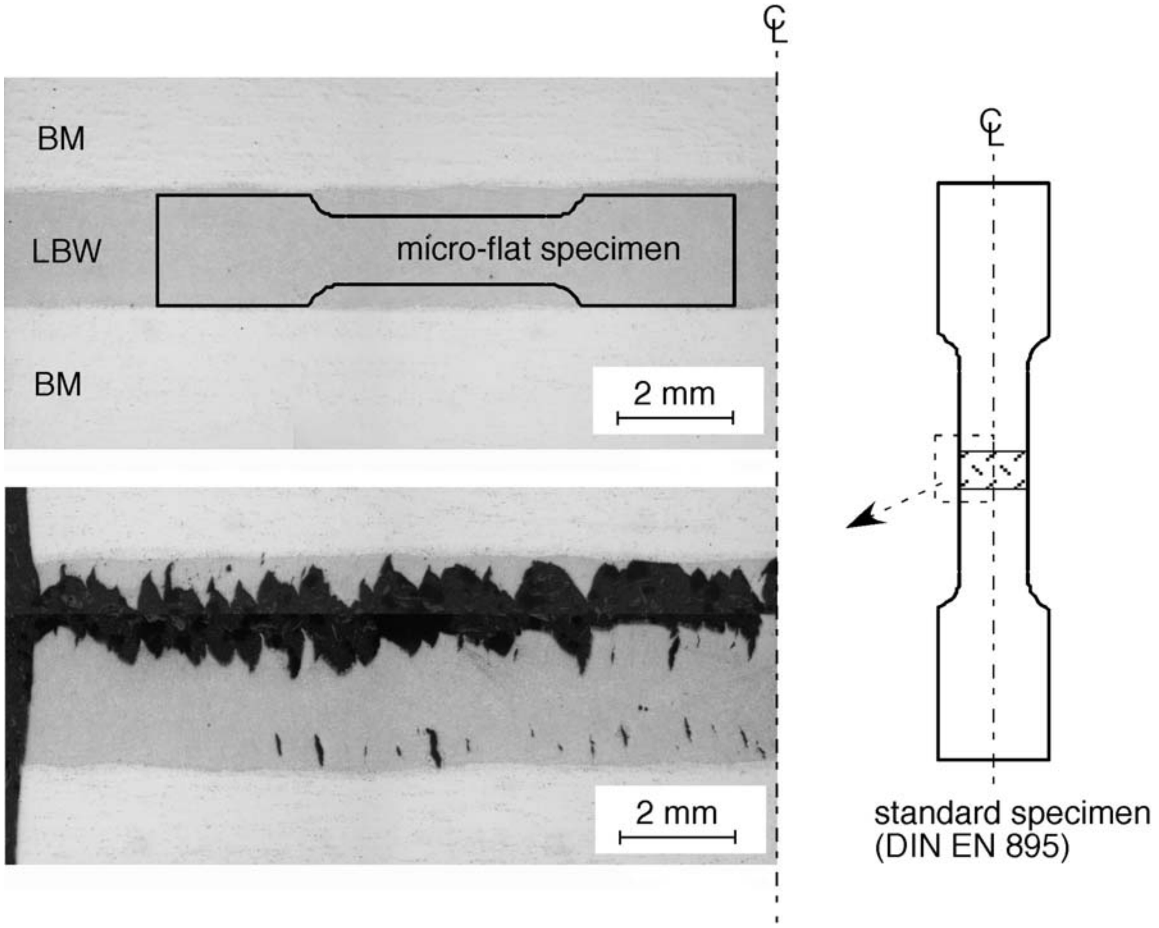

Figure 4.7: Optical macrograph of the LBW joint (L-T plane at mid-thickness) showing the fracture location and the formation of secondary cracks in the weld material. The figure also depicts the orientation of the micro-flat tensile specimen (specimen length not true to scale!) extracted from the LBW weld material.

Comparison between standard and micro-flat tensile specimens

Fig. 4.8 shows the comparison between the stress-strain curves obtained from micro-flat tensile and standard specimens for base material and both LBW joints. In the case of the base material **Fig. 4.8** a), micro-flat specimens exhibit strength values that are lower by 10-15% than those of the standard specimens. However, the plastic parts of the curves are very similar in shape.

A reason for a lower strength of base material micro-flat specimens may be ascribed to the manufacturing process. During the EDM process, the specimen's surface is heated up by electrical sparks causing a "heat treatment" of the material and a possible degradation of the strength properties in a thin surface layer which had contact with the hot wire. The effective cross-sectional area of the original material may therefore be smaller. Since the calculation of stress was based on the total cross-sectional area, the resulting stress values are lower.

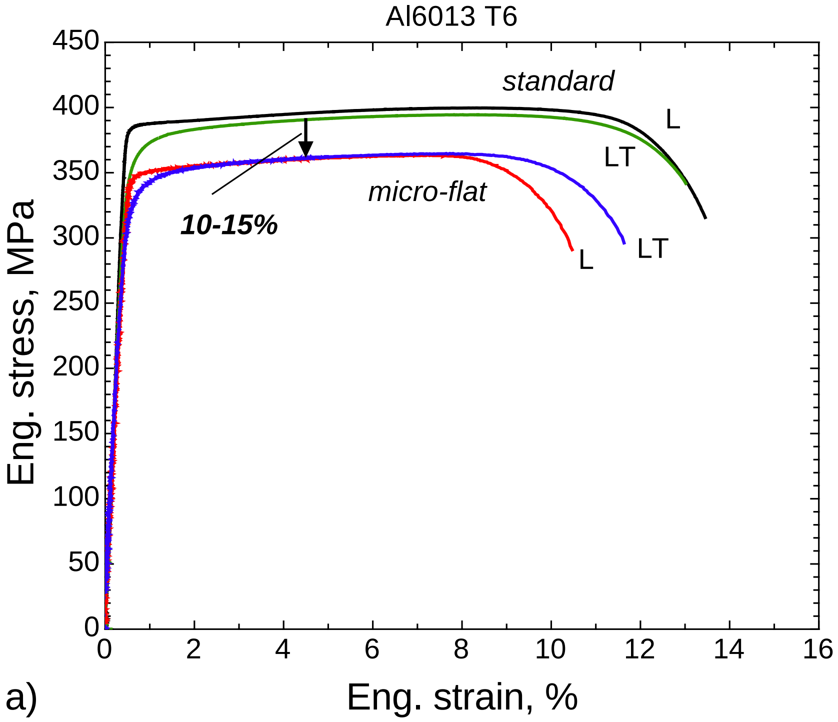

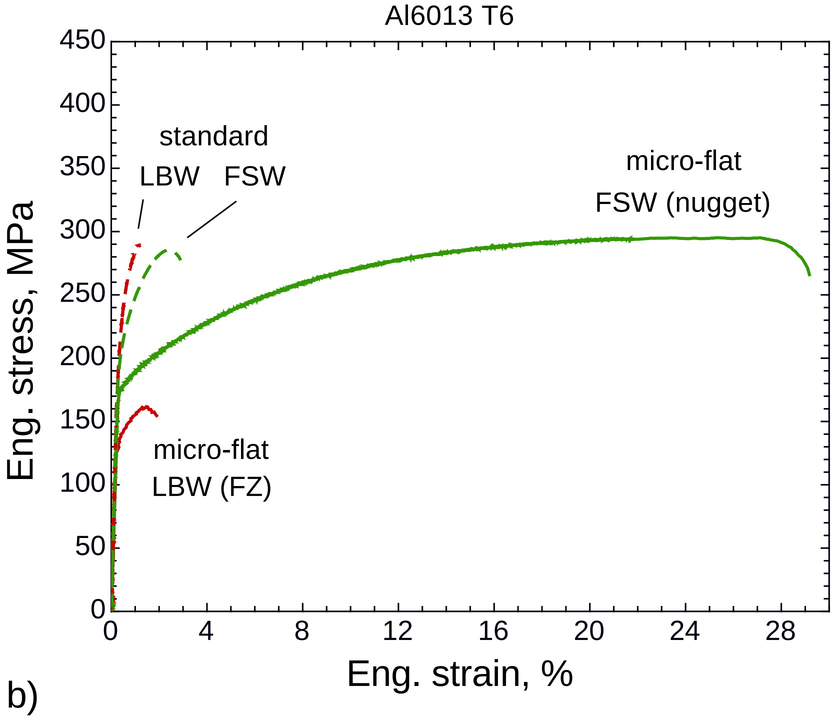

Figure 4.8: Comparison of stress-strain curves obtained from standard and micro-flat tensile specimens for a) base material and b) LBW and FSW joints.

The 3D geometry effect may also be a reason, i.e. small specimens experience lower constraint than the large standard ones. The answer to this uncertainty can be delivered by a 3D FEA. However, an experimental study has shown no effect on the stress-strain curves obtained from base material specimens of the same thickness but different widths (unpublished results at GKSS).

The total elongation of the base material micro-flat specimens is less than in standard ones. It is interesting to note that the tensile strength in both specimen geometries is reached at approximately the same strain value. Beyond this point, material softening due to the local damage evolution (formation and coalescence of microvoids) exceeds the material's strain hardening capability. Assuming the damage process as material specific, the specimen with a larger geometry may experience a larger strain until fracture as observed in standard specimens.

Fig. 4.8 b) depicts the comparison between the stress-strain curves obtained from micro-flat tensile and standard transverse specimens of LBW and FSW joints. In the case of LBW, the low strength and elongation of the micro-flat tensile specimen are ascribed to the secondary cracking within the weld material as discussed in detail in an early paragraph (see also **Fig. 4.7**). In the case of FSW, the micro-flat tensile specimen shows a much higher straining capacity than the standard specimen. In the standard specimen, the plastic deformation of the FSW joint is entirely confined to the weld material, thus reducing the global deformation capacity of the joint.

Determination of the strength mismatch ratio, M

The strength mismatch factor, M, is a relevant input parameter in the SINTAP procedure in the residual strength prediction of welded panels. Since the yield stress of a material with continuous yielding is defined in terms of a proof stress at 0.2% plastic strain, its value obtained from both LBW and FSW standard specimens will be (due to the confined plasticity) dependent on the gauge length selected for the strain (or total elongation) measurement. A particular focus is devoted to this issue in Section 4.4. To specify a unique level of strength mismatching in a welded joint, the real weld material properties should be used as they are provided by the micro-flat tensile specimens. All weld material properties of both LBW and FSW joints used for the application of the SINTAP procedure in Section 6 are taken from micro-flat tensile specimens, whereas the base material properties are taken from standard ones.

Determination of the strain hardening exponent, N

The strain hardening exponent, N, is another major input parameter in the SINTAP procedure. The experimental stress-strain curve can be described analytically by the piece-wise power law in the following form:

$$\sigma = E\,\varepsilon, \qquad \sigma < R_{\mathrm{p0.2}} \tag{4.1}$$

$$\frac{\sigma}{R_{\mathrm{p0.2}}} = \left(\frac{\varepsilon}{\varepsilon_{0.2}}\right)^N, \qquad \sigma \geq R_{\mathrm{p0.2}} \tag{4.2}$$

where σ and ε are engineering stress and strain, respectively, and E is Young's modulus. The strain hardening exponent can be obtained from the slope of the linear regression fit through the plastic part of the stress-strain curve plotted on the double logarithmic scale or more easily by the following analytic expression:

$$N = \frac{\log\left(R_{\mathrm{m}}/R_{\mathrm{p0.2}}\right)}{\log\left(\varepsilon_{\mathrm{m}}/\varepsilon_{0.2}\right)}. \tag{4.3}$$

N is the slope of the line going through the yield ($\varepsilon_{0.2}$ and $R_{\mathrm{p0.2}}$) and tensile strength (ε_{m} and R_{m}) points in the double logarithmic scale (see **Fig. 3.2**). The strain level at the 0.2% proof stress, $R_{\mathrm{p0.2}}$, is:

$$\varepsilon_{0.2} = \frac{R_{\mathrm{p0.2}}}{E} + 0.002\ . \tag{4.4}$$

The calculated strain hardening exponents are given in **Tab. 4.3** for the base and different weld materials using stress-strain curves from micro-flat tensile specimens. The table also gives the strain hardening exponents, N_{SINTAP}, obtained from the formula proposed in the SINTAP procedure providing conservative estimates of the strain hardening behaviour for the range of material regions investigated. The discrepancy between N_{SINTAP} and N-values obtained from Eq. (4.3) is large in the case of the LBW fusion zone (FZ) material. The reason is the low elongation at fracture obtained with this specimen. This leads to a small value in the denominator of Eq. (4.3) resulting in a high N-value. In the case of the base material, Eq. (4.3) yields similar N-values for stress-strain curves from standard specimens due to the parallel shift of the plastic part along the stress axis (see **Fig. 4.8**).

4.2.3 Fracture resistance

A multiple specimen technique using standard compact specimens, C(T) (W = 50 mm) was employed to determine the fracture toughness in terms of CTOD δ_5 R-curves for base material and LBW (FZ only) and FSW including both nugget and TMAZ) joints. Upon introducing a machine notch, the specimens were fatigue precracked to introduce a sharp crack with an initial crack ratio of $a/W = 0.5$ for all C(T) specimens. All specimens were tested with anti-buckling guides in order to prevent the out-of-plane bending which may occur particularly at large crack extensions, **Fig. A.1**.

The tests were carried out at room temperature with a loading rate of 0.2 mm/min. All specimens were unloaded when the desired CTOD δ_5 was reached and postfatigued after the test in order to mark the crack front of the stable crack growth during static loading. The averaged crack extension, Δa, for each specimen was then measured on the fracture surface by means of an optical microscope.

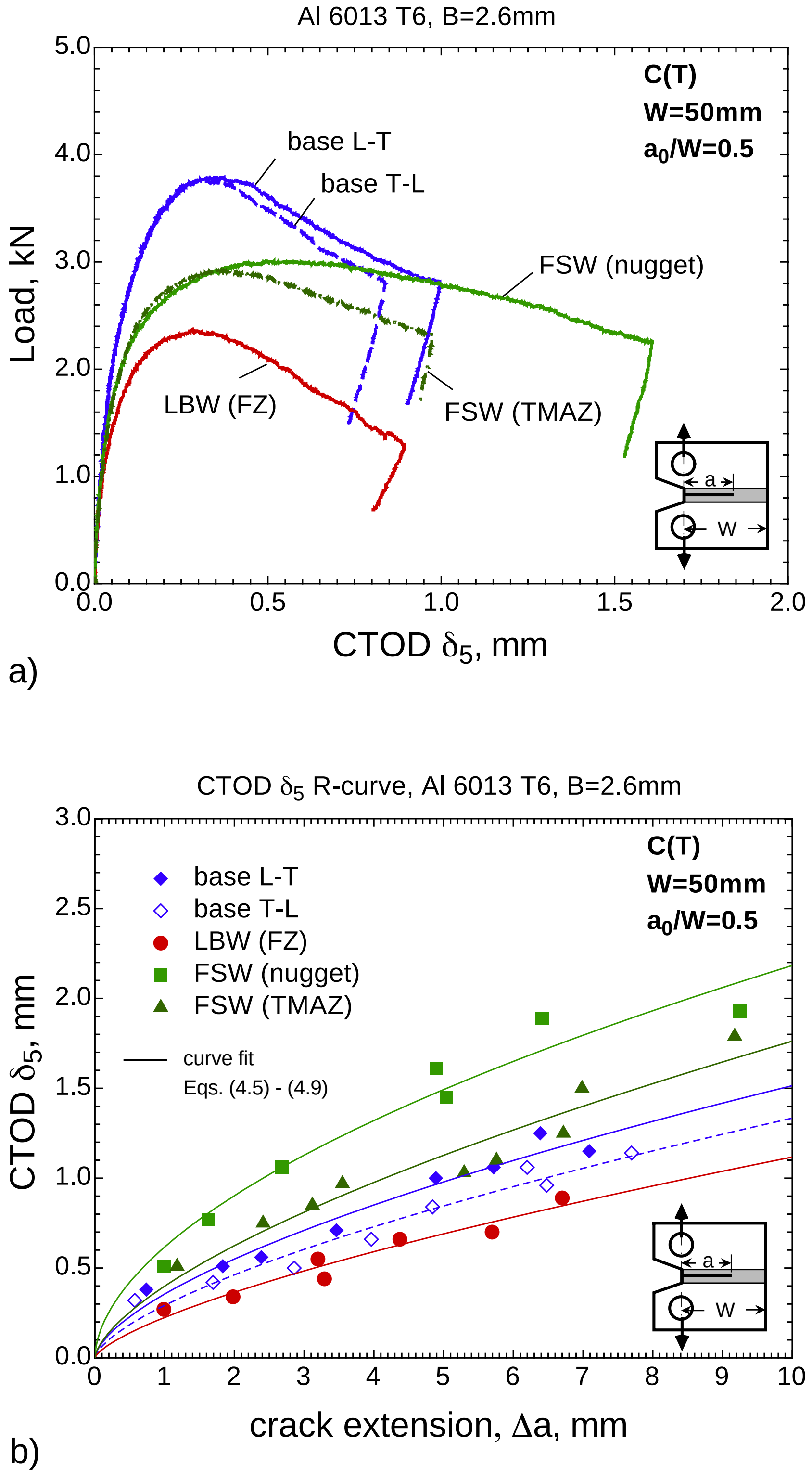

Figure 4.9: a) Load versus CTOD δ_5 plot for base material and welded joints. b) CTOD δ_5 R curves for the base material and welded joints.

Fig. 4.9a) shows the typical load versus CTOD δ_5 curves obtained for the base material in L-T and T-L orientations as well as for the LBW and FSW joints. The maximum load of the base material, which is almost identical for both L-T and T-L orientations, is higher than for welded joints. This variation in the load carrying capacity demonstrates the effect of the material strength.

The CTOD δ_5 R-curves are shown in **Fig. 4.9**b). The nugget and TMAZ regions of the FSW joint have shown the highest and the LBW joint the lowest fracture resistance. All R-curves are fitted by a power law function in order to have a closed form solution for the use in the SINTAP analysis:

$$\delta_5 = 0.356\ (\Delta a)^{0.629} \qquad \text{base L-T} \qquad (4.5)$$

$$\delta_5 = 0.293\ (\Delta a)^{0.658} \qquad \text{base T-L} \qquad (4.6)$$

$$\delta_5 = 0.226\ (\Delta a)^{0.695} \qquad \text{LBW (FZ)} \qquad (4.7)$$

$$\delta_5 = 0.618\ (\Delta a)^{0.548} \qquad \text{FSW (nugget)} \qquad (4.8)$$

$$\delta_5 = 0.400\ (\Delta a)^{0.645} \qquad \text{FSW (TMAZ)} \qquad (4.9)$$

The above curve fits should not be used beyond the crack extension range covered in the tests of respective C(T)50 specimens. These R-curves will be compared with those obtained from the respective large panels in Section 4.3.4.

4.2.4 Fracture surfaces

Fracture surfaces of base material, LBW, and FSW C(T)50 specimens were analyzed using SEM which allows to take a closer look at the fracture mechanisms.

The fractographs of the base material specimens were taken from the tunneling region where the fracture surface is normal to the loading direction, **Fig. 4.10** a) and b). There is no difference in fracture surface appearance and fracture mechanism between T-L and L-T orientations of the base material. Thus, the formation of large dimples must take place on a much smaller scale than the grain size and, therefore, the anisotropy of the material due to the rolling process does not affect the fracture mechanism at the microscopic level.

Rough fracture surfaces with equiaxed dimples are characteristic of a ductile fracture where each dimple corresponds to a void nucleation site. Inclusions of different sizes can be found at the root of dimples that participated in the damage initiation. There are locations where dimples were initiated at inclusions by matrix-particle debonding, but also as a result of particle fracture. Smooth and plane fracture surfaces of the inclusions indicate that the particles are brittle.

The size of dimples in a material is rarely uniform. Depending on the size of the inclusions, dimples may exhibit a wide range of dimensions. A network of much smaller dimples is detectable originated from very fine precipitates that might be Si and Mn rich dispersoids [99]. These smaller dimples are expected to play a role during the void coalescence process.

In contrast to the base material, the fracture surface of the LBW metal exhibits finer equiaxed dimples, **Fig. 4.10** c). It is noticeable that the dimples do not contain inclusions as was the case for the base material. Also slip bands can be observed on the walls of some dimples.

Fig. 4.10 d) shows the fracture surface of an FSW specimen with a crack located in the center of the nugget area. The dimples indicate a ductile type of fracture by microvoid coalescence. Much smaller inclusions were found at the root of the dimples than in the base material, indicating that the large inclusions of the base material were crushed during the stirring process of the FSW tool. Compared with the base material, the dimples are smaller but their depth-to-width ratio is higher testifying that the ductility of the weld material is superior to that of the base and LBW materials. This observation is backed by the micro-flat tensile specimen results. The straining capacity of the nugget material is much higher than that of the base material (see **Fig. 4.6**).

Another evidence of that are the numerous slip bands (unfortunately not clearly visible on the photos of the print-out) on the inside of the dimple flanks. Networks of very fine dimples located between the large dimples can be found as in the base material. Therefore, particles that initiated these fine dimples (these were assumed to be Si and Mn rich dispersoids in the base material [99]) must be still present in the FSW weld material and provided micro-void formations during the coalescence process of larger voids.

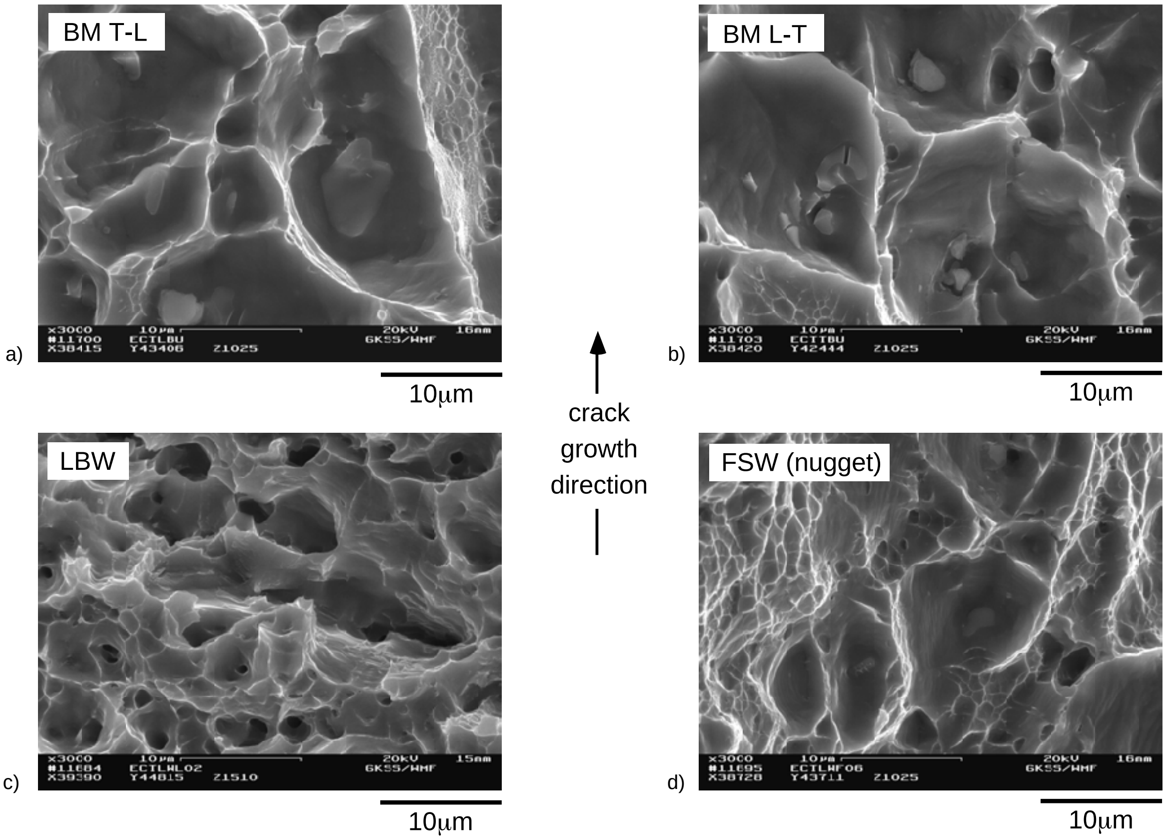

Figure 4.10: SEM fractographs of base material in a) T-L and b) L-T orientations, c) LBW and d) FSW joints.

4.2.5 Fracture path

The crack path in the base and FSW materials contain typical features of a ductile type of fracture driven by microvoid coalescence. To reveal the fracture path in welds during static loading, FSW and LBW C(T)50 specimens were unloaded after a considerable amount of stable crack extension and prepared for the SEM investigation.

The fracture path of a crack located in the nugget area of the FSW joint is shown in **Fig. 4.11**. Tiny pores are visible on the SEM micrograph before they join with the main crack. Also the perforated crack flanks indicate the typical fracture mechanism of the ductile fracture.

LBW joints showed a more complicated fracture behaviour. **Fig. 4.12** a) shows the striking feature of the zig-zag shaped (at the macroscopic level) fracture path in the LBW joint. Numerous secondary cracks can be detected in the weld. This indicates the presence of an as-cast microstructure which promotes the easy path for the crack growth in the form of secondary cracking. The propagation of the main crack is promoted by the formation and the subsequent coalescence of these secondary cracks. At the interface between the weld and base material, the highest constraint is expected to develop causing a remote damage ahead of the main crack, **Fig. 4.12** b). This experimental fact is consistent with the published results of the numerical analyses which have shown the development of secondary stress peaks as reviewed in Section 2.3.6.

The fracture surface of the LBW joint is not uniform. Therefore, two distinctive locations of the fracture surface shown in the overview SEM fractograph **Fig. 4.13** a) were examined in detail and the following observations have been made:

- intergranular ductile fracture (secondary cracks) and
- transgranular ductile fracture by microvoid coalescence.

The intergranular fracture took place along dendritic grain boundaries, **Fig. 4.13** b), and this is the controlling fracture mode in the LBW material. Obviously, the columnar grain boundary precipitation, being rich in Mn and Fe [99], provides a favourable fracture path to the crack. Since these columnar grains are not oriented in the direction of the crack propagation, the crack has to cross dendrites resulting in a transgranular fracture mode. Depending on the arrangement of dendrites, this transgranular fracture mode occurs not only under normal stresses as already discussed in the previous paragraph but also local shear stress regions can be observed creating typical shear dimples flattened and elongated in the direction of local shear displacement during fracture, **Fig. 4.13** c).

Summarizing the results, the following conclusion can be drawn for the fracture mechanism of the LBW material. The favourable fracture mode is intergranular which apparently is a low energy fracture mechanism. If the preferred fracture path along a grain boundary is not continuous, the regions that do not fracture intergranularly exhibit a local transgranular fracture by microvoid coalescence. The orientation of dendrites is, therefore, a factor that greatly influences the fracture mechanism in the LBW material and a reason for the low toughness as shown in **Fig. 4.9** b).

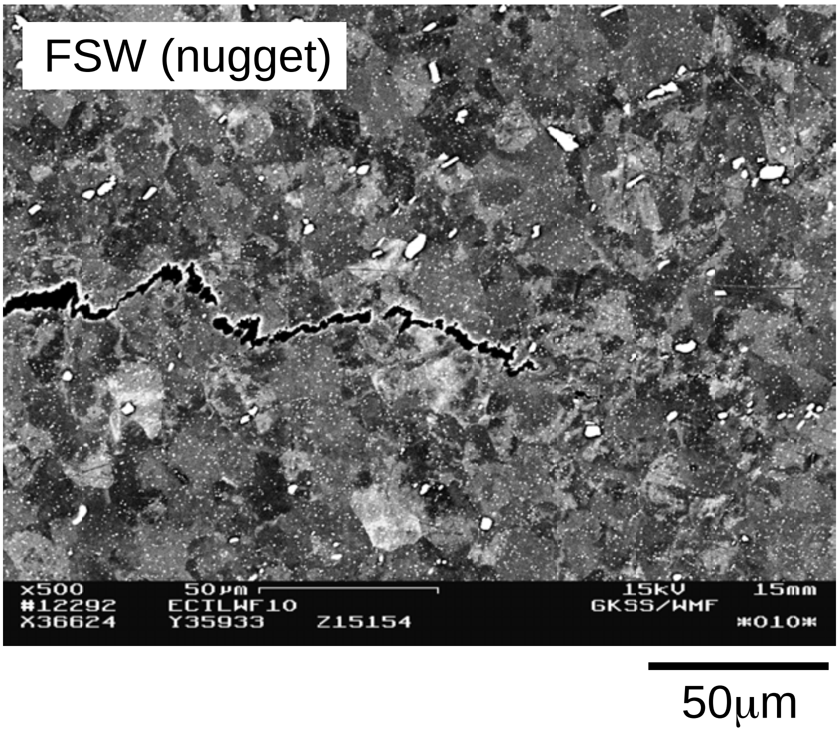

Figure 4.11: SEM micrograph of FSW joint with a crack in the nugget area.

4.2.6 Concluding remarks

The characterization of the base material and LBW and FSW joints in terms of the mechanical properties has been conducted on small scale specimens. The major conclusions are summarized in the following.

The micro-hardness profiles have shown a significant hardness drop in both LBW and FSW weld regions demonstrating the typical feature of strength undermatched welds. The FSW joint has shown hardness minima in TMAZ just outside the nugget zone.

The determination of the tensile properties has been carried out on standard and micro-flat tensile specimens. For the LBW and FSW weld materials the stress-strain curves obtained from micro-flat tensile specimens should be used, particularly if the yield strength of the weld material (and the mismatch factor, M) is sought. The yield strength values obtained from standard LBW and FSW flat tensile specimens are higher and dependent on the length of the strain gauge (this issue will be investigated further in Section 4.4).

The fracture resistance curves (R-curves) in terms of CTOD δ_5 have been measured on C(T)50 specimens. The LBW joint has yielded the lowest R-curve, whereas the FSW joint the highest. The FSW joint has been tested with two different crack locations: in the nugget zone and in the lowest hardness region (TMAZ). The nugget zone has shown the highest R-curve. The base material R-curves lie between the LBW and FSW R-curves.

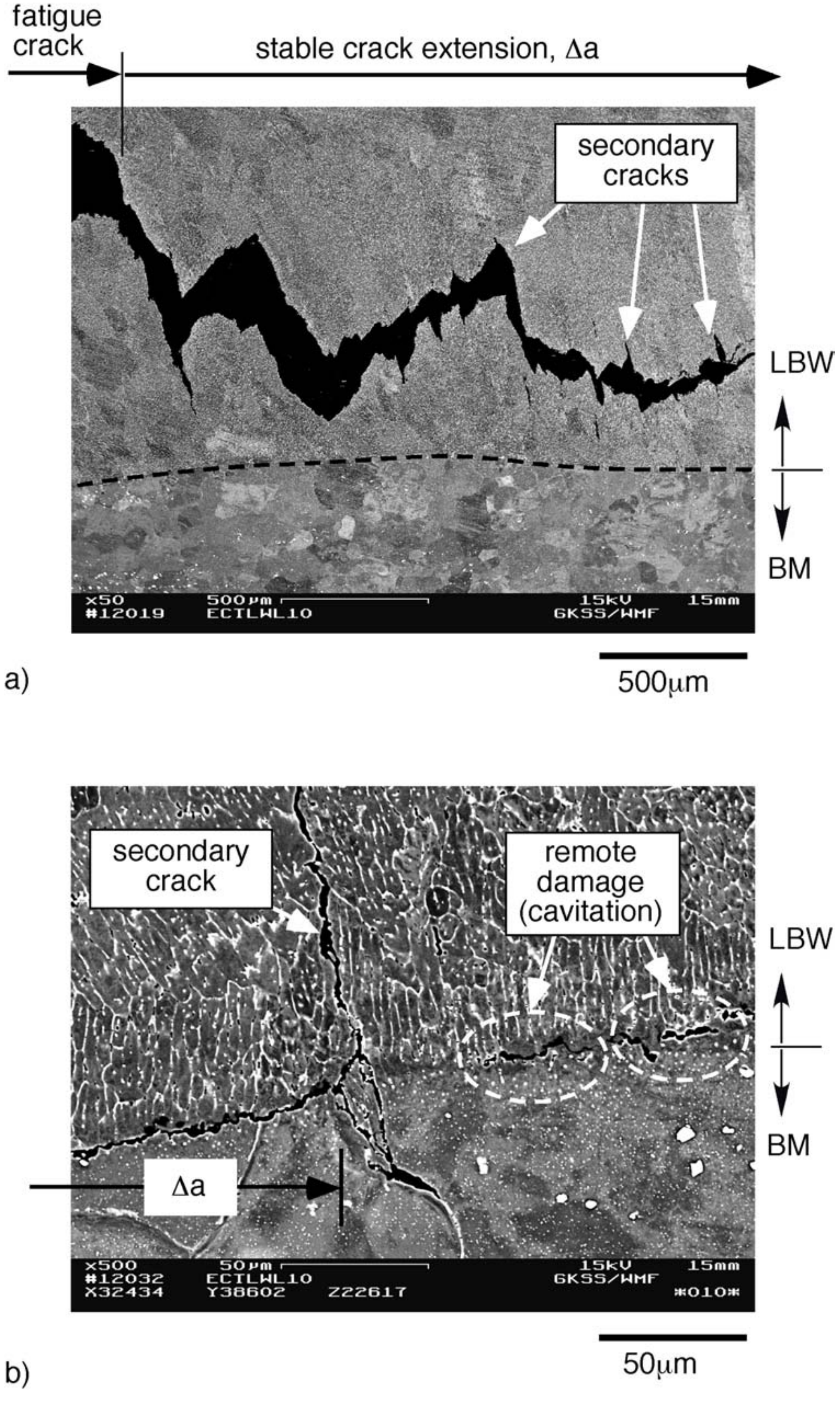

Figure 4.12: SEM micrograph of LBW joint with a crack in the fusion zone.

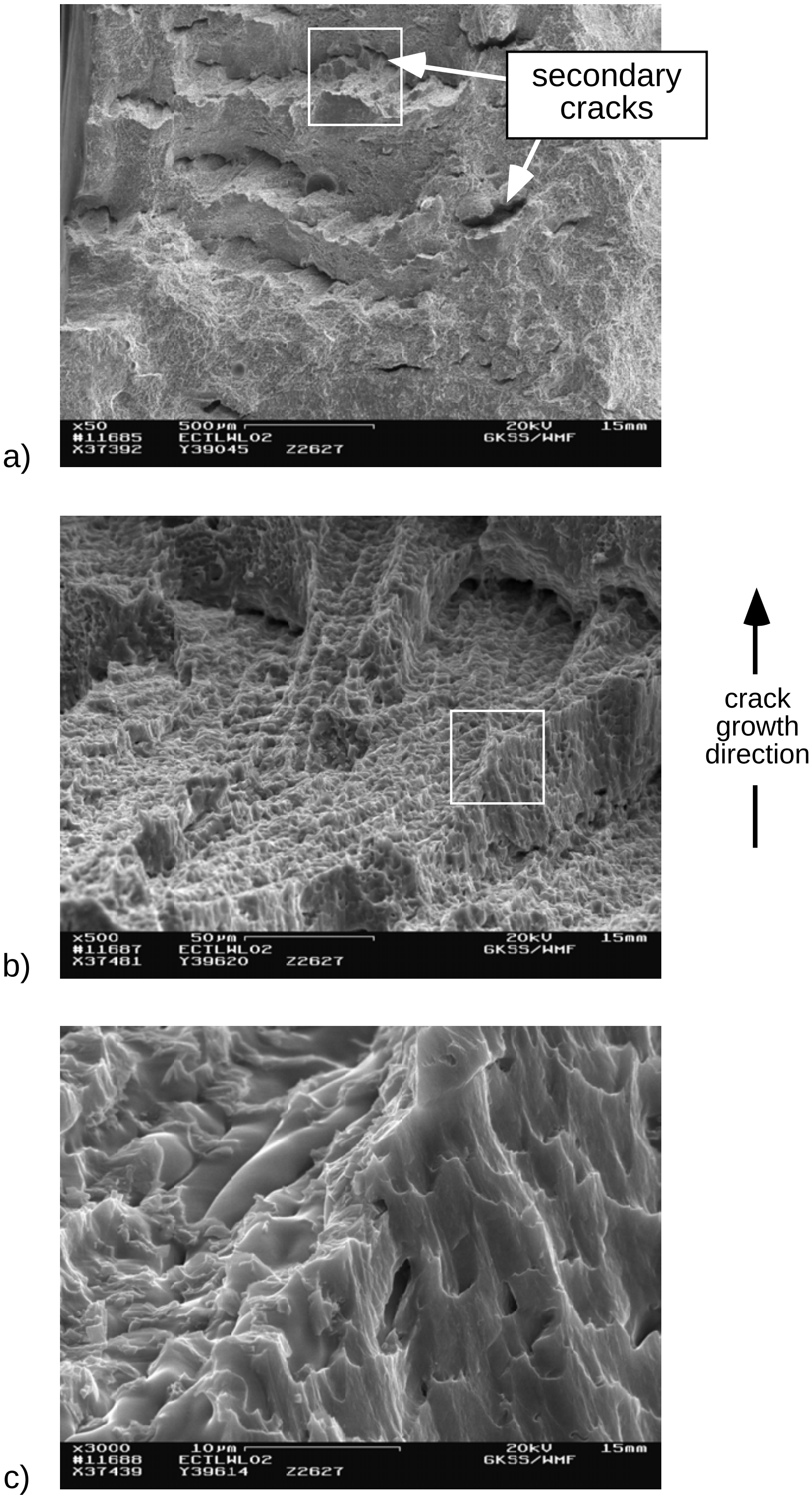

Figure 4.13: SEM micrographs of the LBW joint with a crack in the fusion zone at different magnifications a) 50x, b) 500x, c) 3000x.

4.3 Residual strength tests on unstiffened and stiffened panels

4.3.1 Experimental setup

The experimental matrix of flat stiffened and unstiffened panels with a central crack is summarized in **Tab. 4.4**. The unstiffened base material and welded panels are schematically shown in **Fig. 4.14** along with their physical dimensions. The schematics of stiffened panels are depicted in **Fig. 4.15**, whereas their detailed drawings can be found in **Figs. A.2** and **A.3** in the Appendix.

The residual strength tests were carried out at room temperature on a servo-hydraulic testing machine of 2500 kN maximum capacity, **Fig. 4.16**. The quasi-static displacement controlled loading rate was 0.1 mm/min for all panels. To ensure a pure Mode I loading, buckling was prevented by two 160 mm wide steel beams. The beams had 50 mm wide cut-outs for the installation of the clip gauges and crack length reading by the visual observation of the moving crack. During the preliminary tests, an out-of-plane displacement of the crack flanks was observed within the cut-outs. Therefore, additional inserts were installed closing the cut-outs in the range of the crack length leaving sufficient space for the instrumentation of the clips, **Fig. 4.17**. The beams and inserts were provided with a low friction teflon layer to minimize the load transfer to the anti-buckling guides.

Table 4.4: Specimen matrix of unstiffened and stiffened panels of Al 6013 T6.

Specimen type	Number of panels	L_0 mm	$2W$ mm	B mm	B^* mm	a_0/W -	Test Orientation	Crack Location
M(T) Base	3	1120	760	2.0		0.33	L-T	
	3	1120	760	2.0		0.33	T-L	
M(T) LBW	3	1120	760	2.0	2.6	0.33	T-L	FZ
M(T) FSW	3	1120	750	2.0	2.2	0.33	T-L	nugget
	3	1120	750	2.0	2.2	0.33	T-L	TMAZ
2-stringer	2	585	555	2.0	2.6	0.33	L-T	one-bay crack
3-stringer	2	630	740	2.0	2.6	0.50	L-T	two-bay crack

B^* = skin thickness at weld location, see **Fig. 4.14**

The experimental setup of stiffened panels is similar. The identical anti-buckling guide was used on the flat side of the stiffened panels with the same instrumentation as for the unstiffened panels. However, due to the stringers, a special steel beam was designed with cut-outs for the stringers, **Fig. 4.18**. Since only the skin was loaded, it was necessary to support the guides in order to prevent the out-of-plane bending caused by the asymmetry resulting from the stringers.

All quantities measured in the residual strength tests of unstiffened as well as stiffened panels are shown in **Fig. 4.19**. They are:

- applied load, F, kN
- Crack Mouth Opening Displacement (CMOD), mm
- Crack Tip Opening Displacement (CTOD), δ_5, mm
- total elongation, v_{LL}, of the panel at a gauge length L_0, mm
- stable crack extension, Δa, in unstiffened panels, mm

The stable crack extension was visually measured on the specimen side surface. In front of each crack tip a millimeter scale was applied onto the specimen side surface in order to visually measure the stable crack extension in unstiffened panels. All other quantities were continuously recorded in 0.5 sec steps by a digital data acquisition system.

4.3.2 Specimen preparation

Base material wide plates

In a material manufactured by the rolling process mechanical properties may vary with respect to the rolling direction. Therefore, the residual strength tests on base material wide plates were carried out in two orientations:

- L-T orientation (loading in rolling direction (L), crack placed perpendicular to the rolling direction (LT)),
- T-L orientation (loading in LT, crack placed in L).

The machined notch was precracked under cyclic loading until fatigue cracks of 2-3 mm length were generated at both ends of the notch. The total initial crack length was $2a_0 = 252$ mm which corresponds to a crack ratio of $a_0/W = 0.33$.

LBW wide plates

The LBW panels were welded at IWS Dresden/Germany under the contract of Airbus. The raw sheet material had a larger width of 960 mm than the final width of 760 mm of M(T) panels. The weld was placed in a single run over the entire panel width using the CO_2 laser. The starting and end points of the LBW weld were excluded when extracting the 760 mm wide M(T) specimens.

The LBW butt joints were tested in as-welded condition at room temperature. The 50 mm wide skin reinforcement (**Fig. 4.14**) was not machined off, thus having the original (total) thickness of $B^* = 2.6$ mm (see **Tab. 4.4**).

The crack was placed along the centerline of the LBW weld. The initial mechanical notch of 246 mm length was introduced by EDM using a 0.3 mm wire. The notch was then fatigue precracked under cyclic loading until 2-3 mm long fatigue cracks grew at each crack tip. The total initial crack length was $2a_0 = 252$ mm which corresponds to an initial crack ratio of $a_0/W = 0.33$ as in the base material. The tests were carried out in as-welded condition at room temperature.

Although the crack was exactly placed along the weld centerline, in practical cases the crack may easily grow to the the weld/base material interface due to the very narrow LBW weld. In a previous Section 2.3 it was discussed that the position of a crack relative to the interface plays a minor role in a narrow highly undermatched weld. Therefore, within this study only one crack location was analyzed with LBW panels without placing the initial crack to the heat affected zone.

FSW wide plates

FSW panels were welded at the EADS CRC Ottobrunn/Germany. Since the machine was not able to weld the entire width of 760 mm in a single run, two separate runs were necessary. The two halves of a panel were fixed on the machine table and the first weld was made by traversing the FSW tool from the center to the edge of the panel, **Fig. 4.20**. The second run was made in the same way after rotating the panel 180° about the normal axis. The second run had the same rotational velocity as the first one so that the retreating and advancing sides swap when passing the center of the welded panel. However, due to a symmetrical hardness profile, the influence on the residual strength is expected to be negligibly small.

It is well known that the desired welding parameters (eg. rotating and travel speed) are reached after a certain acceleration phase of the FSW tool. From the weld starting point to the location where the steady state is established, the welding parameters permanently change and so do the weld properties. In order to test a weld with constant properties, it was assured that the distance of the acceleration phase of the FSW tool was within the range where the crack was later placed for the residual strength tests. The crack tips were therefore in the weld area of constant welding parameters.

Unlike the LBW joints, the raw sheet material for the FSW joints was already cut to the final width of 760 mm. To achieve a smooth run-out of the FSW welds, additional small sheets of the same material and thickness were tightly attached to the edges of the panels. Unfortunately, the material at the transition was not properly mixed, resulting in an unacceptable weld, **Fig. 4.21**. This part was removed by cutting a 5 mm wide strip along the longitudinal edge on each side of the panel. The total width of all FSW panels was, therefore, reduced to 750 mm.

As in the base material and LBW panels, a mechanical notch of 246 mm length was placed along the weld centerline using EDM with a 0.3 mm wire. The notched panels were then fatigue precracked under cyclic loading until 2-3 mm long fatigue cracks formed at each crack tip. The initial total crack length was $2a_0 = 252$ mm (initial crack ratio $a_0/W = 0.336$).

The characterization of the FSW joint in terms of hardness showed that beside the low-hardness nugget area there exists a second hardness minimum being located in the TMAZ just outside the highly stirred nugget area. Therefore, in addition to the FSW panels with a weld centerline crack, panels were also prepared with a crack of the same length in the lowest-hardness (TMAZ) region as was the case for small scale C(T)50 specimens to generate the R-curves.

Preparation of stiffened panels

LBW welded stiffened panels were also manufactured at the IWS Dresden/Germany. The stringers extruded from the same material as the skin were welded to the skin using two CO_2 laser sources acting simultaneously from each side of the stringer. Unlike the unstiffened panels, the stringer and skin materials were welded in the T4 condition. After welding the stiffened panels were post weld heat treated to the T6 condition.

The initial notch was introduced by EDM using a 0.3 mm wire and extended by fatigue loading to a one-bay crack in 2-stringer panels and a two-bay crack over a broken central stringer in 3-stringer panels. The fatigue crack tip had a distance of approximately 1.0 mm from the weld but in all cases did not touch it, **Fig. 4.22**.

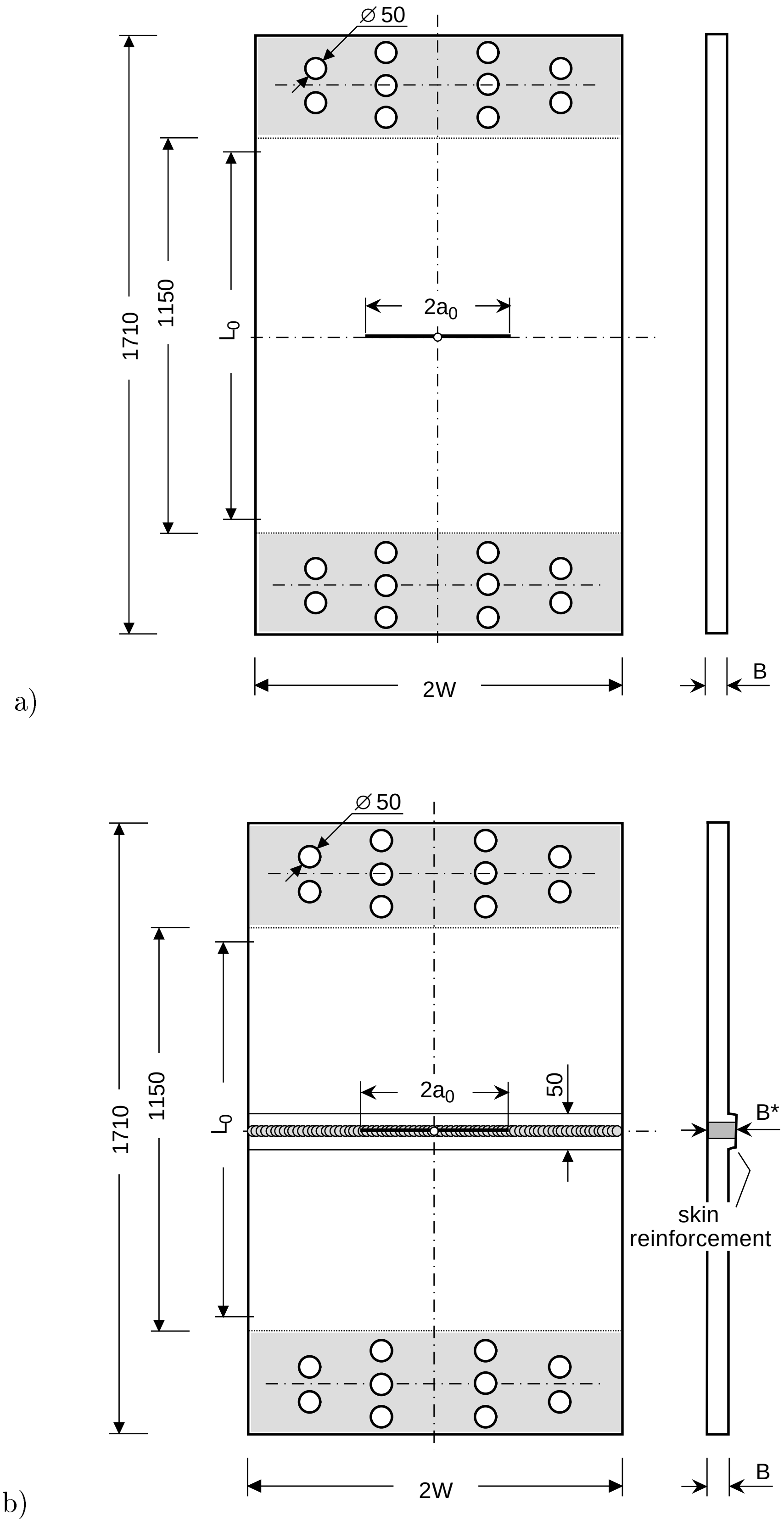

Figure 4.14: Configuration of M(T) specimens: a) base material, b) LBW and FSW panels. B^* represents the skin reinforcement to compensate the weld strength mismatch.

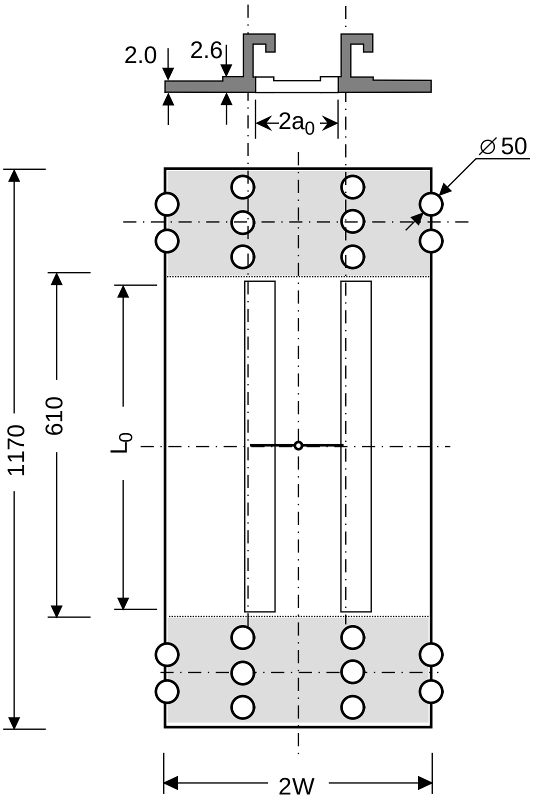
a)

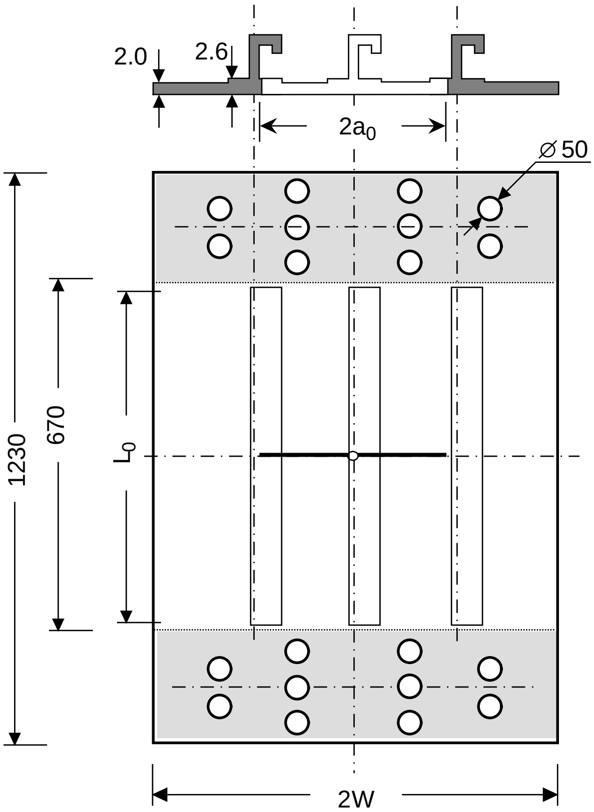
b)

Figure 4.15: Configuration of stiffened panels: a) 2-stringer, b) 3-stringer panel. For detailed drawings see **Figs. A.2** and **A.3** in Appendix.

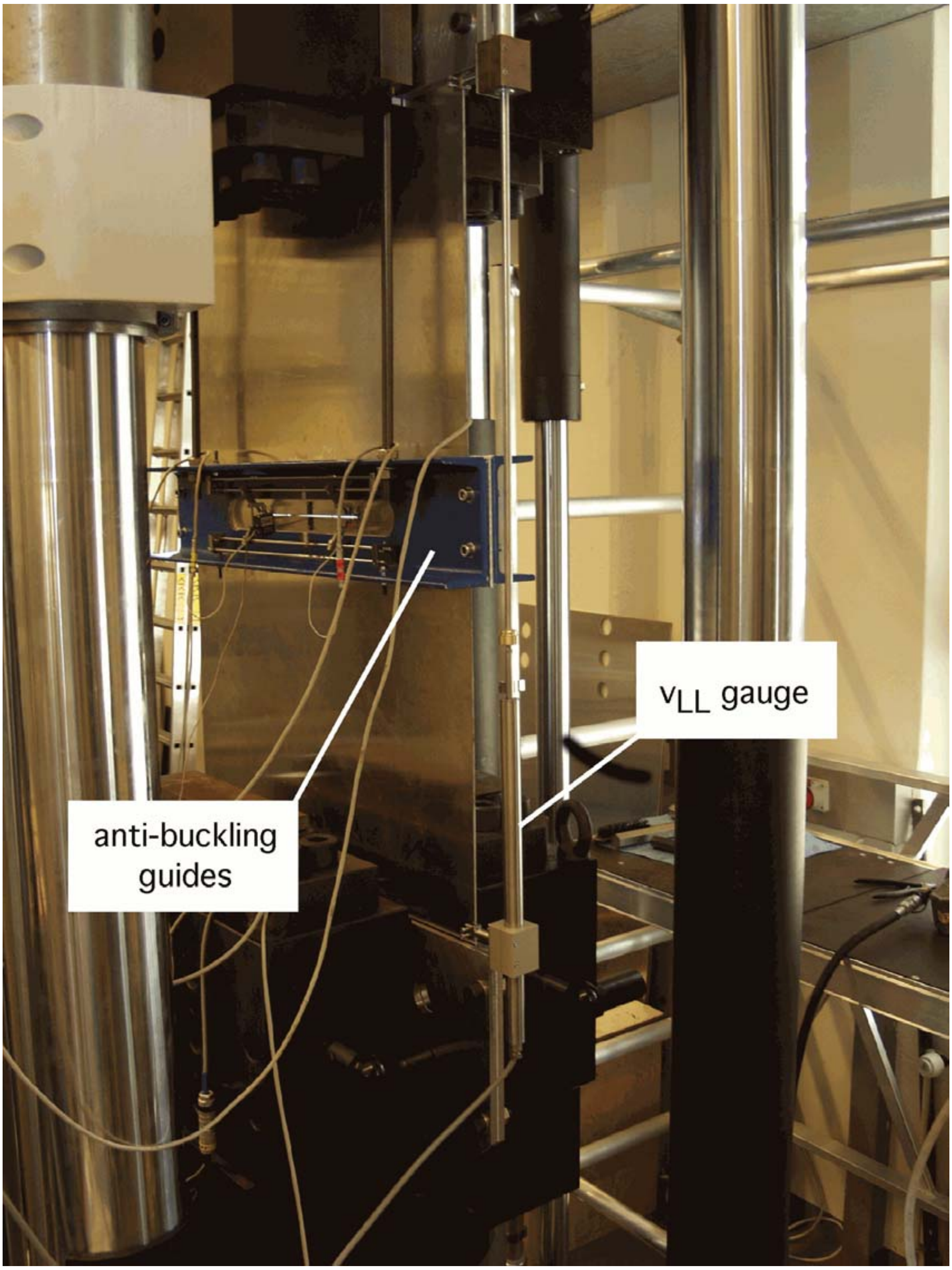

Figure 4.16: Servo-hydraulic testing machine of 2500 kN maximum capacity for the residual strength tests of flat unstiffened and stiffened panels. Here, an instrumented base material panel is shown.

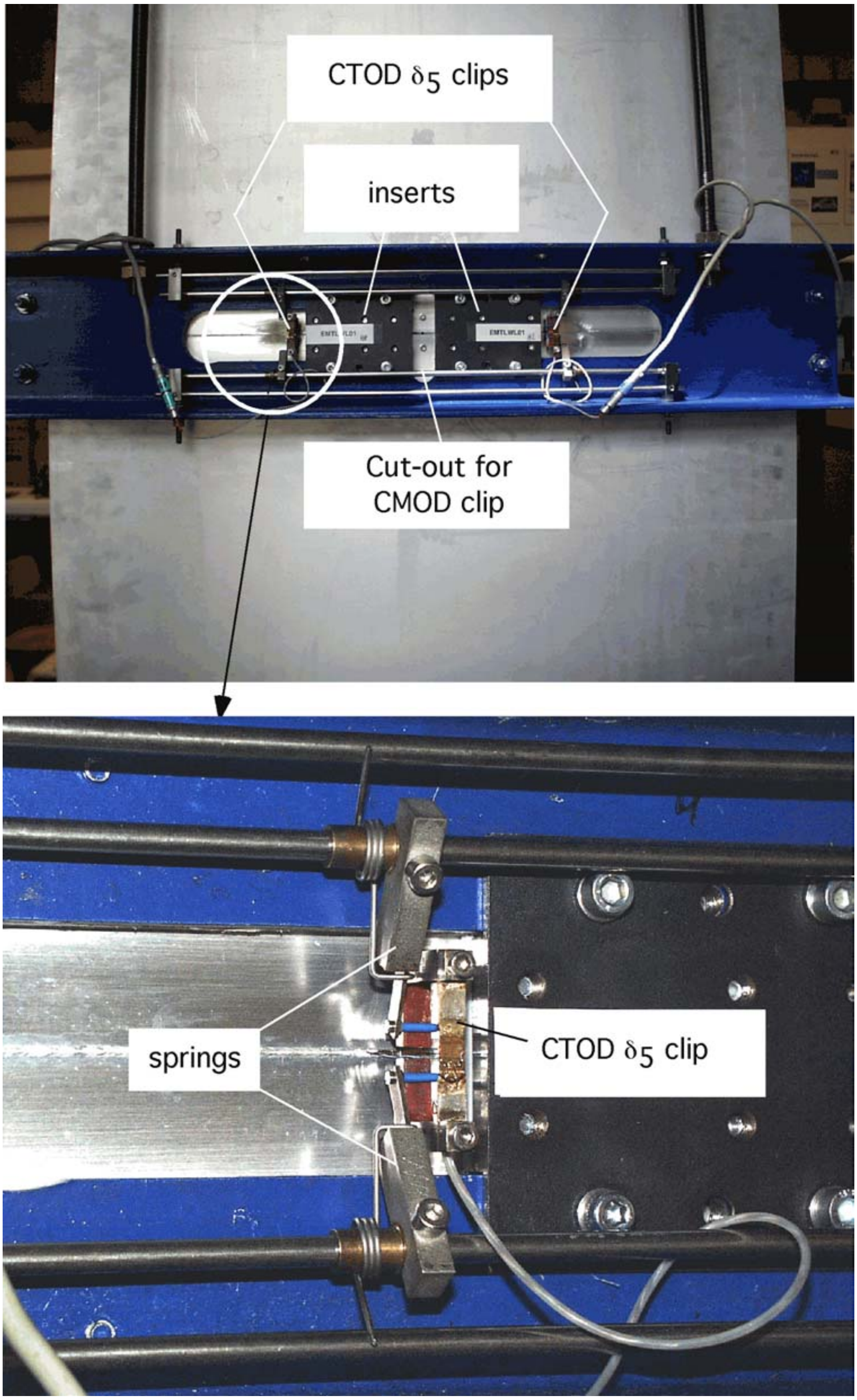

Figure 4.17: Details of anti-buckling guides (top figure) and a CTOD δ_5 clip (bottom figure).

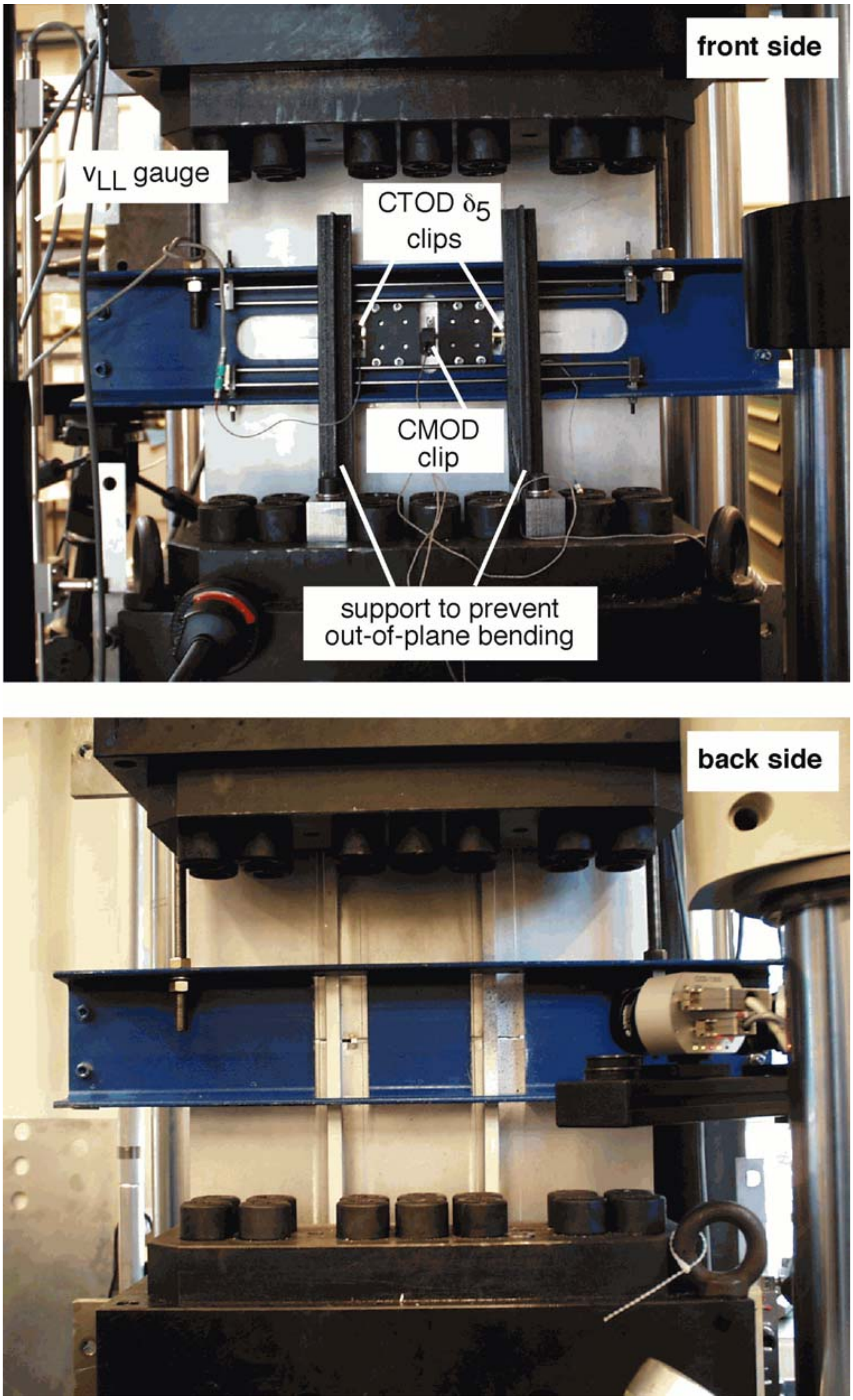

Figure 4.18: Experimental setup of the stiffened panels (setup for 2- and 3-stringer panels is similar). Anti-buckling guides (similar to those of unstiffened panels) were supported in order to prevent the out-of-plane bending.

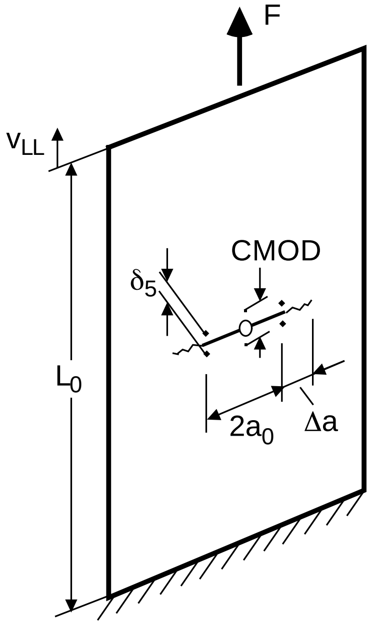

Figure 4.19: Load and displacements measured in residual strength tests of unstiffened and stiffened panels.

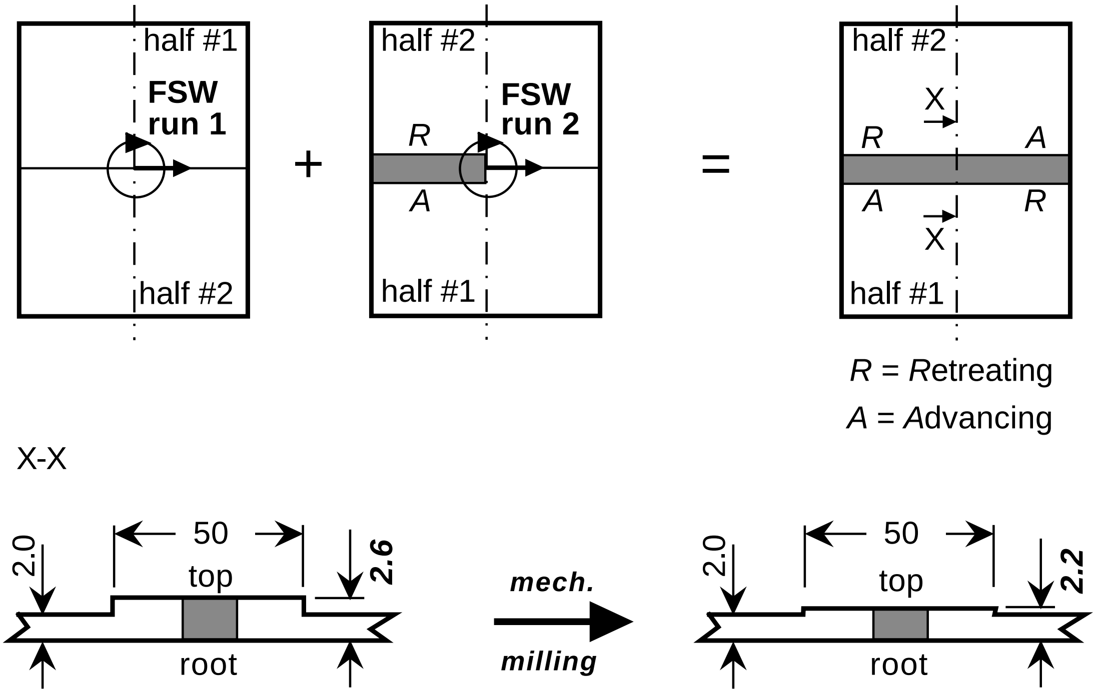

Figure 4.20: FSW welding of M(T) specimens. The panels were welded in two steps. After welding, the skin reinforcement of 2.6 mm was partly machined off by mechanical milling to 2.2 mm.

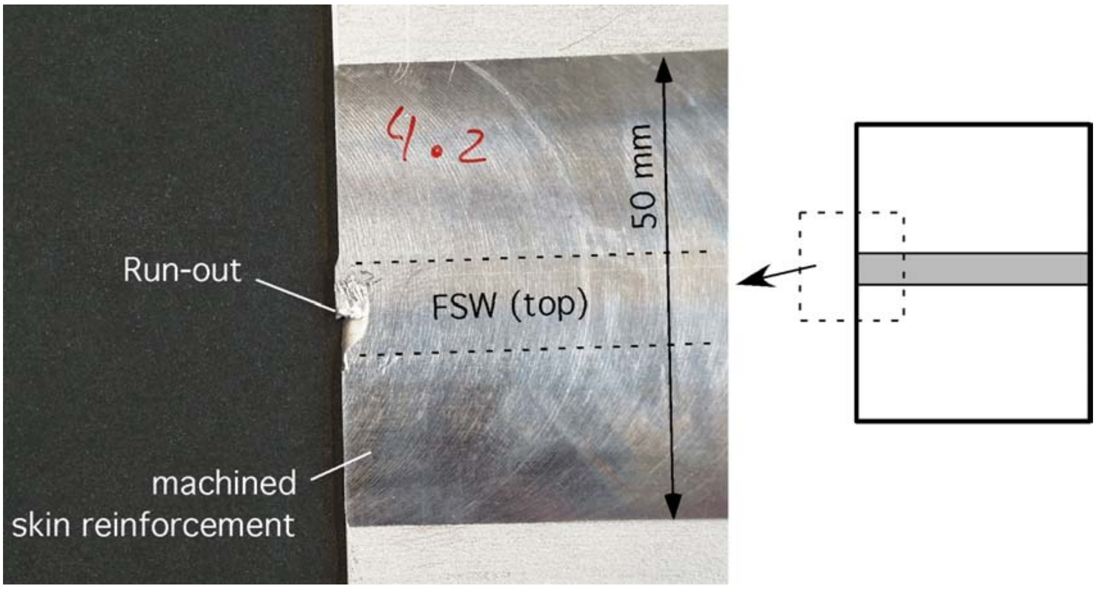

Figure 4.21: Run-out at the edge of an FSW welded panel. This part was removed by cutting a 5 mm wide strip along the longitudinal edge of the panel.

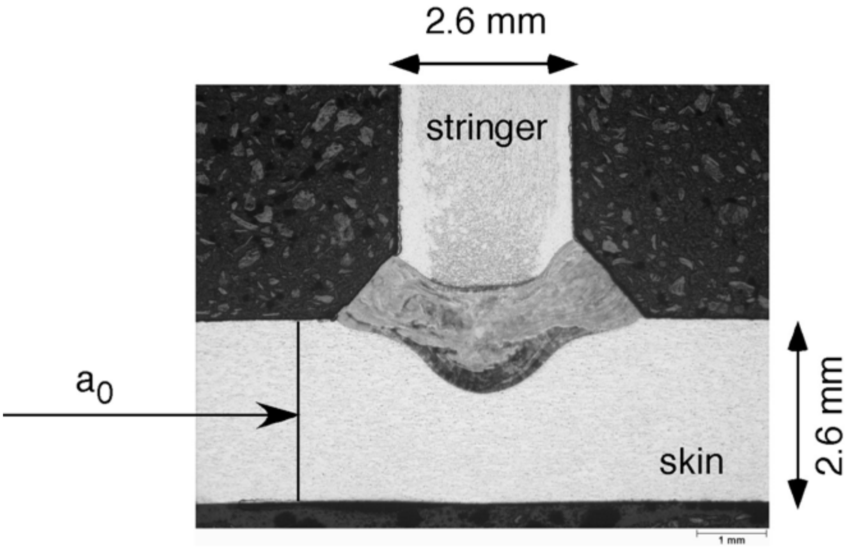

Figure 4.22: Fatigue crack tip location in LBW welded stiffened panels.

4.3.3 Results and discussion of residual strength tests on un-stiffened panels

After the specimen preparation, the cracked base material, LBW, FSW, and stiffened panels were subjected to uniaxial loading in order to determine their maximum load carrying capacity. First the results of unstiffened panels are discussed, then the observation on 2- and 3-stringer panels is reported in the subsequent section.

The deformation behaviour of unstiffened panels in terms of a load-CMOD diagram is illustrated in **Fig. 4.23**. The base material panels in both L-T and T-L orientations did not experience unstable fracture, whereas all welded panels unstably fractured at the point of the maximum load. The residual strength of the base material is superior to that of welded panels which might be expected from the comparison of respective tensile specimens. The LBW M(T) panel attained the lowest maximum load carrying capacity. The lowest hardness region (TMAZ) of the FSW joint has been proved to be the critical fracture location of the FSW joints.

The diagram in terms of load-CTOD δ_5 in **Fig. 4.24** shows the same trend as observed in load-CMOD plots. The presence of a non-linear deformation at the crack tip in the LBW M(T) panel is hardly visible in the load-CMOD plot; however, since CTOD δ_5 is measured locally, it shows that there is a non-linear deformation behaviour at the crack tip induced by stable crack advance and plastic deformation in the crack tip vicinity.

The correlation between CMOD and CTOD δ_5 is shown in **Fig. 4.25**. At low load levels, the CMOD increase is faster than that of CTOD δ_5. Since the position of the CTOD δ_5 clip is stationary at the fatigue crack tip, its physical meaning becomes close to that of CMOD as stable crack extension increases. The crack tip moves further away from the CTOD δ_5 clip which basically measures the relative displacement of crack flanks, similar to the CMOD clip at the crack center. Therefore, with increasing stable crack extension, CTOD δ_5 approaches CMOD values as can be seen for the base material panels.

Fig. 4.26 provides a diagram of CTOD δ_5 as a crack tip loading parameter plotted versus the applied strain in terms of GLS. As expected from the Design Curve approach presented in Section 2.4, CTOD δ_5 is a quadratic function of the applied strain in the initial part of the curves, whereas in the fully plastic regime the relation becomes linear which is clearly visible for the base material curves beyond the maximum load. For a given applied strain, CTOD δ_5 of welded panels is higher than that of the base material. This fact is also consistent with the published results reviewed in Section 2.3 where the crack tip loading in undermatched welds is higher due to the softer/weaker weld material than the respective base material panel strained to the same level. Welded panels should be compared with the T-L orientation since the rolling direction coincides with the welding direction.

The difference between the welded panels is marginal although according to the numerical analysis [39] the crack tip loading in an undermatched weld should be higher for larger weld width. In this study, LBW is considered a narrow and FSW a wide weld. However, the numerical results of Zhang et al. [100] have indicated the importance of the crack length to weld width ratio, a/H, on fracture mechanics parameters. They have demonstrated that strength mismatched welded plates behave similarly to base material plates if the crack length is much larger then the weld width ($a/H \gg 1$). This was also confirmed by experimental findings in plates with long cracks in undermatched [101] as well as overmatched [102] welds.

The concept of gauge length strain representing the global behaviour of the panels may provide a misleading information on the true level of localized strain in the undermatched weld zone. The gauge length of $L_0 = 1120$ mm selected in this investigation is very large compared with the weld dimensions so that the relative contribution of the weld material deformation to the total elongation, v_{LL}, of welded panels is small. Reducing the gauge length will certainly change the applied strain value; however, a unique definition of the applied strain in cracked panels with undermatched welds will be still lacking.

In the author's opinion this gauge length strain concept is most suitable for overmatched welds with a potential shielding effect of a stronger weld material to protect a (short) crack in the weld from an extensive plastic deformation at the crack tip [102]. This protection may lead to a gross section yielding behaviour that can be best illustrated in a crack tip loading versus applied gauge length strain diagram. Such diagram provides a relationship between the weld metal toughness and overall weld joint fracture behaviour.

The fracture path in LBW and FSW M(T) panels is illustrated in **Fig. 4.27**. All welded panels exhibited unstable fracture after a small amount (4-9 mm) of stable crack extension. In FSW M(T) panels with a crack located in the nugget area along the weld centerline the crack deviated into TMAZ during unstable fracture.

The instability in LBW M(T) panels was characterized by two distinctive events. One is a sudden crack growth jump followed by the final unstable fracture, the other is the immediate final fracture, **Fig. 4.28**.

An interesting observation was made on the FSW M(T) panels with a crack in TMAZ. During a test, the displacement controlled loading of the machine was stopped for one panel near the maximum load in order to measure the stable crack extension. However, the panel suddenly failed in an unstable manner, obviously feeding the crack driving force from the elastically stored energy in the panel, **Fig. 4.29**.

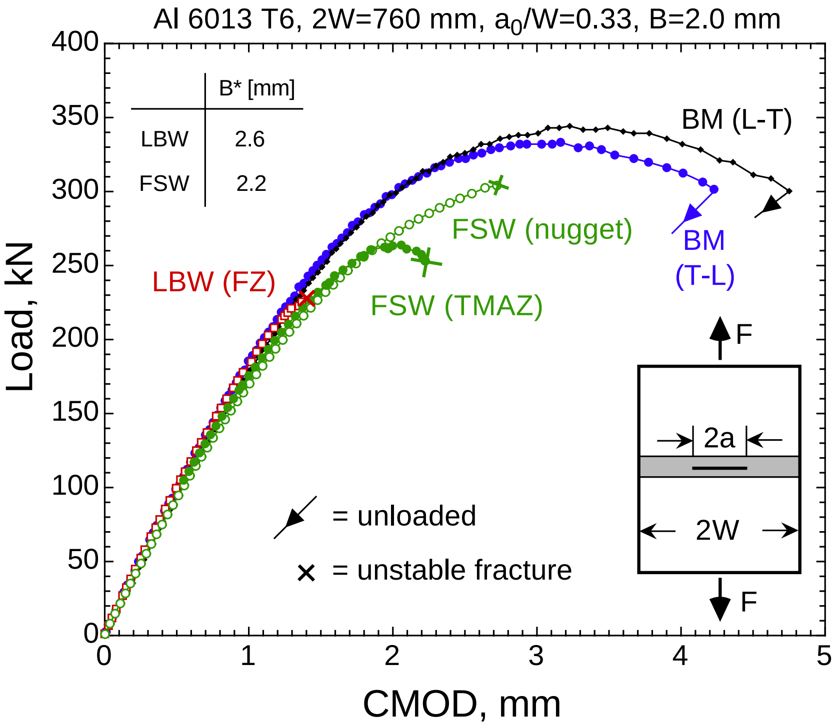

Figure 4.23: Comparison of experimental load vs. CMOD curves for base material (BM) and welded (LBW and FSW) panels.

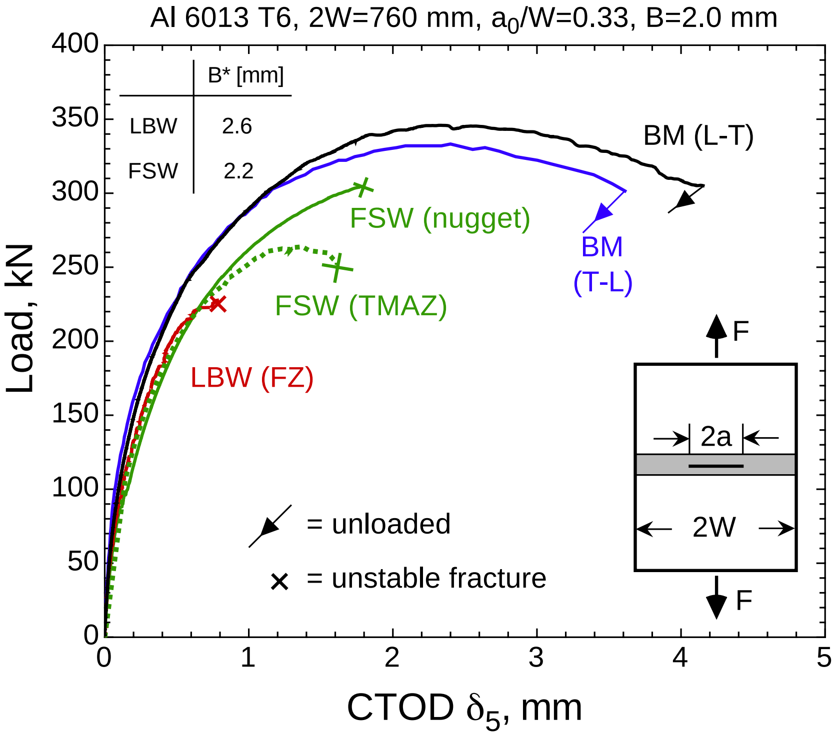

Figure 4.24: Comparison of experimental load vs. CTOD δ_5 curves for base material (BM) and welded (LBW and FSW) panels.

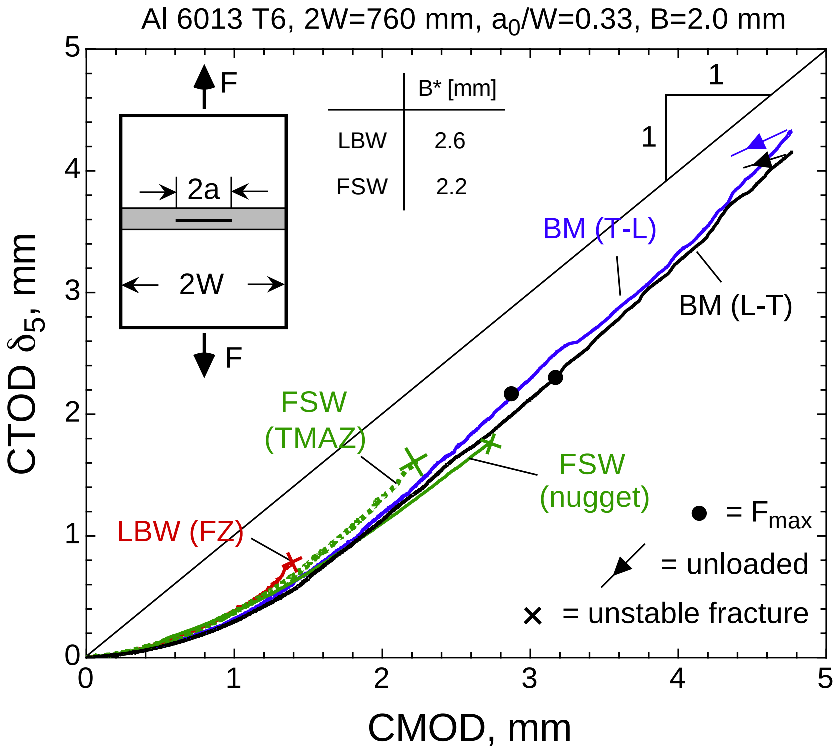

Figure 4.25: Correlation between CTOD δ_5 and CMOD for base material (BM) and welded panels: LBW (FZ) with a crack in the fusion zone (FZ), FSW (nugget) - crack in the weld centerline, and FSW (TMAZ) - crack in the TMAZ.

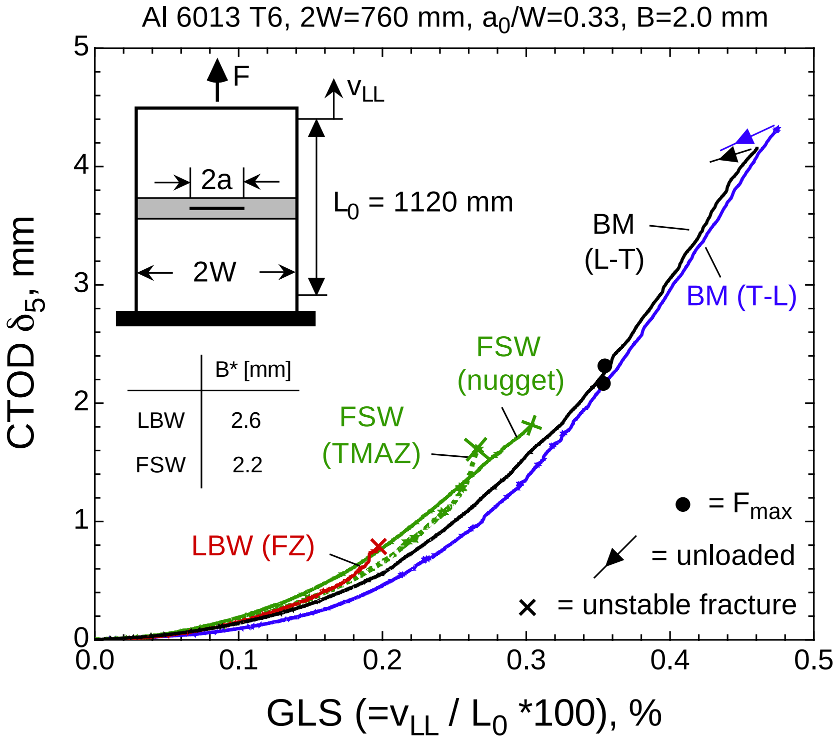

Figure 4.26: Comparison of CTOD δ_5 vs. the gauge length strain (GLS) curves for base material (BM) and welded (LBW and FSW) panels.

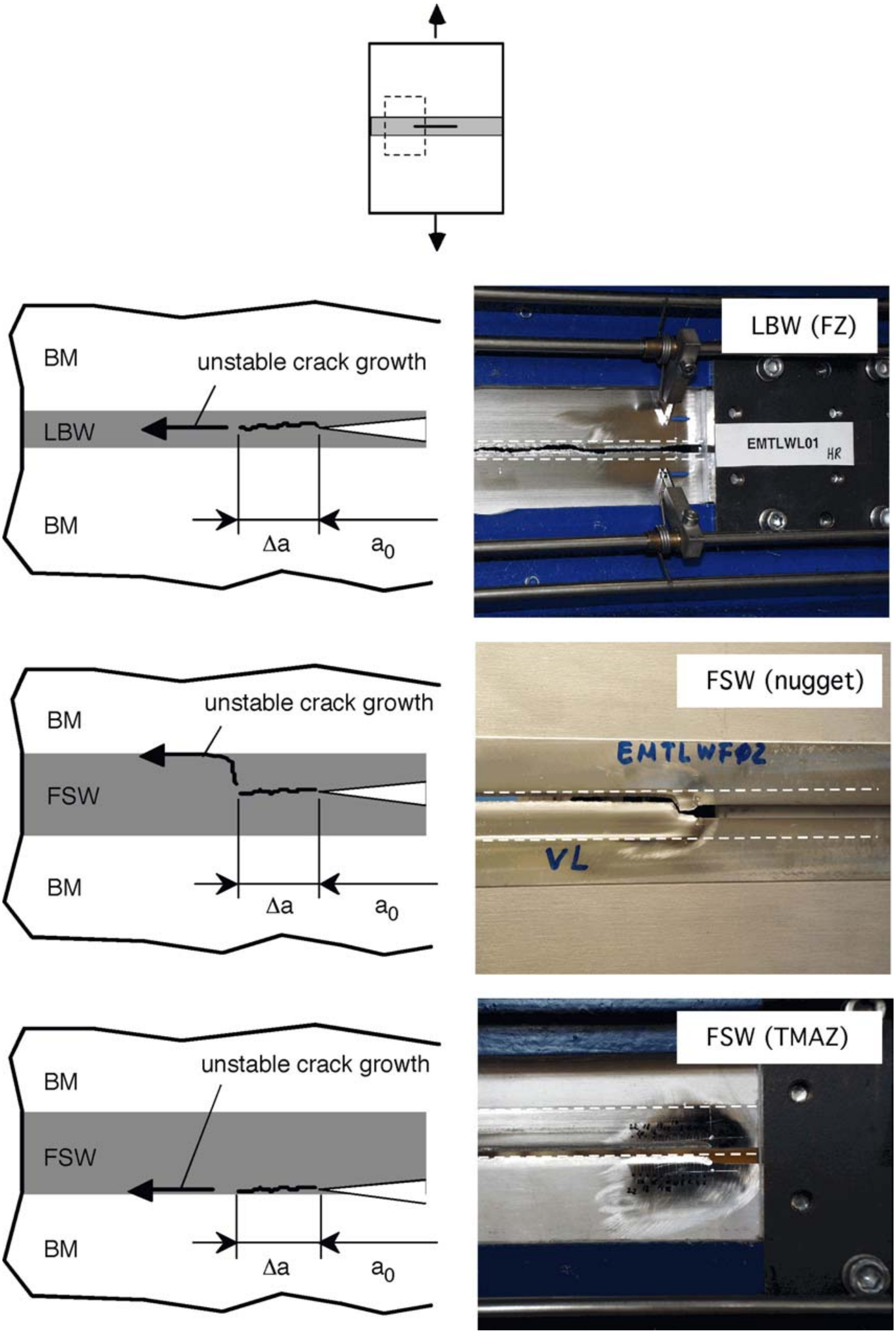

Figure 4.27: Fracture path of welded panels. All welded panels exhibited a small amount (~ 4-9 mm) of stable crack extension, Δa, prior to an unstable fracture. In the FSW panel (FSW(nugget)), the crack located in the nugget zone stably grew along the weld centerline and finally deviated into the TMAZ during the unstable fracture.

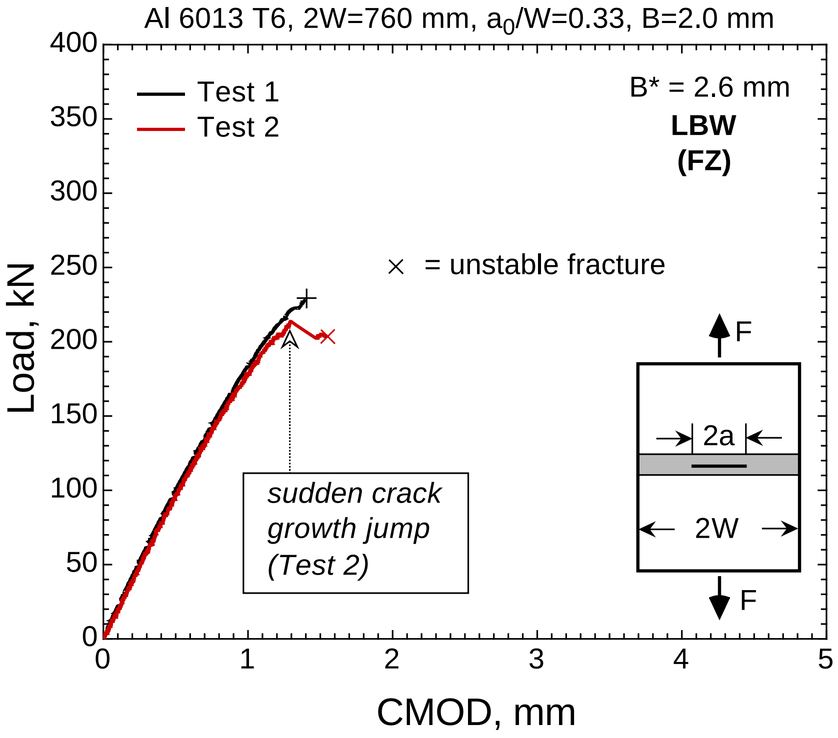

Figure 4.28: Experimental load vs. CMOD plot for LBW panels with a crack located in the fusion zone (FZ). The two tests show the representative failure behaviour of LBW panels: sudden crack growth jump followed by the final fracture of the panel (Test 2) or immediate final fracture (Test 1).

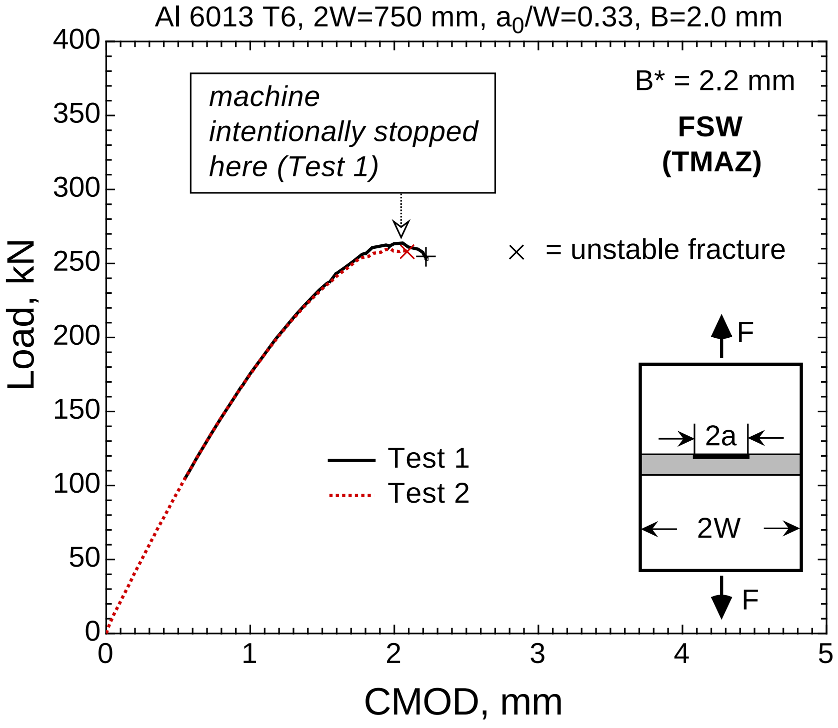

Figure 4.29: Experimental load vs. CMOD plot for FSW panels with cracks located in TMAZ. In Test 1, the machine was intentionally stopped at the maximum load to measure the physical crack extension. However, the panel failed in an unstable manner, obviously feeding the crack driving force from the elastically stored energy in the panel.

4.3.4 Results and discussion of R-curves

The determination of crack resistance curves (R-curves) of thin-walled plate materials and especially their strength undermatched welded joints needs some considerations. The existing ASTM E561 standard [16] provides guidelines for the base material R-curves only, whereas some guidance on R-curve determination for mismatched welded panels is given in the test procedure EFAM GTP 02 [64]. Therefore, this section will discuss the R-curve determination of both base material and welded panels in detail.

Base metal wide plates

Fig. 4.30 shows the R-curves obtained according to the ASTM E561 standard for both orientations (L-T and T-L). The effective crack length was determined using the compliance method and the Irwin correction. It can be seen that beyond the validity limit of the net section yielding ($\sigma_{\mathrm{net}} = \mathrm{R}_{\mathrm{p0.2}}$) the Irwin R-curve is lower. However, within the validity range there is a large intermediate part of the compliance and Irwin R-curves forming a single curve and, regarding the shape of the curves, they can be considered identical. However, fracture toughness value, K_{c}:

$$K_{\mathrm{c}} = \frac{F_{\mathrm{max}}}{2WB}\sqrt{\pi a_{\mathrm{eff,c}}} \times \sqrt{\frac{1}{\cos\dfrac{\pi a_{\mathrm{eff,c}}}{2W}}} \tag{4.10}$$

differs as indicated by the arrows in these diagrams. In Eq. (4.10) F_{max} is the maximum load attained in the test and $a_{\mathrm{eff,c}}$ is the corresponding effective half crack length. The critical stress intensity factors, K_{c}, of the base material according to Eq. (4.10) are summarized in **Tab. 4.5**.

The K_{c}-value can also be determined graphically by finding the tangency condition between the R-curve and the applied stress intensity factor:

$$K_{\mathrm{appl}} = \frac{F}{2WB}\sqrt{\pi a_{\mathrm{eff}}} \times \sqrt{\frac{1}{\cos\dfrac{\pi a_{\mathrm{eff}}}{2W}}} \tag{4.11}$$

where a_{eff} is simply an independent variable. The tangency condition is met at the same K_{c} value as obtained from Eq. (4.10) for $F = F_{\mathrm{max}}$ being the experimental maximum load, **Fig. 4.30**. This is not surprising since the R-curve and the applied stress intensity factor were calculated with identical equations.

The commonly used apparent fracture toughness, K_{c0}, is defined as:

$$K_{\mathrm{c0}} = \frac{F_{\mathrm{max}}}{2WB}\sqrt{\pi a_0} \times \sqrt{\frac{1}{\cos\dfrac{\pi a_0}{2W}}} \tag{4.12}$$

which is also calculated at the maximum load but based on the initial half crack length, a_0.

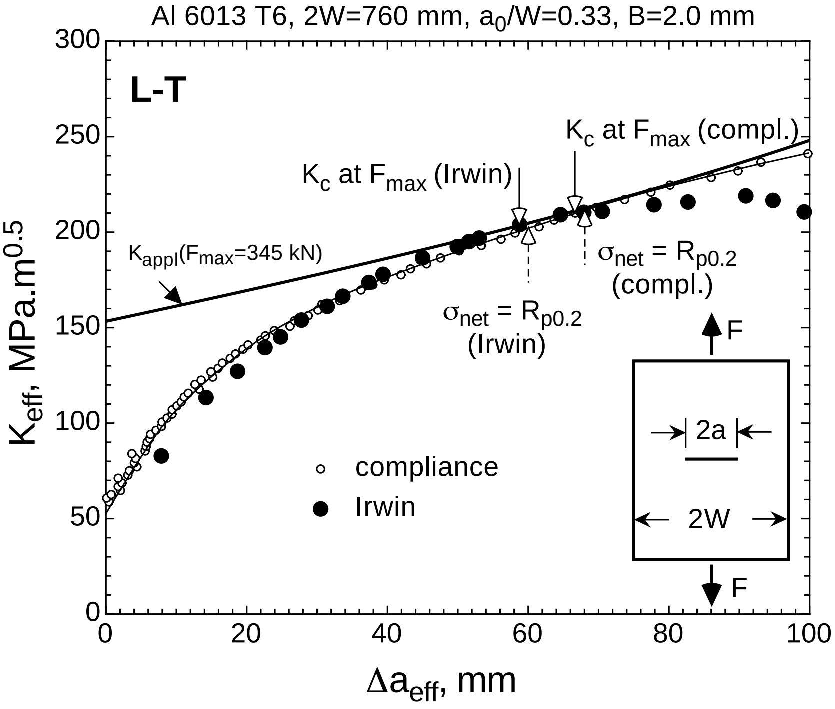

a)

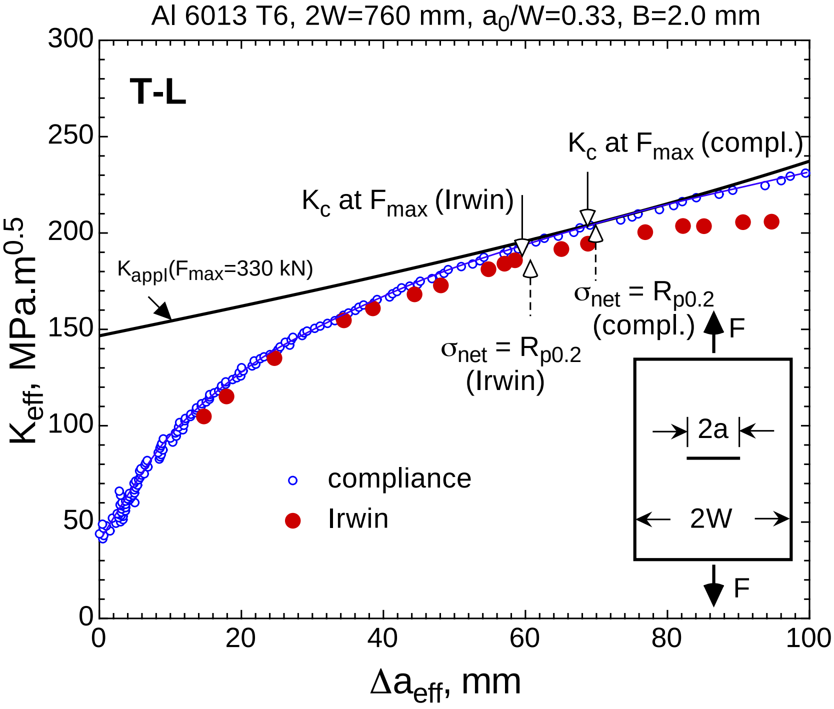

b)

Figure 4.30: K_{eff} R-curves of the base material. a) L-T and b) T-L orientations.

It is therefore less than K_c and provides a conservative fracture toughness value. This definition is very convenient since it does not require the knowledge of the stable crack extension and is often used as a quick toughness estimate (eg. [103]). Since in the LBW and FSW panels the stable crack extension was small compared to the initial crack length, the fracture toughness in terms of K_{c0} might be a close estimate to the K_c-value. K_{c0}-values for the base material and LBW and FSW M(T) panels are summarized in **Tab. 4.6** and plotted in **Fig. 4.31**. The table also contains fracture toughness results of LBW butt joints which have been obtained from M(T) panels with shorter cracks ($a_0/W = 0.15$). The fracture toughness in terms of K_{c0} seems to be within the scatter range of the M(T) panels with ($a_0/W = 0.33$) indicating no size dependence regarding the initial crack length. It should be noted that the number of tests conducted may not be sufficient to verify the size independence. Moreover, the variation of the panel width at a constant a/W ratio should also be conducted to ensure the geometry and size independence, thus, the transferability of this single value fracture toughness to real welded structures.

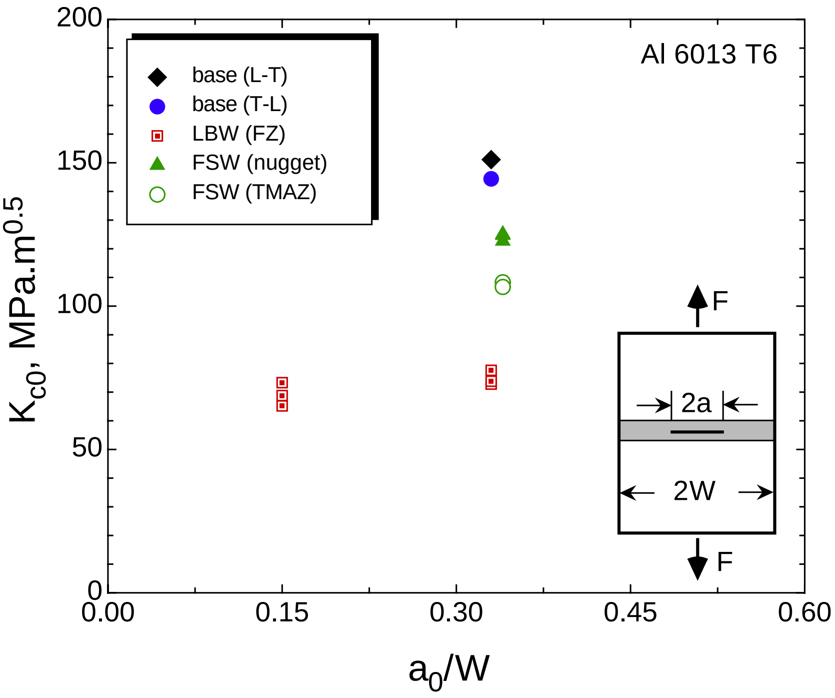

Figure 4.31: Fracture toughness K_{c0} of the base material and LBW and FSW joints obtained from M(T) panels. For exact values see **Tab. 4.6**.

In **Fig. 4.32** the effective crack extensions, Δa_{eff}, obtained from the compliance method and Irwin correction are plotted versus the physical crack extension, Δa. At low Δa values, the Irwin corrected effective crack extension is slightly larger than that from the compliance method. If the formula for the Irwin correction is recalled, this result may be expected. The Irwin correction becomes active as soon as the (theoretical) plastic zone at the crack tip starts to develop which is already the case in the linear elastic regime. This should make the Irwin R-curve start from the origin, whereas the compliance R-curve emanates from a non-zero value at $\Delta a_{\mathrm{eff}} = 0$, **Fig. 4.30**. The reason is also obvious since

Table 4.5: Critical stress intensity factor, K_c, of the base material according to the ASTM E561 standard. Results are averages of 3 panels.

Loading orientation	Half crack length, mm			F_{max} kN	Fracture toughness, MPa$\sqrt{m}$	
	a_0	$a_{eff,c}^{Irwin}$	$a_{eff,c}^{compl.}$		K_c^{Irwin}	$K_c^{compl.}$
base (L-T)	126.0	187.1	195.5	340	202.7	210.1
base (T-L)	126.0	185.0	195.6	325	191.9	201.7

Table 4.6: Fracture toughness in terms of K_{c0} of the base material and welded joints determined from M(T) panels with $a/W = 0.33$ (and also $a/W = 0.15$ for LBW panels).

specimen	$2a_0$ mm	$2W$ mm	a_0/W	B^* mm	F_{max} kN	σ_{max} MPa	$\sigma_{net,max}^{\dagger}$ MPa	K_{c0} MPa$\sqrt{m}$
base (L-T)	252.0	760	0.33	2.0	340	223.7	334.6	**151.1**
base (L-T)	252.0	760	0.33	2.0	325	213.8	319.9	**144.4**
LBW 01	252.0	760	0.33	2.6	213	107.8	161.3	72.8
LBW 02	252.0	760	0.33	2.6	216	109.3	163.5	73.8
LBW 03	252.0	760	0.33	2.6	227	114.9	171.9	77.8
LBW 04	114.0	760	0.15	2.6	300	151.8	178.9	65.2
LBW 05	114.0	760	0.15	3.2	390	160.4	188.7	68.8
LBW 06	114.0	760	0.15	6.0	779	170.8	201.0	73.3
							LBW average:	**71.9**
FSW 01 (nugget)	252.0	750	0.34	2.2	304	184.2	277.5	124.7
FSW 02 (nugget)	252.0	750	0.34	2.2	299	181.2	272.9	122.7
FSW 03 (nugget)	252.0	750	0.34	2.2	305	184.8	278.4	125.1
							FSW (nugget) average:	**124.2**
FSW 01 (TMAZ)	252.0	750	0.34	2.2	264	160.0	241.0	108.3
FSW 02 (TMAZ)	252.0	750	0.34	2.2	260	157.6	237.3	106.7
							FSW (TMAZ) average:	**107.5**

†) $\sigma_{net,max} = \sigma_{max}/(1 - a_0/W)$

the effective crack extension based on the compliance method is zero as long as the load-displacement record is linear elastic and attains non-zero values not until the compliance changes, i.e. deviation of the load-displacement curve from the linear elastic slope.

With further stable crack growth, the effective crack length derived from the compliance method becomes increasingly higher than that based on the Irwin correction. In both diagrams, the dotted vertical line indicates the physical crack extension at which the maximum load of the panel was attained in the test. The corresponding effective crack extension based on the compliance method is larger than that derived from the Irwin correction and, since the maximum load is identical, so is the resulting critical stress intensity factor, K_c, in Eq.(4.10).

Both methods provide a similar R-curve regarding the shape of the curve, which is consistent with results in Ref. [14]. However, for a given physical crack length, the effective crack length, a_{eff}, determined with the Irwin correction differs from that obtained by the compliance method [104]. The effective crack length with Irwin correction is larger at small crack extensions since the plasticity correction according to Irwin takes place as soon as the load is applied, whereas the correction for plasticity using the compliance method is zero during the elastic loading and takes place as soon as the load-displacement curve deviates from the elastic slope, which indicates a compliance change of the specimen. As the stable crack growth progresses under monotonic displacement controlled loading, the effective crack length with Irwin correction becomes less than that of the compliance method, which is usually the case at maximum load [104]. Hence, if the plane stress fracture toughness, K_c, is determined as the critical stress intensity factor at the maximum load, the method with Irwin correction will result in a lower value than with the compliance method.

Additionally, the K_J R-curve approach was applied to the base material only. In the case of welded panels, the nonlinear part of load-CMOD curves was small, particularly for the LBW panel, so that the area under this curve required for the calculation of the J-integral is vanishingly small. Moreover, the record of (small) stable crack extension in welded M(T) panels did not provide sufficient measurement points that can be used for the R-curve determination. **Fig. 4.33** shows the K_J R-curves for the base material in both orientations L-T and T-L where the stable crack extension, Δa, was determined optically from the specimen's surface. The K_J-values designated by "K_J (ext)" in the diagram were obtained from Eq. (3.29) that corrects for stable crack growth. K_J values designated by "K_J (no ext)" were obtained from Eq. (3.28) that does not take into account the stable crack extension during loading. The difference between these two approaches is very small. The limitation suggested in [64] states that the error in J estimations using Eq. (3.28) is negligibly small for crack extensions less than 10% of the uncracked ligament ($0.1(W - a_0)$). The present case even goes beyond this limit reaching 25% of the uncracked ligament (Δa=60 mm in the case of T-L).

Fig. 4.34 shows the CTOD δ_5 R-curves of the base material M(T) panels in both L-T and T-L orientations. Also R-curves obtained from the respective small scale C(T)50 specimens are plotted into the same diagram indicating no geometry dependence of the fracture resistance in terms of CTOD δ_5. The trends for L-T and T-L orientations are consistent with the previous approaches where the L-T orientation yields a higher fracture resistance than that of T-L.

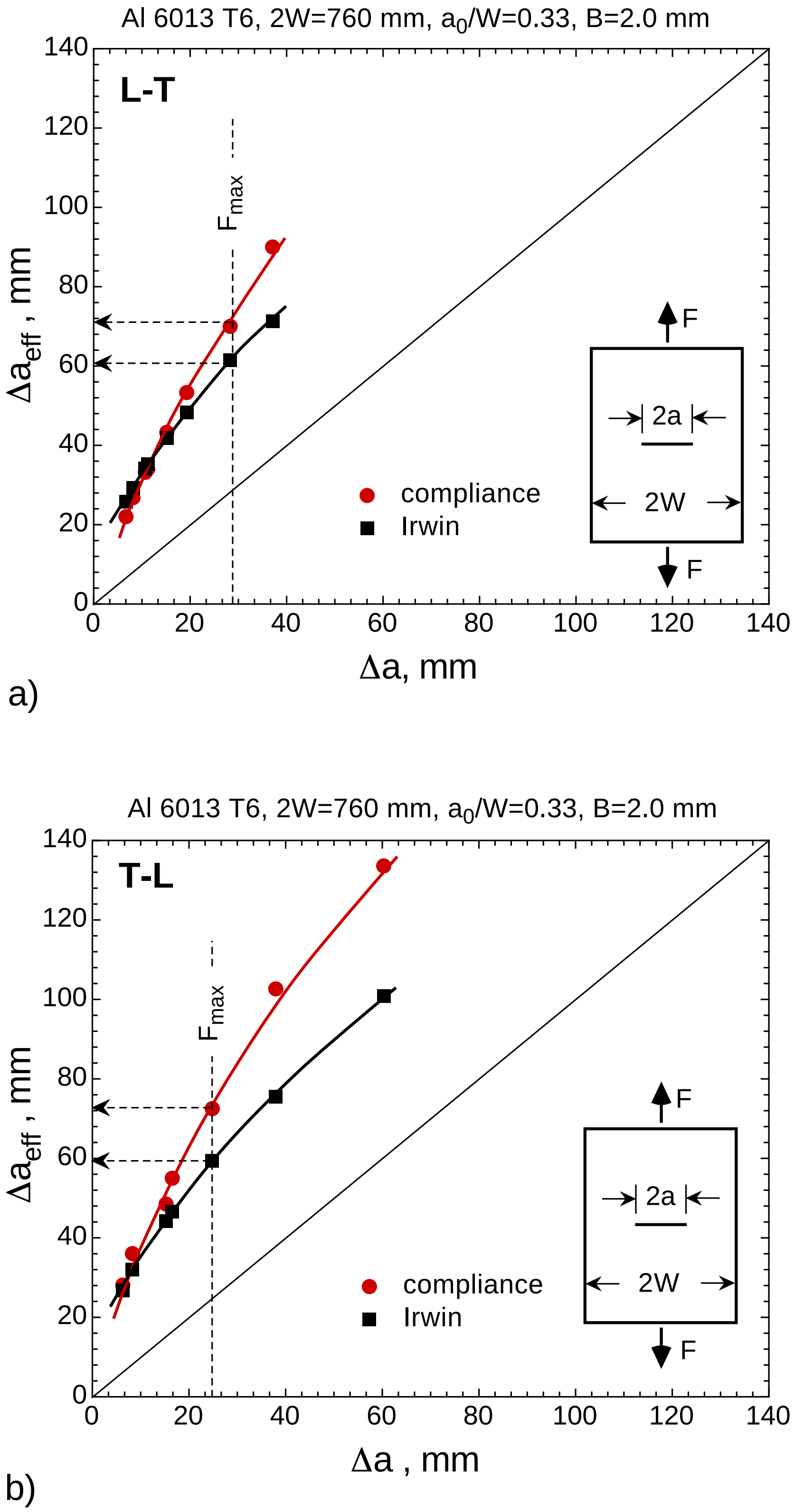

Figure 4.32: Comparison between effective crack extensions, Δa_{eff}, according to the compliance method and Irwin correction plotted versus physical crack extension, Δa, measured from the side surface. a) L-T and b) T-L orientations.

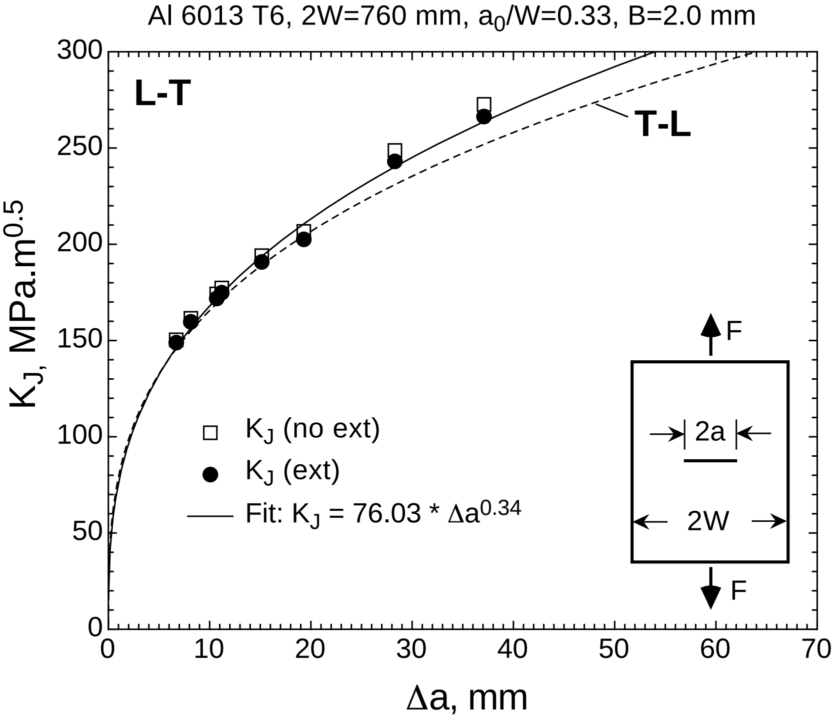

a)

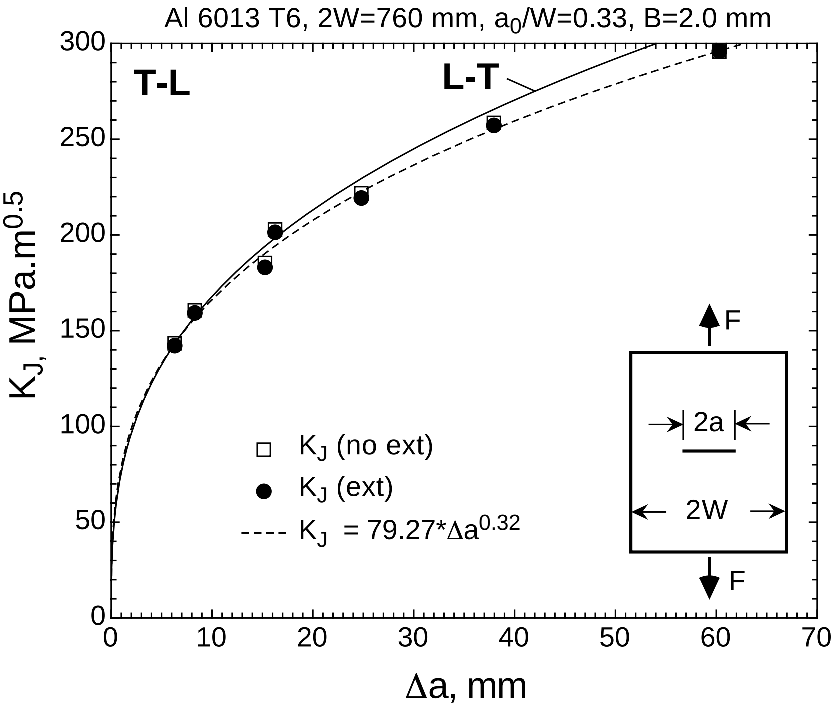

b)

Figure 4.33: K_J R-curves of the base material. a) L-T and b) T-L orientations.

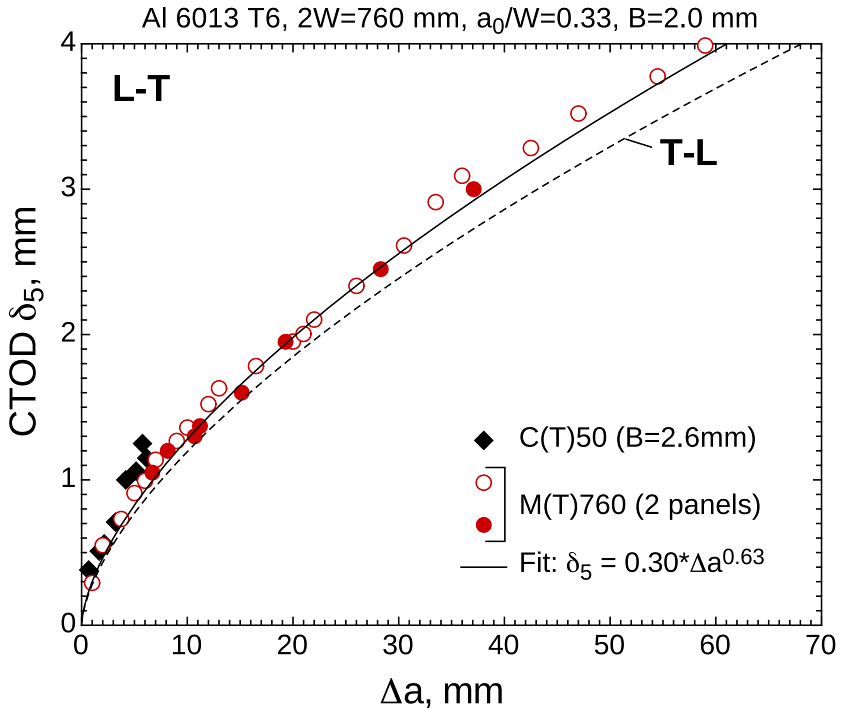

a)

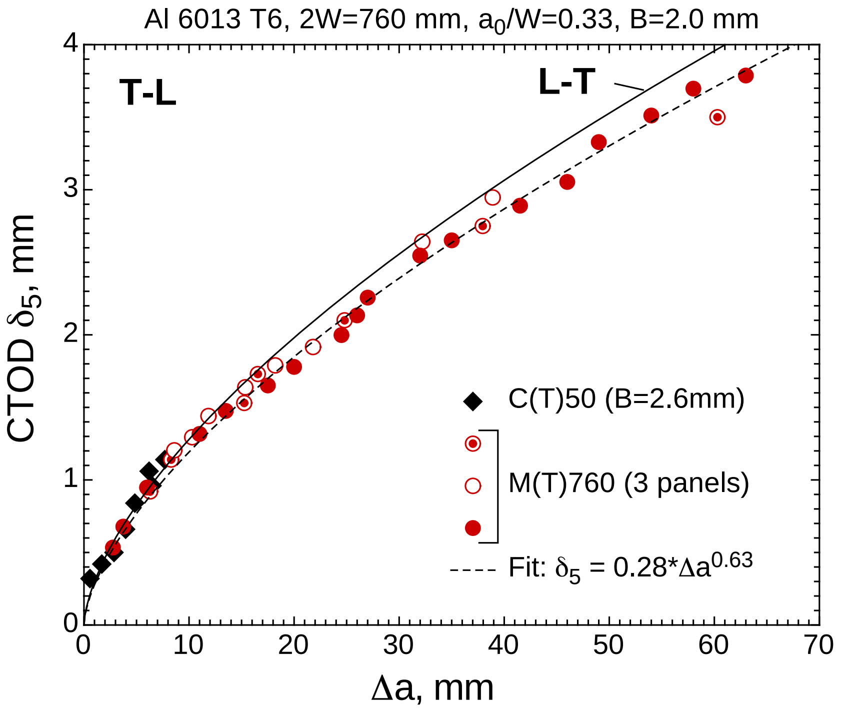

b)

Figure 4.34: CTOD δ_5 R-curves of the base material. a) L-T and b) T-L orientations.

LBW and FSW panels

Fig. 4.35 shows the K_{eff} R-curves for LBW and FSW panels derived from the compliance method as outlined in ASTM E561 [16]. All R-curves of welded panels were evaluated up to the point of unstable fracture. Due to the lower load-CMOD curves of welded panels with respect to the base material, the resulting K_{eff} R-curves should also be expected to be lower. The LBW panel has shown the lowest and the shortest (in terms of effective crack extension, Δa_{eff}) R-curve which is attributed to the low deformation capacity (eg. in terms of CMOD).

The derivation of the plastic zone corrected crack length in ASTM E561 [16] is based on the homogeneous material. The crack tip plastic zone development within a weld is certainly different from that in a homogeneous material. This issue with regard to the plastic zone corrected crack length and its effect on the K_{eff} R-curve in LBW and FSW panels has been investigated in detail in Section 4.4.

The stable crack extension in all welded panels, as described in a previous section, was much shorter compared to that in the base material panels. Additionally, the use of optical measurement technique was very difficult due to their unstable fracture behaviour. However, at least the critical crack extensions, being the stable crack extension at the onset of unstable fracture, were obtained visually in LBW and FSW (nugget) panels. The critical crack extension in the FSW panel with a crack in TMAZ was captured by a high speed CCD camera.

These critical events characterized either by a sudden crack growth jump or an immediate fracture of welded panels are shown in **Fig. 4.36**. In all cases the critical stable crack extensions with the corresponding CTOD δ_5 values lie on the R-curve and also within the Δa range obtained from the respective welded small scale C(T)50 specimens. This fact underpins the geometry independence of R-curves for highly undermatched welds as discussed in Section 2.3.

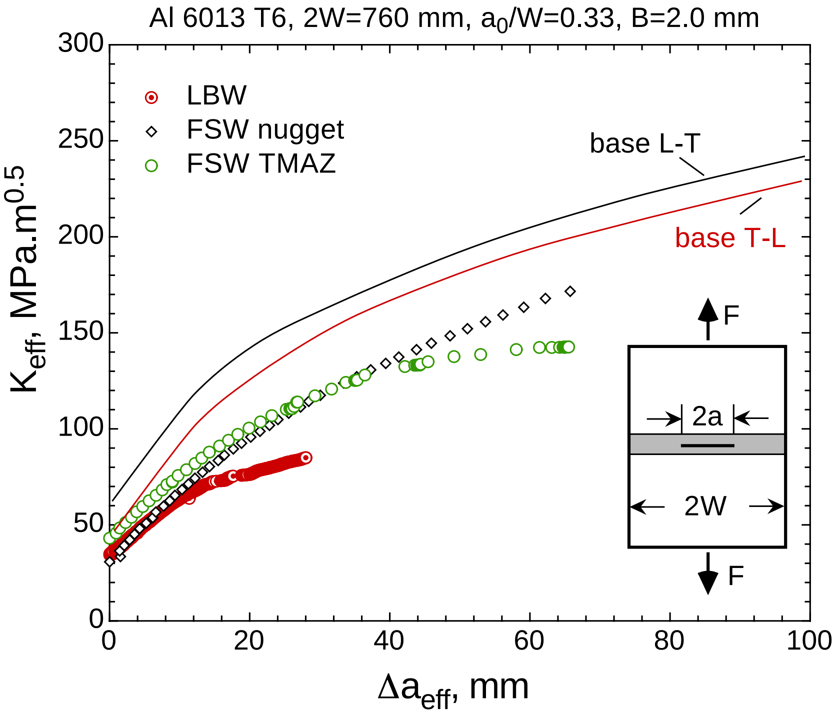

Figure 4.35: K_{eff} R-curves of the welded panels obtained according to the compliance method of the ASTM E561 standard [16].

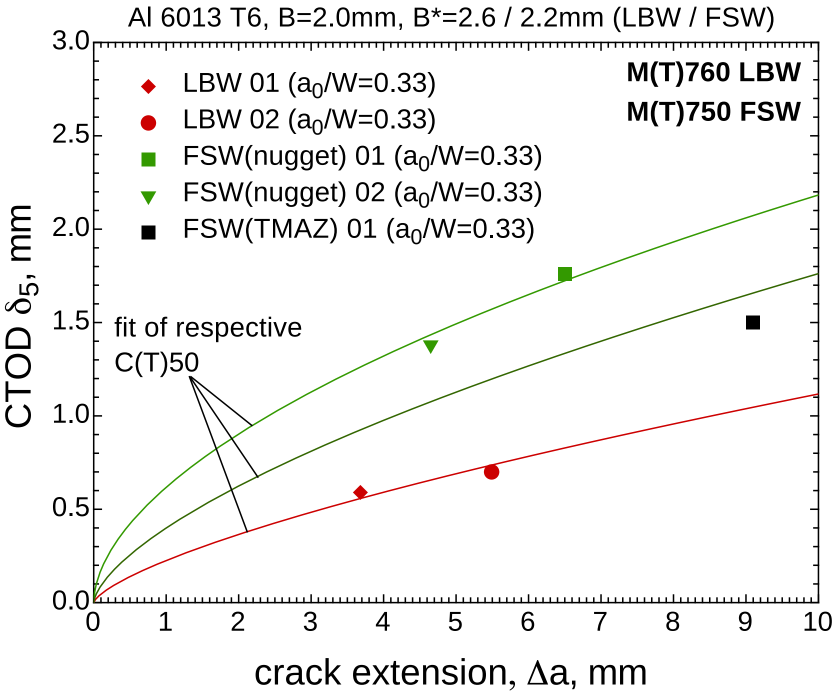

Figure 4.36: Critical events of LBW and FSW welded M(T) specimens in terms of CTOD δ_5 values and the corresponding stable crack extension, Δa, which are the averages of the left and right crack tips. Δa was measured optically on the specimen's side surface. A critical event is either a sudden large crack growth jump followed by a load drop and a subsequent unstable fracture or an immediate final unstable fracture.

4.3.5 Results and discussion of residual strength tests on stiffened panels

This section addresses the experimental results of stiffened panels. 2-stringer panels were intended to simulate a one-bay crack and 3-stringer panels represented a two-bay crack scenario over a broken central stringer. The aim of the experiments was to understand the deformation and fracture behaviour of these panels and to use the results for the validation of the residual strength predictions made with the SINTAP procedure in the next section.

In these tests, the load was introduced through the skin; thus the stringers were not loaded externally. Since the stringer ends in 2- and 3-stringer panels were within the testing length, they provide locations of high stress and strain concentration caused by the geometry discontinuity, i.e. sharp transition from skin to stringer tip, and enhanced by the material mismatch due to LBW. Additionally, LBW seam starts (run-in) and stops (run-outs) at these locations. It is well known that aluminium alloys are sensitive to hot-cracking when fusion welded, particularly in run-ins and run-outs so that these spots may already contain LBW process induced cracks. Currently, an European Community funded project WEL-AIR [105] partly addresses this problem.

A bending moment due to asymmetry of the stringers with respect to the loading plane leads to a loading condition where the stringer ends tend to be pulled off the skin. In all 2- and 3-stiffened panels tested, the stringer separation started at run-outs which were of a quality worse than that of the run-ins, **Fig. 4.37**. However, in some panels small cracks also initiated at run-ins. With further increase of applied displacement, the stringer separation progressed, **Fig. 4.38**. These tests are truly representing the worst case situation in such welded stiffened structures. In the welded stiffened fuselage section, riveted patches are currently being applied to the stringer ends to avoid stringer separation at LBW run-in and run-out locations.

Figs. 4.39 and **4.40** show the applied load versus CMOD and versus CTOD δ_5 plots, respectively, for a 2-stringer panel. The arrows indicate the point where the stringer separation started. In both panels this point was close to the maximum load indicating that in this test the true residual strength has been reached.

The crack driving force in terms of CTOD δ_5 is plotted versus the gauge length strain in **Fig. 4.41** for 2-stringer panels. The stiffening effect of the stringer is clearly demonstrated by comparing the stiffened panels with the plain base material panel. For a given applied strain (GLS), for example 0.3%, the crack tip loading (CTOD δ_5) in the plain base material panel is much higher than in the stiffened panel. The closer the skin crack tip to the stringer, the more load is transferred from the skin to the stringer. Thus, the skin stresses in this region are reduced and consequently the crack tip loading. It should be noted that this comparison is only physically meaningful if the crack-to-width ratio, a/W, of the compared components is identical.

The load-displacement curves measured on the 3-stringer specimens are shown in **Figs. 4.42** and **4.43**. Again, the arrows indicate the onset of stringer separation at LBW run-outs. Unlike in 2-stringer panels, the stringer separation started before the maximum load was attained. The true residual strength of a 3-stringer panel with a two-bay crack over a broken central stringer can, therefore, be assumed higher.

The comparison with a plain base material panel cannot be made since there are no experimental results with a crack-to-width ratio of $a_0/W = 0.5$ in a plain base material panel. However, the stiffening effect of the stringer is expected to be identical to that shown for the 2-stringer panels. Due to larger a_0/W, CTOD δ_5 must be higher than in panels with a lower a_0/W [102] for a given applied strain, **Fig. 4.44**.

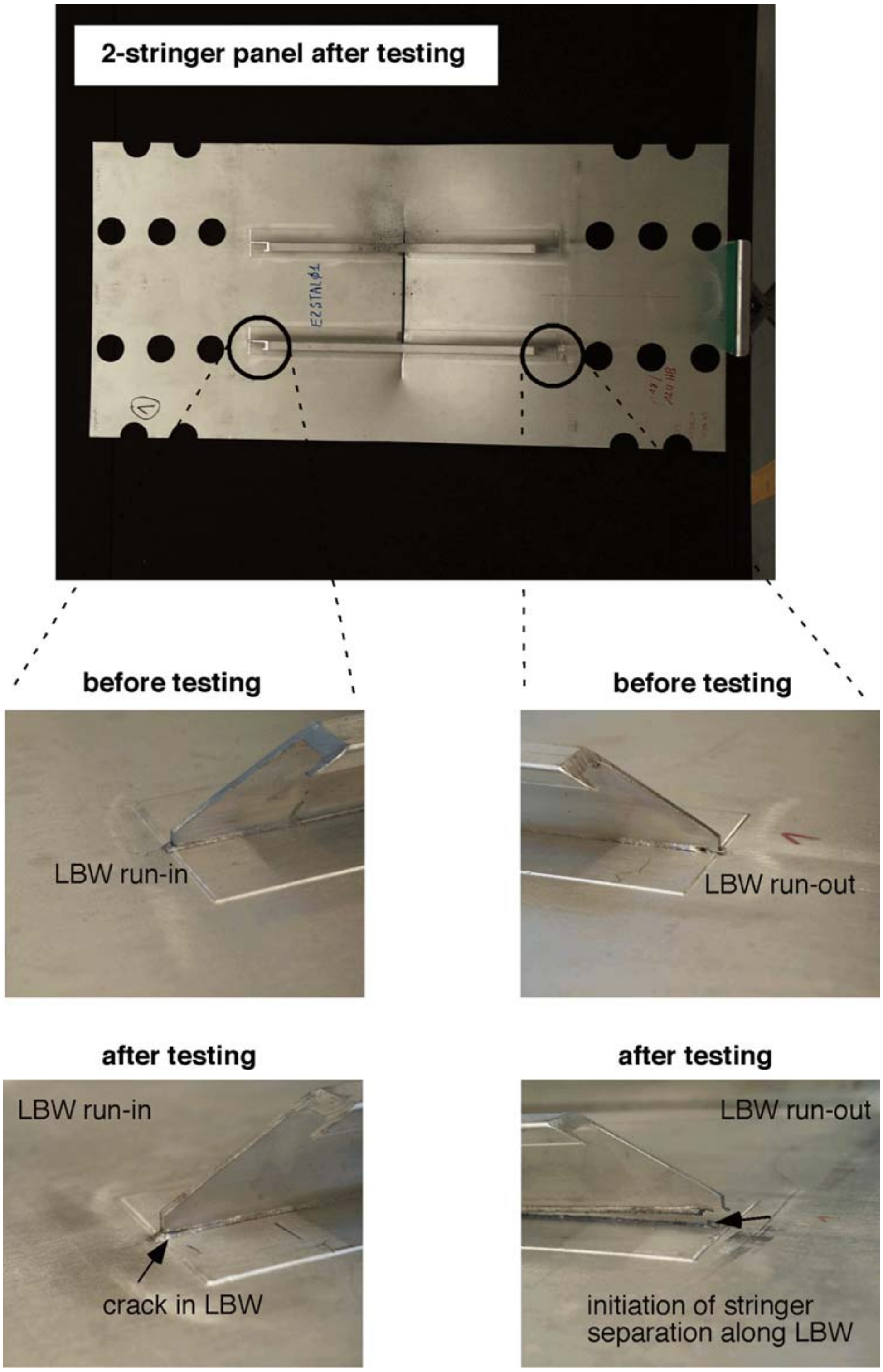

Figure 4.37: LBW run-in and run-out at stringer ends before and after residual strength test. In all tests, the stringer separation started at LBW run-outs, whereas LBW run-ins either remained intact or experienced small initiation cracks. Same behaviour was observed for 3-stringer panels.

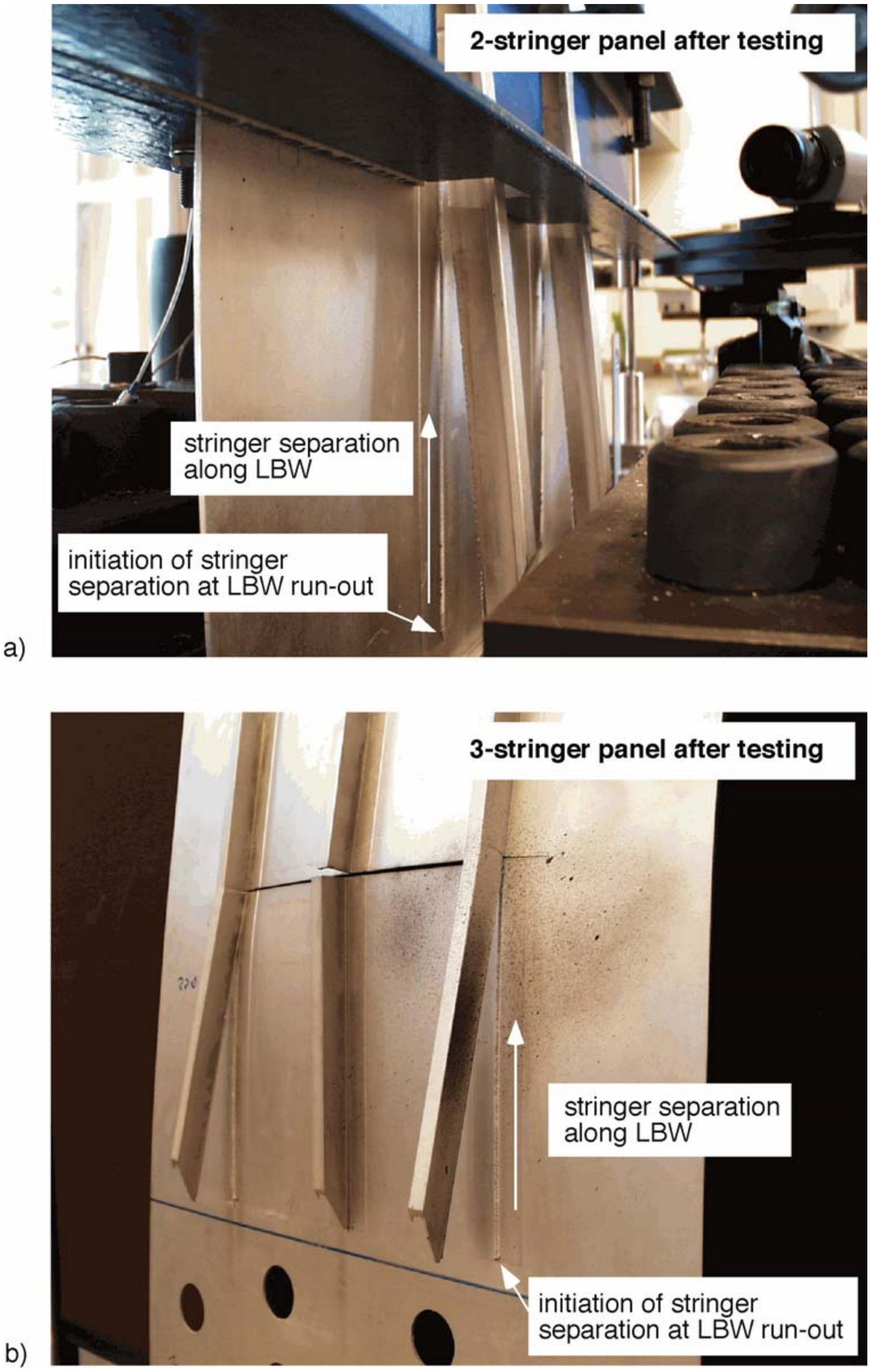

Figure 4.38: Initiation at LBW run-outs and subsequent stringer separation along LBW in a) 2-stringer and b) 3-stringer panels.

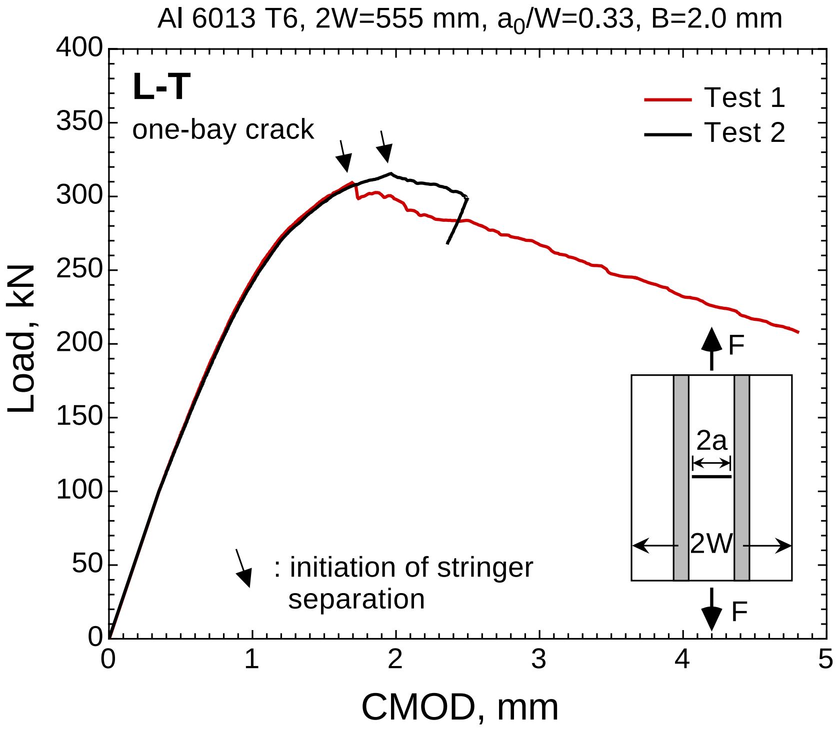

Figure 4.39: Applied load vs. CMOD plot measured on 2-stringer panels.

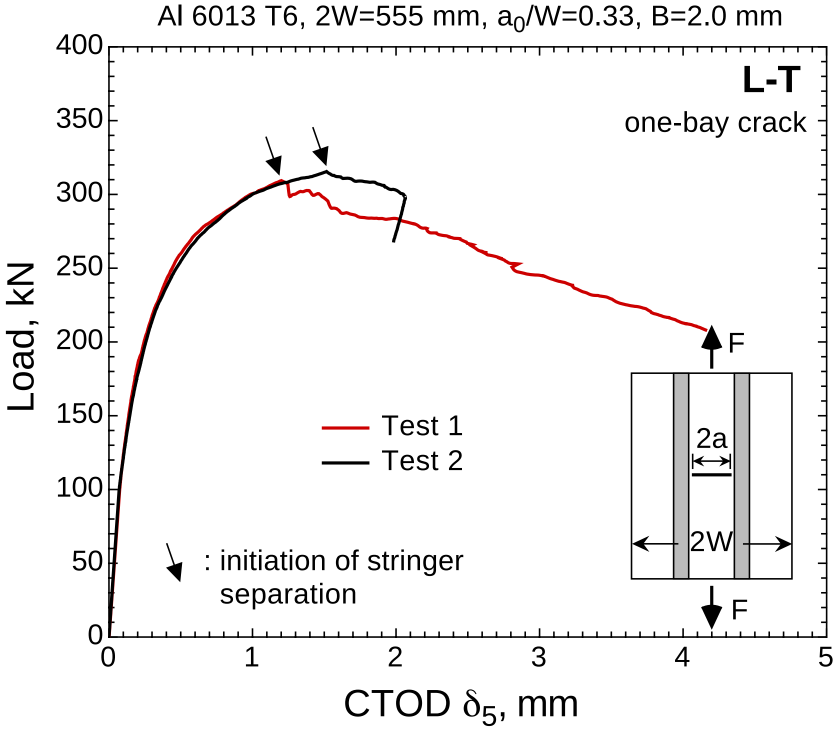

Figure 4.40: Applied load vs. CTOD δ_5 plot measured on 2-stringer panels.

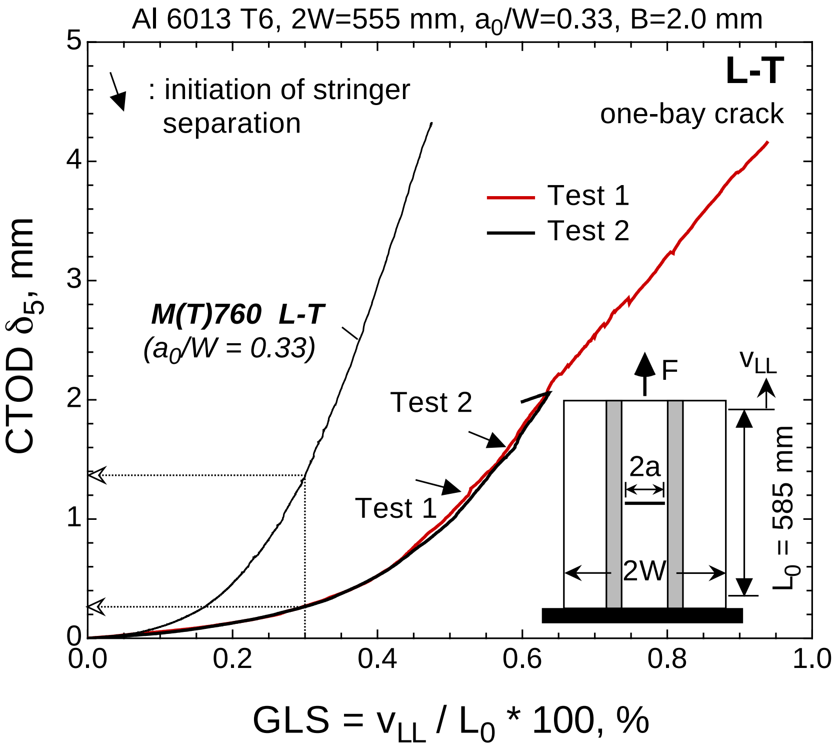

Figure 4.41: Crack tip loading CTOD δ_5 vs. applied gauge length strain (GLS) plot measured on 2-stringer panels.

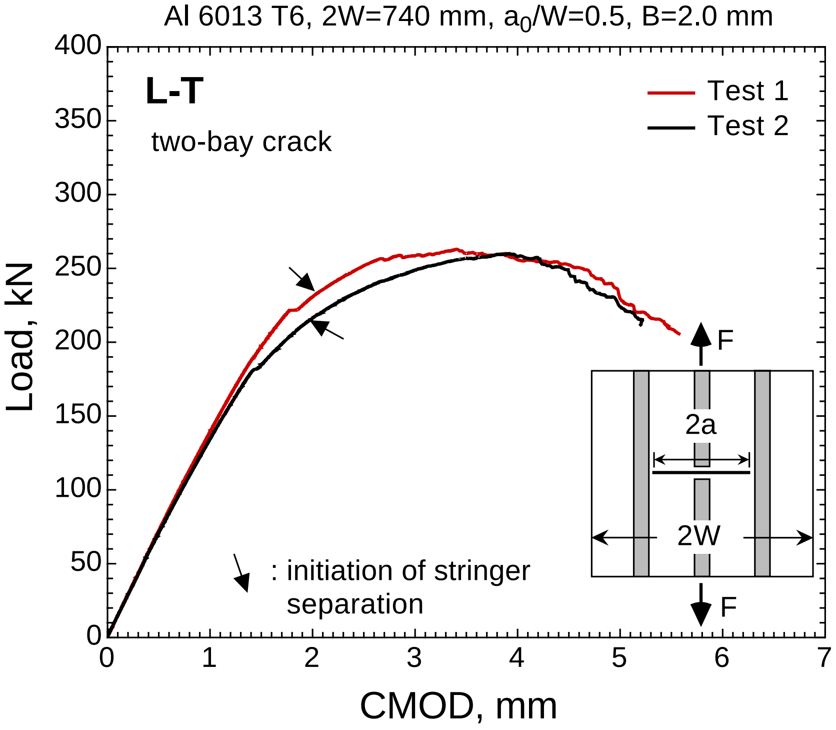

Figure 4.42: Applied load vs. CMOD plot measured on 3-stringer panels.

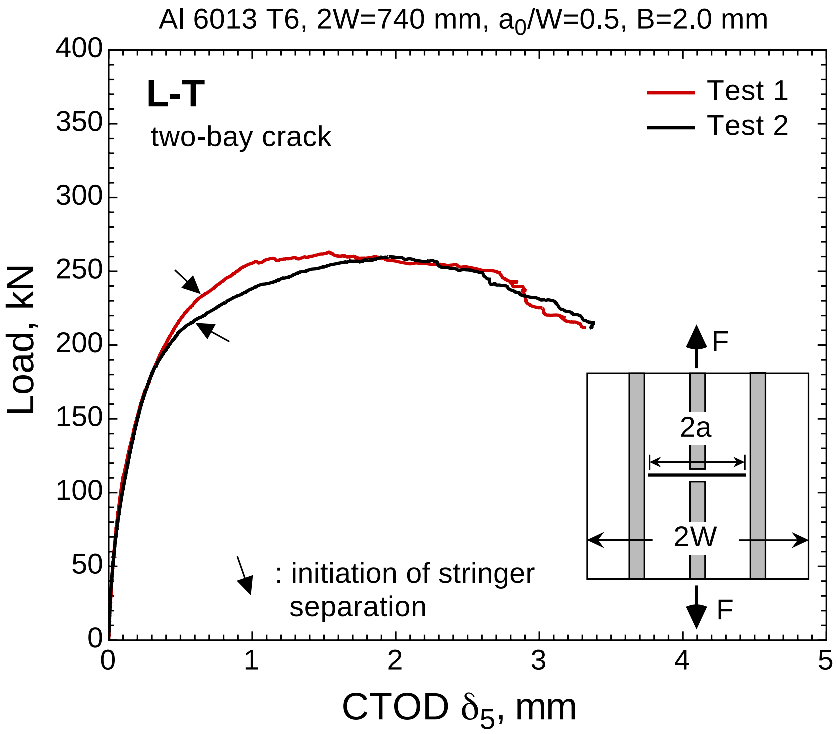

Figure 4.43: Applied load vs. CTOD δ_5 plot measured on 3-stringer panels.

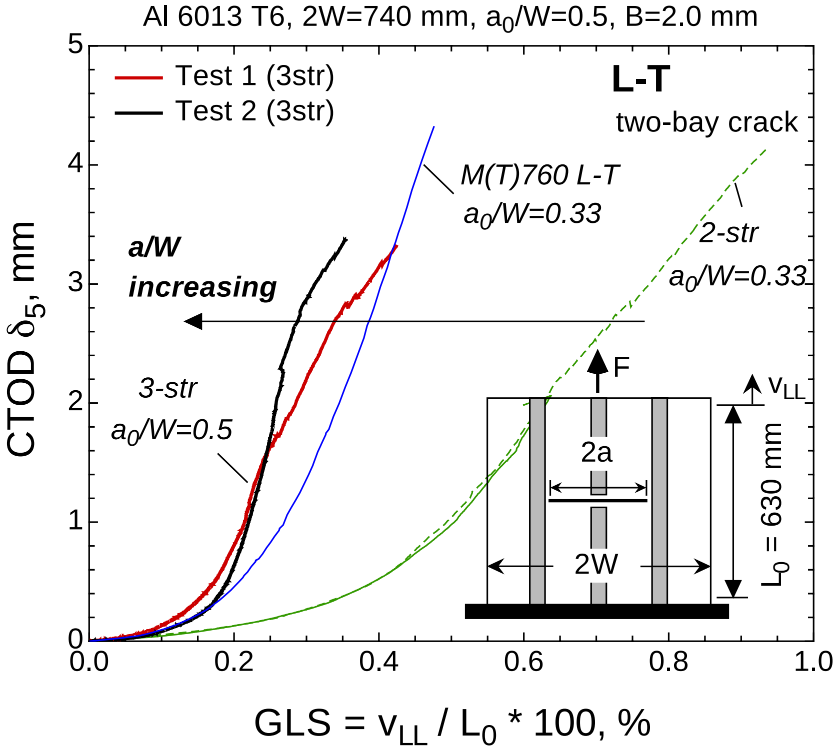

Figure 4.44: Crack tip loading CTOD δ_5 vs. applied gauge length strain (GLS) plot measured on 3-stringer panels. The diagram also shows the respective curves for 2-stringer and unstiffened base material panels.

4.3.6 Concluding remarks

The residual strength tests on un-stiffened panels have shown a much smaller stable crack extension in the welded panels than in the base material panels. Despite the displacement controlled loading, the LBW and FSW panels unstably failed at the maximum load level, whereas the base material panels could be loaded beyond their maximum loads.

The maximum load carrying capacity of welded panels is inferior than that of the base material panels, with LBW panels having the lowest maximum load. In the case of the FSW panels, the crack location in the lowest hardness region (TMAZ) represents the worst case scenario.

The K_{eff} R-curves of the base material are higher than those of the welded panels. The effective crack length, a_{eff}, has been determined according to the compliance method as outlined in the ASTM E561 standard [16].

The R-curves in terms of CTOD δ_5 for the base material have shown a geometry independence, since respective C(T) and M(T) specimens form a common R-curve. In the case of welded panels, the geometry independence could also be observed, since the critical CTOD δ_5 values at the onset of unstable fracture lie on the R-curves obtained from the respective C(T) specimens. The critical stable crack extension in welded panels was within the range covered in tests of respective C(T) specimens.

The stiffened panels have shown stable crack extension with crack branching into the stringer. The amount of the stable crack extension in the stringer was the same as that in the skin of both 2- and 3-stringer panels after crack branching. The remote crack initiation at the ends (so-called run-ins and run-outs) of the stringers took place at maximum load of the 2-stringer panels. However, in the 3-stringer panels, this remote crack initiation started before the maximum load was reached. Hence, the real load carrying capacity of the 3-stringer panel with a two-bay crack is expected to be higher.

4.4 Determination of plastic zone using ARAMIS system

A detailed knowledge on the evolution of the plastic deformation at the crack tip in mismatched structures is essential to develop a methodology to assess its structural significance. For this purpose, a detailed experimental investigation was conducted by using the commercially available technique ARAMIS [106]. This section presents the results of this experimental analysis with regard to the plastic zone corrected crack length and its effect on the K_{eff} R-curves in LBW and FSW panels. A comparison is made between K_{eff} R-curves where the effective crack length has been derived from three different methods: the compliance method, Irwin's plastic zone correction, and experimentally determined plastic zone size measured by the ARAMIS technique.

4.4.1 Basic principles of the ARAMIS method

ARAMIS is a correlation based image evaluation technique to capture the deformation distribution of a sample under load. The system enables the calculation of the surface displacement and surface strain at each deformation step. The sample is viewed by a CCD camera which records the surface deformation in the form of digital images. The first image is taken as the reference and is subdivided into squares (facets) each of them containing $n \times n$ pixels. Initial coordinates are assigned to the center of each facet. In subsequent images, the corresponding deformed facets are located and new coordinates assigned to their centers.

From the coordinates that are known at each deformation or load step, the displacement field $\vec{u} = (u, v)$ is calculated:

$$u = u(x, y), \quad v = v(x, y) \tag{4.13}$$

where $u(x, y)$ and $v(x, y)$ are the displacement components parallel to the x- and y-axes, respectively, in a cartesian coordinate system.

The strain field is then obtained through the first partial derivatives with respect to the corresponding coordinates. The analytical expressions are [107]:

$$\varepsilon_x = \frac{\partial u(x, y)}{\partial x}, \quad \varepsilon_y = \frac{\partial v(x, y)}{\partial y}, \quad \gamma_{xy} = \frac{\partial u(x, y)}{\partial y} + \frac{\partial v(x, y)}{\partial x} \tag{4.14}$$

where ε_x and ε_y are the strain components in x- and y-directions, respectively, and γ_{xy} is the shear strain.

Since the measured displacement field is discretized by facets, the strain field can also be evaluated only at discrete points. The strain values are determined at facet centers using a 3×3 environment. **Fig. 4.45** schematically shows the principle of the strain calculation. To obtain the strain in the middle facet, all eight surrounding facets are included in the differentiation of Eq. (4.14).

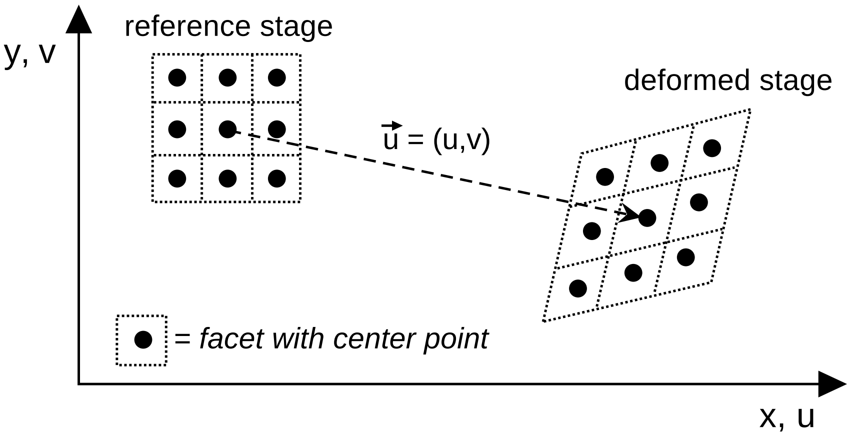

Figure 4.45: 3 × 3 environment for the strain calculation. The dots indicate the center of a facet. The strain is determined at the center of the middle facet by including the eight adjacent facets.

At each deformation step the deformed facets are compared with the reference stage which is taken at zero load level. Therefore, the calculated strain values are total strain values that a material point has experienced compared to its initial stage. Local unloading due to the stable crack advance leads to a stress and strain redistribution ahead of the crack tip. This effect is also captured by the strain calculation process.

The strain values are reported in terms of engineering strain. The unit elongation of a one-dimensional infinitesimally small element is defined as:

$$\lambda = \lim_{l \to 0} \frac{l + \Delta l}{l} \tag{4.15}$$

where l is the length and Δl is the elongation of this element. The engineering strain, ε, is then defined as:

$$\varepsilon = \lambda - 1. \tag{4.16}$$

4.4.2 Specimen preparation and experimental setup

The experimental setups for the application of the ARAMIS system to flat tensile specimens and M(T) panels were identical. A random pattern was sprayed onto the specimen's surface to create a sharp local gradient of black and white transitions. The specimen's surface was first sprayed with white paint to cover the shiny original surface to avoid any light reflection. Black paint was then sprayed onto the white surface so that fine spots were uniformly distributed over the entire range of the desired measurement area. A typical example of this pattern is given in **Fig. 4.46**.

A high speed CCD camera with a resolution of 1280 × 1024 pixels (12-bit digital) was mounted at a distance of ∼ 250 mm and perpendicular to the specimen's surface. The load channel of the testing machine was additionally recorded by the computer of the ARAMIS system in order to correlate the digital images with the corresponding load.

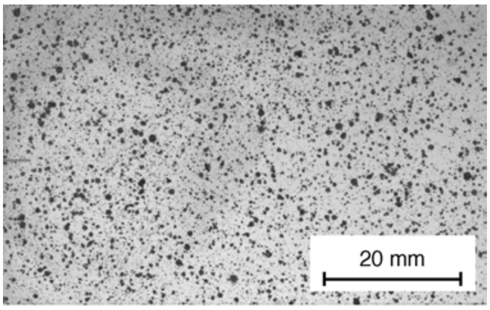

Figure 4.46: Example of a typical random black and white pattern which is sprayed onto the specimen's surface to measure the local deformation fields by the ARAMIS technique.

Besides the measurements required for the ARAMIS system, all other quantities as measured in the previous tests were also recorded by a separate data acquisition system. For the flat tensile specimens, load as well as the elongation was measured with a clip gauge. For the M(T) panels, load, CMOD, CTOD δ_5 (one clip at each crack tip on the front side of the panel), and the total elongation, v_{LL}, were recorded.

4.4.3 Results and discussion of LBW and FSW flat tensile specimens

LBW and FSW welded flat tensile specimens with dimensions according to the DIN EN 895 standard (specimen width = 25 mm) were tested perpendicularly to the weld. The surface deformation was measured using the ARAMIS system enabling a qualitative as well as a quantitative characterization of the strain field in and around the weld. **Figs. 4.47** and **4.48** qualitatively show the distribution of the longitudinal strain component, ε_y, of the LBW and FSW tensile specimens, respectively. In both welds, the plastic strain clearly localizes within the weld material due to the undermatching, whereas the base material has much lower strain values. The base material even remains elastic throughout the entire test since the maximum stress of 290 MPa and 285 MPa attained in both the LBW and FSW specimens is lower than the base material yield strength of 360 MPa (LT direction).

The quantitative characterization of the strain fields is depicted in **Fig. 4.49** and **4.50**. The strain profiles across the weld show the strain distribution at the onset of final fracture and are superimposed on the micro-hardness profile of the respective weld. The strain values in the base material are close to zero, whereas the longitudinal strain component, ε_y, increases in the HAZ at the same location where the hardness decreases. This is true for the LBW as well as the FSW joint.

The longitudinal strain in the LBW joint reaches its maximum of 12% in the fusion zone which is much higher than the measured fracture strain in LBW flat tensile specimens (see **Fig. 4.8** b). This low (2%) strain value is also much higher than the strain value obtained from LBW micro-flat tensile specimens. The latter one is primarily attributed to the grain structure of the LBW material and the loading direction of the micro-flat tensile specimens (see Section 4.2).

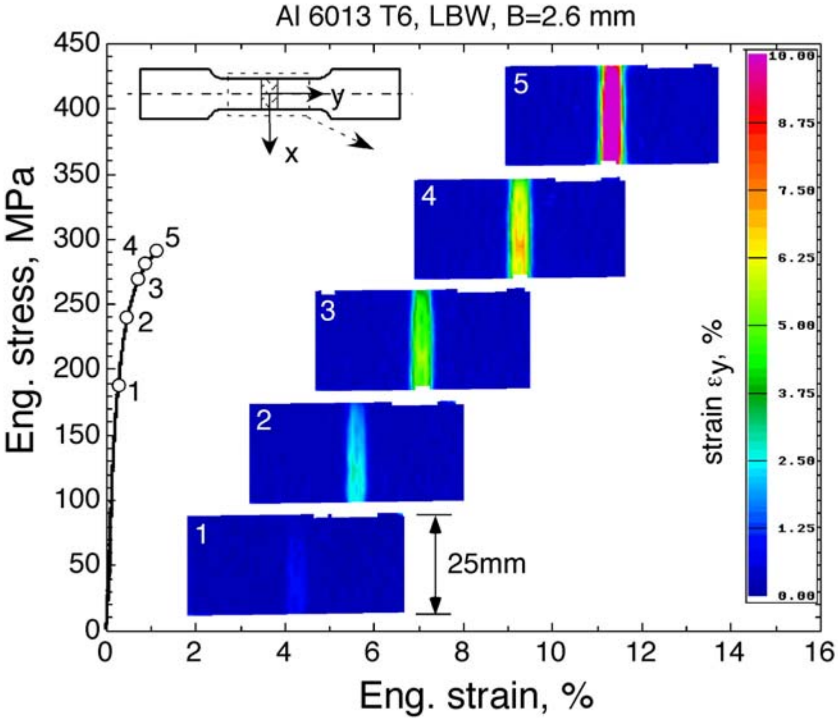

Figure 4.47: Plasticity evolution in the LBW joint measured on a flat tensile specimen.

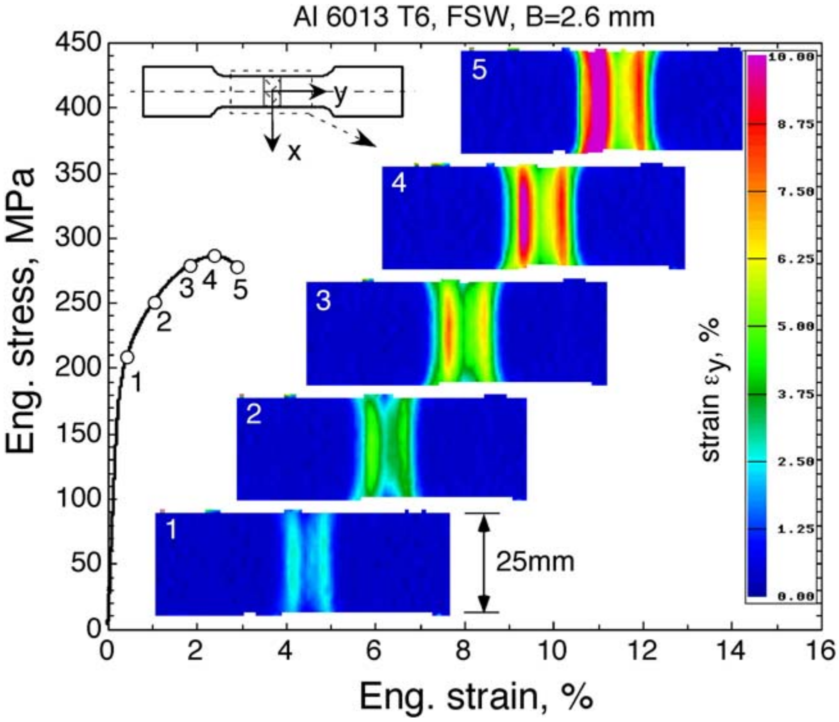

Figure 4.48: Plasticity evolution in the FSW joint measured on a flat tensile specimen.

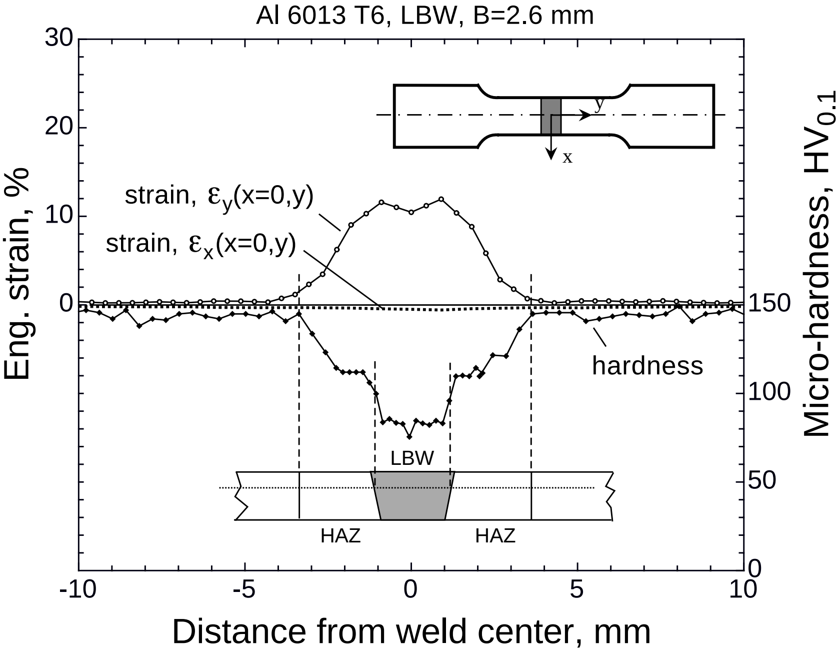

Figure 4.49: Local strain profile in a LBW joint at the onset of final fracture of a flat tensile specimen (stage 5 in **Fig. 4.47**). Strain localization occurs within the low-hardness region. The weld material attains peak values around 11%.

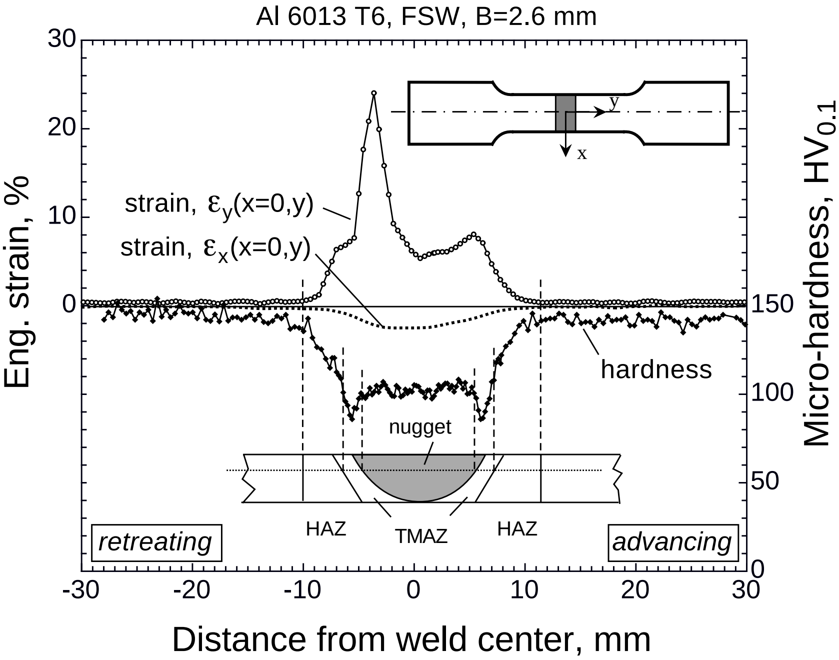

Figure 4.50: Local strain profile in a FSW joint at the onset of final fracture of a flat tensile specimen (stage 5 in **Fig. 4.48**). Strain localization occurs within the low-hardness region. The strain distribution peaks at locations of local hardness minima, i.e. in TMAZ.

The orientation of the secondary cracks (see **Fig. 4.7**) in the LBW joint gives rise to the assumption that stresses perpendicular to the loading axis (in welding direction) must be present. The evidence is given in **Fig. 4.49** showing a vanishingly small strain, ε_x, perpendicular to the loading axis of the standard tensile specimen. The LBW weld material is prevented from deformation in this direction by the stronger base material which leads to the presence of stresses induced by the strong weld strength undermatching.

The local strain profile across the FSW joint at the onset of final fracture of a standard flat tensile specimen is depicted in **Fig. 4.50**. As in the LBW joint, the strain localizes within the weld and clearly peaks in TMAZ, being the locations of local hardness minima. The maximum strain value attains 25% which is similar to that in micro-flat tensile specimens reaching 28% strain at final fracture. Also the tensile strength values obtained from the standard ($R_\mathbf{m} = 285$ MPa) and micro-flat ($R_\mathrm{m} \approx 290$ MPa in nugget and TMAZ) tensile specimens are similar.

The weld width of the FSW joint is larger than that of the LBW joint, so that the FSW weld material is less constrained by the stronger base material in the weld width direction and, therefore, is able to deform in the longitudinal weld direction. **Figs. 4.49** and **4.50** also depict the strain component, ε_x, perpendicular to the loading direction. The LBW joint shows almost no contraction of the weld material, whereas the FSW joint does experience a negative strain, ε_x. Where the weld material is prevented from contraction, there must be assumed tensile stresses in the weld acting parallel to the weld, particularly in the LBW joint.

The constraint in the thickness direction is assumed to be larger in the LBW joint due to the smaller weld width-to-thickness ratio compared to the much higher ratio in the FSW joint. However, relevant evidence cannot be provided by the ARAMIS system since only the surface strain but no deformation in the thickness direction is measured.

If no micro-flat tensile specimens are available, the yield strength of the weld material can be determined from standard flat tensile specimens. This yield strength value will then be an average value for the entire weld metal zone. Since the material analyzed in this investigation shows continuous yielding, i.e. without a Lüders plateau, the yield strength is determined in terms of $R_{\mathrm{p}0.2}$. However, the plastic strain distribution in the standard specimen is not uniform over the gauge length, so that the determination of $R_{\mathrm{p}0.2}$ will be dependent on the gauge length at which the elongation is measured.

With the knowledge of displacement fields measured by the ARAMIS system in both LBW and FSW transverse tensile specimens, stress-strain curves with different gauge lengths, L_0, can be derived from a single test. The strain, ε, is obtained from:

$$\varepsilon = \frac{v_2 - v_1}{L_0} \tag{4.17}$$

where v_1 and v_2 are displacements of the points in loading direction located at a distance L_0. **Figs. 4.51** and **4.52** show the effect of different gauge lengths, L_0, on the stress-strain curves and the resulting yield strength values.

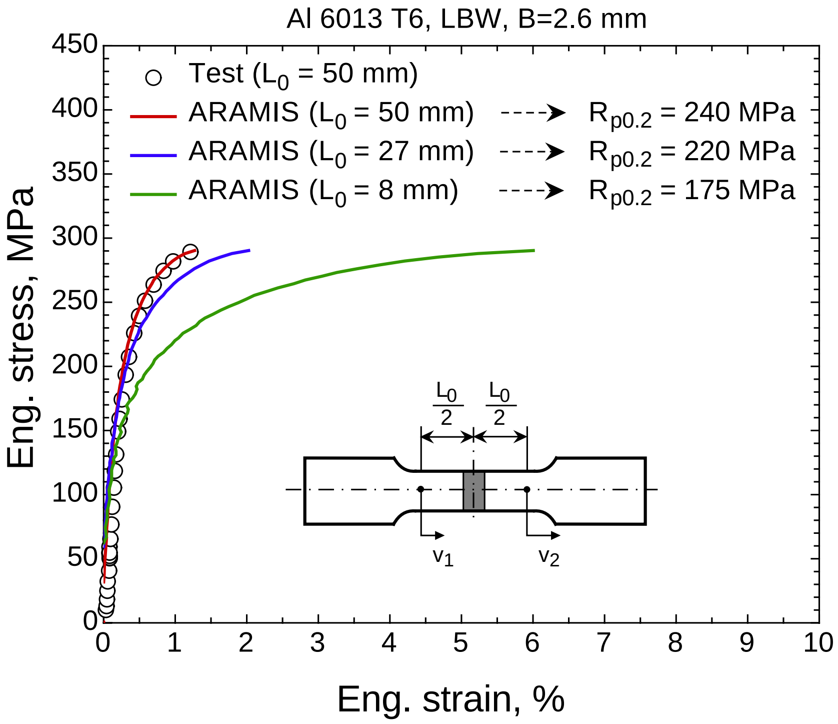

Figure 4.51: Effect of different gauge lengths, L_0, on the engineering stress-strain curve obtained from a transverse flat tensile LBW specimen.

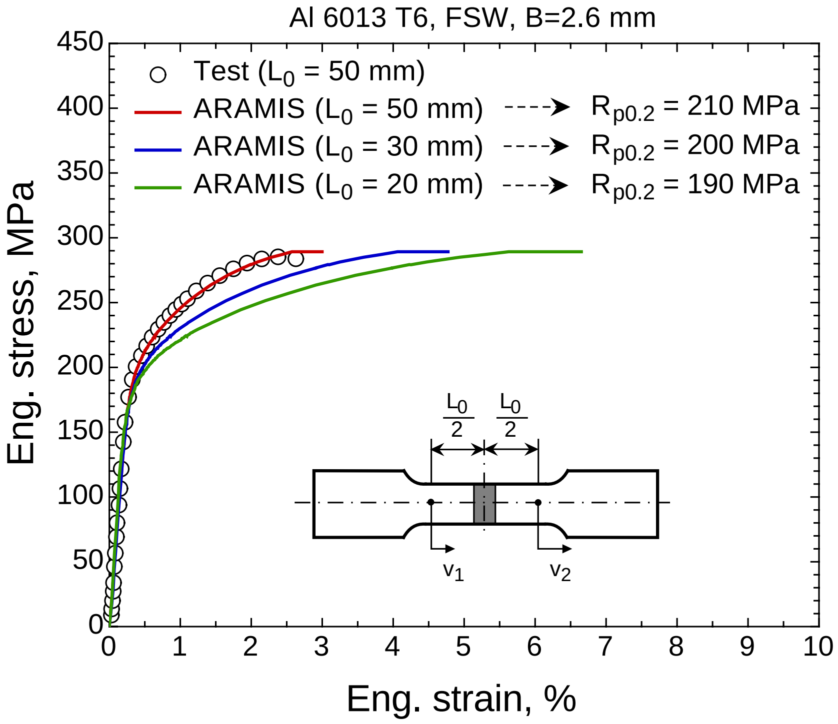

Figure 4.52: Effect of different gauge lengths, L_0, on the engineering stress-strain curve obtained from a transverse flat tensile FSW specimen.

Table 4.7: Yield strength values, $R_{p0.2}$, obtained from standard flat tensile specimens (DIN EN 895) of LBW and FSW joints at different gauge lengths, L_0. For comparison, the yield strength values of weld material obtained from micro-flat tensile specimens are also shown.

	standard			**micro-flat**
LBW	L_0=50 mm	L_0=27 mm	L_0=8 mm	–
	$R_{p0.2}$ [MPa]			
	240	220	175	145
FSW	L_0=50 mm	L_0=30 mm	L_0=20 mm	–
	$R_{p0.2}$ [MPa]			
	210	200	190	185
Base (T-L)	360			

The open circles indicate the curve where the elongation of the specimen was measured with an attached clip at a gauge length of 50 mm. All other curves drawn with solid lines were inferred from the displacement field measured by the ARAMIS system. Three different gauge lengths were selected for each specimen in which the gauge length of $L_0 = 50$ mm was used as a validation of the ARAMIS measurement. For both LBW and FSW specimens the elongations are in very good agreement with those measured with a clip gauge.

Depending on the weld, the shortest gauge length was chosen to be as close as possible to the range where the strain localization occurred. In the case of the LBW joint, the shortest gauge length was 8 mm, in the case of the FSW joint, it was 20 mm. **Tab. 4.7** summarizes the $R_{p0.2}$ values of both LBW and FSW joints. The values for the weld material obtained from the micro-flat tensile specimens are also given in the table for comparison. The shorter the gauge length, the closer the yield strength value to that obtained from the micro-flat tensile specimen. However, due to the constraint effect, the yield stress in the standard welded tensile specimen should be expected to be higher than in the micro-flat tensile specimen which is wholly made of the weld material and can freely deform in all directions.

4.4.4 Results and discussion of LBW and FSW M(T) panels

In this section results of the ARAMIS measurement on LBW and FSW M(T) panels are presented and discussed.

The measurement area captured by the CCD camera was about 70 mm wide so that the welds of maximum this length could be monitored ahead of the crack tip. The plastic zone evolution in LBW M(T)760, FSW nugget M(T)750 and FSW TMAZ M(T)750 panels is qualitatively shown in **Figs. 4.53 - 4.55**, respectively. In all three cases the plastic deformation is entirely confined to the weaker weld material and does not penetrate into the base material.

The determination of the plastic zone size reduces to the determination of its length since the width of the plastic zone is bounded by the base material. To avoid any confusion in the terminology, the following terms will be defined. The plastic zone length is the full physical length of the plastic zone measured in the direction of crack growth, whereas the plastic zone correction, r_p, is used to correct the physical crack length for the plastic deformation at the crack tip and will be defined later.

The plastic zone correction, r_p, was determined by three different methods:

- experimentally by the ARAMIS system,
- Irwin correction,
- from compliance method according to ASTM E561 standard [16].

Definition of plastic zone correction measured by ARAMIS system

The proper definition of the plastic zone is based on a yield criterion (eg. von Mises or Tresca yield criterion [108]) where a material point is considered deformed plastically if the equivalent stress has exceeded the uniaxial yield stress of this material.

However, experimentally only strains are available and for the determination of the plastic zone in front of the crack tip, the following approach has been adopted. Based on the idea of the analytical Irwin plastic zone determination (eg. [5, 6]) where only the stress component normal to the crack plane is incorporated in the calculation, here the normal strain component, ε_y, was used (see **Fig. 4.56**). The material can be assumed to yield if the following condition is met:

$$\varepsilon_y = \varepsilon_{0.2} \tag{4.18}$$

where

$$\varepsilon_{0.2} = \frac{R_{\mathrm{p}0.2}}{E} + 0.002 \tag{4.19}$$

is the total strain value corresponding to the yield stress, $R_{\mathrm{p}0.2}$, of the material. $E = 69000$ MPa is Young's modulus. For the yield stress, the values obtained from the micro-flat tensile specimens of the respective welds were used. The nugget zone and TMAZ of the FSW weld were characterized by the same yield strength value ($R_{\mathrm{p0.2W}} = 185$ MPa for FSW). The yield strain values resulting from Eq. (4.19) for LBW and FSW weld materials, respectively, are given in **Tab. 4.8**. However, the ARAMIS system was not able to resolve such low strains, so that the critical strain value, ε^*, at which yielding was assumed to occur in both LBW and FSW weld materials was selected as:

$$\varepsilon_y = \varepsilon^* = 0.8\% \quad \text{for plastic zone by ARAMIS}\ . \tag{4.20}$$

The plastic zone correction, $r_{\mathrm{p}}^{\mathrm{ARAMIS}}$, in welded panels based on the determination by the ARAMIS system can be defined as:

$$r_{\mathrm{p}}^{\mathrm{ARAMIS}} = \frac{\omega}{2} \tag{4.21}$$

where ω is the experimentally measured length of the plastic zone within which the normal strain is $\varepsilon_y \geq 0.8\%$ (see **Fig. 4.56**).

Definition of plastic zone correction according to Irwin

The idea of defining half of the plastic zone as the plasticity correction for the crack length is based on Irwin's approach where the plastic zone correction, $r_{\mathrm{p}}^{\mathrm{Irwin}}$, is half of the plastic zone size (see Section 2.1.1):

$$r_{\mathrm{p}}^{\mathrm{Irwin}} = \frac{1}{2\pi}\left(\frac{K_{\mathrm{I}}}{R_{\mathrm{p0.2}}}\right)^2 \quad \text{for plane stress.} \tag{4.22}$$

$R_{\mathrm{p0.2}}$ is yield strength of the weld material and K_{I} is the stress intensity factor defined for a M(T) panel as (eg. [84]):

$$K_{\mathrm{I}} = \frac{F}{2WB^*}\sqrt{\pi a_0} \times \sqrt{\frac{1}{\cos\dfrac{\pi a_0}{2W}}} \tag{4.23}$$

where B^* is the total thickness of the skin reinforcement where the weld is located ($B^* =$ 2.6 mm for LBW and $B^* = 2.2$ mm for FSW panels). Since the stable crack extension during loading is very small (Δa=4-9 mm in welded panels which corresponds to 3-7% of the initial crack length) compared to any other physical dimensions of the panel and the crack length, it was neglected in the calculation of the stress intensity factor in Eq. (4.23). Therefore, Eq. (4.23) is simply based on the initial crack length, a_0. This simplification gives a maximum error in K_{I} of about 4% which results in approximately 9% underestimation of $r_{\mathrm{p}}^{\mathrm{Irwin}}$ in Eq. (4.22).

It should be noted that Irwin's analytical approach for the determination of the plastic zone in a cracked body is based on a homogeneous material where the spread of plasticity in front of the crack tip is not affected by any physical boundaries like material interfaces in a welded joint. While the plastic zone in a homogeneous material is basically a function of the stress intensity factor and the material's yield strength, additional parameters such as the yield strength of the weld material, $R_{\mathrm{p0.2W}}$, the weld strength mis-match ratio, M, and the weld width, $2H$, govern the plastic zone size at the crack tip in a welded joint:

$$\text{plastic zone in weld} = f(K_{\mathrm{I}}, R_{\mathrm{p0.2W}}, M, 2H). \tag{4.24}$$

Definition of plastic zone correction according to compliance method

The third method is based on the compliance method according to the ASTM E561 standard [16] and has already been applied to the base material and LBW and FSW panels to determine K_{eff} R-curves (Section 4.3.4). Strictly speaking, the plastic zone correction according to the compliance method is based, like Irwin's method, on the homogeneous material. However, it has formally been applied to cracked LBW and FSW panels to investigate the feasibility of this approach to estimate the the crack tip plastic zone size in undermatched welds. The compliance based plastic zone correction, $r_{\mathrm{p}}^{\mathrm{compliance}}$, is then:

$$r_{\mathrm{p}}^{\mathrm{compliance}} = \Delta a_{\mathrm{eff}} \tag{4.25}$$

where $\Delta a_{\mathrm{eff}} = a_{\mathrm{eff}} - a_0$. The effective crack length, a_{eff}, is directly inferred from the experimentally measured load-CMOD curve without the necessity for measuring the physical crack extension during testing [16]. Therefore, the effective crack length, a_{eff}, includes the stable crack extension and the correction for plasticity at the crack tip.

Comparison of plastic zone correction methods and related R-curves

Figs. 4.57a), **4.58a)** and **4.59a)** show the plastic zone correction, r_{p}, based on the three definitions given above, for LBW M(T)760, FSW M(T)750 (crack in nugget zone) and FSW M(T)750 (crack in TMAZ), respectively.

The net section stress, σ_{net}, in these diagrams is defined as:

$$\sigma_{\mathrm{net}} = \frac{F}{(W - a_0)B^*} \tag{4.26}$$

and is normalized with respect to the yield strength of the respective weld material obtained from micro-flat tensile specimens.

In all three cases, the plastic zone correction measured by the ARAMIS system lies between the two estimated ones with the theoretical methods. Irwin's method can be considered an upper bound and the compliance method a lower bound to the plastic zone size in LBW and FSW welded panels.

All panels reached the failure load (being the maximum load) beyond net section yielding, indicated by the vertical dotted line in each graph. This limit is essential for the application of the effective crack length concept of LEFM being only valid up to ligament yielding as outlined in ASTM E561 [16].

Figs. 4.57b), **4.58b)** and **4.59b)** show the respective R-curves in terms of the effective stress intensity factor, K_{eff}:

$$K_{\mathrm{eff}} = \frac{F}{2WB^{*}}\sqrt{\pi a_{\mathrm{eff}}} \times \sqrt{\frac{1}{\cos\dfrac{\pi a_{\mathrm{eff}}}{2W}}} \tag{4.27}$$

where

$$a_{\mathrm{eff}} = a_0 + r_{\mathrm{p}} \tag{4.28}$$

and r_{p} is the plastic zone correction as described above for the three different methods (see Eqs. (4.21), (4.22) and (4.25)).

In terms of fracture resistance, Irwin's method provides the most conservative R-curve, whereas the compliance method yields the highest R-curve. The R-curve based on the experimental plastic zone measurements by the ARAMIS system lies between the R-curves based on the theoretical derivation of the plastic zone correction.

As stated in Eq. (4.24), the plastic zone size in welds also depends on the weld width, $2H$. **Fig. 4.60** illustrates the effect of the weld geometry on the experimentally determined plastic zone size. The crack location (nugget area and TMAZ) in the FSW panels seems to have a minor effect on the plastic zone size. The difference between a narrow (here LBW with $2H$=6 mm) and wide (here FSW with $2H$=20 mm) weld is, however, clearly demonstrated. At the same normalized net section stress, the plastic zone is three times greater in the narrow LBW joint. In general, at a constant load level the plastic zone length in a highly undermatched weld increases as the weld width decreases.

Weld strain distribution at the crack tip in LBW and FSW joints

The strain distribution ahead of the crack tip is quantified in **Figs. 4.61**, **4.62** and **4.63** showing strain profiles across the welds. The diagrams depict the two measured strain components, ε_x and ε_y, at the maximum load level of each panel extracted from selective locations in front of the crack tip.

Fig. 4.61 shows the strain distribution of the LBW M(T)760 panel with a crack located in the fusion zone. The stable crack growth during loading reached a value of Δa = 5.5 mm at this particular crack tip. It is seen that the strain in the loading direction, ε_y, sharply increases at the transitions from HAZ to the base material, reaching the maximum values in the weld material. The same deformation behaviour was observed in the LBW flat tensile specimen where the strain concentration occurred within the low-hardness region in the weld (see **Fig. 4.49**). Except the highly strained region close to the crack tip showing a slight compression in the weld region (negative ε_x), all other transverse strain profiles, ε_x, are vanishingly small and almost identical in the base and weld materials, indicating an in-plane constraint induced by the stronger base material.

Fig. 4.62 shows the strain profiles in the FSW M(T)750 panel with a crack located in the nugget zone. The strain distribution was taken as in the case of the LBW M(T) panel at different locations in front of the crack tip at the maximum load level. The stable crack advance was $\Delta a = 6.0$ mm at this particular crack tip. It is interesting to note that the region of maximum strain is not directly at the crack tip (strain profile "0, x=10 mm") but further ahead (strain profiles "1, x=27 mm" and "2, x=38 mm"). The strain values at these locations reach up to 25% which is close to the strain distribution observed in the standard FSW flat tensile specimen. From that finding it can be concluded that the failure of the FSW M(T)750 panel with a crack in the nugget zone is not attributed to the critical intensity of the crack stress field but to the plastic collapse of the ligament. Indeed, the net section failure stress of 280 MPa is very close to the tensile strength of 285 MPa of the FSW joint obtained from the standard flat tensile specimen (see **Fig. 4.52**).

Fig. 4.63 shows the strain profiles in the FSW M(T)750 panel with a crack located in the lowest-hardness region, i.e. TMAZ. Unlike the M(T) panel with a crack in the nugget area, here the strain profile with the maximum strain does occur directly at the crack tip, the strain peaks within the narrow band of the lowest hardness reaching values up to 25%. The transverse strain profile, ε_x, is almost constant at values close to zero indicating the inability of the weld material to deform in the in-plane transverse direction, i.e. in-plane constraint.

4.4.5 Concluding remarks

The digital image analysis clearly demonstrated the undermatched nature of the LBW and FSW joints. The plastic deformation is entirely confined to the narrow material strip including the weld material and HAZ. The measured strain profiles in standard flat tensile specimens of LBW and FSW joints showed that even if the strain in the direction of the external loading was high, the transverse strain (perpendicular to the loading direction) remained at very low values in the weld materials, indicating an in-plane constraint and giving rise to transverse stresses.

The determination of the yield strength from standard flat tensile LBW and FSW specimens is highly sensitive to the gauge length selected for the strain measurement. The closer the gauge length to the locations of hardness drop, the more realistic yield strength values can be obtained. However, these values are still greater than the ones determined from the micro-flat tensile specimens extracted directly from the weld region.

The approach based on the Irwin correction provides the most conservative K_{eff} R-curve, whereas the compliance method yields the highest R-curve. The R-curve based on the experimentally measured plastic zone size by the ARAMIS system lies between the two theoretical ones.

Regarding the LBW joint as a narrow weld and the FSW joint as a wide weld, the results of the present investigation have clearly shown that the length of the plastic zone is dependent on the weld width. At the same normalized net section stress (with respect to the yield strength of the weld material), the plastic zone length can be three times larger in the narrow LBW than in the wide FSW joint.

The strain profiles taken across the welds in front of the crack tips showed that in LBW and FSW (crack in TMAZ) panels the material at the crack tip was the most highly strained region. In the FSW panel with the crack in the nugget area, the TMAZ region was most highly strained, not being directly at the crack tip but some distance ahead of it. This is not surprising since this panel fractured in TMAZ by plastic collapse, i.e. at a net section stress equals the tensile strength of the FSW joint.

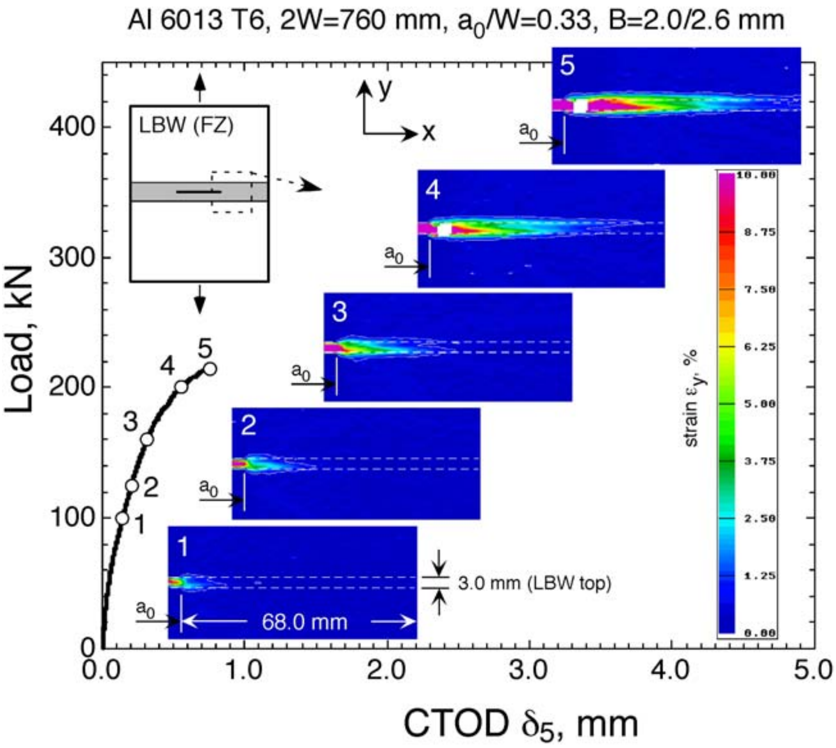

Figure 4.53: Evolution of the plastic zone ahead of the crack tip in the M(T)760 LBW plate.

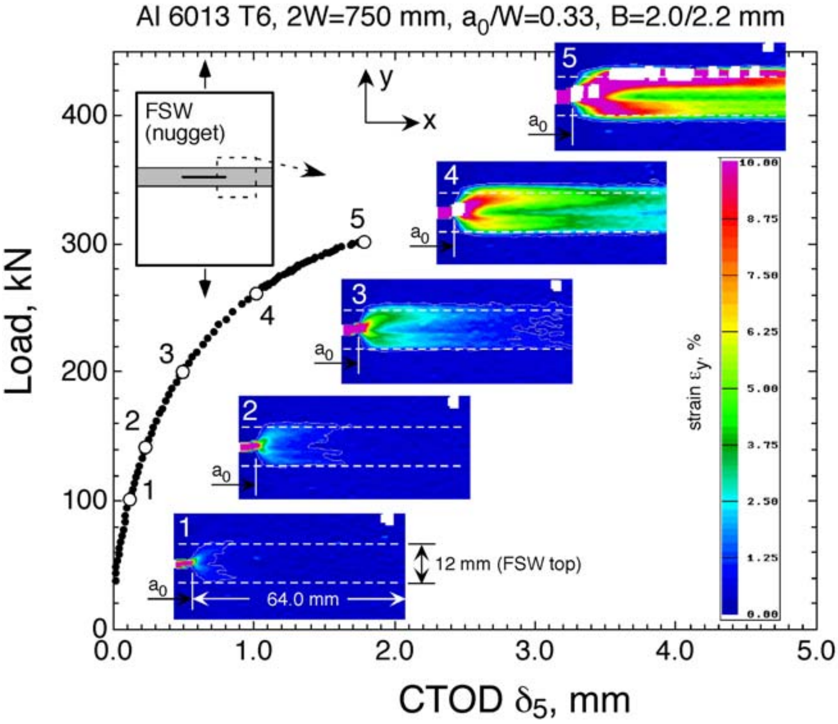

Figure 4.54: Evolution of the plastic zone ahead of the crack tip in the M(T)750 FSW plate with a crack in the nugget area along the weld centerline.

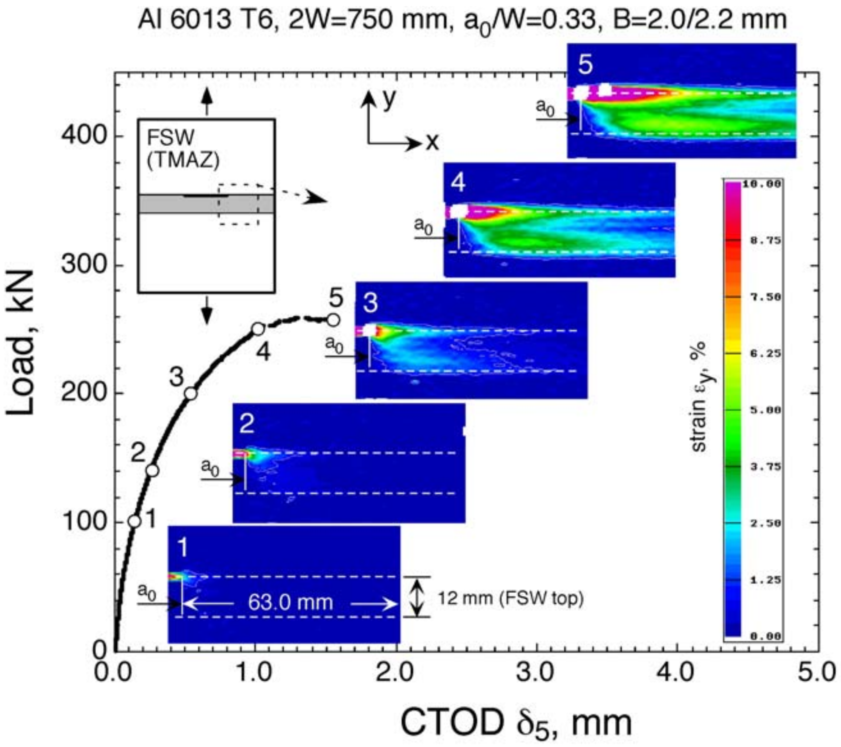

Figure 4.55: Evolution of the plastic zone ahead of the crack tip in the M(T)750 FSW plate with a crack in TMAZ.

Table 4.8: Strain values used for the determination of the plastic zone at the crack tip in LBW and FSW M(T) panels.

	$R_{p0.2W}$ from micro-flat MPa	$\varepsilon_{0.2}$ from Eq. (4.19) %	ε^* used in ARAMIS %
LBW	145	0.41	0.80
FSW	185	0.47	0.80

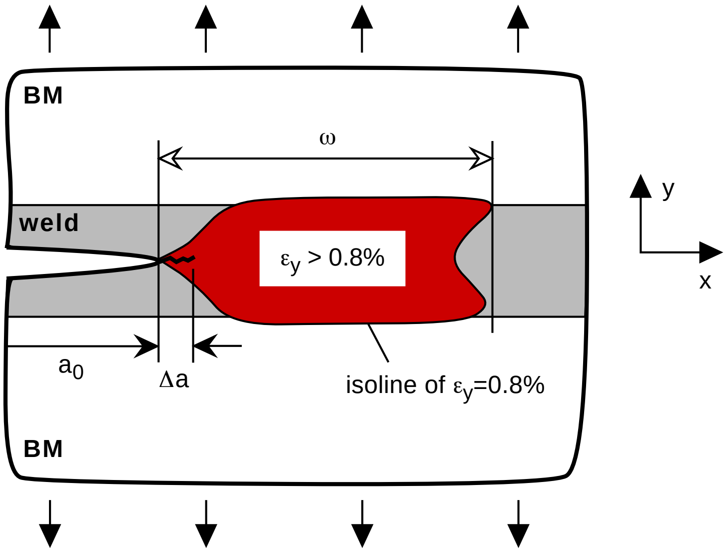

Figure 4.56: Principle of the plastic zone determination using the ARAMIS system.

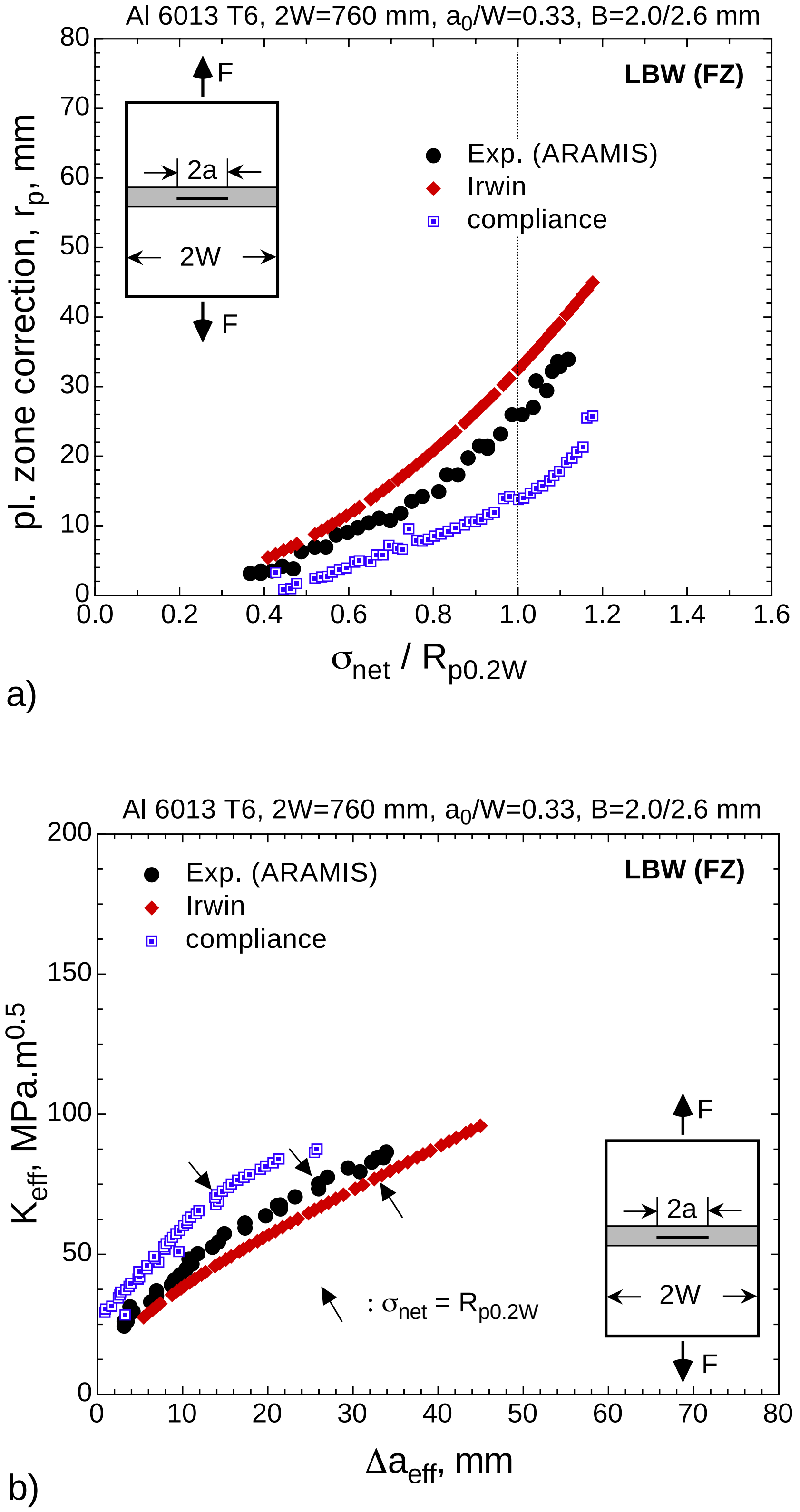

Figure 4.57: a) Comparison between theoretical (Irwin and compliance) and experimental (ARAMIS) plastic zone sizes in the M(T)760 LBW panel. b) Respective K_{eff} R-curves where $\Delta a_{\mathrm{eff}} = r_{\mathrm{p}}$.

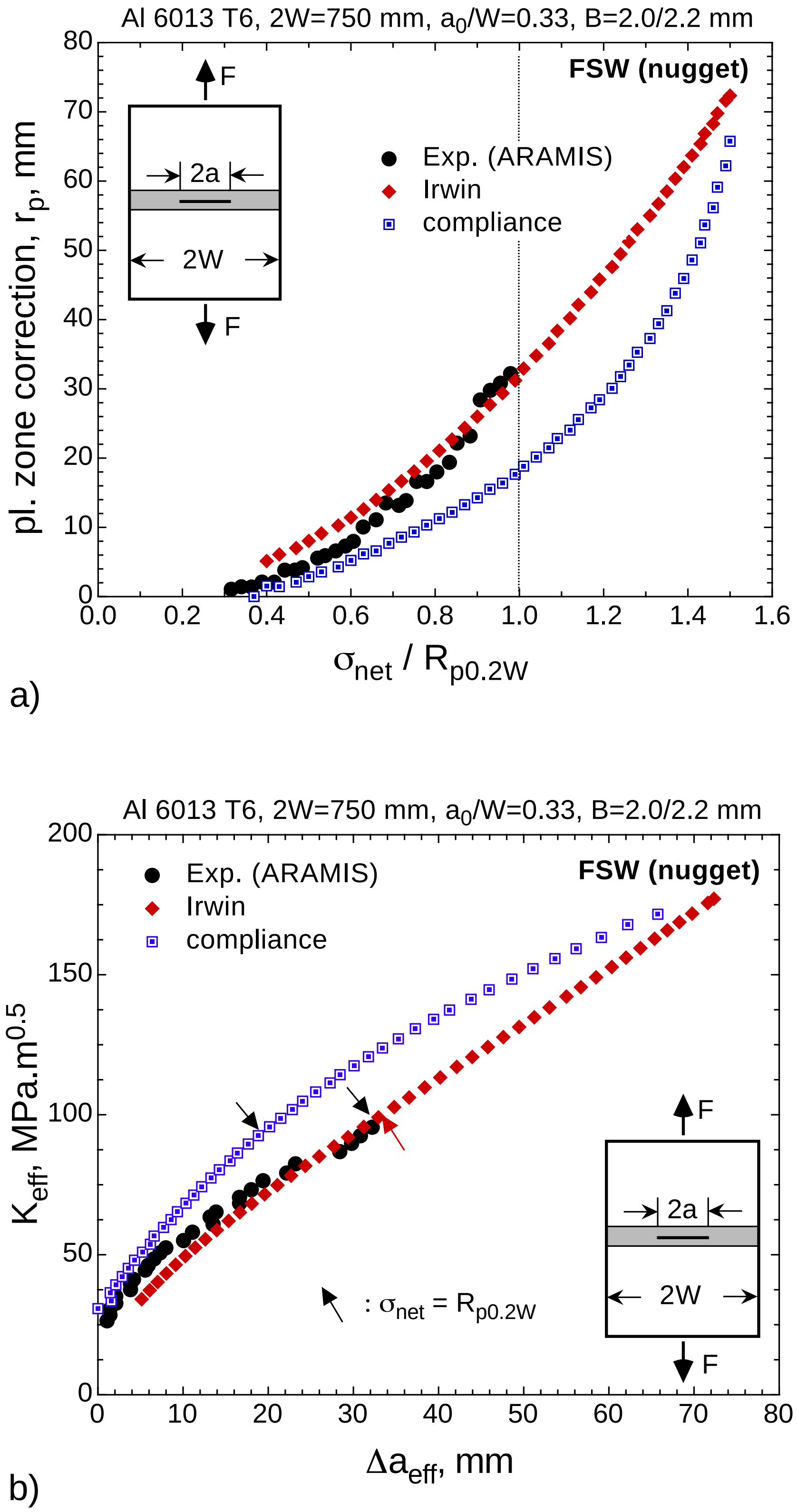

Figure 4.58: a) Comparison between theoretical (Irwin and compliance) and experimental (ARAMIS) plastic zone sizes in the M(T)750 FSW panel with a crack located in the nugget area along the weld centerline. b) Respective K_{eff} R-curves where $\Delta a_{\text{eff}} = r_{\text{p}}$.

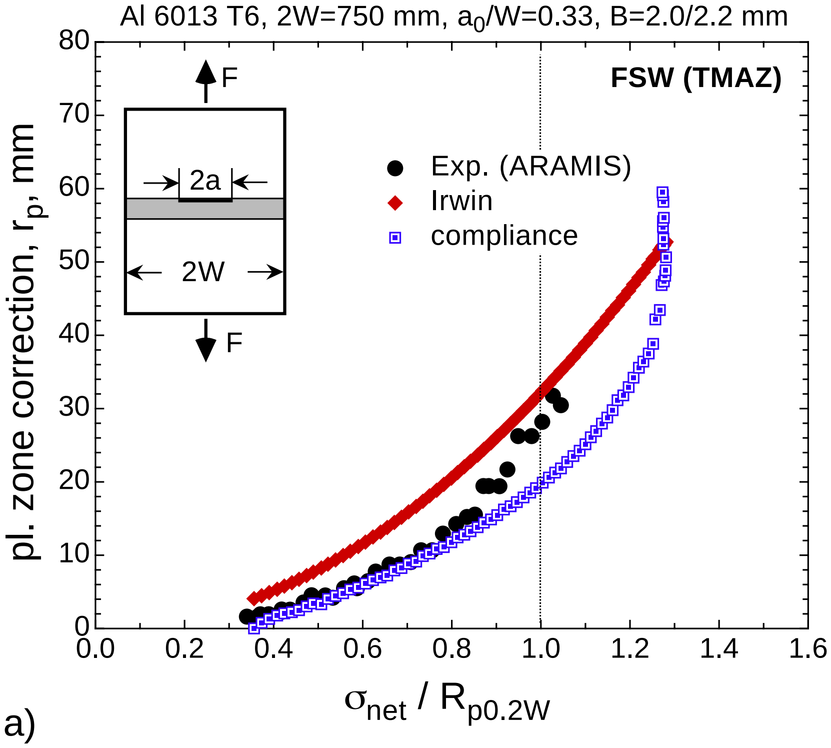

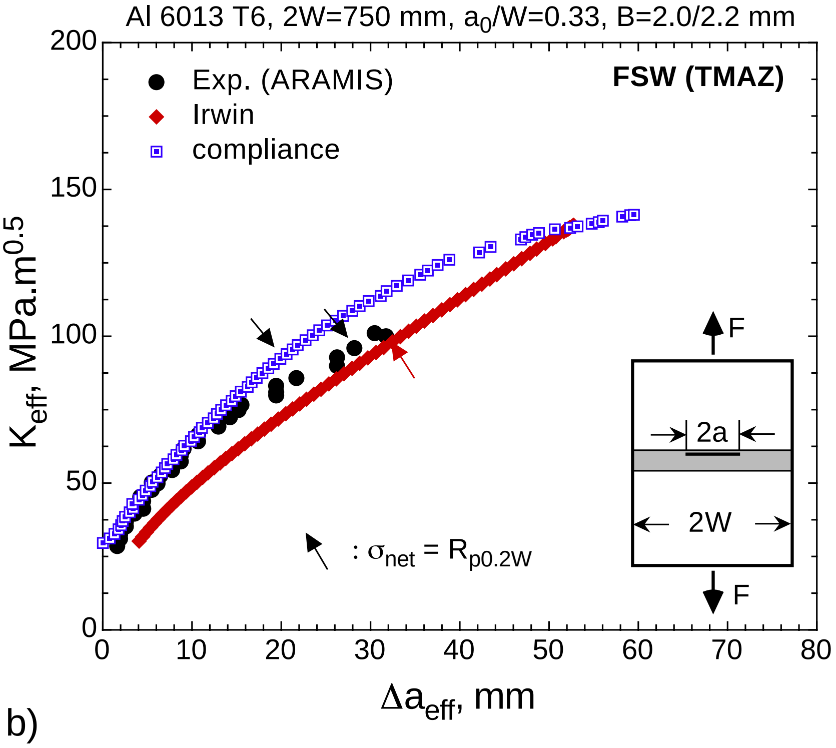

Figure 4.59: a) Comparison between theoretical (Irwin and compliance) and experimental (ARAMIS) plastic zone sizes in the M(T)750 FSW panel with a crack located in TMAZ. b) Respective K_{eff} R-curves where $\Delta a_{\text{eff}} = r_{\text{p}}$.

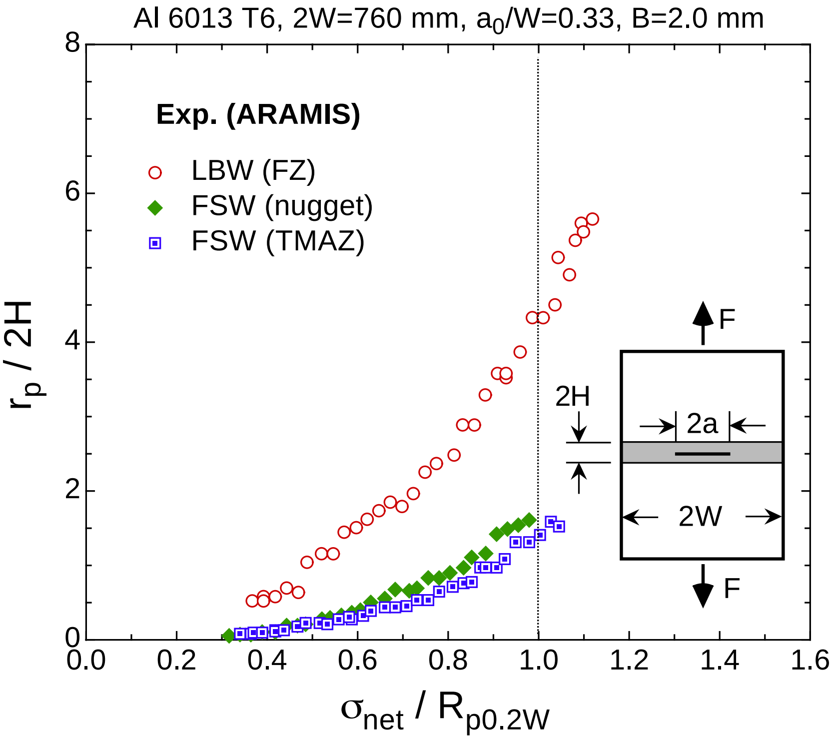

Figure 4.60: Plastic zone correction, r_p, normalized with respect to the weld width, $2H$, of the LBW panel ($2H = 6$ mm) and FSW panels ($2H = 20$ mm).

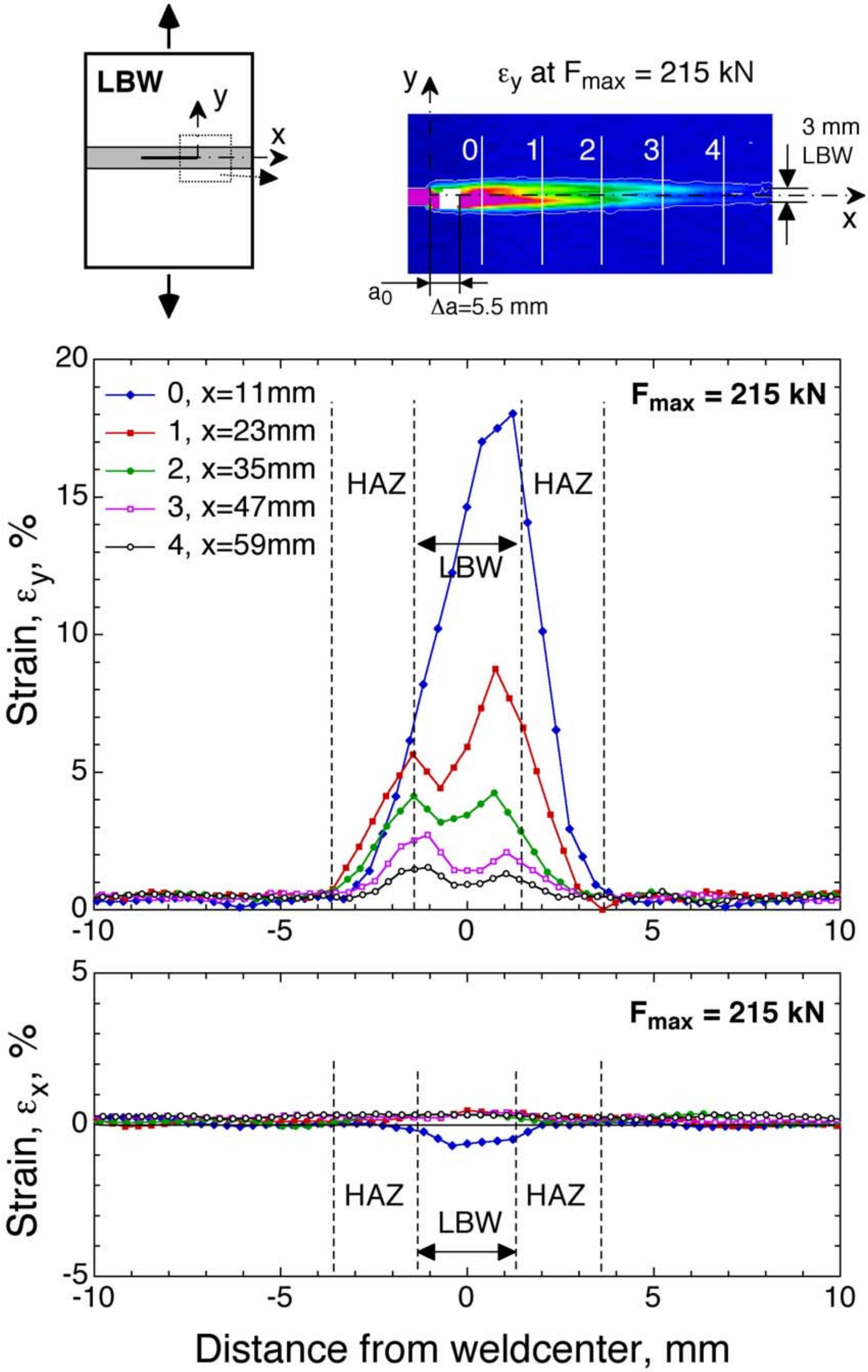

Figure 4.61: Strain distribution across the LBW weld in front of the crack measured on the M(T)760 LBW panel with a crack located in the fusion zone along the weld centerline.

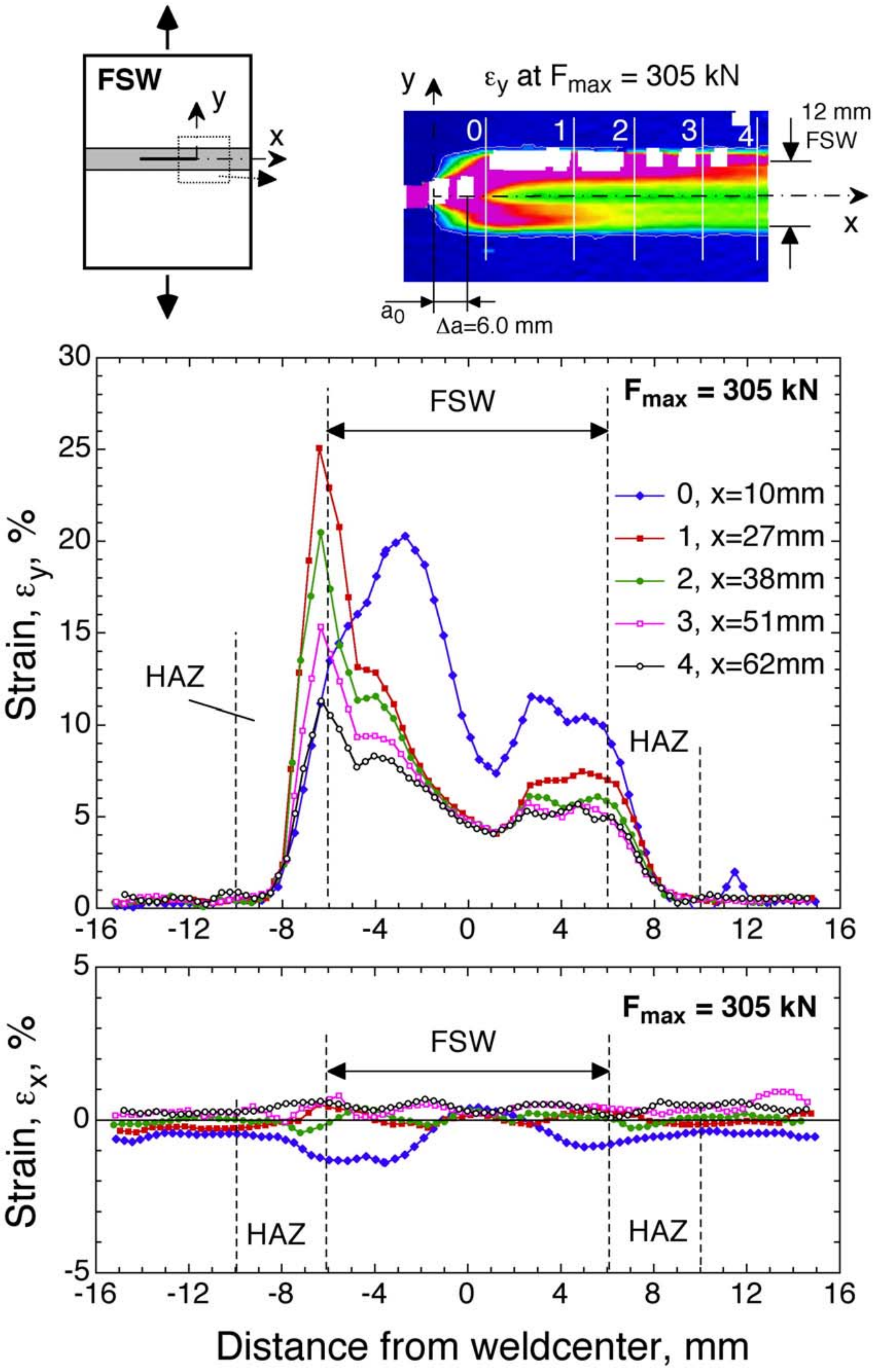

Figure 4.62: Strain distribution across the FSW weld in front of the crack measured on the M(T)750 FSW panel with a crack located in the nugget area along the weld centerline.

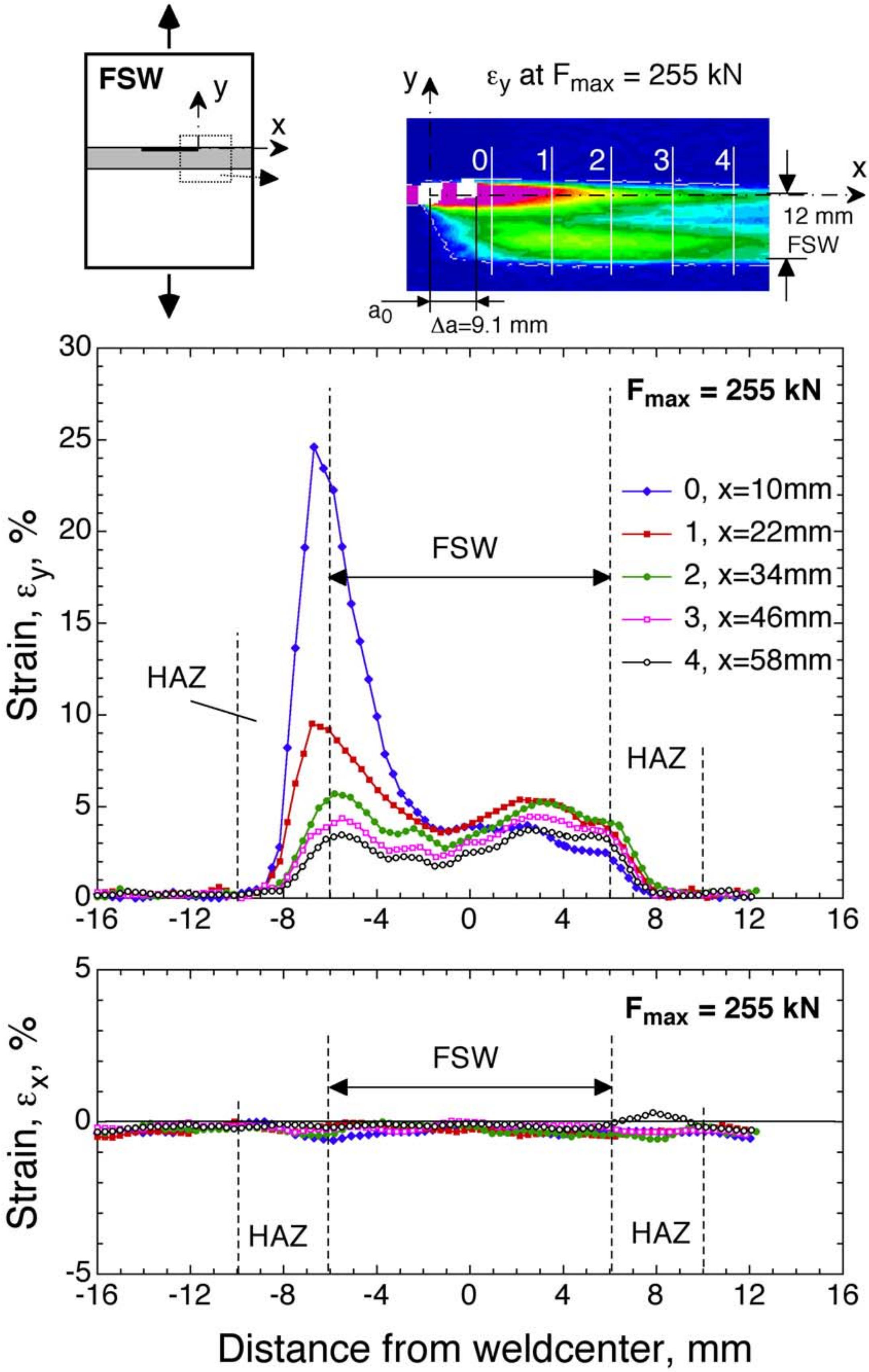

Figure 4.63: Strain distribution across the FSW weld in front of the crack measured on the TMAZ cracked M(T)750 FSW panel.

5 Determination of K-factor and yield load solutions for stiffened panels

To be able to apply the SINTAP procedure to stiffened panels in order to predict their residual strength, the K-factor and yield load solutions for these panels are needed. In the literature only K-factors for riveted panels can be found, eg. [13]. However, these solutions cannot be used for integrally stiffened panels since they do not include the effect of crack branching at the stringer. This section provides the K-factor solution to the skin as well as to the stringer crack after branching in 2- and 3-stringer panels. Also a yield load solution for these stiffened panels is proposed. The generation of the solutions is based on the finite element analysis (FEA).

5.1 Deformation behaviour of stiffened panels

This section provides preliminary information about the deformation behaviour of stiffened panels. The aim is to highlight specific issues related to FEA of such panels. Particular emphasis is placed on differences that may arise from geometrically linear (small strain) and geometrically non-linear (large strain) FE analyses.

Stiffened panels are modelled with shell elements [109] which are widely used for thin-walled structural components in automotive and aerospace industries. The details about the FE mesh design are given in subsequent sections.

The load was introduced through the skin by applying a constant displacement to the skin edge. The stringers were not loaded by any external loads. Since the stringers are attached to the skin on one side, leading to an asymmetric structure with respect to the applied load plane, the stiffened panel will experience out-of-plane bending.

The offset, d, defines the distance between the applied load plane and the resulting internal force in the stiffened panel, **Fig. 5.1**. The resulting bending moment, M_{res},

$$M_{\mathrm{res}} = F\,d \tag{5.1}$$

creates out-of-(skin)plane displacements. In FEA based on the small strain theory (geometrically linear analysis) [109], where the equilibrium state between internal and external forces is calculated on the initial shape of the structure, d results from the initial coordinates and is therefore not influenced by any geometry changes of the structure. The bending moment linearly increases with the applied load, F, and so does the out-of-plane displacement, **Fig. 5.2**. If the out-of-plane displacement is not prevented, this analysis approach leads to unrealistic deformation shapes.

In large (also called finite) strain FEA (geometrically non-linear analysis) [109], the geometrical changes of the structure are considered. For the equilibrium of force, the nodal coordinates are updated by their displacements at the end of each load increment. The

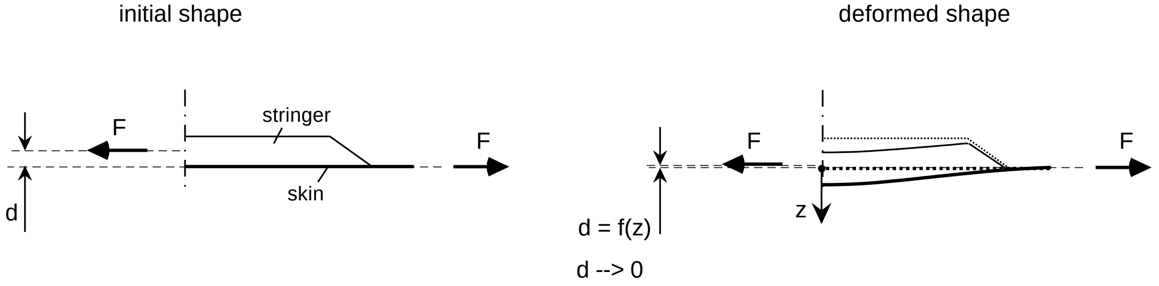

Figure 5.1: Eccentricity, d, causing the out-of-plane bending of the stiffened panel.

offset, d, is coupled with the out-of-plane displacements, so that d approaches zero for sufficiently high applied loads and so does the resulting bending moment. Consequently, the out-of-plane displacement is expected to reach a plateau, which is clearly depicted in **Fig. 5.2**.

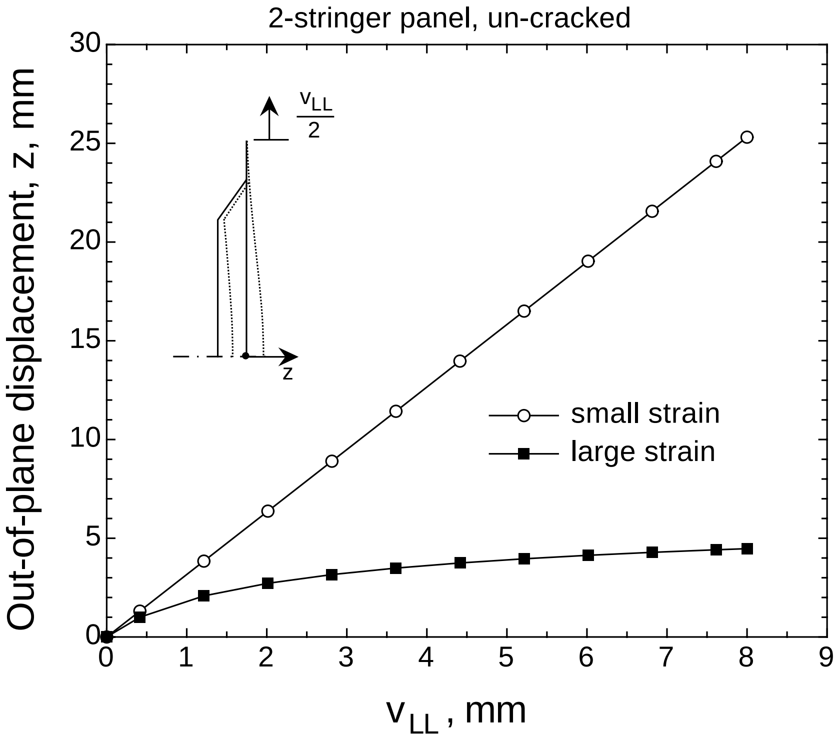

Figure 5.2: Out-of-plane displacement, z, vs. load-line displacement, v_{LL}, diagram. Comparison between small strain and large strain elastic FEA on the example of a 2-stringer panel without a crack. z is measured at the stringer foot.

In any case, the bending moment due to the asymmetry of the stringers with respect to the skin plane introduces additional tension stresses in the skin, particularly in the region close to the stringer. These stresses may be unrealistically high at higher applied loads in the case of a small strain FEA. In view of the determination of the stress intensity factors for the fuselage applications at a given internal cabin pressure in service, this aspect is of particular importance. Besides the bending moment described above, the cabin pressure also causes out-of-plane displacements due to bulging of crack flanks (see eg. [110]) which also may be overestimated by FEA based on the small strain theory.

These results have shown that the deformation behaviour of stiffened panels is described more realistically by the large strain FEA. However, previous numerical investigations (unpublished results at Airbus) have revealed that the out-of-plane displacements of the skin at stringer locations in a pressurized fuselage are much lower than those in the 2-stringer panel under uniaxial tension analyzed in this study.

Stiffened panels with long stringers may experience large out-of-plane displacements whereas short stringers lead to less deformation. Since this type of panels is not standardized, the prevention of out-of-plane displacements through the use of appropriate anti-buckling guides enables a consistency of test results.

During residual strength testing of 2- and 3-stringer panels, stable crack growth was observed. Crack branching occurred so that the skin crack also damaged the stringer. This experimental evidence was incorporated in the numerical analysis. The derivation of the yield load as well as *K*-factors for the stiffened panels was based on the experimental fact that:

$$a_{\mathrm{str}} = a_{\mathrm{sk-beyond}} \tag{5.2}$$

where a_{str} is the length of the stringer crack and $a_{\mathrm{sk-beyond}}$ the length of the skin crack beyond the stringer, **Fig. 5.3**.

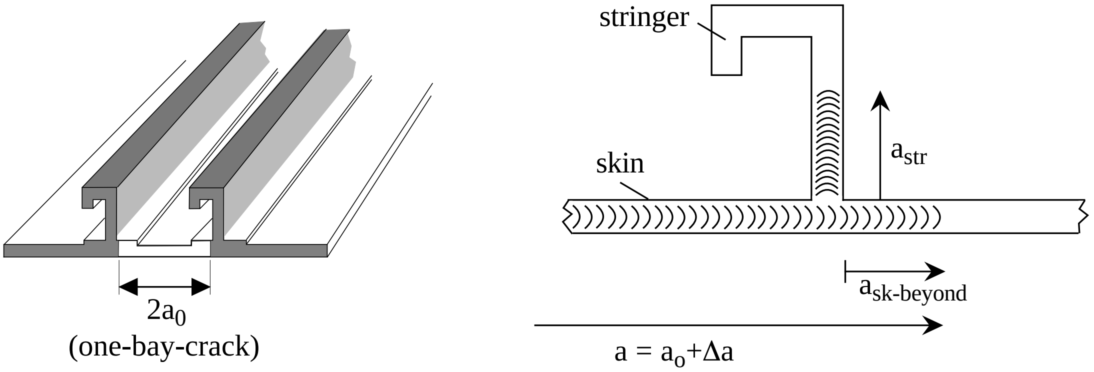

Figure 5.3: Crack branching.

5.2 Determination of *K*-factor

5.2.1 Methodology

The determination of the stress intensity factor (SIF) for 2- and 3-stringer configurations has been carried out using linear elastic FEA and is based on the virtual crack closure integral method [111].

In its analytical form, the crack closure method provides the energy release rate from the amount of work done by the stress in front of the crack tip when the crack is extended

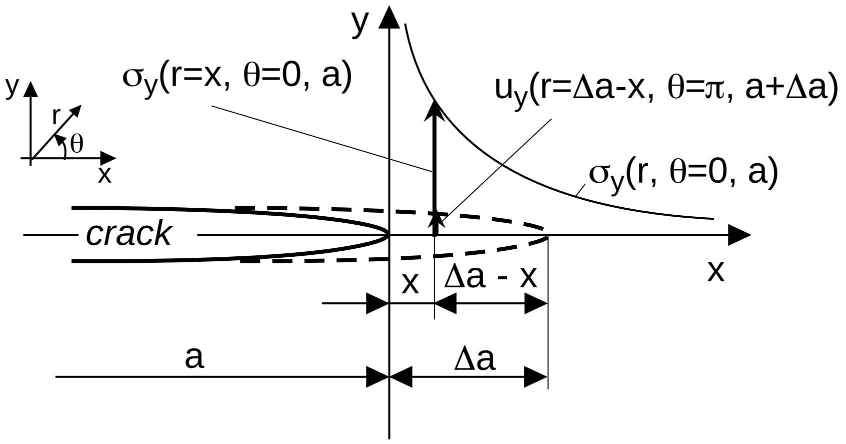

Figure 5.4: Analytical virtual crack closure integral method [111].

over an infinitesimal distance Δa, **Fig. 5.4**:

$$G(a) = \lim_{\Delta a \to 0} \frac{2}{\Delta a} \int_{x=0}^{x=\Delta a} \frac{1}{2} \sigma_{\mathrm{y}}(r = x, \theta = 0, a) \times u_{\mathrm{y}}(r = \Delta a - x, \theta = \pi, a + \Delta a)\, dx \quad (5.3)$$

where $\sigma_{\mathrm{y}}(r = x, \theta = 0, a)$ is the y-component of the elastic stress distribution for the crack length a and $u_{\mathrm{y}}(r = \Delta a - x, \theta = \pi, a + \Delta a)$ are the crack face displacements of the crack $a + \Delta a$ in the y-direction.

In the numerical representation, the strain energy release rate, $G(a)$, for a particular crack length can be obtained with two FE runs using the same model and boundary conditions but with two crack lengths differing by a small amount Δa, **Fig. 5.5**:

$$G(a) = \frac{\Delta U}{B\, \Delta a} \quad (5.4)$$

where ΔU is the change of elastic strain energy of the entire structure due to crack extension Δa and B is the thickness. In other words, ΔU is equal to the work necessary to extend the crack from a to $a + \Delta a$. Reversing the process, ΔU is easily obtained from the work necessary to close the crack tip from $a + \Delta a$ to a:

$$\Delta U = 2 \times \frac{1}{2}(F_{\mathrm{y}} u_{\mathrm{y}} + M_{\mathrm{z}} \varphi_{\mathrm{z}}). \quad (5.5)$$

The factor 2 in the above equation is due to the symmetry of the crack flank displacements. F_{y} and M_{z} are reaction force and reaction moment at the crack tip node obtained from the first FE run with the crack length a. u_{y} and φ_{z} are the displacement and rotation, respectively, of the released node (**Fig. 5.5**) obtained from the second FE run with the crack length $a + \Delta a$. It is important to include the reaction moment in the above formulation of ΔU since the shell elements also transmit moments [109]. It should be noted that Eq. (5.5) is only valid for the linear relationship between the reaction forces/moments and displacements/rotations. This condition is automatically met in the small strain linear elastic analysis. However, it should be proved in the case of linear elastic calculations based on the large strain theory.

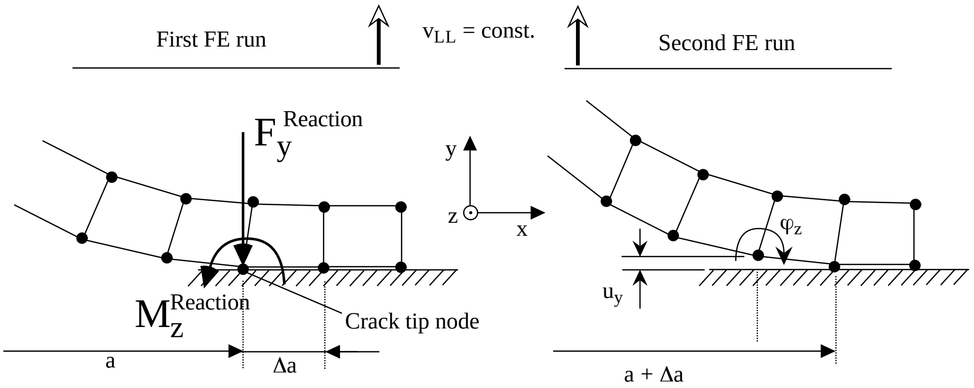

Figure 5.5: Numerical virtual crack closure integral method [111].

There is an alternative method that is also based on the virtual crack closure method but utilizes only a single FE run (eg. [112, 113]). Such a method uses reaction forces at the crack tip and displacements behind the crack tip. Here it is assumed that if the crack extends from a to $a + \Delta a$ the crack opening displacements behind the new crack tip will be approximately the same as those behind the original one. However, preliminary FEA results have shown that for the stiffened panel this method gives inaccurate results since the crack tip opening displacements of the skin crack are highly affected by the stringer, particularly in the case when the skin crack tip is close to the stringer.

The strain energy release rate can finally be converted to SIF, K_I, by the following relationship:

$$K_\mathrm{I}(a) = \sqrt{\frac{G(a)}{E'}} \tag{5.6}$$

where $E' = E$ for plane stress and $E' = E/(1-\nu^2)$ for plane strain. E is Young's modulus and ν is Poisson's ratio. For the calculation of K_I in subsequent sections, a plane stress condition was assumed.

5.2.2 Verification of methodology

The strain energy release rate, G, contains a limit expression ($\lim_{\Delta a \to 0}$) in its analytical formulation, see Eq. (5.3). In the discretized form, the crack extension Δa cannot be smaller than a finite element length. Therefore, there is a need to find an appropriate Δa. It can be done either by mesh convergence studies or by using a specimen with a known analytical solution for calibration. In order to check the accuracy of the virtual crack closure method, it is applied to a M(T) panel subjected to tensile loading. The K-factor obtained by FEA is then compared to the analytical solution:

$$K_\mathrm{I}(a) = \sigma\sqrt{\pi a}\,\beta\left(\frac{a}{W}\right) \tag{5.7}$$

where σ is the applied stress, a is the half crack length, and W is the half panel width. The finite width correction function is [84]:

$$\beta\left(\frac{a}{W}\right) = \sqrt{\sec\frac{\pi a}{2W}}\ . \tag{5.8}$$

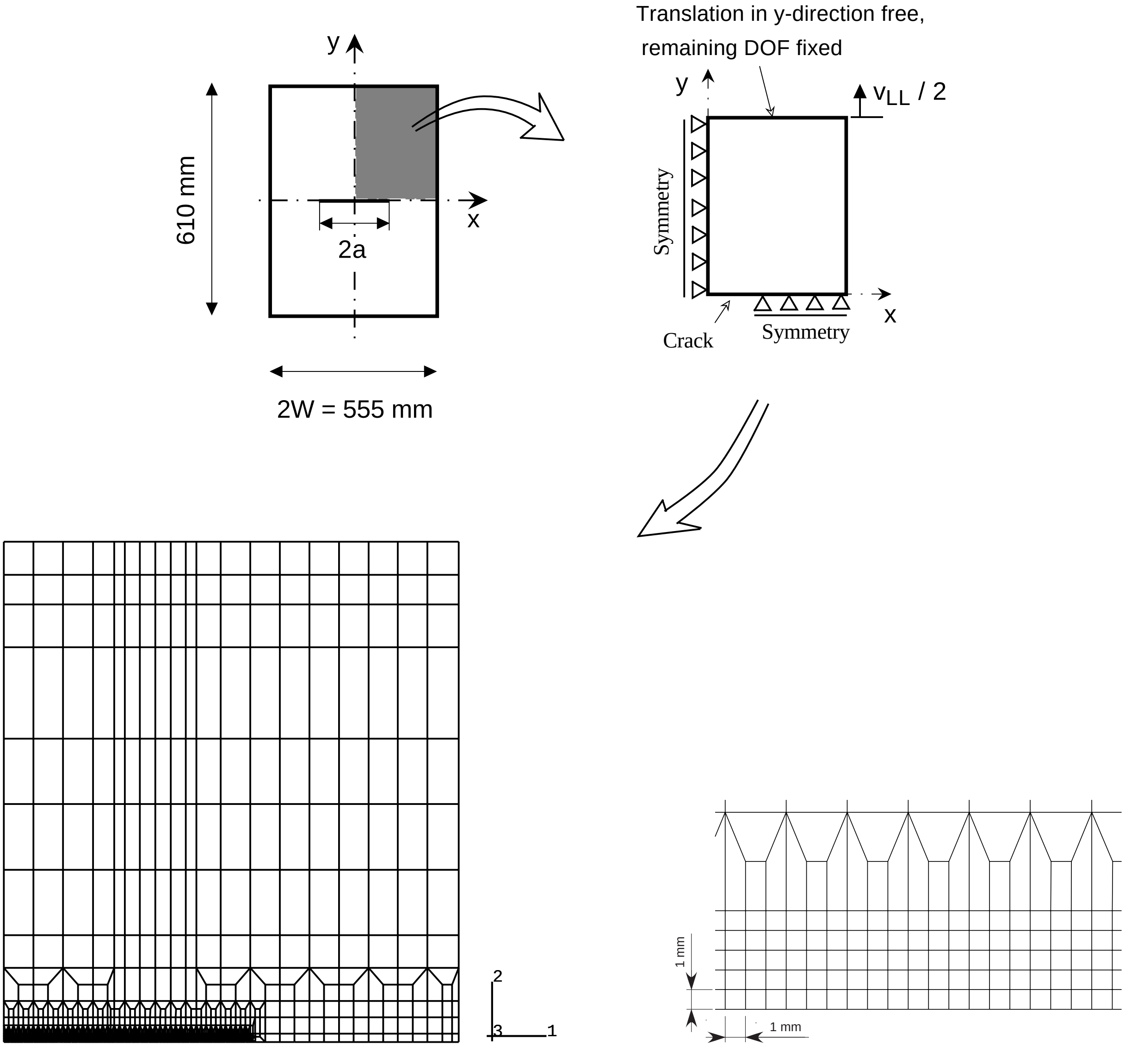

Figure 5.6: FE mesh of the M(T) panel (one quarter due to symmetry).

The M(T) panel of $2W = 555$ mm width, 610 mm length and a constant thickness of $B = 2.0$ mm, representing the skin dimensions of a 2-stringer panel, is discretized with quadrilateral linear shell elements with reduced integration (ABAQUS: S4R). Due to the double symmetry a quarter model is sufficient, **Fig. 5.6**. The smallest element length is 1.0 mm in the crack plane.

The FE analysis was performed in two different ways using the small strain (geometrically linear) and the finite strain theory (geometrically nonlinear) [109].

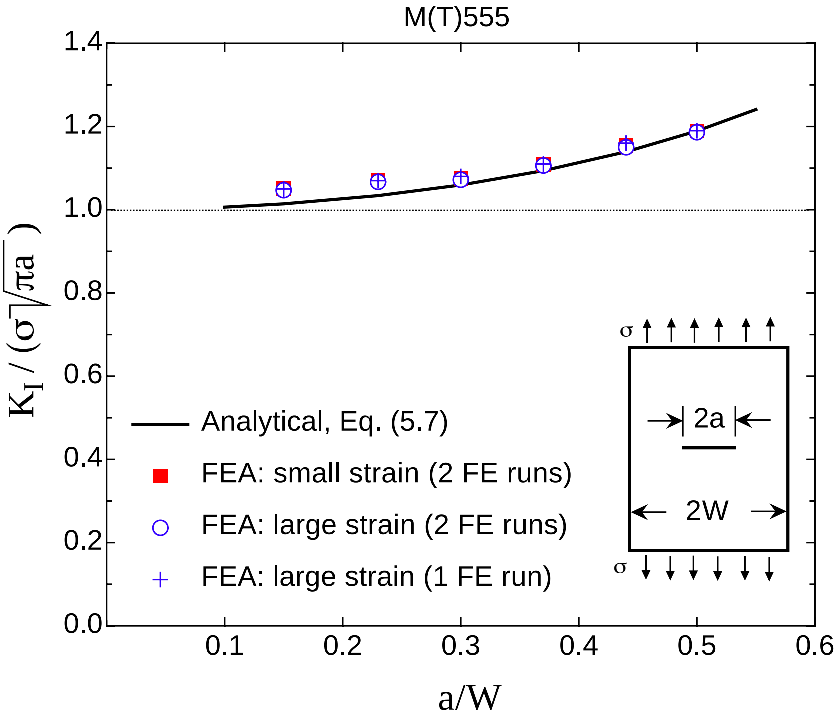

Figure 5.7: Virtual crack closure method applied to an M(T) panel.

However, there is almost no difference between the K-factor solutions obtained from small strain and large strain analyses, **Fig. 5.7**. These results were found from two separate FE runs as described in the beginning of Section 5.2 and indicate a negligibly small difference between the crack tip displacement fields of respective analyses. This suggests the use of a small strain approach which saves computational time.

For the sake of comparison, K-factors were also calculated from a single FE run of a large strain analysis by taking the nodal reactions at the crack tip node and the displacements at the adjacent node behind the crack tip. Since the crack extension Δa is small compared to the crack length and, more importantly, there is no disturbance due to a geometric discontinuity like a stringer, the method with a single FE run yields as accurate results as with two separate FE runs. For the small crack ratios ($a/W < 0.25$) the error is around 3%, for larger crack ratios ($a/W > 0.25$) the error is less than 1% considering all approaches.

The methodology for calculating the K-factors has been verified using the simple M(T) panel for which the analytical K-factor solution is available. The selection of the smallest element length of 1.0 mm leads to fairly accurate results. The FE model will now be extended to stiffened panels.

5.2.3 K-factor solutions for skin and stringer cracks in stiffened panels

Due to the use of anti-buckling guides that are realized in the FE model by suppressing the out-of-plane nodal displacements over the entire range that was covered by the anti-buckling device in the test, Mode III (tearing type) loading was eliminated. Mode II (shearing type) cannot occur due to symmetric boundary conditions. Therefore, pure Mode I crack tip loading can be obtained in this numerical study. The smallest length of 4-noded quadrilateral, non-singular elements in the ligament was 1.0 mm for all meshes used for the determination of K-factors.

The same FE mesh was used for the skin as for the M(T) panel in the previous section. The stringer was added using the same 4-noded quadrilateral shell elements having the same smallest element size of 1.0×1.0 mm^2 in the crack plane. The load was introduced only through the skin by applying constant displacements to the skin edge. The stringers were not loaded. The method with two FE runs was applied to the stiffened panels. Preliminary FE analyses have shown that the difference between the small strain and large strain analyses is negligibly small in stiffened panels. The calculation of the K-factor for 2- and 3-stringer panels will, therefore, be based on the small strain theory which saves computational time. The similarity of small strain and large strain analyses is attributed to the use of anti-buckling guides which do not allow any out-of-plane displacements and make the stiffened panel behave in a similar way as an M(T) panel where large strain analysis has hardly had an effect on the K-factor determination (see **Fig. 5.7**).

Based on the experimental evidence, it has been assumed in this numerical study that an increment of stable crack growth in the skin will cause an equal increment of stable crack growth in the stringer, i.e. $a_{\mathrm{str}} = a_{\mathrm{sk-beyond}}$, see **Fig. 5.3**.

The stress intensity factor of the skin crack in the stiffened panel can be defined as:

$$K_{\mathrm{I\,sk}} = \sigma\sqrt{\pi a}\,\beta_{\mathrm{sk}}\left(\frac{a}{W}\right) \tag{5.9}$$

where $\beta_{\mathrm{sk}}\left(\frac{a}{W}\right)$ is a correction function due to the stiffeners (and in fact also includes the effect of the finite width). The applied stress, σ, is:

$$\sigma = \frac{F}{2WB} \tag{5.10}$$

where F is the applied load, $2W$ is the total width of the stiffened panel, and B (=2.0 mm) is the skin thickness. $K_{\mathrm{I\,sk}}$ is obtained from FEA upon using Eqs. (5.4), (5.5), and (5.6). The correction function, $\beta_{\mathrm{sk}}\left(\frac{a}{W}\right)$, is then obtained from Eq. (5.9):

$$\beta_{\mathrm{sk}}\left(\frac{a}{W}\right) = \frac{K^{\mathrm{FE}}_{\mathrm{I\,sk}}}{\sigma\sqrt{\pi a}}\,. \tag{5.11}$$

Analogously, the stress intensity factor for the stringer crack, $K_{\mathrm{I\,str}}$, is obtained applying Eqs. (5.4), (5.5), and (5.6) to the stringer crack. The correction function, β_{str}, for the stringer crack can be then defined as:

$$\beta_{\mathrm{str}}\left(\frac{a}{W}\right) = \frac{K^{\mathrm{FE}}_{\mathrm{I\,str}}}{\sigma\sqrt{\pi a}}\,. \tag{5.12}$$

Note that a is the skin crack length.

When the skin is cracked, the load is transferred to the stringers. As in the riveted structure, the stringer, towards which the crack is propagating, experiences the highest load increase and, hence, being of particular interest for the failure of a stiffened structure [12, 13, 17, 114, 115]. The load increase in the stringer is expressed by the stringer load concentration factor, L_s:

$$L_\mathrm{s}\left(\frac{a}{W}\right) = \frac{F_\mathrm{str}}{F^*_\mathrm{str}}. \tag{5.13}$$

which defines the ratio of the stringer load, F_str, in the cracked structure and the stringer load, F^*_str, in the intact structure. Since the stringer in the cracked structure carries more load due to the skin cross-section loss in the presence of a skin crack, L_s is always greater than 1.

F^*_str was obtained from the analysis of uncracked stiffened panels. Due to the prevention of the out-of-plane displacement by anti-buckling guides, negligibly small difference was found between the small and large strain theories. The same result was observed for reaction forces and moments at the crack tip node which linearly change with respective nodal displacements and rotations. It can therefore be concluded that for the determination of the K-factor solution, the small strain theory is applicable to stiffened panels as long as the out-of-plane displacement is prevented.

The load-displacement curves of the respective small strain linear elastic FE analyses are given in **Fig. 5.8**, also showing the load in the stringer. In the case of the 2-stringer panel, the stringer carries about 9.5% of the total applied load, F, while the stringer share in the 3-stringer panel is 6.1%:

$$F^*_\mathrm{str} = 0.095\,F \qquad \text{for 2-stringer panel} \tag{5.14}$$

$$F^*_\mathrm{str} = 0.061\,F \qquad \text{for 3-stringer panel} \tag{5.15}$$

These percentages correspond to the percentage of the stringer cross-sectional area with respect to the total cross-sectional area of the respective stiffened panel.

Rewriting Eq. (5.13) using Eqs. (5.14) and (5.15) links the stringer load, F_str, to the total applied load, F, of stiffened panels:

$$L_\mathrm{s}\left(\frac{a}{W}\right) = \frac{F_\mathrm{str}}{0.095\,F} \qquad \text{for 2-stringer panel} \tag{5.16}$$

$$L_\mathrm{s}\left(\frac{a}{W}\right) = \frac{F_\mathrm{str}}{0.061\,F} \qquad \text{for 3-stringer panel} \tag{5.17}$$

Fig. 5.9 shows the correction functions, β_sk and β_str, as a function of the crack ratio, a/W, as well as the stringer load concentration factor, L_s for the 2-stringer panel, . For the 3-stringer panel, the respective relationships are depicted in **Fig. 5.10**. Both figures show a drop of the correction function, β_sk when the skin crack approaches the stringer, while the stringer load increases with increasing skin crack length. However, when the skin crack passes the stringer, introducing a crack in the stringer (crack branching), the contrary is true. β_sk as well as L_s plots experience a sharp kink reversing the trends.

The stress intensity factor of the skin crack increases with increasing skin crack length, whereas the stringer load concentration factor, L_s, decreases.

As mentioned before, the experimental evidence has been incorporated in the present analysis that an increment of the skin crack propagation causes the same increment of the crack extension in the stringer, i.e. $a_\mathrm{str} = a_\mathrm{sk-beyond}$. **Figs. 5.9** and **5.10** also show the correction function, β_str, of the stress intensity factor of the stringer crack. For this particular crack configuration, the stress intensities of the skin and stringer cracks are very close.

Fig. 5.11 depicts the comparison between riveted and welded stiffened panels. The K-factor for the riveted panel with the same geometry and stringer cross-sectional area was determined [116] using the same approach as for the welded panel. The stringer was attached to the skin by rivets of 4.8 mm diameter with a 22.0 mm rivet pitch. The same elastic properties were assigned to the skin, stringer, and rivets. Unlike in the welded panel, the stress intensity factor (β_sk) in the riveted panel keeps on decreasing beyond the stringer. This is due to the fact that the riveted stringer remains intact bridging the skin crack. As the skin crack stably grows, more load is transferred to the stringer which is reflected in the increasing L_s-factor.

Therefore, in the analysis of integrally stiffened welded panels the use of the stress intensity factors of the skin crack may be underestimated when using those of the riveted panels, which may lead to non-conservative predictions.

K-factor solutions for the skin as well as for the stringer crack were derived in this section for 2- and 3-stringer panels. These solutions are indispensable in the residual strength analysis of stiffened panels using the SINTAP procedure. Another important input parameter is the yield load which is addressed in the next section.

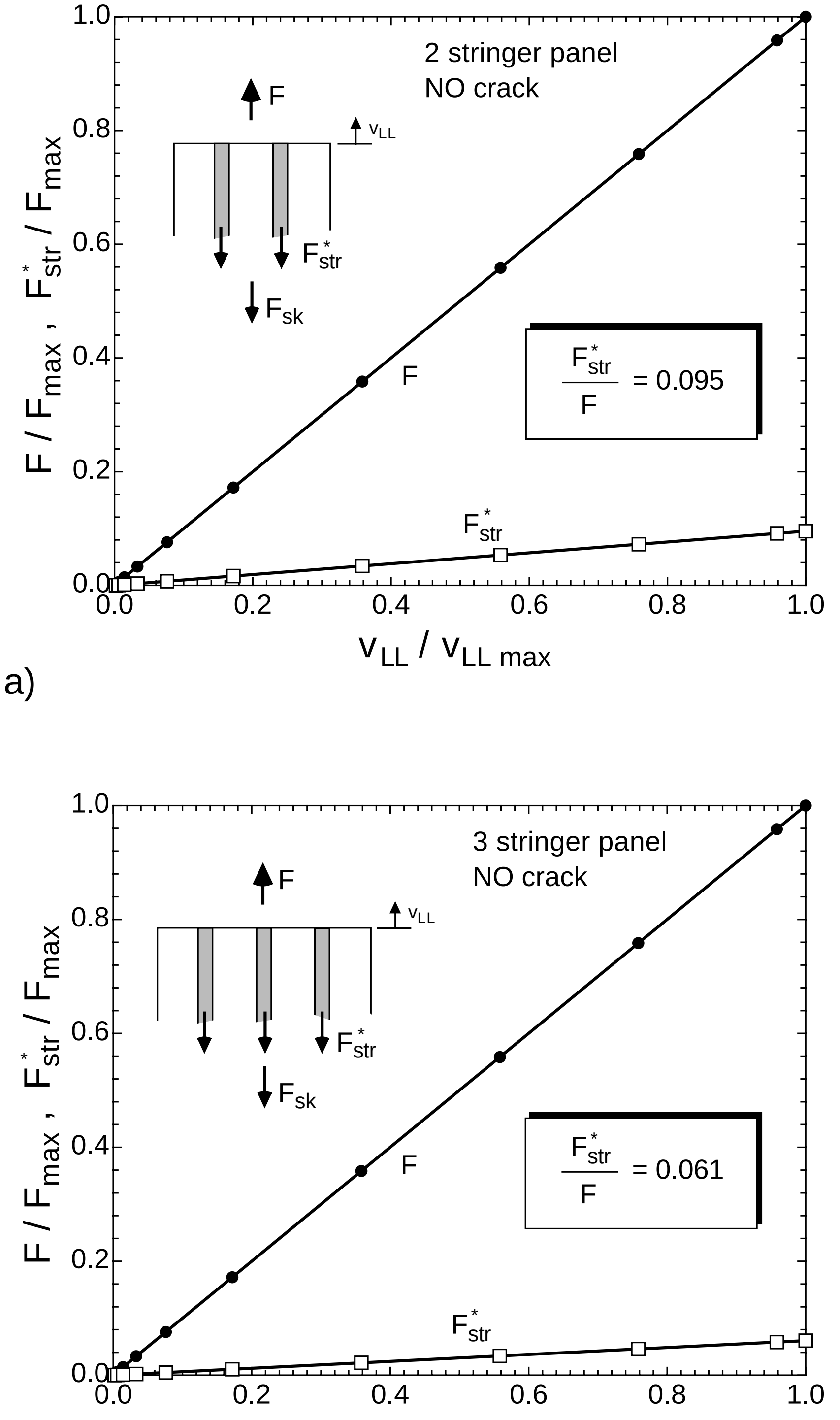

Figure 5.8: Determination of the stringer load, F^*_{str}, in uncracked stiffened panels: a) 2-stringer panel; b) 3-stringer panel.

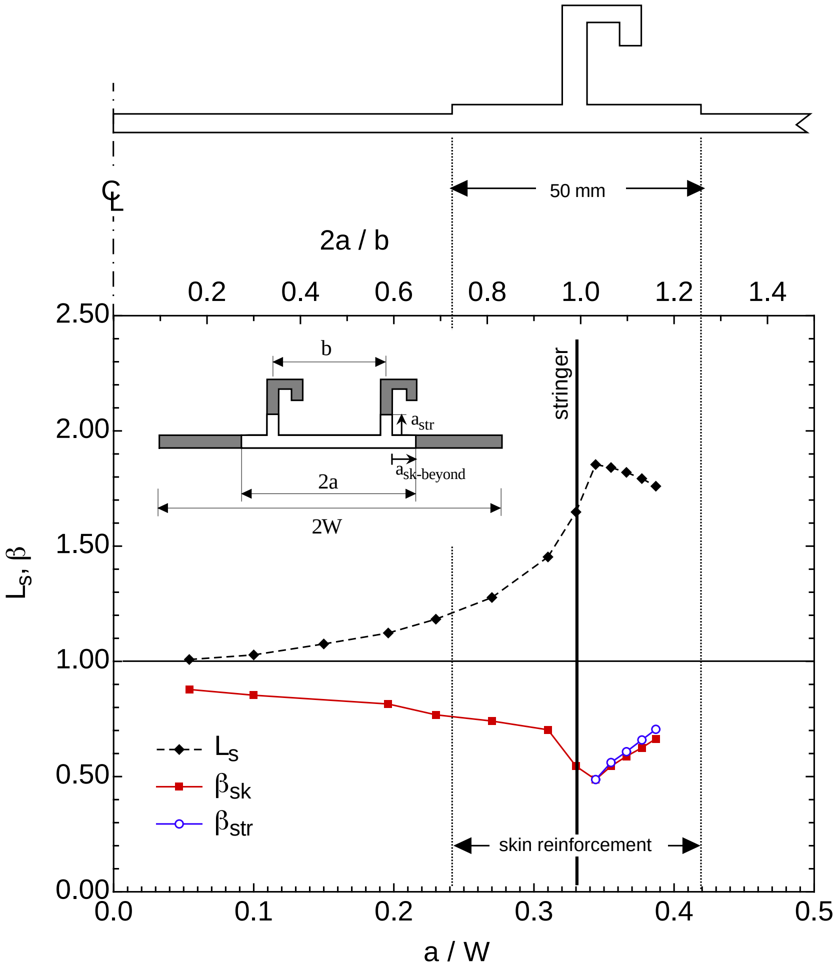

Figure 5.9: Normalized SIF of the skin crack, $\beta_{\rm sk}$, and the stringer crack, $\beta_{\rm str}$, along with the stringer load concentration factor, $L_{\rm s}$, of the 2-stringer specimen. The stable crack extension of the crack in the stringer and the skin is assumed to be equal, i.e. $a_{\rm str} = a_{\rm sk-beyond}$.

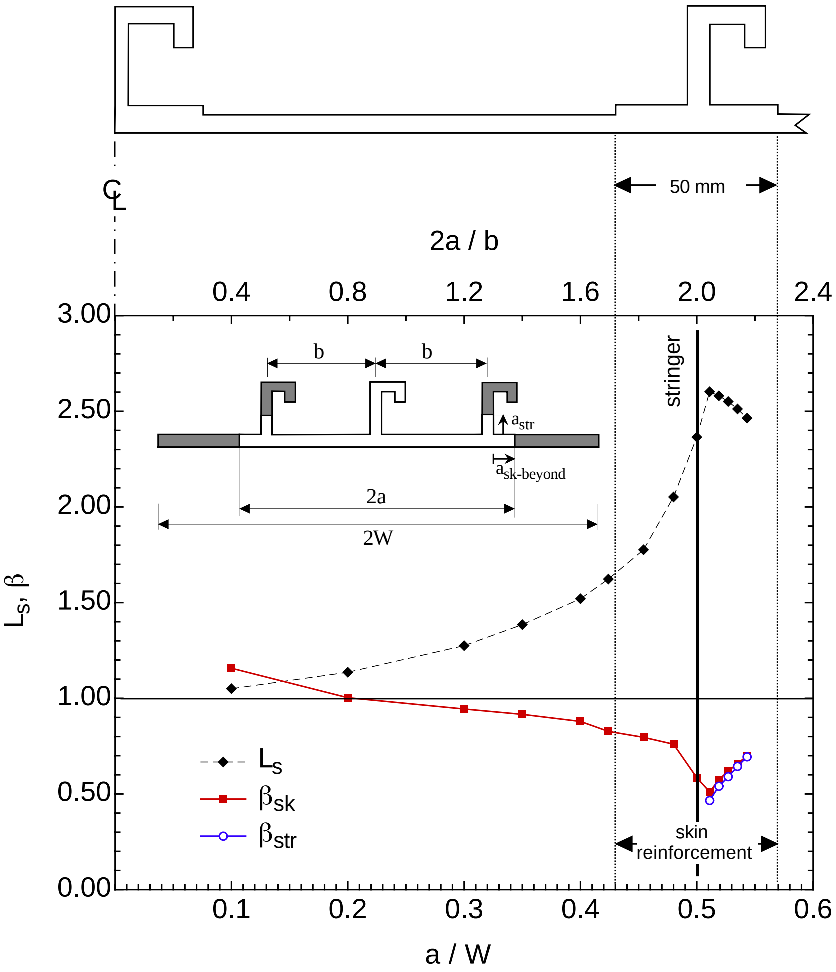

Figure 5.10: Normalized SIF of the skin crack, β_{sk}, and the stringer crack, β_{str}, along with the stringer load concentration factor, L_{s}, of the 3-stringer specimen with broken central stringer. The stable crack extension of the crack in the stringer and the skin is assumed to be equal, i.e. $a_{\text{str}} = a_{\text{sk-beyond}}$.

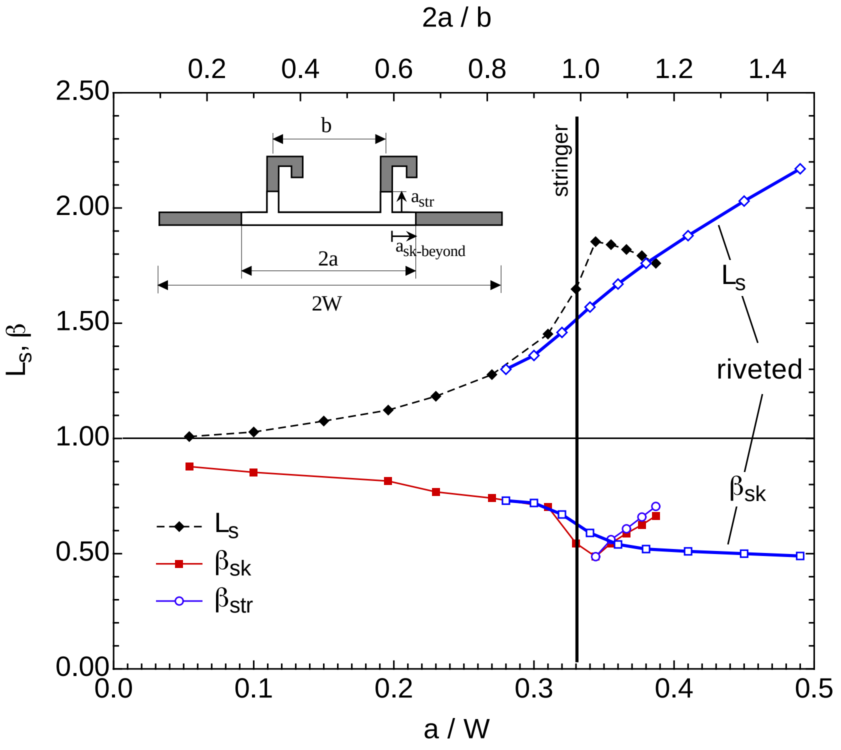

Figure 5.11: Comparison of the normalized SIF β_{sk} and the stringer load concentration factor, L_s, in a welded and riveted 2-stringer panels. The riveted panel was modelled with the same skin mesh and same stiffening ratio as the welded one; 4.8 mm rivets with 22.0 mm rivet pitch [116].

5.3 Yield load determination

In order to avoid confusions of the terms plastic "limit load" and "yield load" which are equally used in fracture mechanics, their definitions are required. The plastic "limit load" is the maximum load a given structure made of a perfectly plastic material can sustain. In this condition, the deformations increase while the load is held constant, i.e. the structure becomes a mechanism. This rarely happens in real structures, and hence, the limit load calculation applies strictly not to a real structure but to a hypothetical one with the following assumptions [117]:

- elastic (or rigid)/perfectly plastic material,
- strain-displacement relations based on small strain theory.

Nevertheless, a load computed on the basis of this analysis concept, called limit analysis (eg. [118,119]), may give a good approximation to the plastic load experienced by the real structure. The effect of large deformations, that can generally lead to strengthening or weakening effects, is not considered in the limit analysis. The limit analysis solution truly defines a plastic collapse load for a material with no strain hardening, but it indicates an incipient plastic load for materials that do strain harden.

The term plastic "yield load" characterizes the net section yielding condition in a cracked component made of a material with strain hardening, **Fig. 5.12**. However, for simplified defect assessments, the limit load, which coincides with the yield load for an ideally plastic material, is commonly used as an approximation (eg. [120,121]).

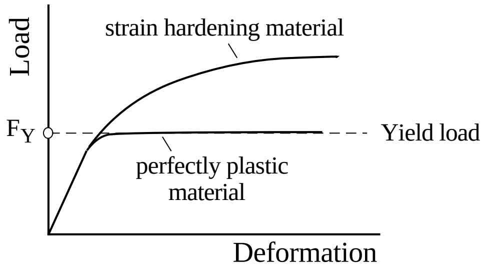

Figure 5.12: Definition of the yield load.

The lower bound to the limit load is obtained by a statically admissible stress field satisfying equilibrium and yield. The upper bound is obtained by a kinematically admissible strain rate field satisfying compatibility and flow rule [118]. Generally, for the sake of conservative predictions, the lower bound is used in defect assessment procedures.

A numerical approach to obtain a lower bound limit load of a cracked component is based on FEA with a perfectly plastic material model. The yield load is then the maximum load that can be attained in the analysis. In subsequent sections, a detailed elastic-plastic FEA was performed to derive an estimate of the yield load solution of cracked stiffened panels. First, a methodology was developed and verified using the analytical solutions of an M(T) panel. Then, the 2D shell model was compared with the 3D model in order to understand the behaviour of shell elements under plastic deformations. Finally, the effect of the softer LBW material on the yield load of stiffened panels was investigated using a 3D FE mesh.

5.3.1 Development of methodology on the example of M(T) panel

Analytical formulae based on the limit analysis need to be validated by a rational determination of the yield load from experimental results. Such a comparison is complicated by the inability to conclusively determine the yield load from load-deformation curves. Existing methods for determining the yield load from load-deformation curves are discretionary in nature [122].

The objective is to develop a methodology for the determination of the yield load of stiffened panels made of thin sheets by means of FEA. The analysis was first performed on a M(T) panel. Subsequently, the analysis was extended to the stiffened 2-stringer panel using the same methodology which was found appropriate through the analysis of the M(T) panel.

Since the stiffened panel is made of a thin sheet material, the stress state is expected to be under the plane stress condition. However, from a geometrical point of view the stiffened structure with stringers joined perpendicularly to the skin is 3-dimensional in space. Therefore, it is not possible to model the stiffened panel by any two-dimensional element types like plane stress (or plane strain) elements but by shell elements that are widely used in industry to model thin sheet structures.

In the computation of the K-factors presented in the previous section, shell elements were used to model the stiffened panels. In order to investigate their ability to capture the elastic-plastic material behaviour, a preliminary analysis was conducted with the same M(T) panel as for K-factor calculations, see **Fig. 5.6**.

The M(T) panel was modelled using three different element types; however, all of them are 4-noded linear elements with reduced integration [109]:

- plane stress elements (ABAQUS: CPS4R)
- plane strain elements (ABAQUS: CPE4R)
- shell elements (ABAQUS: S4R).

The analysis has shown that shell elements and plane stress elements give almost identical results (**Fig. 5.13**). However, small strain and large strain analyses result in a different structural behaviour. Due to the element thickness reduction that is accounted for in the large strain analysis [109] and due to the underlying elastic-perfectly plastic material model, the applied load drops after the uncracked ligament has fully plasticized.

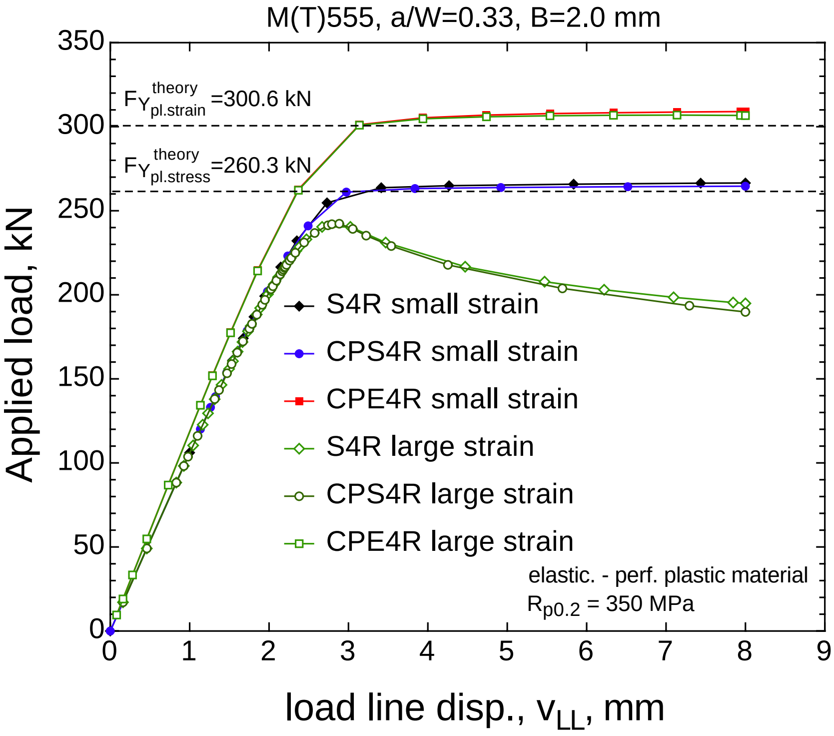

Figure 5.13: Load-displacement plot of the M(T) panel using different element types and strain theories (small and large strain)

A proof for the thickness reduction as the cause of the load drop is given by using plane strain elements. **Fig. 5.13** also shows load-displacement curves for the same M(T) panel modelled with plane strain elements. A very small difference has been observed between the small strain and large strain analyses. These elements do not allow displacements in the thickness direction (plane strain!), leading to a constant thickness of the panel throughout the entire loading range. Therefore, no load drop occurs for the large strain analysis beyond net section yielding.

The theoretical yield load, F_Y, for a M(T) panel is given as [123]:

$$F_Y = \begin{cases} R_{p0.2}\,2WB\left(1-\frac{a}{W}\right) & \text{plane stress} \\ \frac{2}{\sqrt{3}}R_{p0.2}\,2WB\left(1-\frac{a}{W}\right) & \text{plane strain} \end{cases} \tag{5.18}$$

where $R_{p0.2}$ is the uniaxial yield strength, W is the half panel width, B is the panel thickness, and a is the half crack length.

The theoretical yield load values as calculated with Eq. (5.18) for the investigated crack ratio of $a/W = 0.33$ are indicated by horizontal lines in **Fig. 5.13** for the plane stress and plane strain conditions, respectively. The respective numerical values at the plateau are slightly greater (about 2%) than the theoretical ones. This is ascribed to the boundary conditions of the FE model. The edge of the M(T) panel at which the loading in terms of prescribed displacements is applied is prevented from lateral displacements. This constraint leads to a slightly higher yield load compared to the theoretical solution.

Comparing the FEA results with the analytical solutions, the following conclusions are drawn:

- in elastic-plastic analysis, shell elements behave similarly to plane stress elements,
- small strain theory is more suitable for elastic-plastic analysis if shell elements are used.

This approach has been adopted for the numerical determination of the yield load of stiffened panels which is presented in the next section.

5.3.2 Yield load estimate for stiffened panels

Residual strength analysis of thin sheets incorporates stable crack growth leading to a need for a yield load solution as a function of the crack length. Therefore, different crack lengths were analyzed using the same mesh and boundary conditions as in the calculation of the K-factors. **Fig. 5.14** shows the load-displacement curves of a 2-stringer panel for crack ratios ranging from 0.23 to 0.37. The analysis was performed on the basis of an elastic-perfectly plastic material with the assumed yield strength of $R_{\mathrm{p0.2}} = 350\mathrm{MPa}$ for both skin and stringers. In all cases the displacement boundary conditions are applied to the skin only, and the magnitude of the applied deformation was made large enough to bring the panels to their limiting state, i.e. until a clear plateau has developed in the load-displacement diagram. The yield load value was taken at the plateau for each case.

The plateau values of all analyses are plotted versus the respective crack ratios, a/W, where a is the half skin crack length in **Fig. 5.15**. For comparison, the net section yielding line is drawn into the same diagram defined as follows:

$$F_{\mathrm{Y}} = R_{\mathrm{p0.2}}\, A_{\mathrm{net}} \tag{5.19}$$

where A_{net} is the net section area of the stiffened panel, being the total uncracked cross-sectional area:

$$A_{\mathrm{net}} = A_{\mathrm{net,sk}} + 2A_{\mathrm{net,str}} \tag{5.20}$$

with $A_{\mathrm{net,sk}}$ and $A_{\mathrm{net,str}}$ being the net section areas of the skin and stringer, respectively. The factor 2 in the above equation stands for the number of uncracked or partly cracked (in case of crack branching) stringers. Note that Eq. (5.20) also holds for the 3-stringer panel as the central stringer is broken.

The comparison between the FE results and the analytical solution given in Eq. (5.19) is depicted in **Fig. 5.15**. A very good agreement is obtained for skin cracks crossing the stringer. In Eq. (5.19), crack branching was also accounted for. For skin cracks shorter than a bay, Eq. (5.19) gives a conservative estimation of the yield load.

The 3-stringer case has not been analyzed by FEA. However, since the 3-stringer panel with a two-bay crack over the broken central stringer has the same uncracked ligament

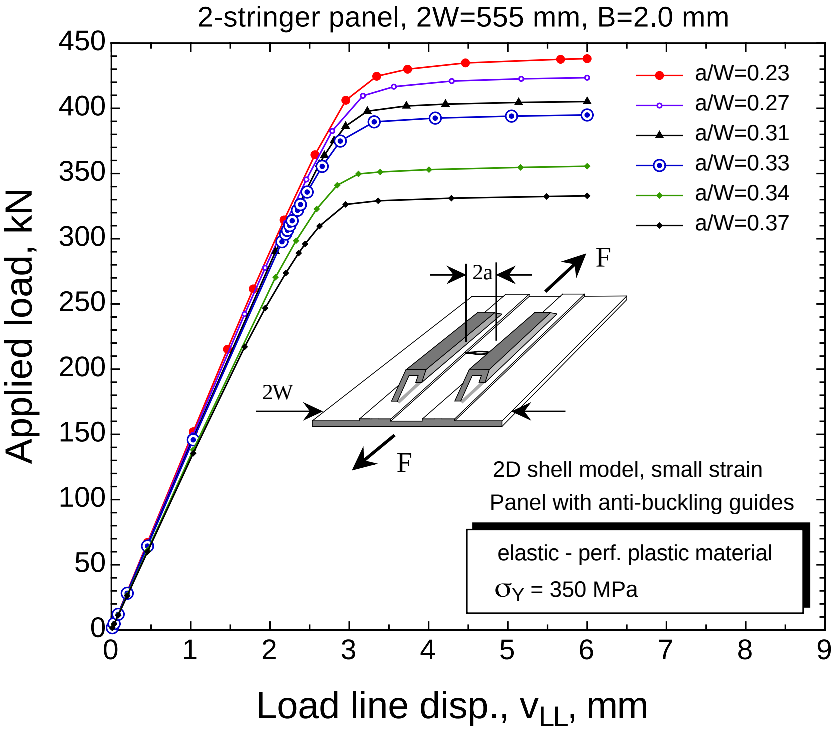

Figure 5.14: Load vs. displacement diagram of a 2-stringer panel with anti-buckling guides.

as the 2-stringer panel with a one-bay crack, the yield load is expected to be similar. Therefore, for the residual strength analysis of these cracked stiffened panels using the SINTAP procedure, Eq. (5.19) is proposed for the yield load solution. A sensitivity analysis with respect to the yield load of stiffened panels will be carried out in Section 6.

5.3.3 2D versus 3D FE model

In the preceding section, it has been shown that there is a significant difference between small strain and large strain 2D-FEA when looking at the structural response in terms of the load-deformation curve. In this section a three dimensional (3D) FE model of the 2-stringer panel is considered with identical boundary conditions including the use of anti-buckling guides. The two different element types were compared:

- 2D model: 4-noded shell elements with reduced integration (ABAQUS: S4R);
- 3D model: 8-noded 3D brick elements with full integration (ABAQUS: C3D8).

The 3D model consists of linear brick elements with two elements through the skin and stringer (foot) thickness, **Fig. 5.16**. The smallest element side length is, as in the 2D model, 1.0 mm in the crack plane. An elastic-perfectly plastic material model is used as in the previous analyses.

Fig. 5.17 shows the load-displacement diagram obtained from different FE models. Using the large strain theory, the shell model exhibits a significant load drop beyond

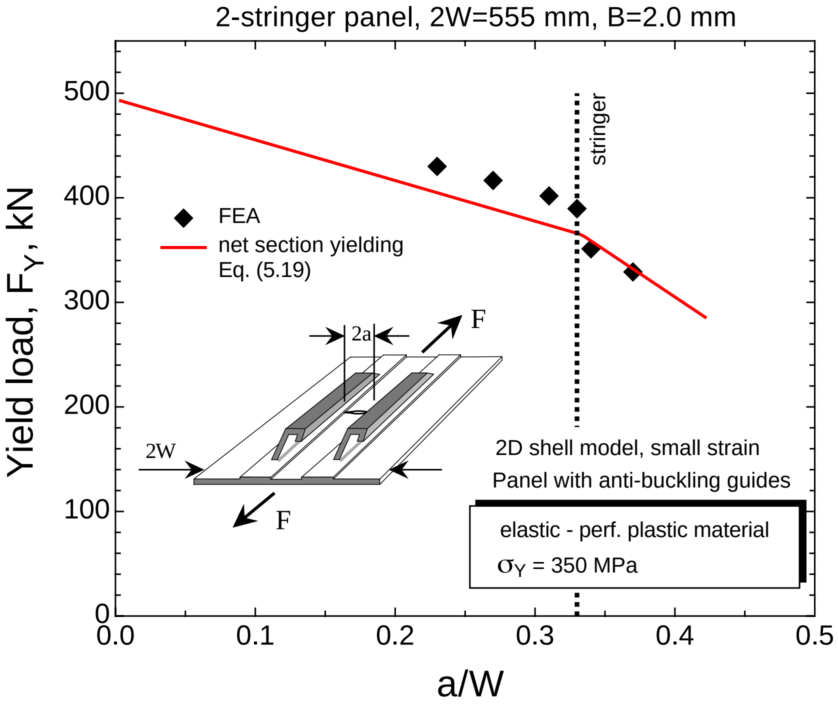

Figure 5.15: Comparison of analytical and numerical solutions for the yield load of a 2-stringer panel with anti-buckling guides.

yield, whereas the response of the 3D model does not show an extensive decrease of the applied load after net section yielding. This outcome indicates that shell elements do not capture the shell thickness reduction properly beyond yielding. There is no experimental evidence of the thickness change to compare with the numerical simulation; however, 3D elements are the closest model to reality.

For small strain theory, both models give identical results and substantiate the determination of the yield load by analyzing the stiffened panel based on the small strain theory. Due to the advantage of a simpler model without the loss of accuracy and shorter computational time, the 2D shell model is proposed for the determination of the yield load.

5.3.4 Effect of laser beam weld on yield load

In the previous analysis, a homogeneous material was assumed, so that the skin and stringers can be thought of as being machined from a single piece of material (eg. extrusion or mechanical milling). In the case of a welded structure, the skin and stringer are connected by a LBW joint having lower strength than that of the base material.

To investigate this effect, an elastic-perfectly plastic material with identical elastic properties but a lower yield strength was assigned to the weld metal. The LBW joint was modelled by four element rows underneath the entire length of the stringer, **Fig. 5.16** b). Two different mismatch ratios were considered by selecting a 20% ($M = 0.80$) and 50%

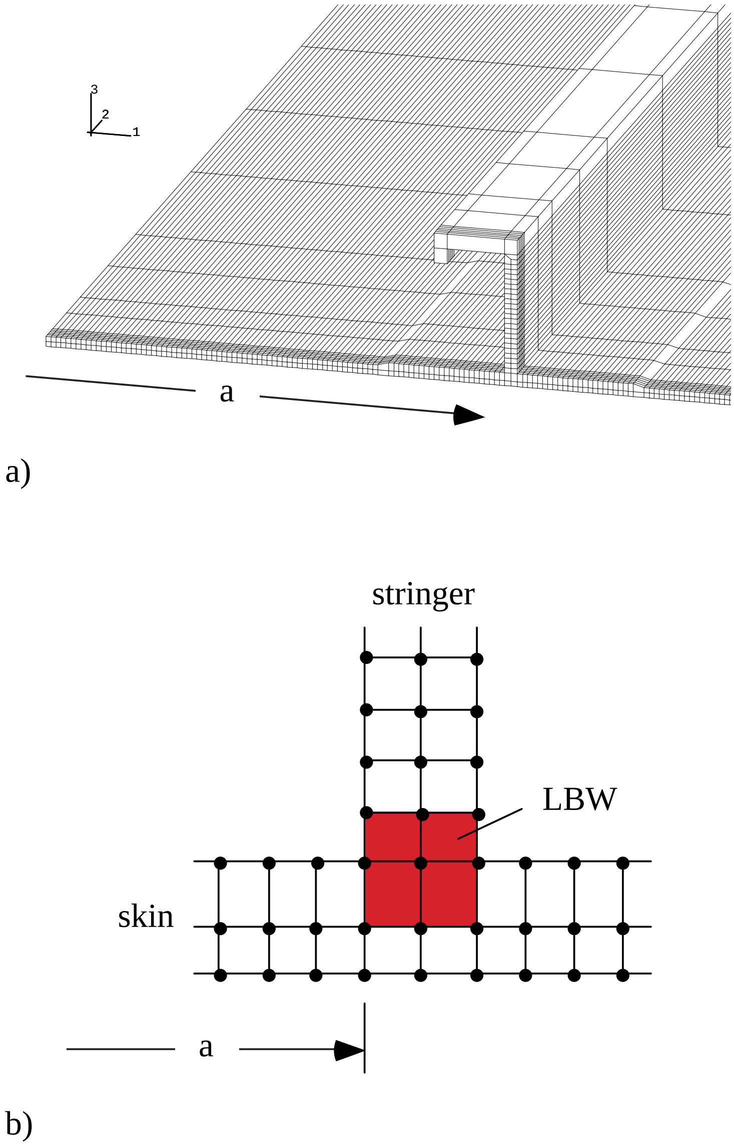

Figure 5.16: a) 3D FE mesh of a 2-stringer panel and b) details of LBW joint modelling.

($M = 0.50$) lower yield strength of the weld material than that of the base metal. The skin and the stringer were of the same material as in all previous FEA (perfectly plastic material).

The effect of the weaker LBW material on the yield load of the stiffened panel is shown in **Fig. 5.18**. Since the cross-sectional area of the weld is a very small fraction of the entire cross-sectional area of the stiffened panel, there is very little influence of the weaker LBW material on the global structural response of the stiffened panel. The maximum load plateau of undermatched panels is slightly lower than in the homogeneous configuration.

It should be noted that the weld material is highly loaded in shear locally due to the load transfer from the skin into the stringer. It constitutes another potential failure mode of the weld and cannot be incorporated in the yield load concept as required in defect assessment methods like the SINTAP procedure.

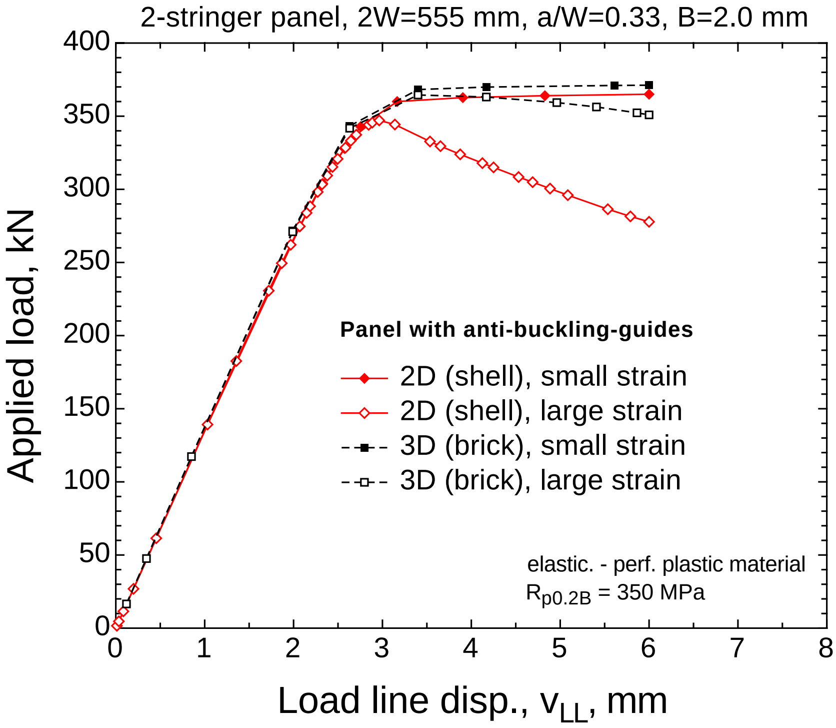

Figure 5.17: Comparison between 2D and 3D models along with the effect of small and large strain theories. Load-displacement curves are computed for a homogeneous 2-stringer panel, i.e. LBW joint is not modelled.

5.4 Concluding remarks

Detailed elastic and elastic-plastic FEA has been carried out in order to obtain the K-factor and yield load solution for cracked 2- and 3-stringer panels. The panels were modelled by linear shell elements (ABAQUS: S4R). Anti-buckling guides have been used in all analyses by prescribing the suitable displacement boundary conditions.

K-factors have been computed for the skin and stringer cracks in both 2- and 3-stringer panels. The approach used is based on the virtual crack closure integral method. If anti-buckling guides are used preventing any out-of-(skin)plane displacements, no differences have been observed between the small and large strain theories. The K-factor solutions necessary for the SINTAP analysis of the 2- and 3-stringer panels are given in **Figs. 5.9** and **5.10**, respectively.

The yield load solution has been provided as function of crack length for both 2- and 3-stringer panels. In the elastic-plastic regime, shell elements have shown an unrealistic necking if large strain theory is used, resulting in a load drop beyond net section yielding of the panel. FEA based on small strain theory is more appropriate. The plastic behaviour of the stiffened panel has been investigated with the 3D FE mesh. Softer LBW material has shown minor effect on the yield load of stiffened panels. The proposed yield load solution for the stiffened panels is (see Eq. (5.19)):

$$F_{\mathrm{Y}} = R_{\mathrm{p0.2}}\, A_{\mathrm{net}}.$$

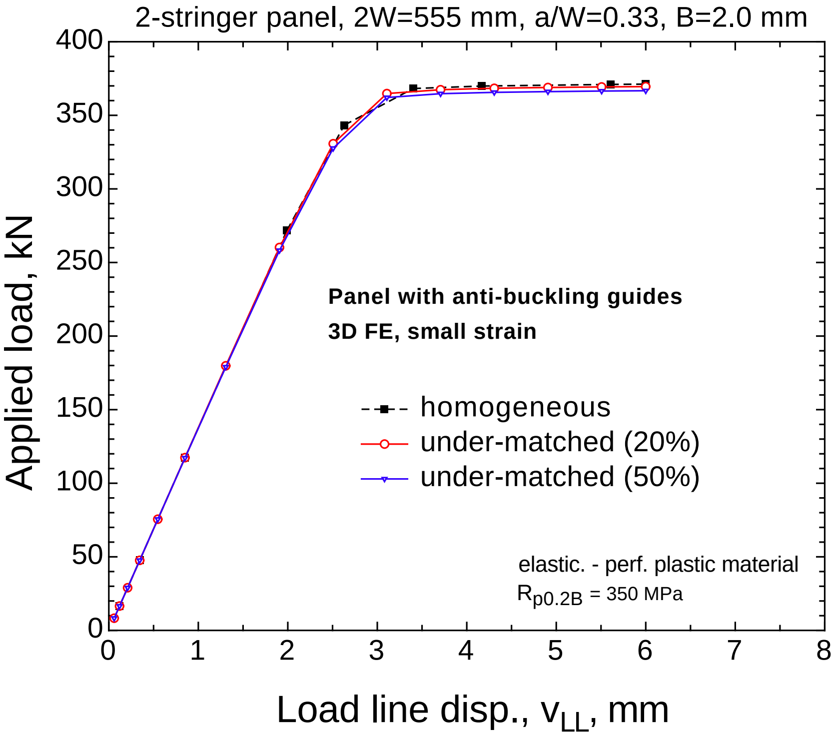

Figure 5.18: Effect of undermatching on computed load-displacement curves of a 2-stringer panel.

$R_{\mathrm{p0.2}}$ is the yield strength of the material. To ensure conservatism, the yield strength of the skin material is to be selected since it is slightly lower than that of the stringer material. A_{net} is the net section area of the stiffened panel, being the total uncracked cross-sectional area (see Eq. (5.20)):

$$A_{\mathrm{net}} = A_{\mathrm{net,sk}} + 2A_{\mathrm{net,str}}.$$

$A_{\mathrm{net,sk}}$ and $A_{\mathrm{net,str}}$ are net section areas of the skin and stringer, respectively. The factor 2 in the above equation stands for the number of uncracked or partly cracked (in case of crack branching) stringers. Note that Eq. (5.20) also holds for the 3-stringer panel as the central stringer is broken.

6 Residual strength prediction of unstiffened and stiffened panels

This section deals with the residual strength prediction of cracked unstiffened and stiffened panels using the SINTAP procedure. First, the residual strength analysis is carried out for the cracked LBW and FSW M(T) panels. Then, stiffened panels with a one-bay (2-stringer panels) and a two-bay (3-stringer panels) cracks are analyzed.

Both the material related (tensile and fracture resistance (R-curve) data in Section 4) and component related data (K-factor and yield load solutions for stiffened panels in Section 5) have been generated so that the validation of the SINTAP procedure can now be carried out.

6.1 Description of the analysis principle

The principle of the residual strength analysis with the SINTAP procedure is schematically shown in **Fig. 6.1**. The crack driving force (CDF) is plotted in one diagram together with the respective R-curve. CDF in terms of the stress intensity factor K_J is defined in Eq. (3.1), whereas CTOD δ_5 in Eq. (3.3), respectively. Throughout the entire analysis, the definition of CTOD δ_5 is used for the crack tip opening displacement δ.

The fracture parameter of CDF is specified by the available R-curve, i.e. if for instance the R-curve is measured in terms of CTOD δ_5, then CDF should also be determined using CTOD δ_5 as the crack tip parameter. The tangency condition between the R-curve and CDF gives the maximum load carrying capacity of the component under consideration. Since the SINTAP procedure requires an R-curve based on the physical crack length, the R-curve in terms of K_eff plotted versus the effective crack length, Δa_eff, has not been used.

At each intersection point between the R-curve and CDF (points "1" ... "4" in **Fig. 6.1**), the respective load together with the stable crack extension and the corresponding crack tip loading are found. By plotting the load versus stable crack extension or load versus crack tip loading, a structural response can be predicted. In this way, the validation of the analysis is not only based on the comparison of the predicted and experimental maximum load values, but also in terms of the load-deformation behaviour.

The experimental determination of the crack driving force in terms of K or J on an arbitrary structure generally requires a support of detailed numerical analyses. At this stage, the advantage of CTOD δ_5 as a crack driving parameter becomes clear, since it can be directly measured by means of an attached clip on any structure without calibration functions and/or being inferred from remotely applied loads. In all tests, CTOD δ_5 was recorded as a crack driving force so that the predicted structural response using the SINTAP procedure is compared with the experiments on the basis of this parameter.

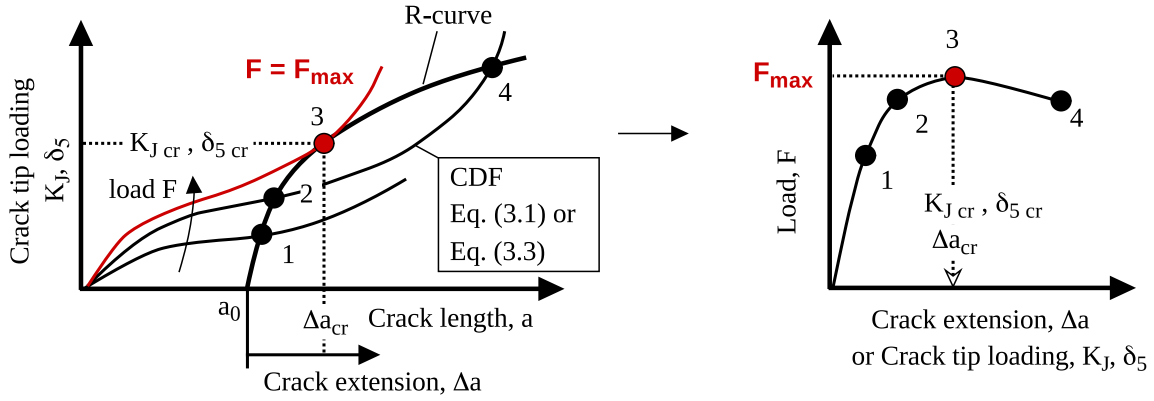

Figure 6.1: Principle of the residual strength analysis in the SINTAP procedure using the CDF approach.

6.2 Component related input data

This section summarizes the stress intensity factor and yield load solutions required for the residual strength analysis of cracked unstiffened (base material, LBW and FSW welded panels) and stiffened panels (2- and 3-stringer panels).

Unlike in the case of the unstiffened panels where the the K-factor and yield load solutions are uniquely defined, these parameters are subject to a variation in the residual strength prediction of the stiffened panels in order to check the sensitivity of the residual strength predictions to these input parameters. The different K-factor and yield load solutions will be varied as given in Sections 6.4.4 and 6.4.5, respectively, including the proposed K-factor and yield load solutions by FEA in Section 5.

6.2.1 K-factor solution

M(T) panels: base material, LBW and FSW

The K-factor solution for an M(T) panel is given by [84]:

$$K_{\mathrm{I}} = \sigma \sqrt{\pi a}\, \beta \left(\frac{a}{W} \right) \tag{6.1}$$

where

$$\sigma = \frac{F}{2W\, B^*} \tag{6.2}$$

is the applied stress and

$$\beta \left(\frac{a}{W} \right) = \sqrt{\sec \frac{\pi a}{2W}} \tag{6.3}$$

the geometry correction function due to the finite width. F is the externally applied load, a is the half crack length, W is the half width of the panel. B^* is the skin thickness of the crack location, i.e. $B^* = B = 2.0$ mm for the base material, $B^* = 2.6$ mm for the LBW panel, and $B^* = 2.2$ mm for the FSW panel.

The stress intensity factor describes the elastic stress state at the crack tip and is a function of specimen's geometry and not of the material. Therefore, the above solution is also valid for welded panels.

Stiffened panels

The K-factor solutions for both the skin crack and the stringer crack (stringer crack after crack branching only) in 2- and 3-stringer panels have been generated in Section 5. These solutions are used pointwise in the SINTAP analysis.

The K-factor for the skin crack is defined as:

$$K_{\mathrm{I\,sk}} = \sigma\sqrt{\pi a}\,\beta_{\mathrm{sk}}\left(\frac{a}{W}\right). \tag{6.4}$$

The geometry function $\beta_{\mathrm{sk}}\left(\frac{a}{W}\right)$ is defined in **Figs. 5.9** and **5.10** for the 2- and 3-stringer panels, respectively. The applied stress is defined as:

$$\sigma = \frac{F}{2W\,B} \tag{6.5}$$

where F is the applied load, $2W$ is the panel width, and $B = 2.0$ mm is the skin thickness.

The K-factor for the stringer crack is defined as:

$$K_{\mathrm{I\,str}} = \sigma\sqrt{\pi a}\,\beta_{\mathrm{str}}\left(\frac{a}{W}\right). \tag{6.6}$$

Note that a is the skin crack length. The geometry function $\beta_{\mathrm{str}}\left(\frac{a}{W}\right)$ is defined in **Fig. 5.9** and **5.10** for the 2- and 3-stringer panels, respectively. The applied stress is given in Eq. (6.5).

6.2.2 Yield load solution

M(T) panels: base material

The yield load solution, F_{YB}, for a homogeneous middle cracked M(T) panel under plane stress conditions is given by [123]:

$$F_{\mathrm{YB}} = 2R_{\mathrm{p0.2}}\,B(W-a) \tag{6.7}$$

where $R_{\mathrm{p0.2}}$ is the yield strength of the (base) material. B, W, and a are the thickness, half width, and half crack length of the panel, respectively.

M(T) panels: LBW and FSW

The mismatch yield load solution, F_{YM}, for a butt welded middle cracked M(T) panel with a highly undermatched weld so that the plastic deformation at the crack tip is entirely confined to the weld material is given by [31]:

$$\frac{F_{\text{YM}}}{F_{\text{YB}}} = \begin{cases} M & \text{for } 0 \leq \psi \leq 1.43 \\ M\left[\frac{2}{\sqrt{3}} - \left(\frac{2-\sqrt{3}}{\sqrt{3}}\right)\frac{1.43}{\psi}\right] & \text{for } \psi > 1.43 \end{cases} \tag{6.8}$$

where M is the weld strength mismatch ratio and

$$\psi = \frac{W-a}{H} \tag{6.9}$$

defines the ratio of the ligament length, $W-a$, to the weld width, $2H$.

Eq. (6.8) is graphically depicted in **Fig. 6.2** which also shows the yield load solution for an overmatched M(T) panel. The respective analytical equations for the weld strength overmatched butt joints are [31]:

$$\frac{F_{\text{YM}}}{F_{\text{YB}}} = \begin{cases} M & \text{for } \psi \leq \psi_1 \\ \frac{24(M-1)}{25}\frac{\psi_1}{\psi} + \frac{M+24}{25} & \text{for } \psi > \psi_1 \end{cases} \tag{6.10}$$

where

$$\psi_1 = \left(1 + 0.43\, e^{-5(M-1)}\right) e^{-(M-1)/5} \,. \tag{6.11}$$

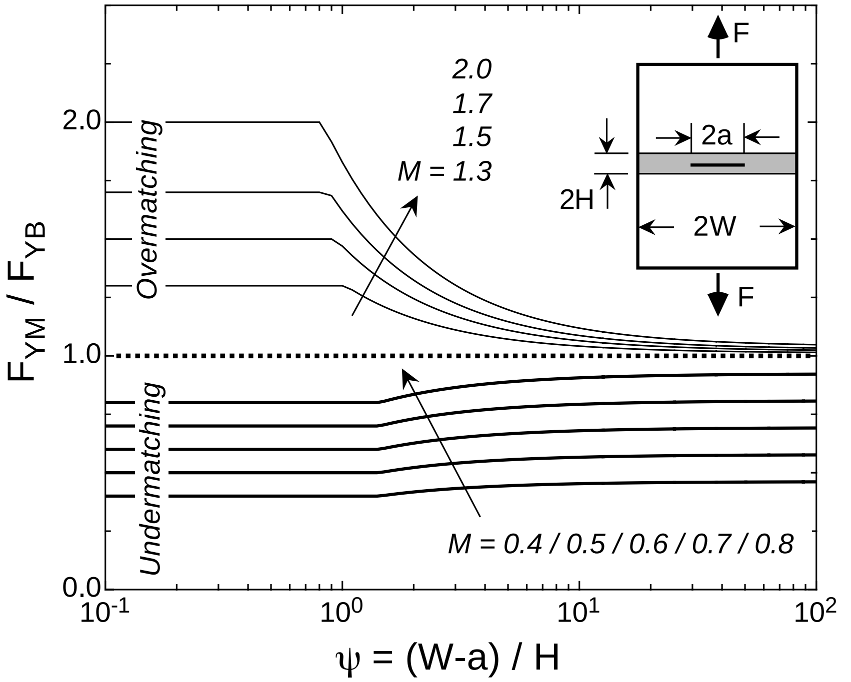

Figure 6.2: Mismatch yield load solution of a M(T) panel with a crack in the weld center [31].

Stiffened panels

A yield load solution for cracked 2- and 3-stringer panels has been proposed in Section 5, see Eq. (5.19):

$$F_\mathrm{Y} = R_\mathrm{p0.2}\ A_\mathrm{net}.$$

$R_\mathrm{p0.2}$ is the yield strength of the material. To ensure conservatism, the yield strength of the skin material has been selected since it is slightly lower than that of the stringer material. A_net is the net section area of the stiffened panel, being the total uncracked cross-sectional area, see Eq. (5.20):

$$A_\mathrm{net} = A_\mathrm{net,sk} + 2A_\mathrm{net,str}.$$

$A_\mathrm{net,sk}$ and $A_\mathrm{net,str}$ are net section areas of the skin and stringer, respectively. The factor 2 in the above equation stands for the number of uncracked or partly cracked (in case of crack branching) stringers. Note that Eq. (5.20) also holds for the 3-stringer panel as the central stringer is broken. The sensitivity of the SINTAP predictions to the yield load definition for the stiffened panels will be analyzed in Section 6.4.

6.3 Results of unstiffened panels

6.3.1 Base metal wide plates

Analysis levels 1 and 3 of the SINTAP procedure have been applied to the base material M(T) panels to predict their residual strength. These two levels enable a fracture assessment of cracked components made of a homogeneous material. The required material input parameters are tensile and fracture resistance properties. For the analysis level 1, yield and tensile strengths and for the analysis level 3, the complete true stress-strain curve of the material are needed. The fracture resistance is described by an R-curve in both analysis levels. The R-curve definition is based on two fracture controlling parameters, CTOD δ_5 and K_J, and can be equivalently used in the SINTAP procedure. All material related input information is summarized in **Tab. 6.1**.

The comparison between the SINTAP predictions and experimental results for the T-L orientation is shown in **Fig. 6.3** where the SINTAP analysis is based on the CTOD δ_5 R-curve and in **Fig. 6.4** where the SINTAP analysis is based on the K_J R-curve. Analogously, the comparison for the L-T orientation is given in **Figs. 6.5** and **6.6**. Regardless of the R-curve type, the maximum load as well as the deformation behaviour in terms of load-Δa and load-CTOD δ_5 curves are in a very good agreement with the measured values. Due to the very low hardening capacity of the base material almost approaching a perfectly plastic behaviour, the difference between the SINTAP analysis level 1 and level 3 is very small. The predicted maximum load in each analysis level is close to the yield load which is depicted by the dotted line in all graphs. The equivalence between the CDF and FAD approaches within the SINTAP procedure is demonstrated

Table 6.1: Material properties required as input information in the residual strength analysis of base material M(T) panels using SINTAP analysis levels 1 and 3.

SINTAP		tensile properties	fracture resistance
Level 1	T-L	$R_{\mathrm{p0.2}} = 360$ MPa $R_{\mathrm{m}} = 395$ MPa	*R-curve from C(T)50 and M(T)760:* $\delta_5 = 0.28\,(\Delta a)^{0.63}$ *R-curve from M(T)760:* $K_{\mathrm{J}} = 79.27\,(\Delta a)^{0.32}$
	L-T	$R_{\mathrm{p0.2}} = 385$ MPa $R_{\mathrm{m}} = 400$ MPa	*R-curve from C(T)50 and M(T)760:* $\delta_5 = 0.30\,(\Delta a)^{0.63}$ *R-curve from M(T)760:* $K_{\mathrm{J}} = 76.03\,(\Delta a)^{0.34}$
Level 3	T-L	full true stress-strain curve	same as in Level 1
	L-T	full true stress-strain curve	same as in Level 1

on the M(T) base material panels. In **Figs. A.9** and **A.10** this equivalence is shown for the T-L orientation for the analysis levels 1 and 3, respectively, and in **Figs. A.11** and **A.12** for the L-T orientation. This equivalence is also valid for the SINTAP analysis level 2 (mismatch) and, therefore, only the CDF approach will be used throughout this thesis.

The correlation between K_{J} and CTOD δ_5 when estimating the crack driving force in the SINTAP procedure is governed by:

$$\delta_5 = \frac{K_{\mathrm{J}}^2}{m\, R_{\mathrm{p0.2}}\, E} \qquad \text{with} \qquad m = 1.0 \qquad \text{for BM}\ . \tag{6.12}$$

The above relationship is the only link between these two fracture parameters in the SINTAP procedure so that the SINTAP route must give very similar predictions provided the relationship in Eq. (6.12) is also valid for the respective R-curves. **Fig. 6.7** shows this R-curve relationship between K_{J}^2/E (E is Young's modulus) and CTOD δ_5 for both T-L and L-T orientations. It remains linear over the entire range of the measured stable crack extension in M(T)760 panels. For the T-L orientation, the proportionality factor is $0.97R_{\mathrm{p0.2}}^{\mathrm{T-L}}$ which corresponds to $m = 0.97$ in Eq. (6.12), whereas $m = 0.84$ is obtained for the L-T orientation. Due to the small deviation from $m = 1.0$ as used on the applied side, the predicted SINTAP curves based on the CTOD δ_5 R-curve are slightly higher than those based on the K_{J} R-curve, **Fig. 6.8**.

It should be noted that the R-curves used in the SINTAP analysis of cracked base material panels have been measured on the same panels. In this way the transferability problem of R-curves from one specimen geometry to another is solved per se. As all other input parameters on the material side (tensile properties) as well as on the applied side (yield load and K-factor solutions) are uniquely defined with sufficient accuracy, these results of base material panels can be regarded as a proof of the ability of the SINTAP procedure to estimate the crack tip loading in a cracked thin sheet using the set of equations given in analysis levels 1 and 3. The predicted crack driving force in terms of CTOD δ_5 agrees very well with the measured values providing confidence in the application of the SINTAP route to more complex structures like stiffened panels. The residual strength analysis of stiffened panels using SINTAP analysis levels 1 and 3 will be presented in a subsequent section.

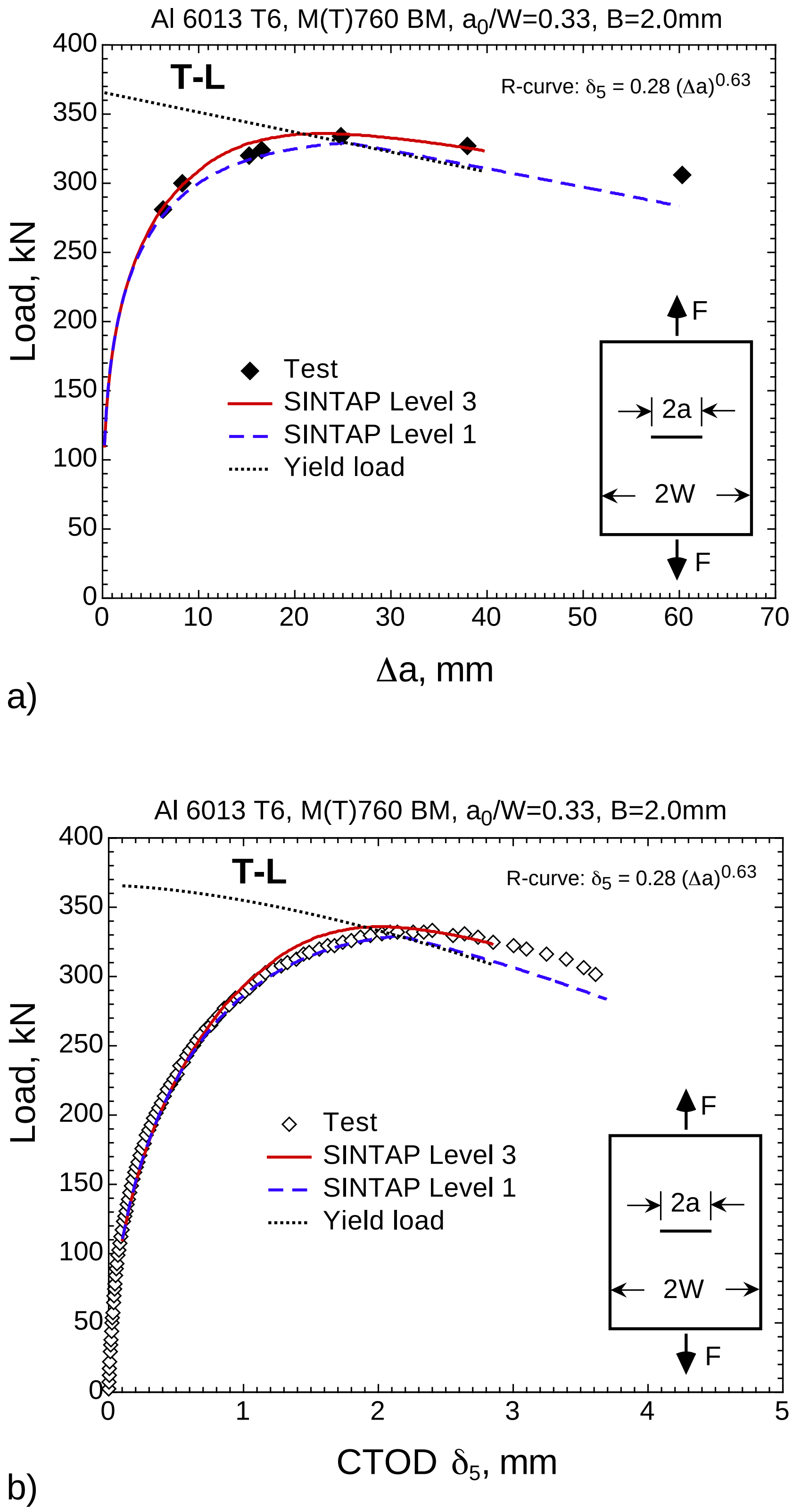

Figure 6.3: Comparison between SINTAP predictions and experimental results for the base material panels in T-L orientation. Analysis is based on the CTOD δ_5 R-curve. a) load-Δa curve; b) load-CTOD δ_5 curve.

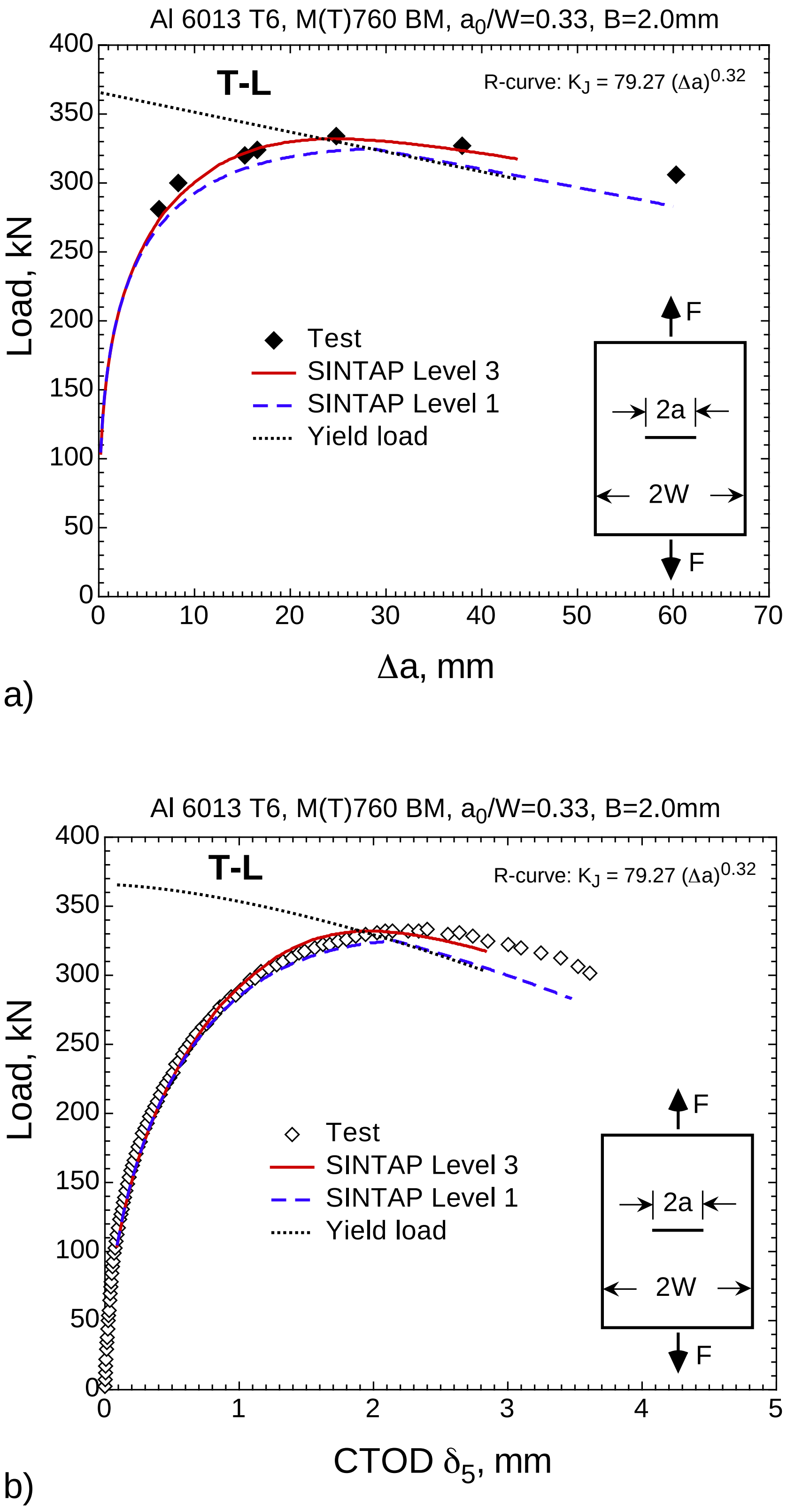

Figure 6.4: Comparison between SINTAP predictions and experimental results for the base material panels in T-L orientation. Analysis is based on the K_J R-curve. a) load-Δa curve; b) load-CTOD δ_5 curve.

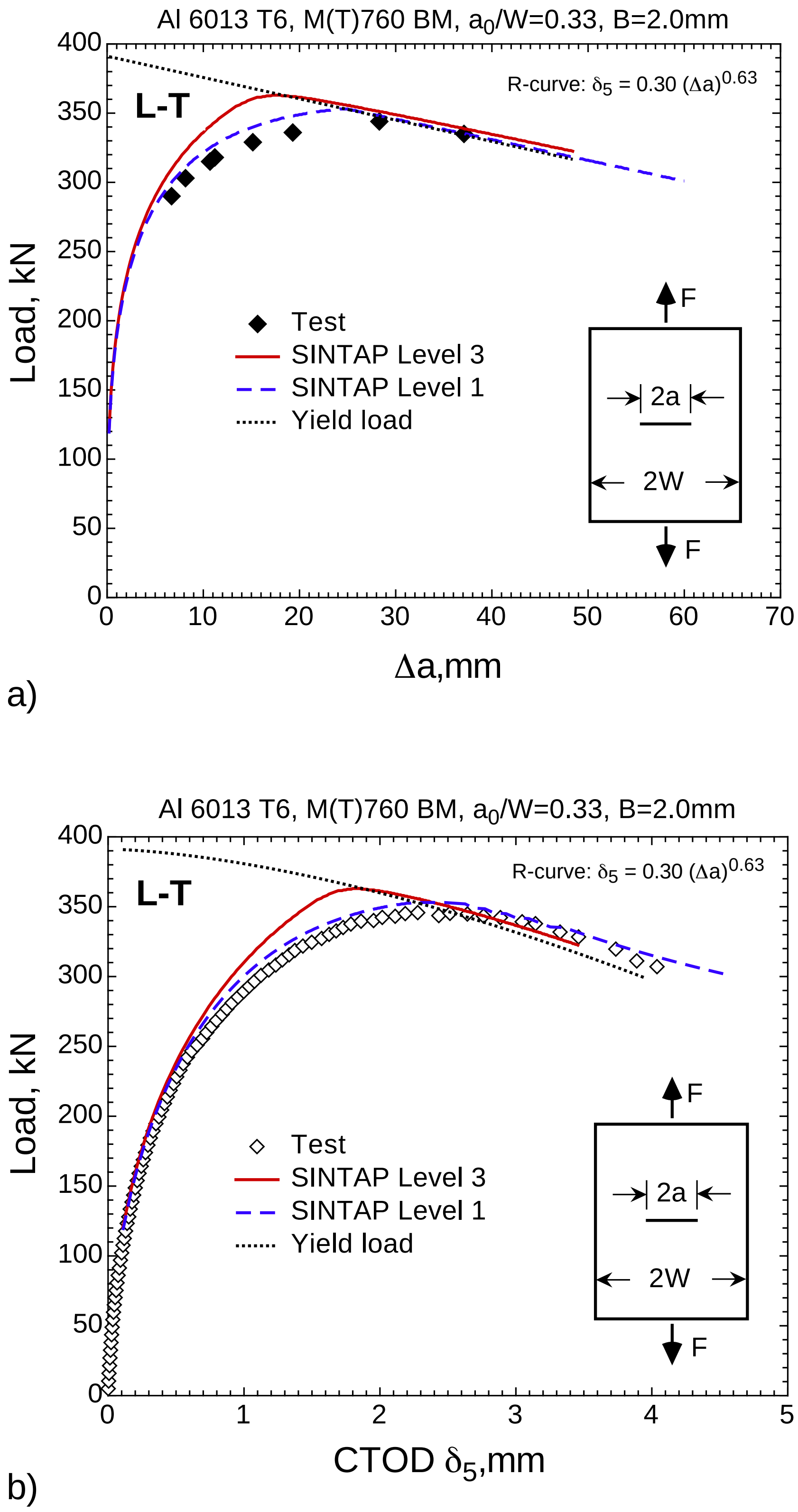

Figure 6.5: Comparison between SINTAP predictions and experimental results for the base material panels in L-T orientation. Analysis is based on the CTOD δ_5 R-curve. a) load-Δa curve; b) load-CTOD δ_5 curve.

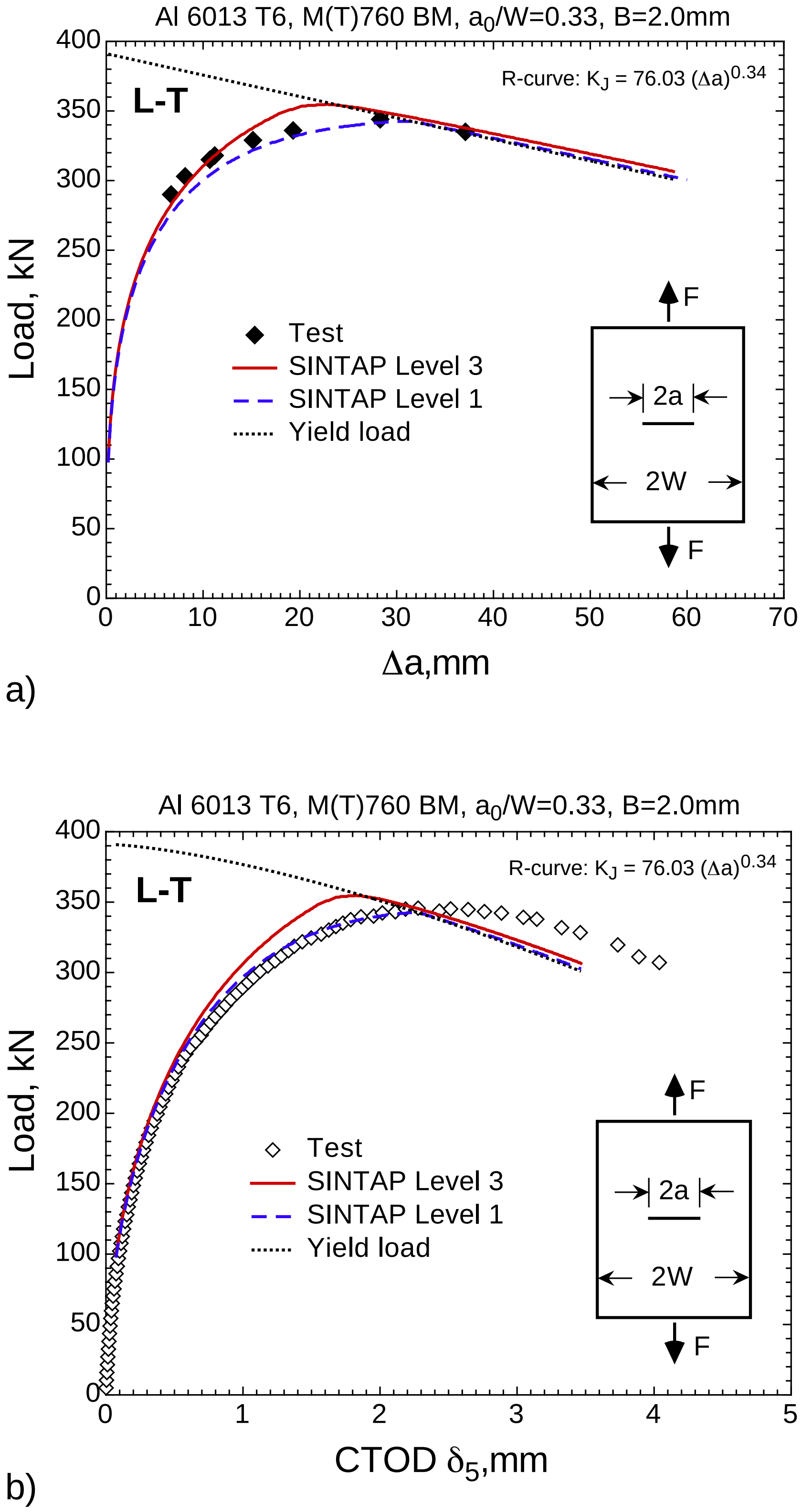

Figure 6.6: Comparison between SINTAP predictions and experimental results for the base material panels in L-T orientation. Analysis is based on the K_J R-curve. a) load-Δa curve; b) load-CTOD δ_5 curve.

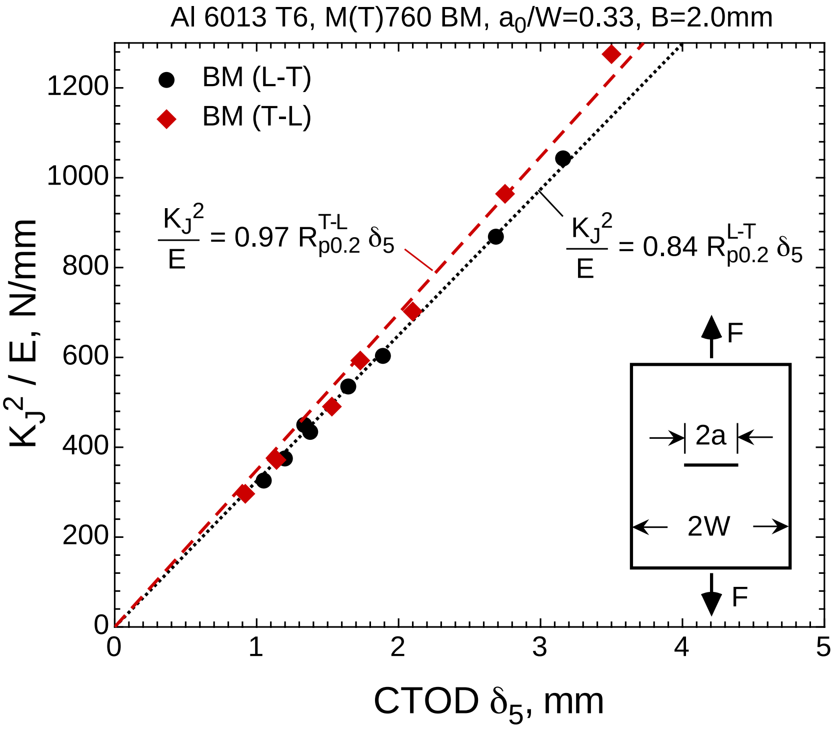

Figure 6.7: Relationship between K_J^2/E and CTOD δ_5 of the base material panels in L-T and T-L orientations.

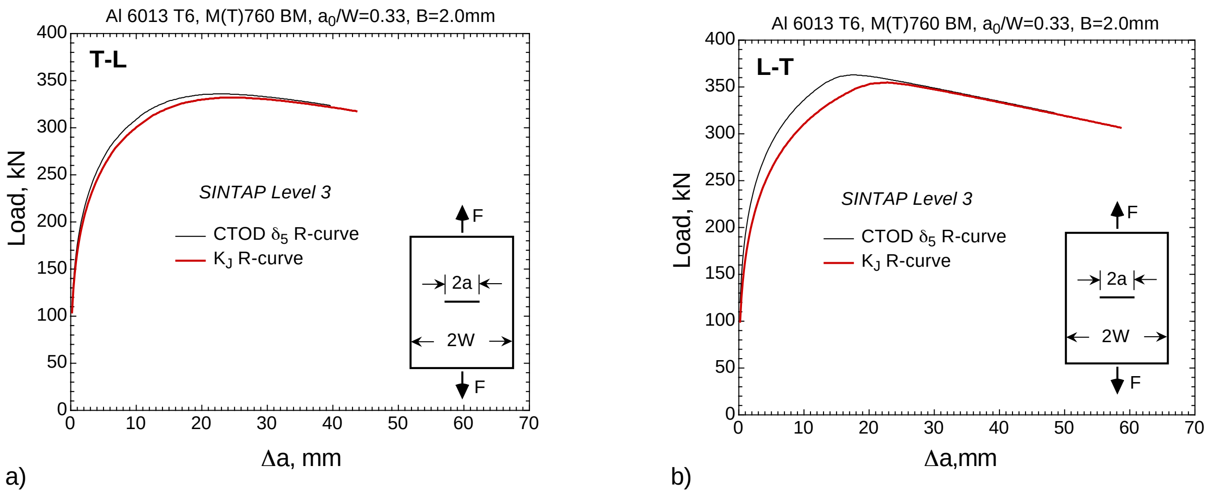

Figure 6.8: Comparison of the SINTAP predictions (level 3) showing the effect of R-curves used in the analysis of the base material panels in a) T-L and b) L-T orientations.

6.3.2 LBW wide plates

The mismatch option of the SINTAP procedure (analysis level 2) was applied to LBW M(T) panels in order to predict their maximum load carrying capacity. The component related data such as the K-factor and yield load solutions for a butt-welded panel are available in closed form and can be found in the literature (eg. [31, 84, 123]), see Section 6.2.

The material related input data such as yield and tensile strengths of both base and LBW materials as well as the R-curve of the LBW joint were determined experimentally (see Section 4) and are summarized in **Tab. 6.2**.

Table 6.2: Material properties required as input information in the residual strength analysis of LBW M(T) panels using SINTAP level 2 (mismatch).

SINTAP	tensile properties	fracture resistance
Level 2 (mismatch)	*BM (standard specimens):* $R_{\mathrm{p0.2B}} = 360$ MPa $R_{\mathrm{mB}} = 395$ MPa *LBW (micro-flat specimens):* $R_{\mathrm{p0.2W}} = 145$ MPa $R_{\mathrm{mW}} = 165$ MPa	*R-curve from LBW C(T)50:* $\delta_5 = 0.226\,(\Delta a)^{0.695}$

Tensile properties of the base material were obtained from standard tensile specimens, whereas those of the LBW material were obtained from micro-flat tensile specimens. The fracture resistance in terms of the CTOD δ_5 R-curve was obtained from C(T) specimens with a width of $W = 50$ mm and an initial crack length-to-width ratio of $a_0/W = 0.5$ using the multiple specimens technique. A power law curve fit through all LBW C(T)50 specimens tested resulted in a function given in **Tab. 6.2**.

Fig. 6.9 a) shows the CDF approach of the SINTAP procedure applied to the cracked LBW panels. The tangency condition is met at a load level of 216 kN which is in very good agreement with the experimental failure load. Also the predicted critical stable crack extension of 6 mm (at tangency point) is close to that observed in the experiments, being in the range of 4-6 mm. It should be noted the the instability point was reached within the range of the R-curve that was covered during the R-curve determination with C(T)50 specimens.

Fig. 6.9 b) shows the comparison of the experimental load-CTOD δ_5 curve with the SINTAP predictions together with the variation of the parameter m. The dotted line indicates the mismatch yield load level, F_{YM}, according to Eq. (6.8). To obtain a mismatch yield load vs. CTOD δ_5 relationship, the stable crack extension, Δa, and CTOD δ_5 are correlated through the respective R-curve.

The load carrying capability, F_{TS}, of the cracked LBW M(T) panel is reached if the net section stress attains the tensile strength of the LBW joint:

$$F_{\mathrm{TS}} = 2R_{\mathrm{m}}\, B^*(W - a) \tag{6.13}$$

where R_{m} is the tensile strength of the LBW joint obtained from standard transverse flat tensile specimens (LBW joint: $R_{\mathrm{m}} = 290$ MPa), $B^* = 2.6$ mm is the panel thickness of the weld location.

The mismatch yield load and load carrying capability levels of the cracked panels provide information on the stress state in the uncracked ligament. The yield load indicates the load level at which the entire uncracked ligament yields and the application of LEFM is no longer valid. The upper bound is given by the load carrying capability level, F_{TS}, at which the net section stress in the uncracked ligament attains the tensile strength of the material or weld joint. In the present case, the failure of the LBW panel occurred above the yield load indicating an elastic-plastic regime but far below the tensile strength of the LBW joint giving rise to failure caused by a critical crack tip condition and not by plastic collapse.

The variation of the parameter m shows that for larger m, the predicted load-CTOD δ_5 curve becomes stiffer, reaching its maximum at smaller CTOD δ_5 values. For $m = 2.0$, the SINTAP prediction is in good agreement with the experimental failure load as well as the deformation behaviour in terms of the load-CTOD δ_5 curve. The parameter m is intended to quantify the constraint at the crack tip. Larger m reflects a larger constraint at the crack tip which requires higher loads to be applied to the structural component or specimen in order to reach the same crack tip opening displacement. Based on this observation, the value $m = 2.0$ is proposed for the residual strength analysis of LBW welded panels.

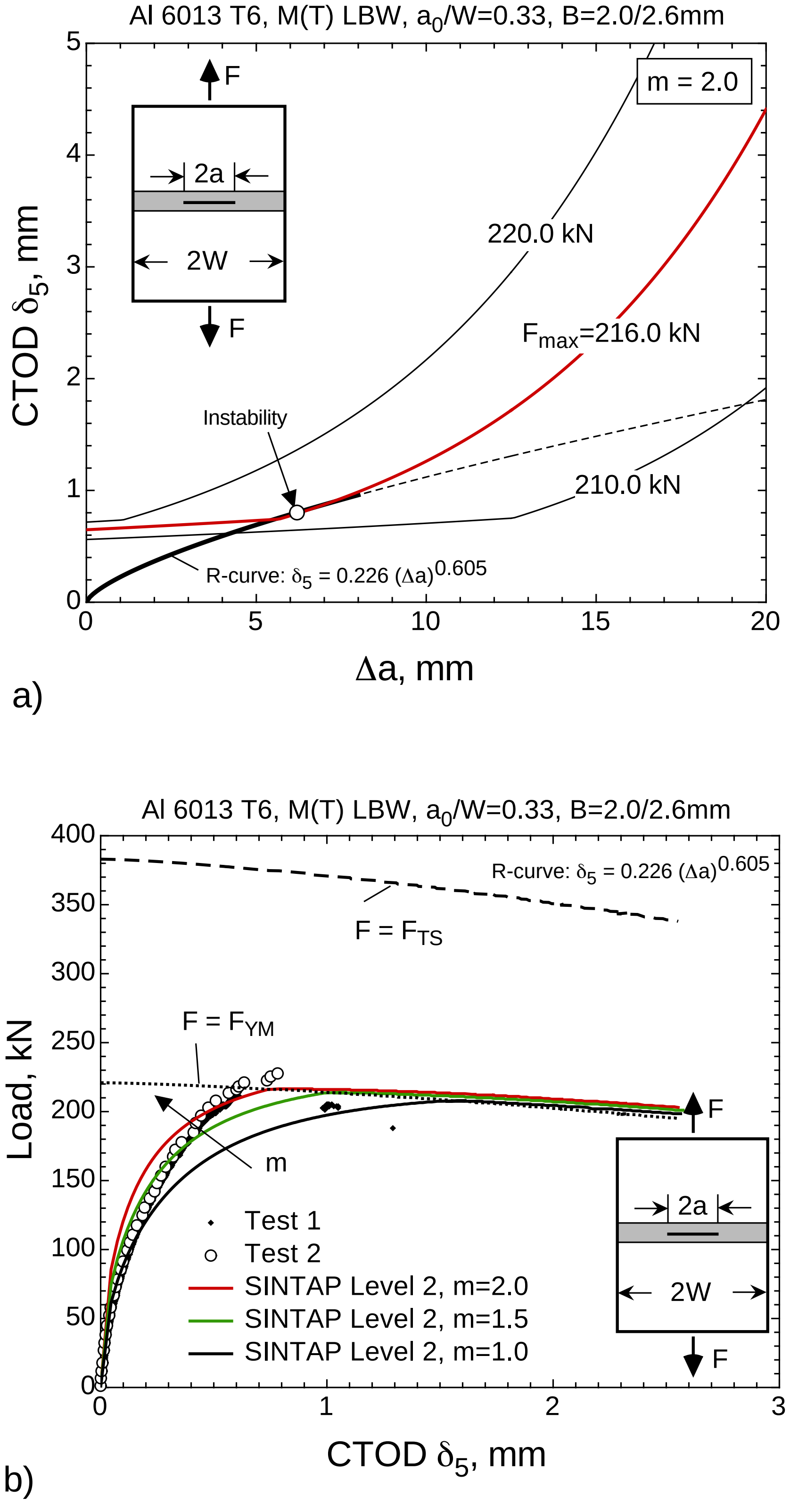

Figure 6.9: SINTAP prediction of the residual strength of LBW M(T) panels. a) CDF approach showing the tangency condition (instability) at the maximum load (m=2.0); b) comparison between the experimental load-CTOD δ_5 curves and the SINTAP predictions including the variation of the parameter m.

6.3.3 FSW wide plates

Two types of M(T) panels containing an FSW joint were investigated: one with a crack located in the nugget area along the weld centerline and the other with a crack in TMAZ, being the softest region of the FSW joint. Both types of M(T) panels experienced unstable fracture prior to developing a clear maximum in the load-displacement record during the displacement controlled loading. More details on the fracture behaviour are given in Section 4.

The necessary material input information for the application of the SINTAP analysis level 2 (mismatch) in order to predict the residual strength of these M(T) panels are given in **Tab. 6.3**.

For the FSW M(T) panel with a crack in the nugget area, the tangency condition between the crack driving force and the R-curve is met at a critical load of $F = 239$ kN which is 21% lower than the experimental maximum load (**Fig. 6.10** a)). Note that the instability point is within the R-curve range covered in the fracture toughness tests. The size of small C(T) specimens ($W = 50$ mm) that has been used for the R-curve determination of the FSW nugget material is, therefore, sufficient. This R-curve part is represented by the thick solid line whereas the dashed line is an extrapolation based on the curve fit equation given in the same figure.

Table 6.3: Material properties required as input information in the residual strength analysis of FSW M(T) panels using SINTAP level 2 (mismatch).

SINTAP	tensile properties	fracture resistance
Level 2	*BM (standard specimens):* $R_{\mathrm{p0.2B}} = 360$ MPa $R_{\mathrm{mB}} = 395$ MPa *FSW (micro-flat specimens):* $R_{\mathrm{p0.2W}} = 185$ MPa $R_{\mathrm{mW}} = 295$ MPa	*R-curve from FSW C(T)50:* $\delta_5 = 0.618\,(\Delta a)^{0.548}$ (nugget crack) $\delta_5 = 0.400\,(\Delta a)^{0.645}$ (TMAZ crack)

The comparison between the SINTAP predictions and the experimental results in terms of load-CTOD δ_5 is depicted in **Fig. 6.10** b) along with the variation of the parameter m. The higher the value of m, the stiffer is the prediction of the structural response. For $m = 2.0$ the maximum load prediction is less conservative and the deformation behaviour is predicted more accurately.

The relatively high conservatism may be attributed to the failure mode of the panel. Recall that the crack in this plate stably grew along the weld centerline and finally deviated into softer TMAZ during the unstable fracture. The net section stress reached the tensile strength of the FSW joint as indicated by the dashed line in **Fig. 6.10** b) which represents the load carrying capability, F_{TS}:

$$F_{\mathrm{TS}} = 2R_{\mathrm{m}}\,B^{*}(W - a). \tag{6.14}$$

R_{m} is the tensile strength of the FSW joint obtained from standard transverse flat tensile specimens (FSW joint: $R_{\mathrm{m}} = 285$ MPa), and $B^{*} = 2.2$ mm is the panel thickness of the weld location. Thus, the panel failure was governed by the plastic collapse and not by the critical crack tip condition. In the SINTAP procedure, the plastic collapse limit is defined through $L_{\mathrm{r\,max}}$ and, for the sake of conservative predictions, is based on the flow stress definition. Hence, it defines a lower stress state in the uncracked ligament than the tensile strength of the weld joint or material. Therefore, the observed behaviour of this FSW panel can be at best, i.e. least conservative, predicted by plastic collapse. However, the SINTAP analysis predicted a critical load due to the unstable crack growth prior to reaching the plastic collapse limit defined in the SINTAP procedure. This increases the conservatism of the prediction.

The second type of the FSW M(T) panels with the crack in the softest region of the FSW joint (TMAZ) failed at a lower load level as that with a crack in the nugget area. The tensile properties of the weld material are the same as in the analysis of the nugget crack. The softest TMAZ region is very narrow so that no micro-flat tensile specimens could be extracted wholly made of the material from that weld region. However, to be on the conservative side, the lowest tensile properties that could be obtained from tensile testing of the FSW weld material have been used in the SINTAP analysis as given in **Tab. 6.3**.

The fracture resistance was obtained from C(T)50 specimens with the crack location in TMAZ of the FSW joint.

The maximum load is predicted at $F = 235.5$ kN which is 9.5% lower than the experimental value (**Fig. 6.11**a)). The instability point lies on the part of the R-curve that was covered in the fracture toughness tests. C(T)50 specimens were, therefore, of sufficient size for the R-curve determination in order to predict the fracture behaviour of large M(T) panels.

The comparison between the predicted and measured load-CTOD δ_5 curves is shown in **Fig. 6.11**b) including the variation of the parameter m. Since the same yield strength of the weld material and tensile strength of the FSW joint are used as in the case of the nugget crack, the yield load and load carrying capability (F_{TS} as defined in Eq. (6.14)) levels are identical to those in the analysis of the nugget crack. Since the experimental maximum load lies between the yield load and the load carrying capability levels, the panel failure is governed by the critical stress intensity in the elastic-plastic regime. For $m = 2.0$, the maximum load prediction is least conservative and the predicted load-CTOD δ_5 curve is in good agreement with the experimental one.

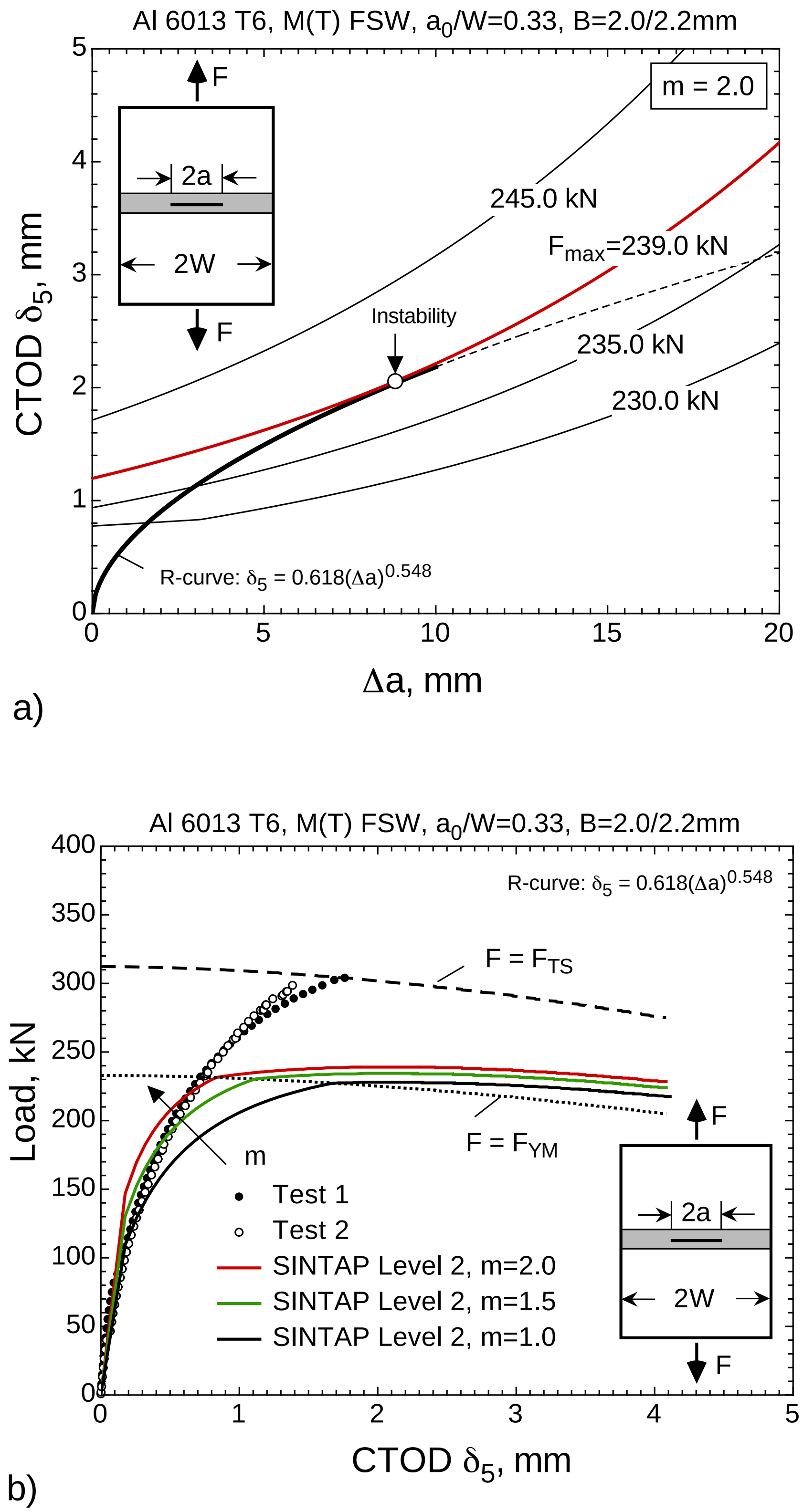

Figure 6.10: SINTAP prediction of the residual strength of FSW M(T) panels with a crack located in the nugget area along the weld centerline. a) CDF approach showing the tangency condition (instability) at the maximum load (m=2.0); b) comparison between the predicted and experimental load-CTOD δ_5 curves along with the variation of the parameter m.

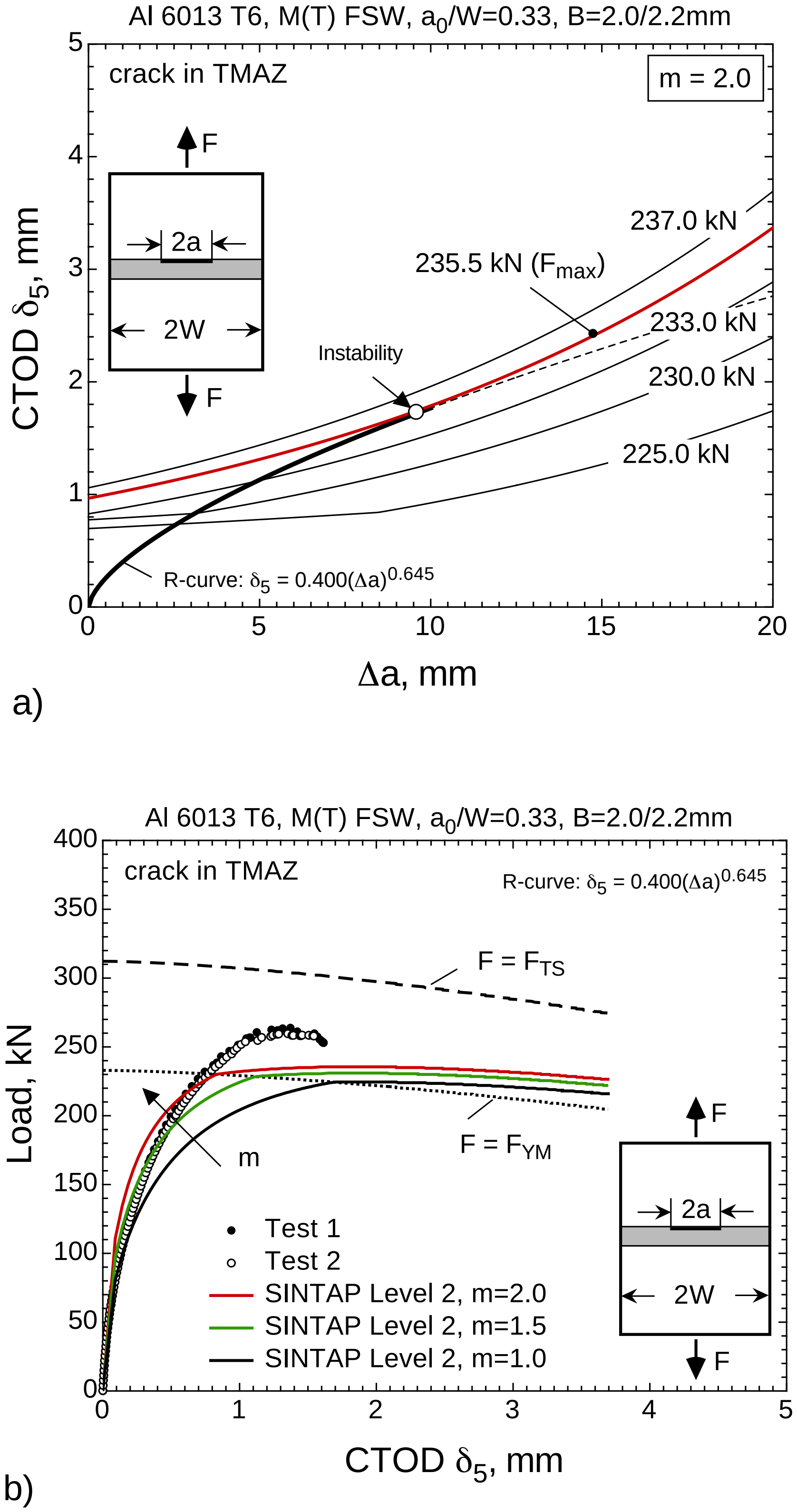

Figure 6.11: SINTAP prediction of the residual strength of FSW M(T) panels with a crack located in TMAZ. a) CDF approach showing the tangency condition (instability) at the maximum load (m=2.0); b) comparison between the predicted and experimental load-CTOD δ_5 curves including the variation of the parameter m.

6.3.4 Sensitivity analysis

The sensitivity analysis has been carried out for the LBW panel only. However, the effect of the varied parameters is transferable to both FSW panels (crack in the nugget area and TMAZ). The sensitivity has been checked for the following input parameters:

- weld width, $2H$,
- yield strength of the weld material, $R_{\mathrm{p0.2W}}$, and
- strain hardening exponent of the weld material, N_{W}.

These parameters are important input data to the SINTAP procedure; however, they are difficult to determine and/or lack a unique definition.

Effect of weld width, $2H$

The weld width, $2H$, is not uniquely defined. It is not clear whether only the weld material or also HAZ should be included in the definition of the weld width. In the case of undermatched welds, the plastic deformation is confined to the region which has a lower hardness than the base material, as has been shown by the optical strain measurement in Section 4.4. This suggests to include HAZ in the definition of $2H$. In a general case of strength undermatched welds, the entire region which exhibits a lower hardness as the base material should be taken as the weld width and is to be determined from the hardness profile.

The effect of the variation of the weld width, $2H$, on the SINTAP predictions is demonstrated in **Fig. 6.12**. The value of $2H = 3$ mm corresponds to the width of the weld material only which can be simply measured at the surface of the LBW joint. When including HAZ, the weld width results in $2H = 6$ mm. The predicted load-CTOD δ_5 curves are identical despite an increase of the weld width up to $2H = 8$ mm. Although the weld width is expected to be a sensitive parameter regarding the restraint plastic flow of the weld material at the crack tip, the weld width has apparently no effect on the crack driving force in the SINTAP analysis. Indeed, $2H$ only occurs in the yield load solution hidden in the parameter $\psi = (W - a)/H$. However, for large values of ψ, i.e. a long uncracked ligament and/or a narrow weld, the yield load solution becomes insensitive to ψ and, hence, to $2H$. From Eq. (6.8) it follows that [31]:

$$\frac{F_{\mathrm{YM}}}{F_{\mathrm{YB}}} = M\left[\frac{2}{\sqrt{3}} - \left(\frac{2-\sqrt{3}}{\sqrt{3}}\right)\frac{1.43}{\psi}\right] \quad \longrightarrow \quad \frac{2}{\sqrt{3}}M \qquad \text{for large } \psi. \tag{6.15}$$

In the present analysis, the ψ values reach large values ($\psi_{\mathrm{LBW}} \approx 85$ and $\psi_{\mathrm{FSW}} \approx 25$) where the yield load solution hardly changes with ψ as shown in **Fig. 6.2**. **Fig. 6.12** also shows the mismatch yield load solution, F_{YM}, where different $2H$ values display a negligibly small effect.

Effect of weld metal yield strength, $R_{\mathrm{p0.2W}}$

In Section 4, different approaches to the determination of the weld metal tensile properties have been presented. One technique is based on the standard transverse flat tensile, the other on the micro-flat tensile specimens. The tensile properties of the LBW material used to analyze their effect on the SINTAP predictions are summarized in **Tab. 6.4**.

Table 6.4: Variation of the LBW yield strength, $R_{\mathrm{p0.2W}}$, in the sensitivity analysis.

tensile specimen type	$R_{\mathrm{p0.2W}}$ MPa	R_{mW} MPa	difference of $R_{\mathrm{p0.2W}}$ %	predicted max. load kN	difference of pred. max. load %
micro-flat	145	165		216	
standard	175	290	**+21**	265	**+23**

The effect of these input parameters on the residual strength prediction is displayed in **Fig. 6.13** where all other input parameters were kept constant. The SINTAP analysis based on the higher strength values from the standard transverse specimens overestimates the experimental residual strength of the cracked LBW panel by $\sim 20\%$. The higher yield strength of the weld material increases the yield load of the cracked panel through the mismatch ratio M. The predicted maximum load is close to the yield load of the LBW panel. This leads to the conclusion that the SINTAP prediction of the residual strength is sensitive to the LBW material yield strength. An increase of the LBW yield strength from 145 MPa to 175 MPa (+21%) resulted in an increase of the predicted residual strength from 216 kN to 265 kN (+23%) indicating an almost linear relationship between the weld metal yield strength and the predicted residual strength. It should be mentioned that the variation of the weld metal yield strength using the tensile properties of the different specimens (micro-flat and standard) implied the variation of the tensile strength. This effect is addressed in the subsequent section through the variation of the strain hardening exponent of the weld metal.

Effect of weld metal strain hardening exponent, N_{W}

It should be noted that when taking the weld metal tensile properties from micro-flat and standard transverse specimens, the strain hardening exponent also changes. The strain hardening exponent, N_{W}, is a mandatory parameter in the SINTAP procedure entering the analysis indirectly through the estimation from the yield-to-tensile strength ratio. In the SINTAP procedure, the strain hardening exponent exerts influence on the crack driving force only if the applied load exceeds the yield load. Different N_{W} values were obtained by keeping the LBW yield strength constant while changing the tensile

Table 6.5: Variation of the strain hardening exponent, N_W, of the weld material (LBW) in the sensitivity analysis.

$R_\mathrm{p0.2}^\mathrm{LBW}$ MPa	$R_\mathrm{m}^\mathrm{LBW}$ MPa	N_W^* –	difference of N_W %	predicted max. load kN	difference of pred. max. load %
145	165	0.036		216	
145	185	0.065	**+78**	217	**+0.46**
145	205	0.088	**+141**	218	**+0.93**
145	240	0.119	**+227**	219	**+1.39**

*) $= 0.3\left(1 - \frac{R_\mathrm{p0.2}^\mathrm{LBW}}{R_\mathrm{m}^\mathrm{LBW}}\right)$, see Eq. (3.16)

strength of the weld material. The variation is given in **Tab. 6.5**. The effect of the variation of N_W on the SINTAP residual strength prediction for the LBW M(T) panels is depicted in **Fig. 6.14**. For larger N_W, the tangency point moves upwards along the R-curve so that the instability event is predicted at larger crack extensions, **Fig. 6.14**a). Note that the instability for higher N_W values lies on the R-curve part which has been extrapolated (indicated by the dashed line) by the power law fit equation beyond the R-curve range covered in the fracture toughness tests (indicated by the thick solid line). However, assuming that the R-curve will not experience a sharp kink, the variation of N_W for the LBW material does not significantly affect the prediction of the maximum load as shown in **Fig. 6.14**b). It can also be seen that the predicted load-CTOD δ_5 curves are identical below the mismatch yield load of the LBW M(T) panel and the effect of different N_W values becomes only relevant if the applied load is above the mismatch yield load. Despite a large variation of N_W, the predicted maximum load levels are hardly affected (see also **Tab. 6.5**).

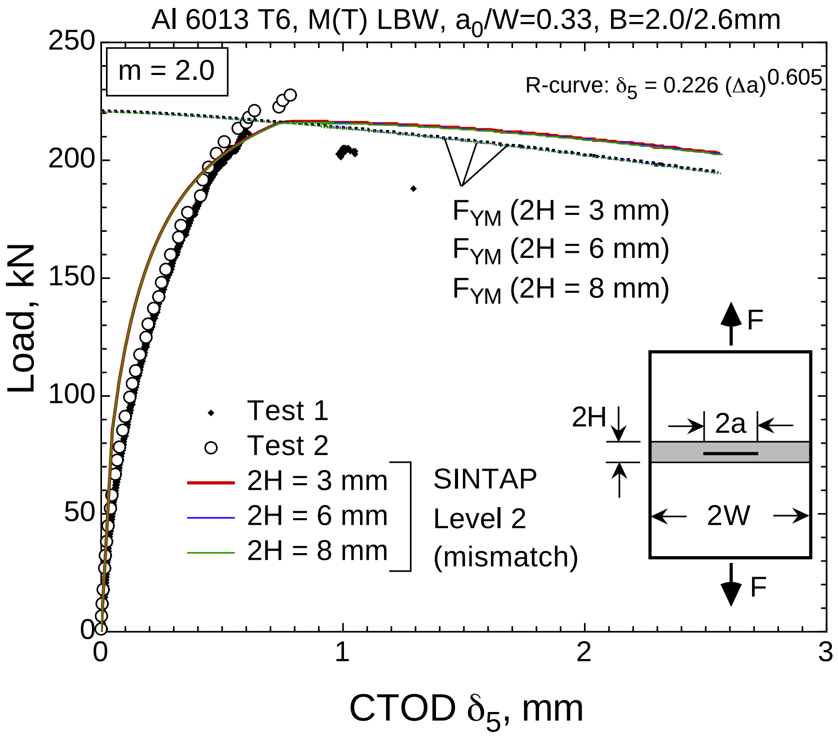

Figure 6.12: Effect of the weld width, $2H$, on the SINTAP prediction shown for the LBW M(T) panels.

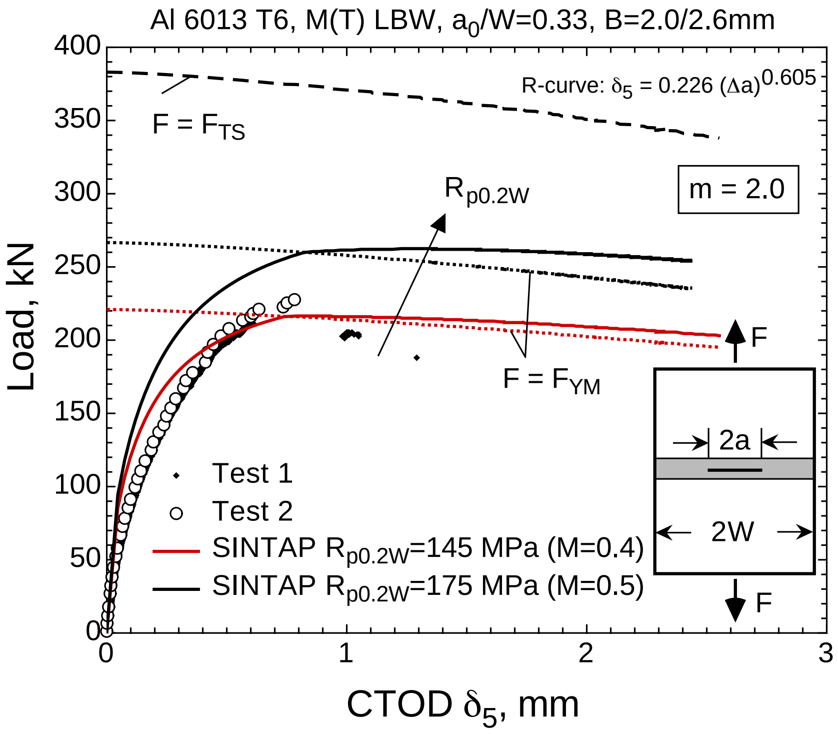

Figure 6.13: Effect of the weld metal yield strength, $R_{\mathrm{p0.2W}}$, on the SINTAP level 2 (mismatch) prediction shown for the LBW M(T) panels. In the SINTAP analysis, tensile properties were taken from micro-flat (lower load-CTOD δ_5 curve) and standard transverse flat tensile specimens (higher, i.e. over-estimated, load-CTOD δ_5 curve).

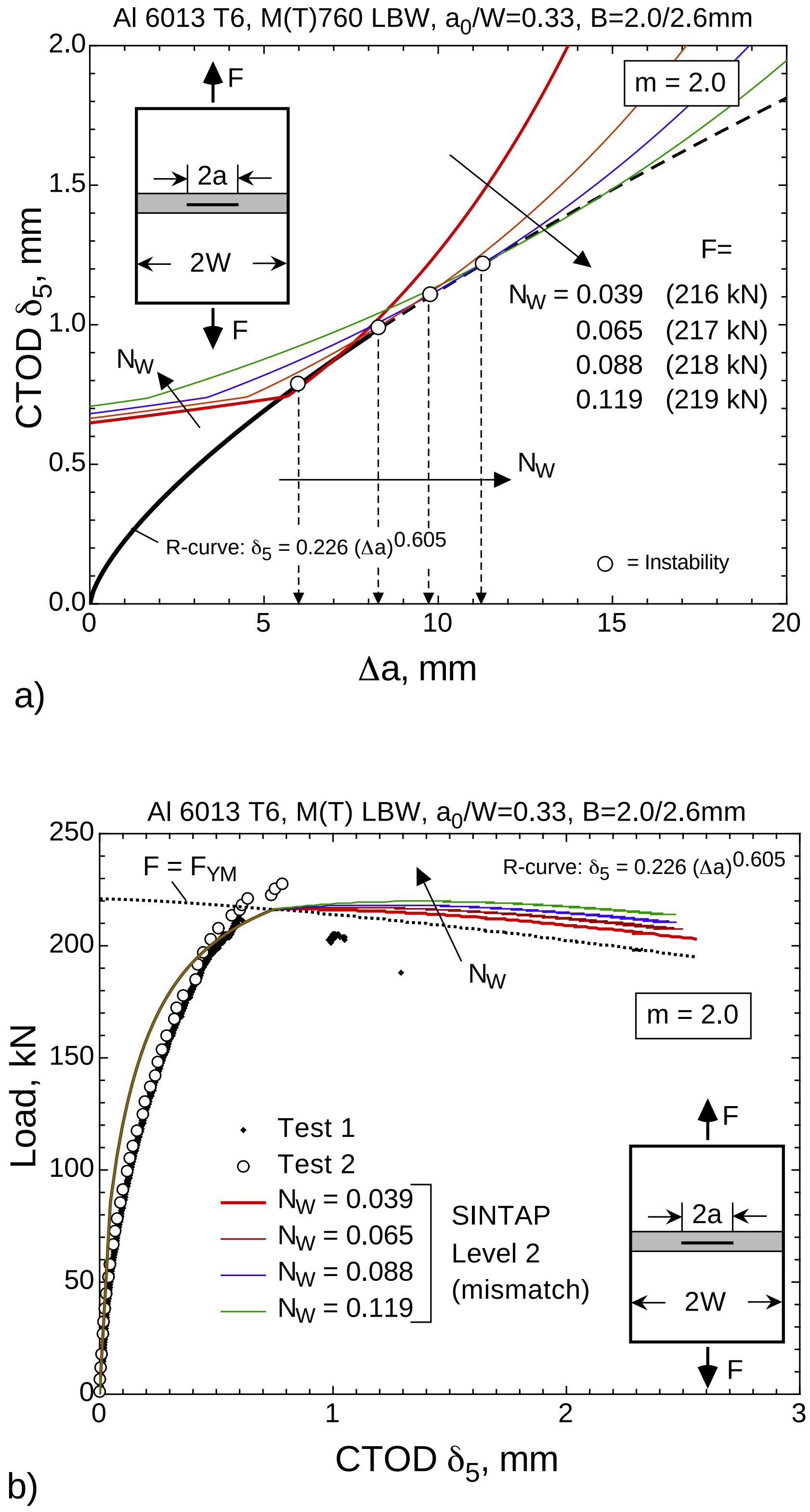

Figure 6.14: Effect of the variation of the strain hardening exponent, N_W, on the SINTAP residual strength prediction of the LBW M(T) panels. a) CDF approach showing the tangency condition (instability) at the maximum load (m=2.0); b) comparison between the experimental load-CTOD δ_5 curves and SINTAP predictions.

6.3.5 Summary

The accuracy of the residual strength predictions of the unstiffened panels using the SINTAP procedure is shown in **Fig. 6.15**. The maximum load of LBW and FSW (with a crack in TMAZ) panels is estimated fairly accurately using the mismatch option (level 2), whereas the maximum load prediction of the FSW panel with a crack in the nugget area shows a higher conservatism (-21%). The residual strength prediction of the base material panels is accurate within the range of -2% and +5% using analysis levels 1 and 3.

The variation of selected input parameters have shown that the residual strength predictions are less sensitive to the weld width, $2H$, and the weld metal strain hardening exponent, N_{W}. The variation of the weld metal yield strength, $R_{\mathrm{p0.2W}}$, however, has highly affected the residual strength predictions of the welded panels.

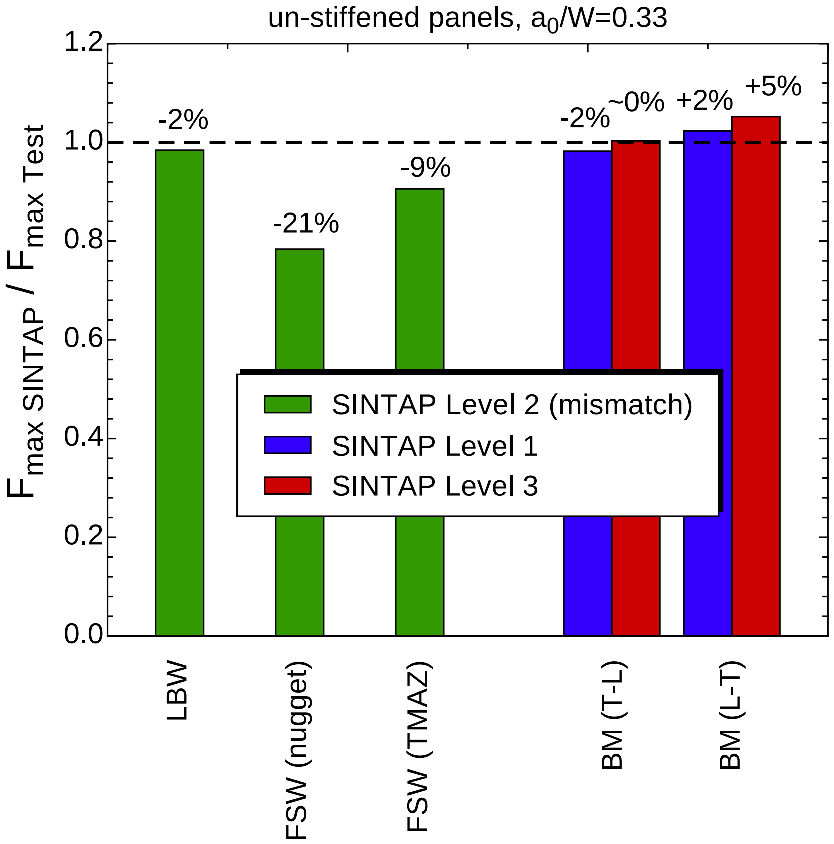

Figure 6.15: Summary of residual strength predictions with the SINTAP procedure for unstiffened cracked base material (BM), LBW and FSW (crack in the nugget area and TMAZ) panels.

6.4 Results of stiffened panels

The residual strength of a riveted stiffened structure is defined by the failure load of the cracked skin as well as of the stiffening element. Also the rivets provide a potential failure source in such stiffened structures. The skin failure occurs if the crack tip stress intensity exceeds a critical value, whereas the stiffening element fails if the stress level exceeds the tensile strength of the stiffener material. Due to the nature of integrally stiffened welded structures, the skin crack propagates also into the stiffener. Therefore, the stiffener failure may also be caused by an unstable growth of the stiffener crack. Unlike in the riveted structure, the prediction of the stiffener failure load requires a fracture mechanics based analysis.

This section presents the results of the SINTAP analysis of 2-stringer and 3-stringer welded panels. The analyses are based on two failure criteria: skin failure and stringer failure. The residual strength of the stiffened panels is dictated by the criterion which is met first, i.e. at a lower applied load.

The SINTAP analysis of stiffened panels was carried out by selecting different yield load and K-factor solutions starting with the simplest plate solution and gradually proceeding to more refined solutions, finally arriving at the yield load and K-factor solutions obtained by FEA in Section 5. In all these analysis steps, the material side was kept constant.

It has been shown for the base material panels in Section 6.3.1 that the use of the R-curves in terms of K_J and CTOD δ_5 in the SINTAP procedure yields very similar results. Therefore, only the CTOD δ_5 R-curve will be used in the residual strength analysis of stiffened panels.

The LBW T-joint has not been accounted for. The selection of the base material R-curve is legitimate since the amount of the stable crack extension across the weld is relatively small and the main part of the stable crack extension has taken place in the base material (skin and stringer). Moreover, no effect of the LBW T-joint on the stable crack extension such as sudden crack growth jumps across the weld has been observed in the experiments. Also the proposed yield load solution for stiffened panels has not been affected by the softer weld material (see Section 5.3.4).

6.4.1 Definition of skin failure criterion

The skin and stringer analyses are separate and do not interact while carrying them out. However, they are coupled through the K-factor solutions. It is obvious that the stress intensity at the skin crack tip is highly affected by the amount of the stringer damage, i.e. the length of the stringer crack. In the numerical analysis, the assumption (based on the experimental evidence) of equal lengths of the stringer crack and the part of the skin crack beyond the stringer has been made leading to a K-factor solution which is unique for this particular skin and stringer crack constellation.

For the application of the SINTAP procedure to the skin crack problem, the yield load, F_Y, and K-factor solutions are needed in order to calculate the crack tip loading. Using the special definition of CTOD δ in terms of CTOD δ_5, the crack tip loading of the skin crack is given by:

$$\delta_5 = \delta_{5e} \times [f(L_\mathrm{r})]^{-2} \tag{6.16}$$

with

$$\delta_{5e} = \frac{K^2_{\mathrm{I\,sk}}}{mR_{\mathrm{p0.2}}E} \qquad \text{with} \qquad m = 1.0 \tag{6.17}$$

where $R_{\mathrm{p0.2}}$ is the yield strength and E is the Young's modulus of the base material. $K_{\mathrm{I\,sk}}$ is the stress intensity factor of the skin crack.

Moreover,

$$L_\mathrm{r} = \frac{F}{F_\mathrm{Y}(a)} \tag{6.18}$$

where F is the applied load and $F_\mathrm{Y}(a)$ is the yield load as a function of the skin crack length, a.

The residual strength of the stiffened panel based on the skin failure criterion is defined by the unstable growth of the skin crack (tangency condition between the crack driving force and the R-curve):

$$\delta_5 = \delta_{5R} \qquad \text{and} \qquad \frac{\partial \delta_5}{\partial a} = \frac{\partial \delta_{5R}}{\partial a} \tag{6.19}$$

where δ_{5R} is the R-curve of the skin material.

The plastic collapse condition is met, if the applied load provokes a net section stress reaching the collapse stress of the skin material:

$$L_\mathrm{r} \geq L_{\mathrm{r\,max}} \tag{6.20}$$

with

$$L_{\mathrm{r\,max}} = \frac{1}{2}\frac{R_{\mathrm{p0.2}} + R_\mathrm{m}}{R_{\mathrm{p0.2}}} \tag{6.21}$$

where R_m is the tensile strength of the skin material.

The flow chart for the SINTAP analysis of stiffened panels based on the skin failure criterion is given in **Fig. A.5** (level 1) and **Fig. A.7** (level 3) and is fully automated in a FORTRAN program.

6.4.2 Definition of stringer failure criterion

The stringer failure criterion is similar to that of the skin analysis. The stringer is treated as a separate structural element containing a crack.

The stringer yield load, $F_\mathrm{Y}^{\mathrm{str}}$, is defined in terms of the stringer net section yielding as follows:

$$F_\mathrm{Y}^{\mathrm{str}}(a) = R_{\mathrm{p0.2}}^{\mathrm{str}}(A_{\mathrm{str}} - a_{\mathrm{str}}B_{\mathrm{str}}) \tag{6.22}$$

where $R_{\mathrm{p0.2}}^{\mathrm{str}}$ is the yield strength of the stringer material, A_{str} is the stringer total cross-sectional area, a_{str} is the stringer crack length, and B_{str} is the thickness of the stringer foot. The stringer yield load, $F_{\mathrm{Y}}^{\mathrm{str}}$, is a particular stringer load level acting in the stringer due to the total externally applied load to the stiffened panel at which the stringer net section yielding occurs. Due to the assumption $a_{\mathrm{str}} = a_{\mathrm{sk-beyond}}$ (**Fig. 5.3**), the stringer crack length, a_{str}, is linked to the skin crack length, a. Thus, the stringer yield load results in a function of a.

The application of SINTAP analysis levels 1 and 3 to the cracked stringer is identical to that of the skin problem. The parameter $L_{\mathrm{r}}^{\mathrm{str}}$ defines the degree of the stringer plastification and is calculated as:

$$L_{\mathrm{r}}^{\mathrm{str}} = \frac{F_{\mathrm{str}}}{F_{\mathrm{Y}}^{\mathrm{str}}(a)} \tag{6.23}$$

where F_{str} is the load in the stringer.

The plasticity correction function, $f(L_{\mathrm{r}}^{\mathrm{str}})$, of SINTAP level 1 and 3 is obtained in the same way as in the skin analysis but using the stringer material properties. The crack driving force of the stringer crack in terms of CTOD δ_5 is then:

$$\delta_5^{\mathrm{str}} = \delta_{5e}^{\mathrm{str}} \times \left[f(L_{\mathrm{r}}^{\mathrm{str}})\right]^{-2} \tag{6.24}$$

where

$$\delta_{5e}^{\mathrm{str}} = \frac{K_{\mathrm{I\,str}}^2}{m R_{\mathrm{p0.2}}^{\mathrm{str}} E} \quad \text{with} \quad m = 1.0 \tag{6.25}$$

where E is Young's modulus of the stringer material and is assumed to be the same as for the skin material. $K_{\mathrm{I\,str}}$ is the stress intensity factor of the stringer crack.

The residual strength of the stiffened panel based on the stringer failure criterion is defined either by an unstable growth of the stringer crack (tangency condition between the crack driving force and the R-curve):

$$\delta_5^{\mathrm{str}} = \delta_{5R}^{\mathrm{str}} \qquad \text{and} \qquad \frac{\partial \delta_5^{\mathrm{str}}}{\partial a_{\mathrm{str}}} = \frac{\partial \delta_{5R}^{\mathrm{str}}}{\partial a_{\mathrm{str}}} \tag{6.26}$$

where $\delta_{5R}^{\mathrm{str}}$ is the R-curve of the stringer material or by the plastic collapse of the stringer, whichever occurs first. The plastic collapse of the stringer is defined by the following condition:

$$L_{\mathrm{r}}^{\mathrm{str}} \geq L_{\mathrm{r\,max}}^{\mathrm{str}} \tag{6.27}$$

with

$$L_{\mathrm{r\,max}}^{\mathrm{str}} = \frac{1}{2} \frac{R_{\mathrm{p0.2}}^{\mathrm{str}} + R_{\mathrm{m}}^{\mathrm{str}}}{R_{\mathrm{p0.2}}^{\mathrm{str}}} \tag{6.28}$$

where $R_{\mathrm{m}}^{\mathrm{str}}$ is the tensile strength of the stringer material.

In order to find the structural response of the stiffened panel based on the stringer failure criterion, the link between the stringer load, F_{str}, and the total applied load, F, to the

Table 6.6: Skin and stringer material properties required as input information in the residual strength analysis of 2-stringer and 3-stringer panels.

	tensile properties	fracture resistance
Level 1 skin analysis	$E = 69000$ MPa $R^{\mathrm{sk}}_{\mathrm{p0.2}} = 385$ MPa $R^{\mathrm{sk}}_{\mathrm{m}} = 400$ MPa	$\delta_5 = 0.30(\Delta a)^{0.63}$ from C(T)50 and M(T)760 L-T orientation
Level 1 stringer analysis	$E = 69000$ MPa $R^{\mathrm{str}}_{\mathrm{p0.2}} = 405$ MPa $R^{\mathrm{str}}_{\mathrm{m}} = 425$ MPa	$\delta_5 = 0.30(\Delta a)^{0.63}$ same as for skin
Level 3 skin analysis	$E = 69000$ MPa true stress-strain curve	$\delta_5 = 0.30(\Delta a)^{0.63}$ same as in Level 1
Level 3 stringer analysis	$E = 69000$ MPa true stress-strain curve	$\delta_5 = 0.30(\Delta a)^{0.63}$ same as for skin

stiffened panel is needed. This link is given through the stringer load concentration factor $L_{\mathrm{s}}\left(\frac{a}{W}\right)$:

$$F = \frac{F_{\mathrm{str}}}{\chi L_{\mathrm{s}}\left(\frac{a}{W}\right)} \quad \text{with} \quad \chi = \begin{cases} 0.095 & \text{for 2-stringer panels} \\ 0.061 & \text{for 3-stringer panels.} \end{cases} \tag{6.29}$$

For the determination of χ see Eqs. (5.14) and (5.15). $L_{\mathrm{s}}\left(\frac{a}{W}\right)$ is defined in **Figs. 5.9** and **5.10** for the 2- and 3-stringer panels, respectively.

The flow chart for the SINTAP analysis based on the stringer failure criterion is given in **Fig. A.8** for both SINTAP levels 1 and 3. Both analysis levels are fully automated in a FORTRAN program.

6.4.3 Material related input data

The material related information like the tensile properties and the R-curve is summarized in **Tab. 6.6** and has been kept constant throughout the entire SINTAP analysis of the 2- and 3-stringer panels.

6.4.4 Prediction for 2-stringer panels (one-bay crack)

This section addresses the results of the SINTAP application to the cracked 2-stringer panels to predict their residual strength. SINTAP analysis levels 1 and 3 were used.

The SINTAP analysis of the 2-stringer panels has been carried out by selecting different yield load and K-factor solutions as summarized in **Tab. 6.7** in order to investigate the sensitivity of the SINTAP predictions to these input parameters. In total four different variations have been considered starting with the simplest plate solution and gradually proceeding to more refined solutions. In all these analysis steps, the material side, as given in **Tab. 6.6**, was kept constant.

Fig. 6.16 shows the prediction of the SINTAP procedure using levels 1 and 3 with the yield load and K-factor solutions given in variation 1 of **Tab. 6.7**. The 2-stringer panel is treated as a simple M(T) panel with a width of $2W = 555$ mm and a thickness of $B = 2.0$ mm (skin thickness only). The yield load, F_Y, as well as the K-factor solutions are taken from an M(T) panel having the same crack length and width as the skin. In other words, the effect of stringers has been completely ignored. Despite these simplifications, the prediction of the residual strength is not too conservative. The calculated maximum load is 14% lower than the experimental value. At a given applied load, the predicted CTOD δ_5 value is larger, i.e. overestimated, than the measured one. The diagram also depicts the yield load level by the dotted line which, obviously, decreases with increasing CTOD δ_5 due to the stable crack growth. The predicted maximum load is close to the yield load as has already been concluded from the analysis of cracked base material panels suggesting that the prediction may be sensitive to the yield load solution.

In **Fig. 6.17** the 2-stringer panel is treated as an M(T) panel with a width of $2W = 555$ mm as in the previous case but with an equivalent thickness, B_{eq}:

$$B_{\text{eq}} = \frac{A_{\text{sk}} + 2A_{\text{str}}}{2W} = 2.55 \text{ mm} \qquad \text{(2-stringer panel)} \tag{6.30}$$

where A_{sk} and A_{str} are cross-sectional areas of the skin and stringer, respectively (see variation 2 in **Tab. 6.7**). The material of the two stringers is evenly distributed over the entire width of the stiffened panel, thus, increasing the equivalent thickness and, therefore, the yield load as represented by the dotted line in **Fig. 6.17**. The residual strength prediction is 8% higher than the experimental maximum load. Compared to the previous analysis, the predicted curves are scaled to higher load levels. The predicted maximum loads in each analysis are reached at the same CTOD δ_5 value, i.e. same tangency point on the R-curve but at different loads.

Indeed, the predicted load-CTOD δ_5 curves of variations 1 and 2 are obviously identical if plotted in terms of the applied stress, $\sigma = F/(2W\,B')$ with $B' = B$ or $B' = B_{\text{eq}}$ of the respective analysis, **Fig. 6.18**. The thickness variation changes the yield load but

Table 6.7: Variation of the yield load, F_Y, and stress intensity factor, K_I, in the residual strength analysis of 2-stringer panels.

variation	yield load, F_Y	SIF, K_I	SINTAP results in Fig.
1	$F_\mathrm{Y} = R_\mathrm{p0.2} 2W\,B(1-a/W)$ $B = 2.0$ mm (skin only)	$K_\mathrm{I} = \frac{F}{2W\,B}\sqrt{\pi a} \times \sqrt{1/\cos\frac{\pi a}{2W}}$	**Fig. 6.16**
	no stringer analysis		
2	$F_\mathrm{Y} = R_\mathrm{p0.2} 2W\,B_\mathrm{eq}(1-a/W)$ $B_\mathrm{eq} = 2.55$ mm	$K_\mathrm{I} = \frac{F}{2W\,B_\mathrm{eq}}\sqrt{\pi a} \times \sqrt{1/\cos\frac{\pi a}{2W}}$	**Fig. 6.17**
	no stringer analysis		
3	*skin analysis*		**Fig. 6.19**
	$F_\mathrm{Y} = R_\mathrm{p0.2} 2W\,B(1-a/W)$ $B = 2.0$ mm (skin only) same as in variation 1	$K_{\mathrm{I\,sk}} = \frac{F}{2W\,B}\sqrt{\pi a}\,\beta_\mathrm{sk}\left(\frac{a}{W}\right)$ see Eq. (6.4) (from FEA)	
	stringer analysis		
	$F_\mathrm{Y}^\mathrm{str} = R_\mathrm{p0.2}^\mathrm{str}(A_\mathrm{str} - a_\mathrm{str} B_\mathrm{str})$	$K_{\mathrm{I\,str}} = \frac{F}{2W\,B}\sqrt{\pi a}\,\beta_\mathrm{str}\left(\frac{a}{W}\right)$ see Eq. (6.6) (from FEA)	
4	*skin analysis*		**Fig. 6.20**
	$F_\mathrm{Y} = R_\mathrm{p0.2}\ A_\mathrm{net}$ see Eq. (5.19) (from FEA)	same as in variation 3	
	stringer analysis		
	same as in variation 3	same as in variation 3	

also the K-factor solution. However, when operating in terms of stress, the thickness is "hidden" in the stress expression resulting in identical applied stress versus CTOD δ_5 curves. The applied stress of the experimental curve is defined as $\sigma = F/(2W\,B)$ where $B = 2.0$ mm is the skin thickness.

In the two preceding analyses the stringer effect of reducing the stress intensity at the crack tip was not accounted for. Also the stringer damage, i.e. stringer crack after crack branching, was completely ignored. In the next two analyses, the stringer is considered as a structural element that contributes to the load carrying capacity of the stiffened panels. The residual strength of the whole stiffened panel is defined either by the skin or stringer failure, whichever occurs first.

Fig. 6.19 shows the SINTAP predictions in terms of load-CTOD δ_5 curves using both the skin and stringer failure criteria. The yield load, F_{Y}, and K-factor solutions are given as variation 3 in **Tab. 6.7**. In the analysis based on the skin failure criterion, the yield load solution is taken as that of an M(T) panel (same solution as in variation 1), i.e. the skin is assumed to yield at the same load level as a simple M(T) panel of the same width and thickness. However, the K-factor solution here incorporates the stringer effect and was derived from FEA. In the analysis based on the stringer failure criterion, the stringer yield load is simply based on the stringer net section yielding. The K-factor solution for the stringer crack is also derived from FEA as for the skin crack (see variation 3 in **Tab. 6.7**). The result of this analysis shows that the residual strength of the stiffened panel is defined by the skin failure since the analysis based on the skin failure criterion predicts a lower maximum load than that based on the stringer failure criterion. The skin crack would become unstable at a lower applied load while at the same load level the stringer crack remains stable. When comparing the predicted with the experimental load-CTOD δ_5 curves, it is clearly visible that at a given applied load the predicted CTOD δ_5 value is underestimated. More discussion on this issue will be given in a later paragraph.

Fig. 6.20 shows SINTAP predictions using the input information given in variation 4 of **Tab. 6.7**. The yield load solution was derived from FEA where also the cross-sectional area of the two stringers is included. This leads to an increase in load-bearing cross section and thus the yield load compared to the solution given in variation 3.

In the analysis based on the skin failure criterion, the increase in the yield load, while keeping the same K-factor solution as in variation 3, increases the predicted maximum load of the stiffened panel.

It was observed in the first two analyses (variations 1 and 2) that the predicted maximum load levels were attained at the same CTOD δ_5 value. Here, however, the higher yield load of variation 4 compared to variation 3 is not achieved by a simple thickness increase but by a completely different approach. The modification of the yield load solution of variation 4 is not linked to the K-factor solution. At a given applied load and crack length the K-factor solutions of variation 3 and 4 are really identical while the yield load solutions differ. Due to this fact, the predicted maximum load levels of variations 3 and 4 are not at the same CTOD δ_5 value.

It should be mentioned that the analysis based on the stringer failure criterion is identical to that shown in **Fig. 6.19**. Since the stringer crack becomes unstable at a lower predicted applied load, the residual strength of the stiffened panel in this analysis case is defined by the stringer failure while the skin crack remains subcritical.

Fig. 6.21 shows the effect of the K-factor solution (skin crack) on the residual strength prediction of the 2-stringer panel by comparing variations 1 and 3. The yield load solution in these two cases is identical and plotted by the dotted line. If the K-factor solution derived from FEA is used (see analysis of variation 3), the predicted CTOD δ_5 is underestimated compared to the experimental value. Whereas the use of the K-factor solution taken from an M(T) panel (see analysis of variation 1) leads to an overestimation of CTOD δ_5. Since the yield load is identical in these two cases (and also the material side!), the observed deviation of CTOD δ_5 can only be related to the K-factor solutions which are plotted for comparison in **Fig. 6.22**. It is obvious that the K-factor solution of an M(T) panel overestimates the real stress intensity at the skin crack tip of a stiffened panel since the stringer effect of the stress reduction is entirely ignored.

On the other hand, the K-factor solution derived from FEA obviously underestimates the real stress intensity at the skin crack tip. The boundary condition of no out-of-plane displacements was perfectly met in FEA by suppressing the displacements in the out-of-plane direction. In the test, however, this requirement might not be perfectly fulfilled despite very careful installation of the supports to prevent the out-of-plane displacements. Thus, small out-of-plane displacements arise which in turn cause a secondary bending increasing the stresses at the skin crack tip. The real K-factor can be expected to be higher. The same trend was reported by Swift [124] for riveted stringers.

The second reason for a higher experimental CTOD δ_5 might be the stress redistribution as a result of the plasticity spread at the skin and stringer crack tips. The two crack tips affect the stress fields of each other; however, this redistribution due to the plastic deformation - particularly in the stringer - cannot be accounted for in FEA based on the theory of elasticity which is necessary for the determination of the linear elastic stress intensity factor K. Indeed, if the plastic deformation of the rivets and the stringer is accounted for in a riveted structure, the resulting K-factor of the skin crack increases [124].

All of the above analyses, where the material side was kept constant but the yield load and K-factor solutions were varied, have shown that the predicted load-displacement curve in terms of CTOD δ_5 are sensitive to these variations. The sensitivity trends are summarized in the schematic diagram in **Fig. 6.30**. The increase of the yield load shifts the predicted curve to higher loads. Higher K-factors make the predicted load-CTOD δ_5 curve more compliant while the maximum load slightly decreases.

The residual strength predictions for the 2-stringer panels using different yield load and K-factor solutions (variations 1-4 as given in **Tab. 6.7**) are summarized in the bar chart in **Fig. 6.31**a).

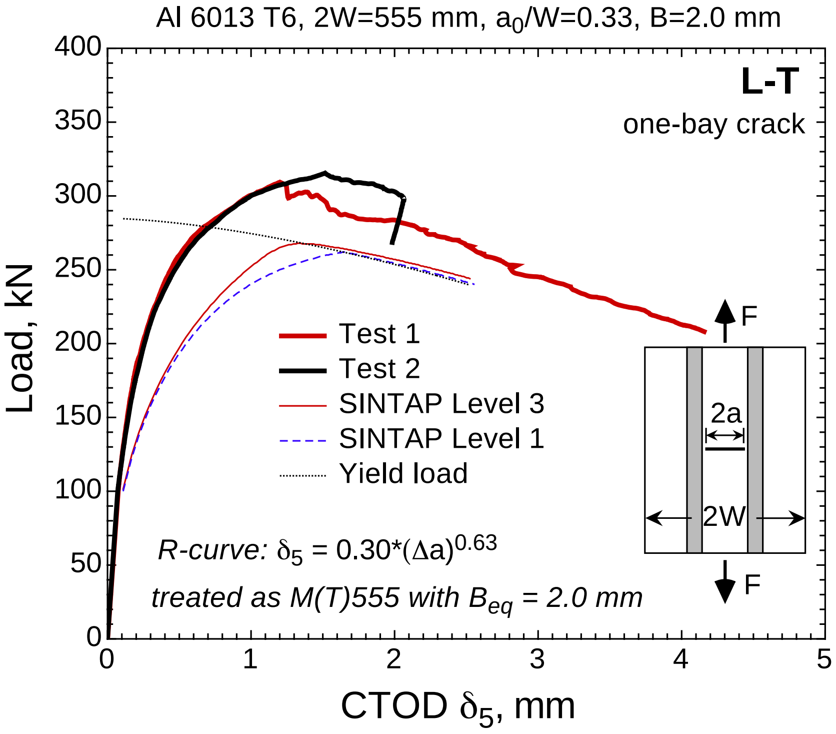

Figure 6.16: SINTAP prediction of the residual strength of the 2-stringer panels. The stiffened panels are treated as M(T)555 panels with a thickness of $B = 2.0$ mm (skin thickness only), i.e. ignoring the stringers and their effect on the stress intensity factor. F_Y and K_I are given in variation 1 in **Tab. 6.7**.

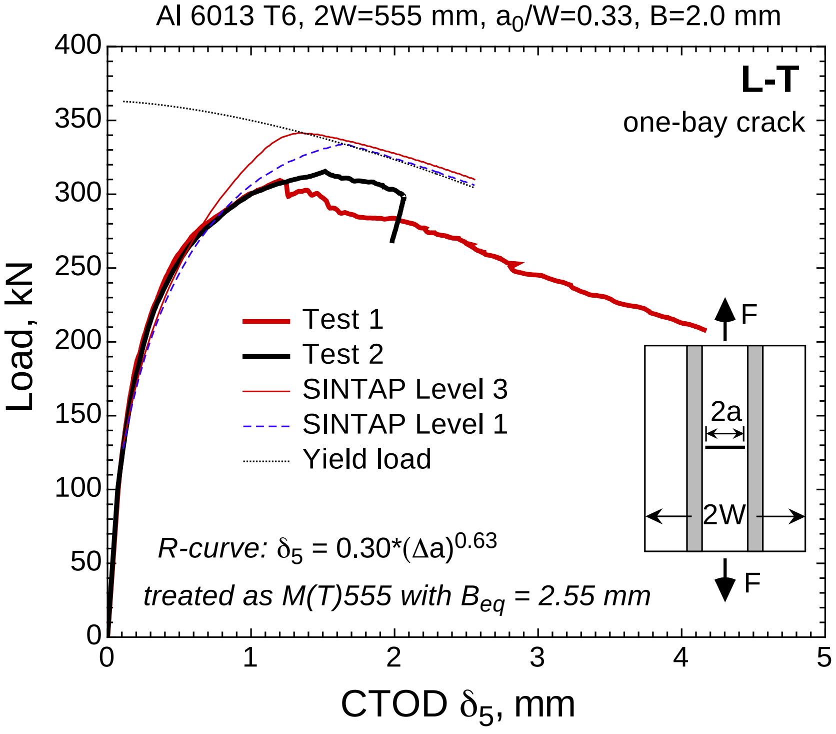

Figure 6.17: SINTAP prediction of the residual strength of the 2-stringer panels. The stiffened panels are treated as M(T)555 panels with an equivalent thickness of $B_{\mathrm{eq}} = 2.55$ mm, i.e. including the two stringers in the total cross-sectional area but ignoring their effect on the stress intensity factor. F_Y and K_I are given in variation 2 in **Tab. 6.7**.

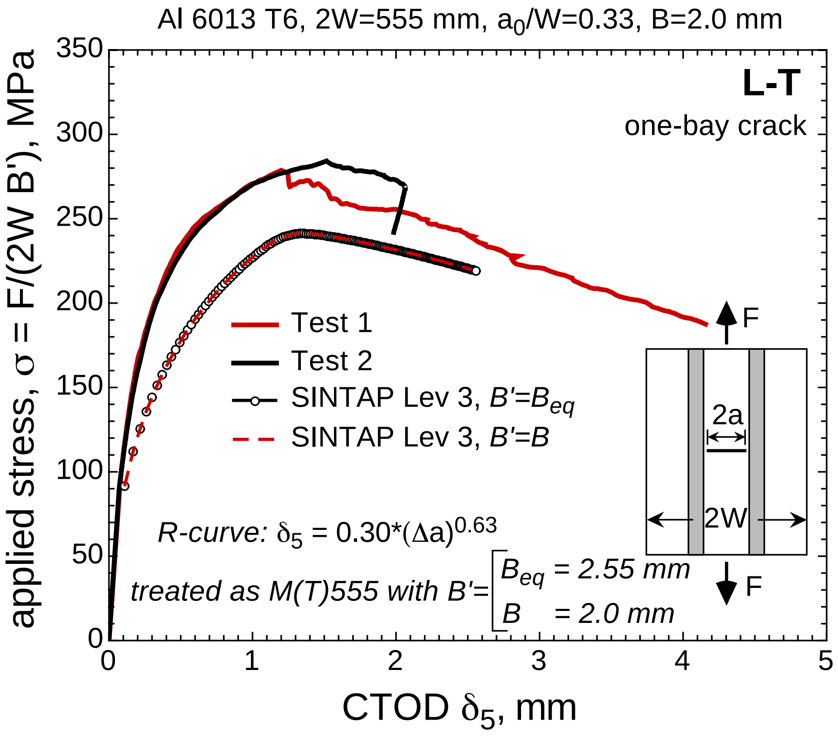

Figure 6.18: Identity of predictions of variation 1 ($B' = B$) and variation 2 ($B' = B_{\mathrm{eq}}$) if plotted in terms of applied stress versus CTOD δ_5 curves. F_{Y} and K_{I} of respective analyses are given in **Tab. 6.7**. The applied stress of the experimental curve is $\sigma = F/(2W\,B)$.

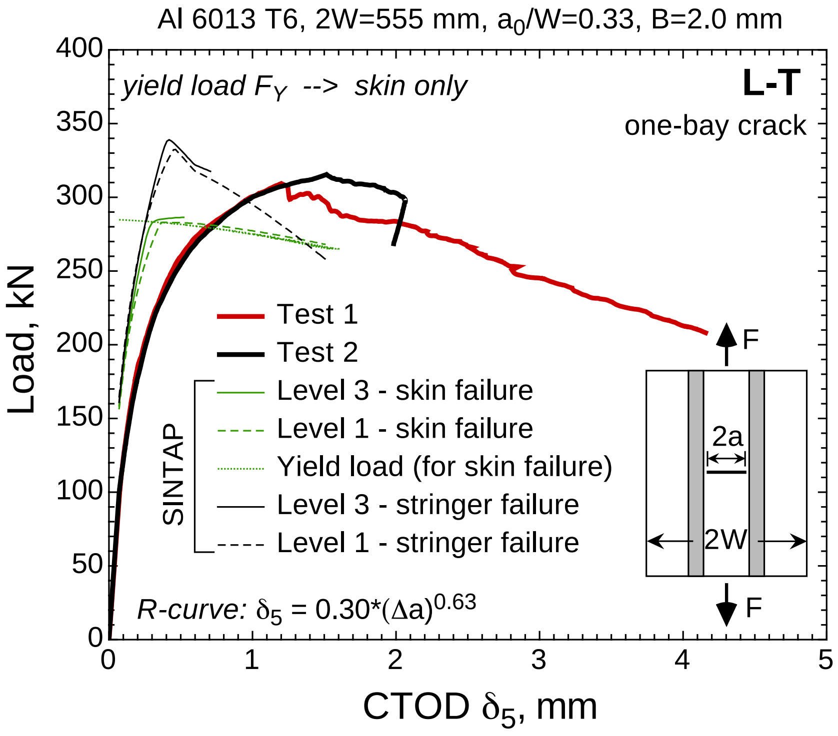

Figure 6.19: SINTAP prediction of the residual strength of the 2-stringer panels based on separate skin and stringer failure criteria. In the skin failure analysis, the yield load is based on skin material only, the stress intensity factor solution is based on the FE analysis of the stiffened 2-stringer panel. F_{Y} and K_{I} are given in variation 3 in **Tab. 6.7**.

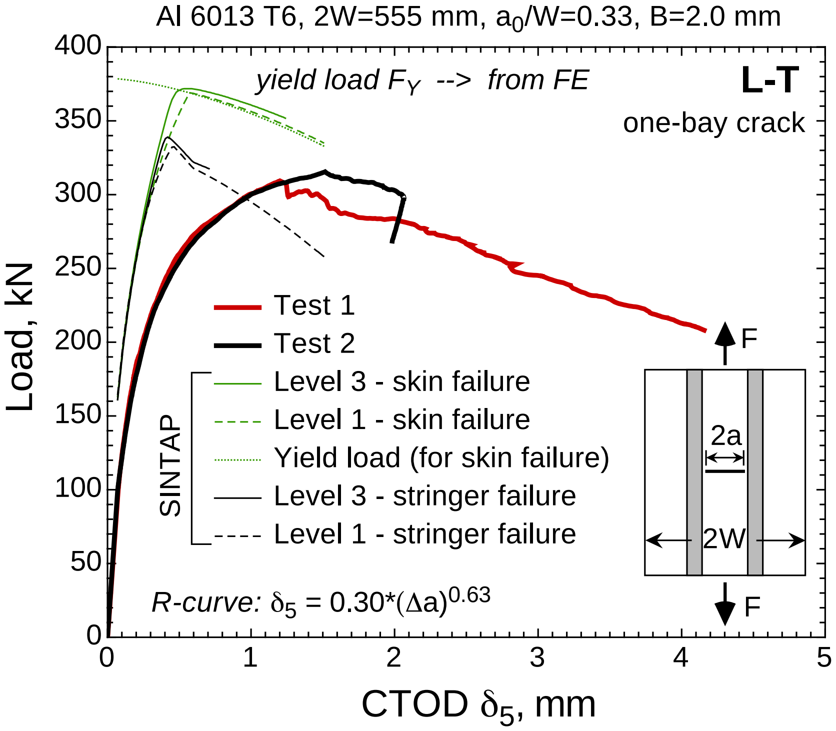

Figure 6.20: SINTAP prediction of the residual strength of the 2-stringer panels based on separate skin and stringer failure (same as in **Fig. 6.19**) criteria. In the skin failure analysis, the yield load as well as the stress intensity factor solutions are obtained from the FE analysis of stiffened panels. F_Y and K_I are given in variation 4 in **Tab. 6.7**.

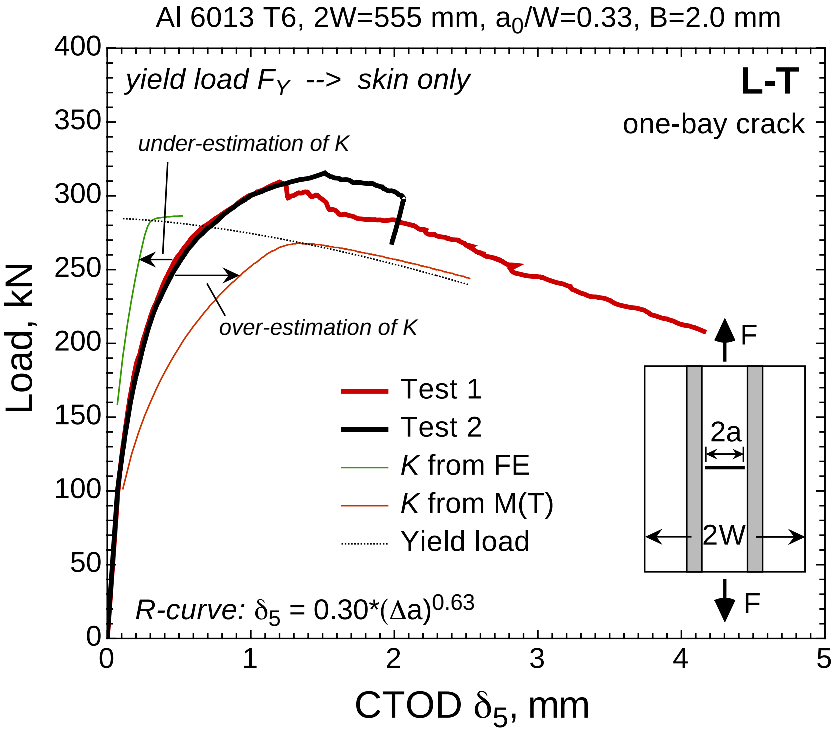

Figure 6.21: Effect of the stress intensity factor, K, on the SINTAP prediction (level 3) of the residual strength of the 2-stringer panels (skin failure analysis).

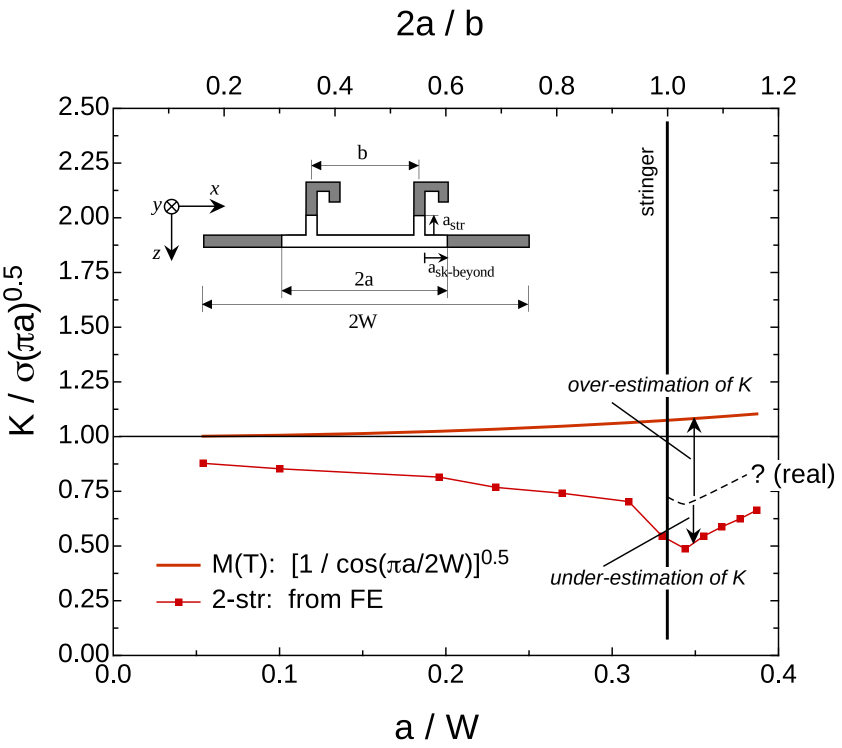

Figure 6.22: Correction factors of K for an M(T) panel and a 2-stringer panel.

6.4.5 Prediction for 3-stringer panels (two-bay crack)

The 3-stringer panel represents a two-bay crack scenario with a broken central stringer. The ratio of the initial crack length ($2a_0$) to the total panel width ($2W$) is $a_0/W = 0.5$. The objective of this analysis is to predict the residual strength of these cracked stiffened 3-stringer panels using the SINTAP procedure. SINTAP analysis levels 1 and 3 were used.

The approach in the analysis of 3-stringer panels is similar to that of 2-stringer panels. The input information for the SINTAP analysis on the material side like the tensile data of skin and stringer materials and the R-curve are the same as in the analysis of 2-stringer panels (see **Tab. 6.6**). The yield load, F_Y, and K-factor solutions are varied analogously to the 2-stringer panels while the material side was kept constant. All variations of F_Y and K-factor solutions are summarized in **Tab. 6.8**.

In the first variation (variation 1 in **Tab. 6.8**), the stringers are completely ignored and the 3-stringer panel is treated as a simple M(T) panel with the skin width of $2W = 740$ mm and the skin thickness of $B = 2.0$ mm. **Fig. 6.23** shows the comparison of the predicted load-CTOD δ_5 curve using SINTAP analysis levels 1 and 3 with the experimental curve. In terms of maximum load, the SINTAP prediction is very accurate meeting almost exactly the experimental maximum load value in the highest analysis level 3. As already observed in the analysis of the cracked base material and 2-stringer panels, the predicted maximum load is close to the yield load, which is indicated by the dotted line in the graph, suggesting a sensitivity of the prediction to the yield load solution.

In the next variation (variation 2 in **Tab. 6.8**), the 3-stringer panel is again treated as an M(T) panel as in variation 1 but with an equivalent thickness, B_{eq}:

$$B_{\mathrm{eq}} = \frac{A_{\mathrm{sk}} + 2A_{\mathrm{str}}}{2W} = 2.41 \text{ mm} \qquad \text{(3-stringer panel)} \tag{6.31}$$

where A_{sk} and A_{str} are cross-sectional areas of the skin and stringer, respectively. Due to the fact that the central stringer is broken and, therefore, does not carry load, only two stringers (factor 2 in the above equation) are included in the calculation of the effective cross-sectional area. Similar to the results of the 2-stringer panel, the predicted maximum load is non-conservative resulting in an overestimation by 19%, **Fig. 6.24**.

The difference between variations 1 and 2 is only the thickness. As shown in the analysis of the 2-stringer panels, these two approaches yield identical results if the predicted residual strength is reported in terms of the applied stress. Then, the thickness does not appear as a parameter but is "hidden" in the stress definition in the yield load as well as in the K-factor expressions, respectively. The applied stress-CTOD δ_5 curves are depicted in **Fig. 6.25** showing the identity of variations 1 and 2. The applied stress of the experimental curve is defined as $\sigma = F/(2W\,B)$ where $B = 2.0$ mm is the skin thickness.

Table 6.8: Variation of the yield load, F_{Y}, and stress intensity factor, K_{I}, in the residual strength analysis of 3-stringer panels (analogous to 2-stringer panels).

variation	yield load, F_{Y}	SIF, K_{I}	SINTAP results in Fig.
1	$F_{\mathrm{Y}} = R_{\mathrm{p0.2}} 2W\,B(1 - a/W)$ $B = 2.0$ mm (skin only)	$K_{\mathrm{I}} = \frac{F}{2W\,B}\sqrt{\pi a} \times \sqrt{1/\cos\frac{\pi a}{2W}}$	**Fig. 6.23**
	no stringer analysis		
2	$F_{\mathrm{Y}} = R_{\mathrm{p0.2}} 2W\,B_{\mathrm{eq}}(1 - a/W)$ $B_{\mathrm{eq}} = 2.41$ mm	$K_{\mathrm{I}} = \frac{F}{2W\,B_{\mathrm{eq}}}\sqrt{\pi a} \times \sqrt{1/\cos\frac{\pi a}{2W}}$	**Fig. 6.24**
	no stringer analysis		
3	*skin analysis*		**Fig. 6.19**
	$F_{\mathrm{Y}} = R_{\mathrm{p0.2}} 2W\,B(1 - a/W)$ $B = 2.0$ mm (skin only) same as in variation 1	$K_{\mathrm{I\,sk}} = \frac{F}{2W\,B}\sqrt{\pi a}\beta_{\mathrm{sk}}\left(\frac{a}{W}\right)$ see Eq. (6.4) (from FEA)	
	stringer analysis		
	$F_{\mathrm{Y}}^{\mathrm{str}} = R_{\mathrm{p0.2}}^{\mathrm{str}}(A_{\mathrm{str}} - a_{\mathrm{str}}B_{\mathrm{str}})$	$K_{\mathrm{I\,str}} = \frac{F}{2W\,B}\sqrt{\pi a}\beta_{\mathrm{str}}\left(\frac{a}{W}\right)$ see Eq. (6.6) (from FEA)	
4	*skin analysis*		**Fig. 6.20**
	$F_{\mathrm{Y}} = R_{\mathrm{p0.2}}\,A_{\mathrm{net}}$ see Eq. (5.19) (from FEA)	same as in variation 3	
	stringer analysis		
	same as in variation 3	same as in variation 3	

Fig. 6.26 illustrates the results of the analysis with the yield load and K-factor solutions given in variation 3 in **Tab. 6.8**. Here the SINTAP analysis is based on the skin and stringer failure criteria, respectively. In the skin failure analysis, the yield load, F_{Y}, is the same as in variation 1, i.e. the skin is assumed to yield at the same load level as an M(T) panel with the same width and thickness. The K-factor solution has been derived for this specific case of a 3-stringer panel by FEA. The stringer analysis includes the yield load solution of the stringer based on the net section yielding (same stringer solution as in the case of the 2-stringer panel). The K-factor solution of the stringer crack is also derived by FEA.

The predicted load-CTOD δ_5 curves are compared with the experimental curves in **Fig. 6.26**. Using the yield load and K-factor solutions of variation 3, the residual strength is defined by the skin failure since the maximum load is reached at a lower load level than in the analysis based on the stringer failure criterion. The predicted residual strength of the 3-stringer panel exceeds the experimental maximum load value by 9%. It should be recalled at this stage that the stringer separation from the skin material at LBW run-outs took place before the maximum load was reached in the test of 3-stringer panels (Section 4.3). The true residual strength of these panels, i.e. if the stringers remained intact, can, therefore, be assumed higher. The non-conservatism of this analysis may then even result in a conservative prediction.

At a given load level, the SINTAP analysis predicts a lower CTOD δ_5 than the experimental value. The reason is the same as in the case of the 2-stringer panels and will be elaborated for the case of the 3-stringer panels in a later paragraph.

Fig. 6.27 depicts the SINTAP analysis results using the input information of variation 4 as given in **Tab. 6.8**. The analysis is based on both skin and stringer failure criteria, whereas the stringer analysis is identical to the previous one (variation 3). In the skin analysis, only the yield load solution, F_{Y}, which has been derived from FEA of the 3-stringer panel, is different from variation 3 while the K-factor solution remained the same (from FEA).

The residual strength prediction of the skin analysis is highly non-conservative (42%). Moreover, the analysis based on the stringer failure criterion predicts a lower maximum load. Thus, the residual strength of the 3-stringer panel in this analysis case is defined by stringer failure due to an unstable growth of the stringer crack. The skin crack is predicted to remain stable at the failure load of the stringer.

Fig. 6.28 shows the effect of the K-factor solution of the skin crack on the SINTAP predictions by comparing the results of variations 1 and 3. The yield load solution in these two cases is identical and is plotted by the dotted line. The only difference between these two analyses is the K-factor solution. Variation 1 uses the K-factor solution of an M(T) panel, whereas variation 3 that derived from FEA of the 3-stringer panel. Both solutions are shown for a direct comparison in **Fig. 6.29**. Using the K-factor solution of the M(T) panel, the predicted CTOD δ_5 is overestimated, while the use of the FEA solution leads to an underestimation suggesting that the real K-factor solution must lie somewhere in between. It is obvious that the M(T) solution gives higher K values since the stringer effect of the stress reduction is ignored. The FEA solution yields K-factors that are apparently too low for which two reasons have been suggested: secondary bending and plastic deformation of the stringer. Their detailed explanation is given in Section 6.4.4.

The residual strength predictions for the 3-stringer panels using different yield load and K-factor solutions (variations 1-4 as given in **Tab. 6.8**) are summarized in the bar chart of **Fig. 6.31** b).

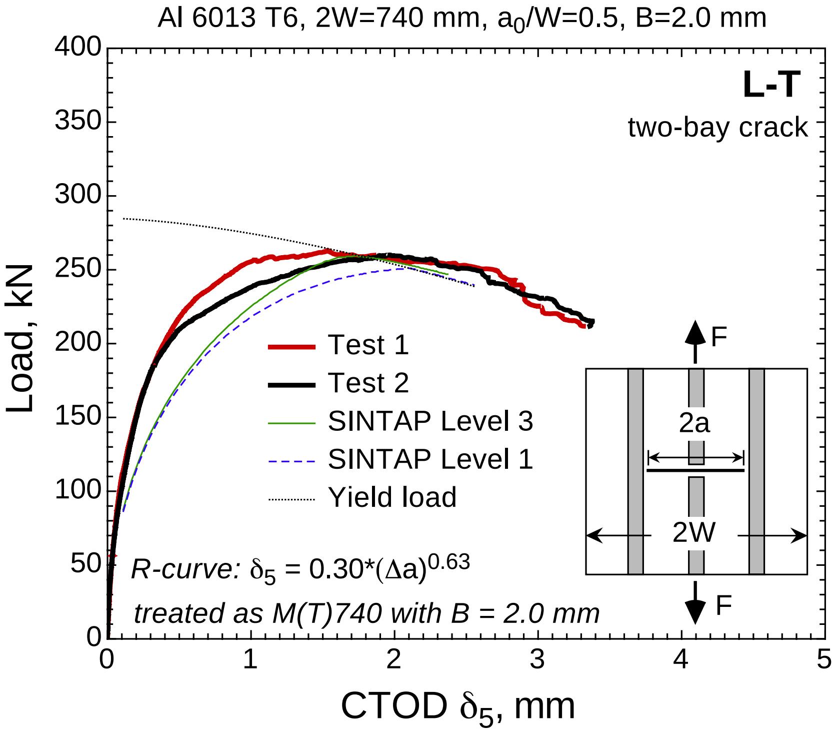

Figure 6.23: SINTAP prediction of the residual strength of the 3-stringer panels. The stiffened panels were treated as M(T)740 panels with a thickness of $B = 2.0$ mm (skin thickness), i.e. ignoring the stringers and their effect on the stress intensity factor. F_Y and K_I are given in variation 1 in **Tab. 6.8**.

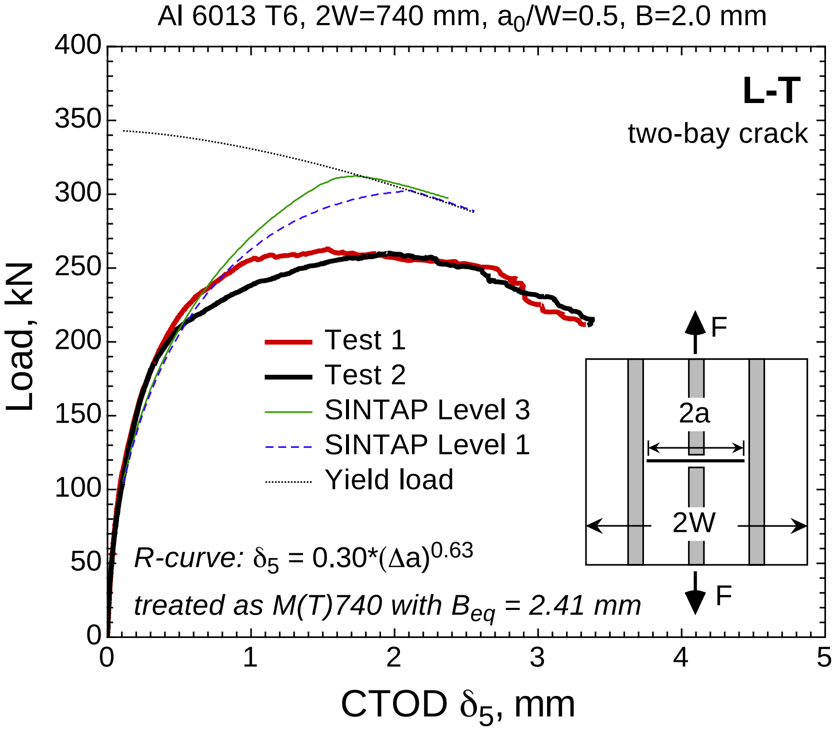

Figure 6.24: SINTAP prediction of the residual strength of the 3-stringer panels. The stiffened panels were treated as M(T)740 panels with an equivalent thickness of $B_{\mathrm{eq}} = 2.41$ mm, i.e. including the two (broken central stringer is not included!) stringers in the total cross-sectional area but ignoring their effect on the stress intensity factor. F_Y and K_I are given in variation 2 in **Tab. 6.8**.

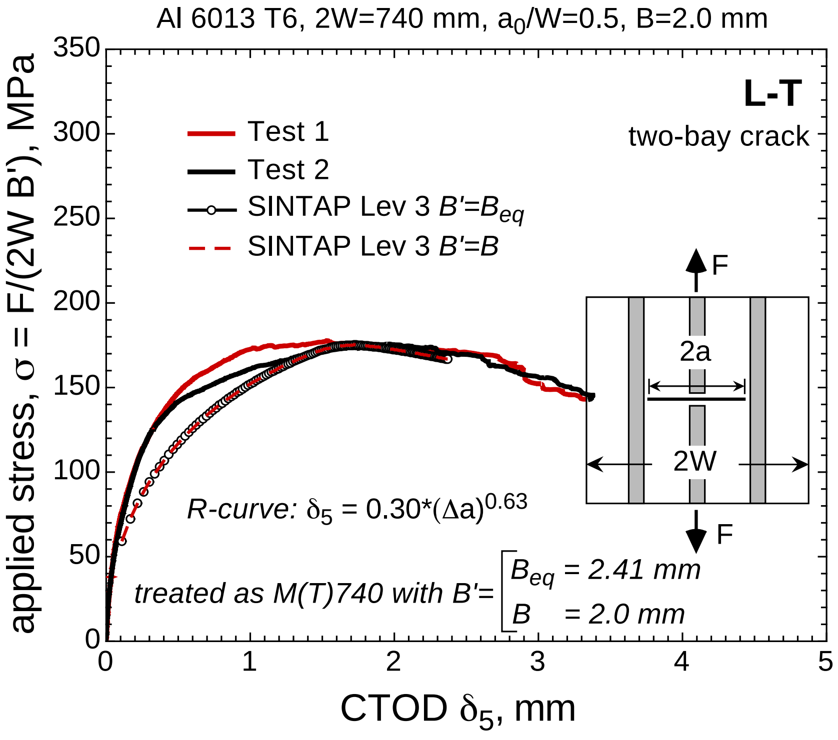

Figure 6.25: Identity of predictions of variation 1 ($B' = B$) and variation 2 ($B' = B_{\mathrm{eq}}$) if plotted in terms of the applied stress versus CTOD δ_5 curves. F_{Y} and K_{I} of respective analyses are given in **Tab. 6.8**. The applied stress of the experimental curve is $\sigma = F/(2W\,B)$.

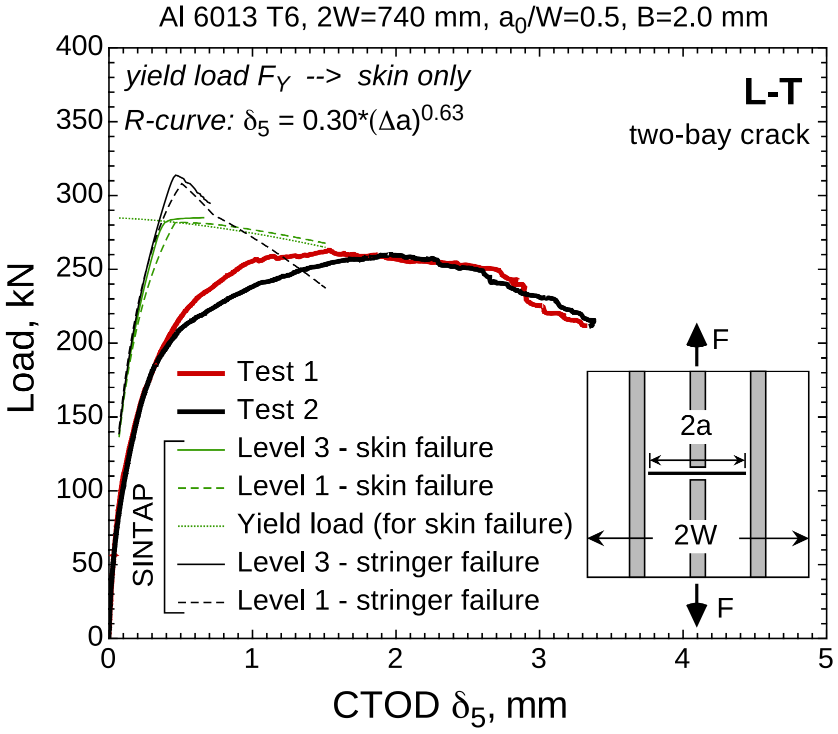

Figure 6.26: SINTAP prediction of the residual strength of the 3-stringer panels based on separate skin and stringer failure criteria. In the skin failure analysis, the yield load was based on skin material only, the stress intensity factor solution is based on the FE analysis of the stiffened panels. F_{Y} and K_{I} are given in variation 3 in **Tab. 6.8**.

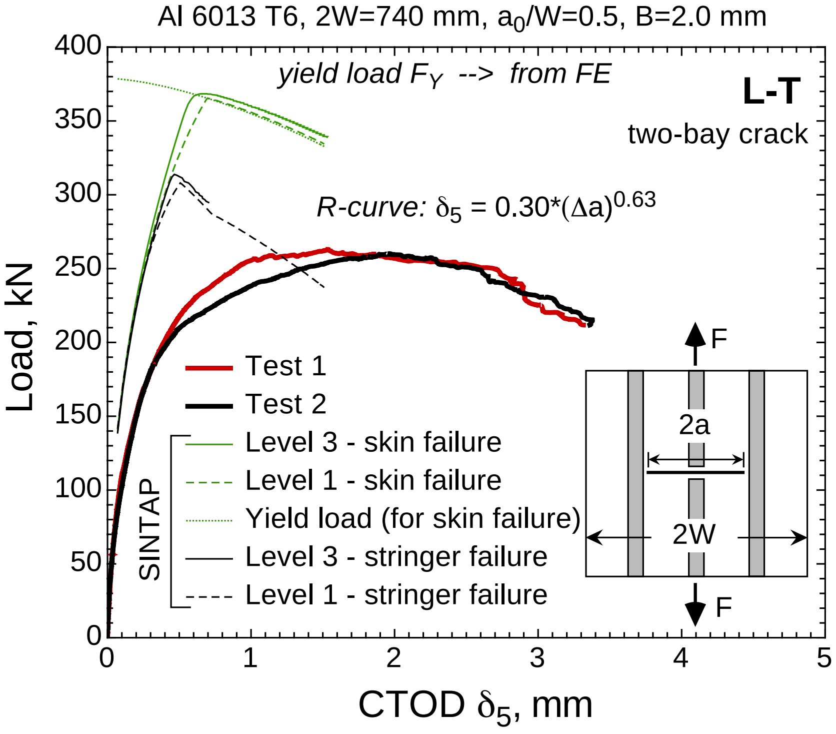

Figure 6.27: SINTAP prediction of the residual strength of the 3-stringer panels based on the separate skin and stringer failure (same as in **Fig. 6.26**) criteria. In the skin failure analysis, the yield load as well as the stress intensity factor solutions were obtained from the FE analysis of stiffened panels. F_Y and K_I are given in variation 4 in **Tab. 6.8**.

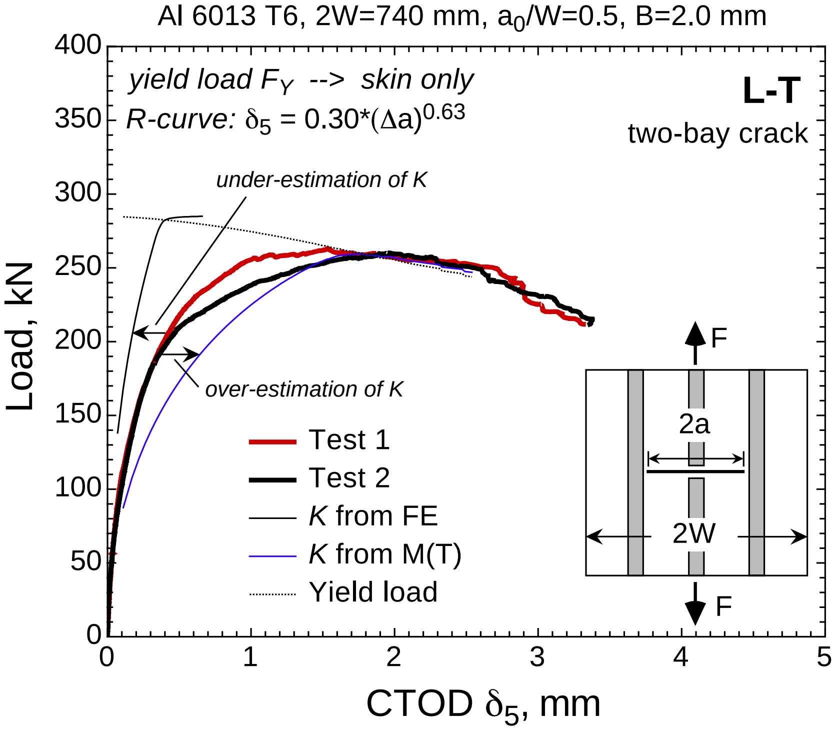

Figure 6.28: Effect of the stress intensity factor, K, on the SINTAP prediction (level 3) of the residual strength of the 3-stringer panels (skin failure analysis).

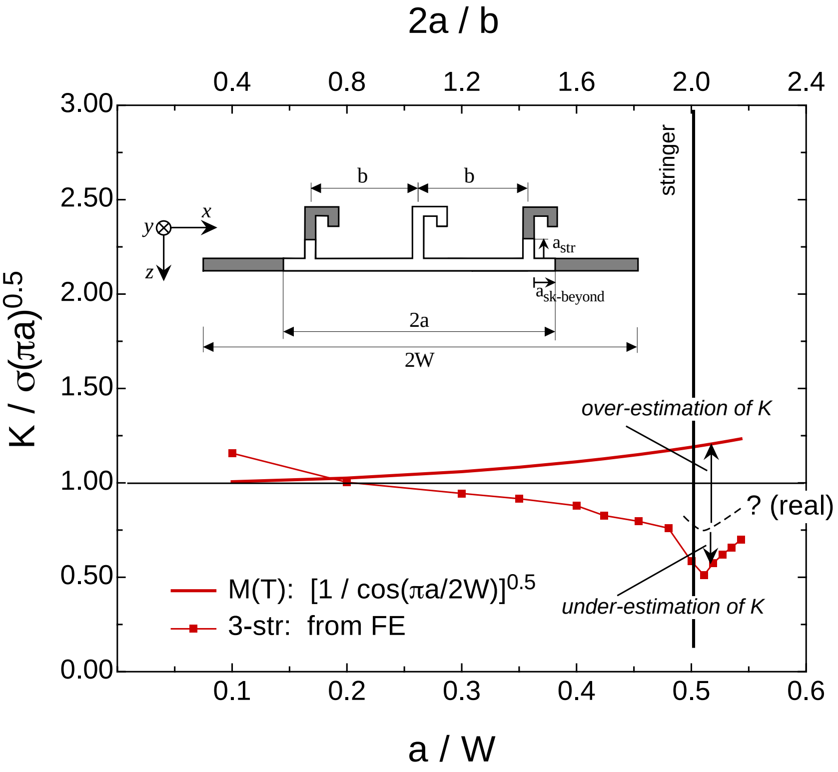

Figure 6.29: Correction factors of K for an M(T) panel and a 3-stringer panel.

6.4.6 Summary

The variation of the K-factor and yield load solutions for both 2- and 3-stringer panels with central cracks has shown a trend schematically illustrated in **Fig. 6.30**. An increase in the yield load results in an increase in the predicted residual strength, **Fig. 6.30** a). If the K-factor is assumed higher for a given applied load, the predicted crack driving parameter in terms of CTOD δ_5 is larger, **Fig. 6.30** b). However, the K-factor sensitivity has shown a minor effect on the maximum load prediction.

The accuracy of the residual strength predictions of 2- and 3-stringer panels using the SINTAP procedure is depicted in **Fig. 6.31**. The proposed route incorporates the variation 3 in both 2- and 3-stringer analyses. According to variation 3, the definition of the yield load of the stiffened panel is simply based on the M(T) solution with skin dimensions, thus, ignoring the stringers. The K-factor solution, however, is based on FEA which includes the stringer effect of the stress reduction at the skin crack tip. Using this approach, the failure of both 2- and 3-stringer panels has been predicted by unstable crack growth in the skin which occurs at a lower applied load than the instability of the stringer crack.

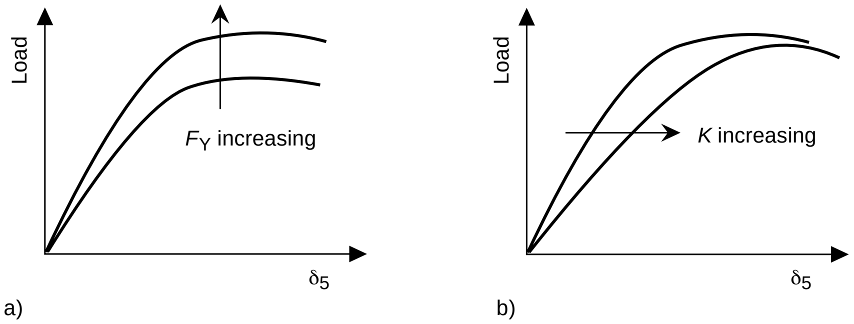

Figure 6.30: Schematic representation of load-CTOD δ_5 predictions and their sensitivity to a) yield load, F_Y, and b) K-factor.

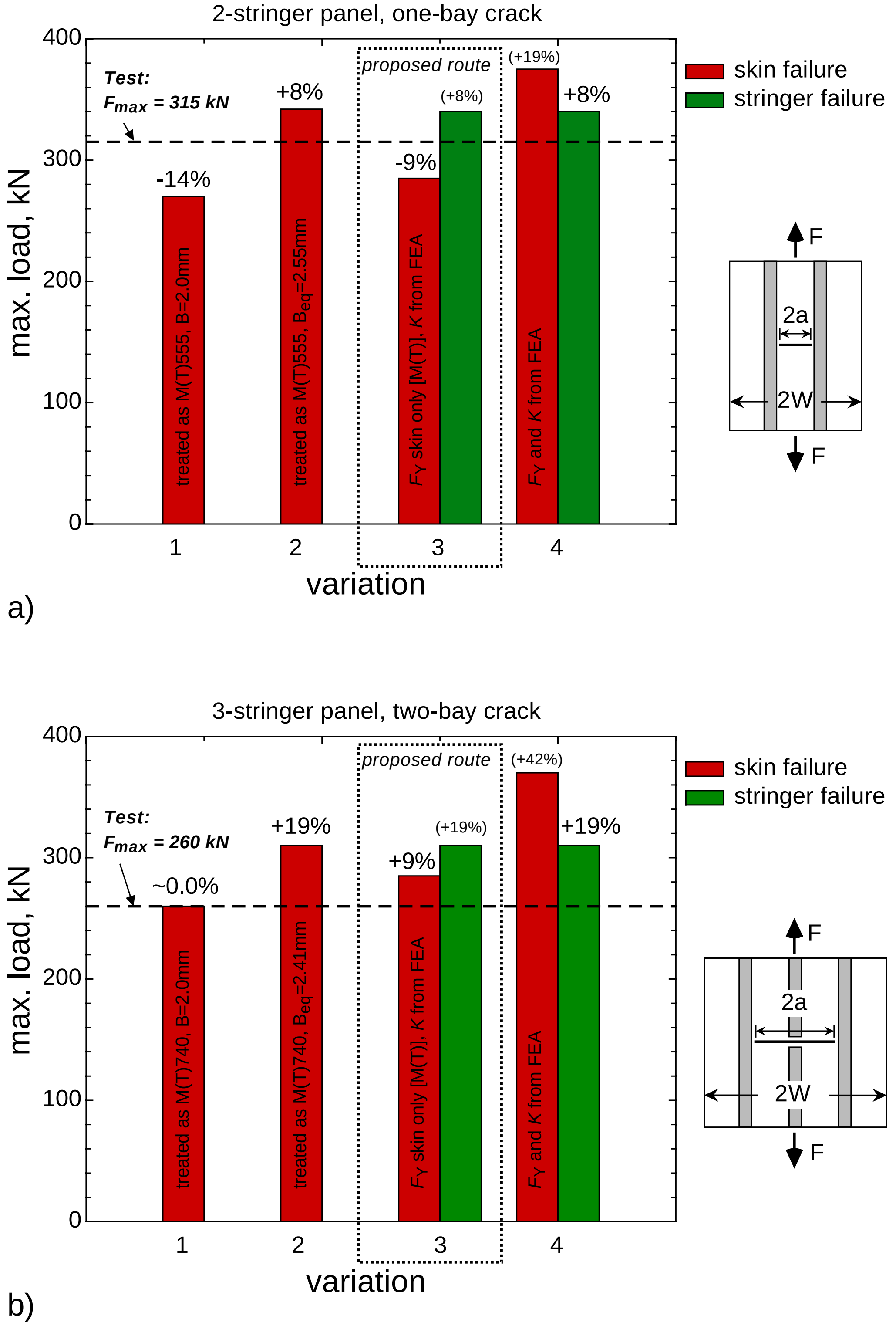

Figure 6.31: Summary of the residual strength predictions for a) 2-stringer welded stiffened panels with a one-bay crack and b) 3-stringer welded stiffened panel with a two-bay crack. The variations of the K-factor and yield load solutions are given in **Tab. 6.7** for the 2-stringer panel and in **Tab. 6.8** for the 3-stringer panel.

7 Conclusions

Damage tolerance behaviour of the integral (welded) aluminium airframe structures has a paramount significance for the further development of the new fabrication and design approaches of light-weight and cost-effective civil airplanes. Therefore, the main objectives of this study were to improve the current understanding of the failure behaviour and to propose a verified approach to predict the residual strength behaviour of the welded aircraft fuselage panels.

A systematic analysis to clarify the deformation and fracture behaviour of the laser beam (LBW) and friction stir welded (FSW) new weldable Al-alloy 6013 in T6 temper condition has been conducted in cooperation with AIRBUS using small and large scale specimens.

Both LBW and FSW joints have yielded highly strength undermatched welds. The lower strength level of the weld zone strongly determined the deformation and fracture behaviour of the butt-welds. The occurrence of the confined plasticity within the weld zone has been clearly demonstrated using the digital image analysis technique. The experimentally measured plastic zone size at the crack tip in LBW and FSW joints has improved the determination of the effective crack length. This type of the plasticity development and peaks of the plastic strain distribution within the FSW and LBW weld zone has determined the fracture path and overall has led to unstable fracture at the lower applied strain and stress levels as compared to the base material. The LBW panels have shown the lowest residual strength capacity. In the case of the FSW joints, the crack located in TMAZ, which has exhibited the lowest hardness, has been found more critical than the crack in the nugget area along the weld centerline.

The European structural integrity assessment procedure (SINTAP) has been used to predict the critical structural conditions of unstiffened and stiffened thin-walled welded aluminium panels under static loading. This study has demonstrated and verified the applicability of the SINTAP procedure to the assessment of flaws in integral airframe configurations containing LBW and FSW joints with significant strength undermatching. In this context, it is a pioneering work by providing an engineering approach to predict the residual strength of these panels after having conducted a series of sensitivity analyses. The special features of the strength undermatched welds in butt-joints have been taken into account in these analyses and, hence, recommendations in terms of the selection of SINTAP input parameters have been made to obtain conservative predictions.

The SINTAP predictions for the cracked base material panels in terms of maximum load as well as in terms of deformation behaviour have shown excellent agreement with the experimental results. The constraint parameter $m = 1.0$ has been selected underpinning the assumption of a plane stress condition at the crack tip in these thin base material panels.

The application of the SINTAP mismatch option, which accounts for the strength mismatch in welded joints, to LBW and FSW panels has yielded conservative estimates of the maximum load carrying capacity.

The variation of selected input parameters has shown that the residual strength predictions are less sensitive to the weld width, $2H$, and the weld metal strain hardening exponent, N_{W}. The variation of the weld metal yield strength, $R_{\mathrm{p0.2W}}$, however, has highly affected the residual strength predictions of the welded panels. It is, therefore, recommended to determine the weld material yield strength from micro-flat tensile specimens. Yield strength values obtained from welded standard tensile specimens may result in non-conservative residual strength predictions.

The variation of the constraint parameter m has shown that the value $m = 2.0$ is suitable for highly undermatched LBW and FSW panels in order not only to predict the maximum load but also the deformation behaviour of these panels more accurately. This suggests that the stress state at the crack tip located in an undermatched weld is governed by the plane strain condition (which corresponds to $m = 2.0$) despite the fact of the overall thin sheets.

The results of the SINTAP analysis of the stiffened panels have shown that their residual strength can be predicted with good accuracy. The residual strength analysis of the 2-stringer panels with a one-bay crack and 3-stringer panels with a two-bay crack has been based on the skin and stringer failure criteria. The panel failure has been assumed if one of the criteria is met. Unlike in the conventional residual strength analysis route for riveted structures where the stringer failure is attained if the stringer stress exceeds the ultimate tensile strength of the stringer material, a new stringer failure criterion has been introduced in the analysis of these integrally stiffened panels which has a fracture mechanics foundation.

Since the stringer contains a crack due to crack branching, the definition of the stringer failure criterion has been based on either the unstable growth of the stringer crack or plastic collapse of the stringer net section.

It has been found in the analyses of both 2- and 3-stringer panels that the predicted panel failure is driven by skin failure. The stringer failure criterion has been met at a higher applied load than the skin failure criterion. The stringer failure has been governed by unstable growth of the stringer crack. Hence, any type of an analysis incorporating the stringer failure due to plastic collapse only, as it is the case in the conventional residual strength analysis route for riveted structures, would yield non-conservative predictions.

Various yield load solutions for the cracked stiffened panels have been investigated in the SINTAP analysis in order to find the most suitable solution. The analyses have shown that the yielding behaviour of the cracked skin is best approximated by the simple analytical solution of an equivalent M(T) panel, i.e. the crack length and the width of this panel are the same as in the respective stiffened panel. However, the K-factor solutions of the skin crack accounting for the stiffening effect of the stringer and crack branching, as derived within this work, are recommended.

8 Further work

- Due to the very small stable crack extension in LBW and FSW panels compared to the initial crack length, K_{c0} may be a potential fracture controlling parameter of undermatched welds in thin sheets. However, it should be noted that the number of tests for the variation of the a/W ratio at a given panel width conducted within this study may not be sufficient to conclude the size and geometry independence of the single value fracture toughness, K_{c0}, of cracked LBW and FSW panels. Moreover, the variation of the panel width at a constant a/W ratio should also be conducted to ensure the size and geometry independence, thus, the transferability of K_{c0} to real welded structures.

- The scope of application within this work was limited to flat welded stiffened panels. The next step will be to apply the SINTAP procedure to larger components like curved stiffened fuselage panels using the input information developed and verified within this thesis on the basis of 2- and 3-stringer panels as well as LBW and FSW butt welds.

- For the application of the SINTAP procedure to the real fuselage, the definition of the appropriate yield load is needed. Due to the absence of a physical boundary in a fuselage like the width in panels, the yield load (expressed in terms of stress) should be defined as a "local" yield load. The applied stress level at which a specified region in front of a crack reaches the yield stress of the material under consideration is then defined as the yield load. The choice of that region is discretionary and so is the yield load. The yield load, however, is a crucial parameter in the SINTAP procedure as has been shown in a previous section. The residual strength predictions are, therefore, expected to be highly dependent on the definition of the yield load.

  One approach to the solution to the problem of the yield load definition is through fitting the predicted results of the analytical assessment levels of the SINTAP procedure to test results. By varying the width of the region to yield (local yield load) in the SINTAP analysis while keeping all other parameters constant, the correct width can be found with the best agreement of the predicted residual strength with the experimental value.

  Another approach is fully numerical and is based on the J-integral determination. Two separate FE runs should be carried out. One is based on the linear elastic material to obtain the elastic part of the J-integral, J_e (which is related to the K-factor). Using the same FE model, the second FE run is based on the material stress-strain curve of the structure to get the total value of the J-integral. Recalling the following definition in the SINTAP procedure:

  $$J = J_e \times [f(L_r)]^{-2}$$

  where

  $$L_r = \frac{\sigma_{\mathrm{ref}}}{R_{p0.2}}$$

the reference stress σ_{ref} can be iteratively determined by finding a suitable definition.

- As long as the skin crack remains shorter than one bay in a one-bay crack scenario and shorter than two bays in a two-bay crack scenario, i.e. before crack branching, the residual strength analysis can be performed using the K-factor and stringer load concentration factor, L_{s}, solutions for riveted structures by selecting the smallest rivet pitch in order to approach the solutions of an integrally stiffened welded structure as closely as possible. However, if the crack crosses the stringer during stable crack growth leading to crack branching, the K-factor at the skin crack tip might be underestimated when using the solution of the riveted structure. To predict the residual strength of integrally stiffened welded panels, both cracks in skin and stringer should be assessed on the basis of fracture mechanics which implies the knowledge of the K-factor solution. For this purpose, the methodology used within this thesis on the basis of FEA can be easily applied to newly designed integral structures.

References

[1] K.-H. Rendigs. Aluminium structures used in aerospace – status and prospects. *Materials Science Forum*, 242:11–24, 1997.

[2] B. Irving. Why aren't airplanes welded. *Welding Journal*, 76(1):31–42, 1997.

[3] G. R. Irwin. Analysis of stresses and strains near the end of a crack traversing a plate. *Journal of Applied Mechanics*, 24:361–364, 1957.

[4] H. M. Westergaard. Bearing pressures and cracks. *Journal of Applied Mechanics*, 6:49–53, 1939.

[5] D. Broek. *Elementary Engineering Fracture Mechanics.* Martinus Nijhoff Publishers, fourth revised edition, 1986.

[6] T. L. Anderson. *Fracture Mechanics: Fundamentals and Applications.* CRC Press, 2nd edition, 1995.

[7] A. A. Wells. Unstable Crack Propagation in Metals: Cleavage and Fast Fracture. In *Proceedings of the Crack Propagation Symposium: Cranfield, September 1961*, pages 210–230, 1961.

[8] C. P. Cherepanov. Crack propagation in continous media. *Appl. Math. Mech*, 31:476–488, 1969.

[9] J. R. Rice. A path independent integral and the approximate analysis of strain concentrations by notches and cracks. *Journal of Applied Mechanics*, 35:379–389, 1968.

[10] J. W. Hutchinson. Singular behaviour at the end of a tensile crack in a hardening material. *Journal of Mechanics and Physics of Solids*, 16:13–31, 1968.

[11] J. R. Rice and G. F. Rosengren. Plane strain deformation near a crack tip in a power-law hardening material. *Journal of Mechanics and Physics of Solids*, 16:1–12, 1968.

[12] H. Vlieger. The Residual Strength Characteristics of Stiffened Panels Containing Fatigue Cracks. *Engineering Fracture Mechanics*, 5:447–477, 1973.

[13] C. C. Poe, Jr. Stress intensity factor for a cracked sheet with riveted and uniformly spaced stringers. *NASA TR R-358*, 1971.

[14] K.-H. Schwalbe and W. Setz. R-curve and fracture toughness of thin sheet materials. *Journal of Testing and Evaluation*, 7:182–194, 1981.

[15] J. E. Srawley and W. F. Brown, Jr. Fracture toughness testing methods. In *Fracture Toughness Testing and Its Applications, ASTM STP 381*, pages 133–196, 1965.

[16] ASTM E561. Standard practice for R-curve determination. In *Annual book of ASTM standards, Vol. 03.01.*, 1994.

[17] T. Swift. Fracture Analysis of Stiffened Panels. In *Damage Tolerance of Metallic Structures: Analysis Methods and Application, ASTM STP 842*, pages 69–107, 1984.

[18] Proceedings of International Symposium. *Mis-Matching of Welds – Performance of Strength Mis-Matched Welded or Bonded Joints*, 1993. Lüneburg/Germany, 26-28 May.

[19] Proceedings of Second International Symposium. *Mis-Matching of Interfaces and Welds – Performance of Strength Mis-Matched Welded or Bonded Joints*, 1996. Lüneburg/Germany, 24-26 April.

[20] W. Brocks and W. Schmitt. The second parameter in J-R curves: constraint or triaxiality. In *Constraint effects in fracture – theory and applications: second volume, ASTM STP 1244*, pages 209–231, 1995.

[21] M. L. Williams. On the stress distribution at the base of a stationary crack. *Journal of Applied Mechanics*, pages 109–114, 1957.

[22] S. G. Larsson and A. J. Carlsson. Influence of non-singular stress terms and specimen geometry on small-scale yielding at crack tips in elastic-plastic materials. *Journal of Mechanics and Physics of Solids*, 21:263–277, 1973.

[23] T. M. Edmunds and J. R. Willis. Matched asymptotic expansions in nonlinear fracture mechanics–III. In-plane loading of an elastic-perfectly plastic symmetric specimen. *Journal of Mechanics and Physics of Solids*, 25:423–455, 1977.

[24] N. P. O'Dowd and C. F. Shih. Family of crack-tip fields characterized by a triaxiality parameter–III. Structure of fields. *Journal of Mechanics and Physics of Solids*, 39:989–1015, 1991.

[25] Y. J. Chao, S. Yang, and M. A. Sutton. On the fracture of solids characterised by one or two parameters: theory and practice. *Journal of Mechanics and Physics of Solids*, 42:629–647, 1994.

[26] G. P. Nikishkov, A. Brückner-Foit, and D. Munz. Calculation of the second fracture parameter for finite cracked bodies using a three-term elastic-plastic asymptotic expansion. *Engineering Fracture Mechanics*, 52(4):685–701, 1995.

[27] Z. L. Zhang, M. Hauge, and C. Thaulow. Two parameter characterization of the near tip stress fields for bi-material elastic-plastic interface cracks. *International Journal of Fracture*, 79(1):65–83, 1996.

[28] Z. L. Zhang, C. Thaulow, and M. Hauge. Effects of crack size and weld metal mismatch on HAZ cleavage toughness. *Engineering Fracture Mechanics*, 57(6):653–664, 1997.

[29] M. C. Burstow, I. C. Howard, and R. A. Ainsworth. The influence of constraint on crack tip stress fields in strength mismatch welded joints. *Journal of Mechanics and Physics of Solids*, 46(5):845–872, 1998.

[30] A. G. Varias, Z. Suo, and C. F. Shih. Ductile failure of a constrained metal layer. *Journal of Mechanics and Physics of Solids*, 39(7):963–986, 1991.

[31] K.-H. Schwalbe, Y.-J. Kim, S. Hao, A. Cornec, and M. Koçak. EFAM ETM-MM 96 – the ETM Method for assessing the significance of crack-like defects in joints with mechanical heterogeneity (strength mismatch). *GKSS 97/E/9*, 1997.

[32] Y.-J. Kim and K.-H. Schwalbe. Numerical analysis of strength mis-match effect on local stresses for ideally plastic material. *Engineering Fracture Mechanics*, 71:1177–1199, 2004.

[33] D. Hellmann and K.-H. Schwalbe. Geometry and size effects on J-R and δ-R curves under plane stress conditions. In *Fracture Mechanics: Fifteenth Symposium, ASTM STP 833*, pages 577–605, 1984.

[34] K.-H. Schwalbe, A. Cornec, and K. Baustian. Application of fracture mechanics principles to austenitic steels. *Fatigue and Fracture of Engineering Materials and Structures*, 65:193–207, 1996.

[35] H. W. Liu and T. Zhuang. A dual-parameter elastic-plastic fracture criterion. *International Journal of Fracture*, 27:R87–R91, 1985.

[36] Y. P. Lei, Y. W. Shi, H. Murakawa, and Y. Luo. The effect of mechanical heterogeneity and limit load of a weld joint with longitudinal weld crack on the J-integral and failure assessement curves. *International Journal of Pressure Vessels and Piping*, 75:625–632, 1998.

[37] S. Hao, K.-H. Schwalbe, and A. Cornec. The effect of yield strength mis-match on the fracture analysis of welded joints: slip-line field solutions for pure bending. *International Journal of Solids and Structures*, 37:5385–5411, 2000.

[38] P. Dong and J. R. Gordon. The effect of under and overmatching on fracture prediction models. In M. Koçak, editor, *Welding-90 Technilogy, Material, Fracture*, pages 363–370, 1990.

[39] M. T. Kirk and R. H. Dodds, Jr. Effect of weld strength mis-match on elastic-plastic fracture parameters for small tension loaded cracks. In K.-H. Schwalbe and M. Koçak, editors, *Mis-Matching of Welds*, pages 369–385, 1994.

[40] M. Koçak, M. Pakdil, and G. Çam. Fracture behaviour of diffusion bonded titanium alloys with strength mismatch. *Science and Technology of Welding and Joining*, 7(4):187–196, 2002.

[41] M. C. Burstow and I. C. Howard. Damage mechanics models of ductile crack growth in welded specimens. *Fatigue and Fracture of Engineering Materials and Structures*, 23(8):691–708, 2000.

[42] G. Rousselier. Ductile fracture models and their potential in local approach of fracture. *Nuclear Engineering and Design*, 105:97–111, 1987.

[43] M. Koçak, J. dos Santos, and S. Riekehr. Trends in laser beam welding technology and fracture assessement of weld joints. *Science and Technology of Welding and Joining*, 6(6):347–350, 2001.

[44] J. R. Rice. Limitations to the small scale yielding for crack tip plasticity. *Journal of Mechanics and Physics of Solids*, 22:17–26, 1974.

[45] B. J. Dalgleish, K. P. Trumble, and A. G. Evans. The strength and fracture of alumina bonded with aluminum alloys. *Acta Metallurgica*, 37(7):1923–1931, 1989.

[46] I. E. Reimanis, B. J. Dalgleish, M. Brahy, M. Rühle, and A. G. Evans. Effect of plasticity on the crack propagation resistance of a metal/ceramic interface. *Acta Metallurgica et Materialia*, 38(12):2645–2652, 1990.

[47] G. Çam, M. Koçak, D. Dobi, L. Heikinheimo, and M. Siren. Fracture behaviour of diffusion bonded bi-material (Ti-Al) joints. In K.-H. Schwalbe and M. Koçak, editors, *Mis-matching of interfaces and welds*, pages 435–450, 1997. GKSS Research Center Publications, Geesthacht.

[48] S. Hao, A. Cornec, and K.-H. Schwalbe. Plastic stress-strain fields and limit loads of plane strain cracked tensile panel with a mismatched welded joint. *International Journal of Solids and Structures*, 34(3):297–326, 1997.

[49] V. Tvergaard and J. W. Hutchinson. On the toughness of ductile adhesive joints. *Journal of Mechanics and Physics of Solids*, 44(5):789–800, 1996.

[50] G. Lin, Y.-J. Kim, A. Cornec, and K.-H. Schwalbe. Fracture toughness of a constraint metal layer. *Computational Materials Science*, 9:36–47, 1997.

[51] Y.-J. Kim, G. Lin, A. Cornec, W. Brocks, and K.-H. Schwalbe. On the maximum stresses in the constrained ductile layer under small scale yielding. *International Journal of Fracture*, 75:R9–R16, 1996.

[52] A. A. Wells. Application of fracture mechanics at and beyond general yielding. *British Welding Journal*, 10:563–570, 1963.

[53] C. E. Turner. A J-based engineering usage of fracture mechanics. In *International Conference on Fracture, ICF 5*, pages 1–22, Cannes, 1981. Vol. 3.

[54] F. M. Burdekin and M. G. Dawes. Practical use of linear elastic and yielding fracture mechanics with particular reference to pressure vessels. In *Conference on Application of Fracture Mechanics to Pressure Vessel Technology*, pages 28–37, Institution of Mechanical Engineers, London, 1971.

[55] WES 2805-1997. Method of assessment for flaws in fusion welded joints with respect to brittle fracture and fatigue growth. Japan Welding Engineering Society, Tokyo, 1997.

[56] Q. P. Zhong et al. Safety Assessment of In-Service Pressure Vessels Containing Defects. SAPV-95 (in Chinese), 1995.

[57] P. N. Li, Y. Lei, Q. P. Zhong, and X. R. Li. A Chinese Structural Integrity Assessment Procedure for Pressure Vessels Containing Defects. *International Journal of Pressure Vessels and Piping*, 77:945–952, 2000.

[58] R. P. Harrison, K. Loosemore, and I. Milne. Assessment of the Integrity of Structures Containing Defects. CEGB Report R/H/R6, 1976.

[59] PD6493-80. Guidance on Methods for Assessing the Acceptability of Flaws in Fusion Welded Structures. British Standards Institution, London, 1980.

[60] British Standard BS7910. Guidance on Methods for Assessing the Acceptability of Flaws in the Metallic Structures. British Standards Institution, 2000.

[61] SINTAP. **S**tructural **INT**egrity **A**ssessment **P**rocedure. Final Revision. EU-Project BE 95-1462. Brite Euram Programme, 1999.

[62] K.-H. Schwalbe and A. Cornec. The engineering treatment model (ETM) and its practical application. *Fatigue and Fracture of Engineering Materials and Structures*, 14:405–415, 1991.

[63] K.-H. Schwalbe. The engineering flaw assessment method EFAM. *Fatigue and Fracture of Engineering Materials and Structures*, 21:1203–1213, 1998.

[64] K.-H. Schwalbe, J. Heerens, U. Zerbst, H. Pisarski, and M. Koçak. EFAM GTP 02 - the GKSS test procedure for determining the fracture behaviour of materials. *GKSS report GKSS 2002/24*, 2002.

[65] B. Brickstad, M. Bergman, P. Andersson, L. Dahlberg, I. Sattari-Far, and F. Nilsson. Procedure used in Sweden for Safety Assessment of Components with Cracks. *International Journal of Pressure Vessels and Piping*, 77:877–881, 2000.

[66] C. S. Wiesner, S. J. Maddox, W. Xu, G. A. Webster, F. M. Burdekin, R. M. Andrews, and J. D. Harrison. Engineering Critical Analyses to BS 7910 – the UK Guide on Methods for Assessing the Acceptability of Flaws in Metallic Structures. *International Journal of Pressure Vessels and Piping*, 77:883–893, 2000.

[67] P. J. Budden, J. K. Sharples, and A. R. Dowling. The R6 Procedure: Recent Developments and Comparison with Alternative Approaches. *International Journal of Pressure Vessels and Piping*, 77:895–903, 2000.

[68] K.-H. Schwalbe and U. Zerbst. The Engineering Treatment Model. *International Journal of Pressure Vessels and Piping*, 77:905–918, 2000.

[69] C. Faidy. RSE-M. A General Presentation of the French Codified Flaw Evaluation Procedure. *International Journal of Pressure Vessels and Piping*, 77:919–927, 2000.

[70] H. Kobayashi et al. Development of a Flaw Evaluation Handbook of the High Pressure Institute of Japan. *International Journal of Pressure Vessels and Piping*, 77:929–936, 2000.

[71] T. L. Anderson and D. A. Osage. API 579: A Comprehensive Fitness-for-service Guide. *International Journal of Pressure Vessels and Piping*, 77:953–963, 2000.

[72] M. Bergman, B. Brickstad, L. Dahlberg, F. Nilsson, and I. Sattari-Far. A procedure for safety assessment of components with cracks – Handbook. SA/FoU Report, 91/01, AB Svensk Anläggningsprovning, SAQ Swedish Plant Inspection Ltd., 1991.

[73] RSE-M Code. Rules for In-Service Inspection of Nuclear Power Plant Components. 1997 Edition + 1998 and 2000 addenda, 2000.

[74] R. A. Ainsworth. The Assessments of Defects in Structures of Strain Hardening Material. *Engineering Fracture Mechanics*, 19(4):633–642, 1984.

[75] API. Recommended practice for fitness-for-service. API 579. Washington, DC: American Petroleum Institute, 2000.

[76] Forschungskuratorium Maschinenbau. *FKM-Richtlinie: Bruchmechanischer Festigkeitsnachweis*, 2001. VDMA-Verlag GmbH.

[77] M. Koçak. Fitness for service analysis of structures using the FITNET procedure: an overview. In *Proceedings of the 24th International Conference on Offshore Mechanics and Arctic Engineering (OMAE), Halkidiki, Greece, 12-17 June*, 2005.

[78] M. Koçak, E. Seib, and A. Motarjemi. Improvements to the fracture assessment of welds using FITNET fitness for service assessment procedure. In *Proceedings of the 24th International Conference on Offshore Mechanics and Arctic Engineering (OMAE), Halkidiki, Greece, 12-17 June*, 2005.

[79] K.-H. Schwalbe, U. Zerbst, W. Brocks, A. Cornec, J. Heerens, and H. Amstutz. The Engineering Treatment Model for Assessing the Significance of Crack-like Defects in Engineering Structures EFAM-ETM 95. GKSS Forschungszentrum, 1996.

[80] R. A. Ainsworth, A. C. Bannister, and U. Zerbst. An Overview of the European Flaw Assessment Procedure SINTAP and its Validation. *International Journal of Pressure Vessels and Piping*, 77:869–876, 2000.

[81] R. A. Ainsworth. The initiation of creep crack growth. *International Journal of Solids and Structures*, 18:873–881, 1982.

[82] I. Milne, R. A. Ainsworth, A. R. Dowling, and A. T. Steward. Background to and validation of CEGB Report R/H/R6-Revision 3. *International Journal of Pressure Vessels and Piping*, 32:105–196, 1988.

[83] L. Eftis and H. Liebowitz. On the modified Westergaard equations for certain plane crack problems. *International Journal of Fracture Mechanics*, 8(4):383–392, 1972.

[84] H. Tada, P. C. Paris, and G. R. Irwin. *The Stress Analysis of Cracks Handbook.* New York: ASME Press, 3rd edition, 2000.

[85] B. Farahmand. *Fatigue and Fracture Mechanics of High Risk Parts.* International Thomson Publishing, 1997.

[86] J. R. Rice, P. C. Paris, and J. G. Merkle. Some further analysis of J-integral analysis and estimates. In *Progress in flow growth and fracture toughness testing, ASTM STP 536*, pages 231–245, 1973.

[87] P. Hornet and C. Eripret. Experimental J evaluation from a load-displacement curve for homogeneous and overmatched SENB or CCT specimen. *Fatigue and Fracture of Engineering Materials and Structures*, 18:679–692, 1995.

[88] C. Eripret and P. Hornet. Fracture toughness testing procedures for strength mismatched structures. In K.-H. Schwalbe and M. Koçak, editors, *Mis-Matching of Interfaces and Welds – Performance of Strength Mis-Matched Welded or Bonded Joints*, pages 17–34, 1997.

[89] K.-H. Schwalbe, R. A. Ainsworth, C. Eripret, Ch. Franco, Ph. Gilles, M. Koçak, H. Pisarski, and Y. Y. Wang. Common views on the effects of yield strength mismatch on testing and structural assessment. In K.-H. Schwalbe and M. Koçak, editors, *Mis-Matching of Interfaces and Welds – Performance of Strength Mis-Matched Welded or Bonded Joints*, pages 99–132, 1997.

[90] K.-H. Schwalbe. Introduction of δ_5 as an operational definition of the ctod and its practical use. In *Fracture Mechanics, ASTM STP 1236*, pages 763–778, 1995.

[91] G. Lütjering. Property optimization through microstructural control in titanium and aluminum alloys. *Materials Science and Engineering A*, 263:117–126, 1999.

[92] G. T. Hahn and A. R. Rosenfield. Metallurgical factors affecting fracture toughness of aluminum alloys. *Metallurgical Transactions A*, 6A:653–668, 1975.

[93] T. Ma and G. den Ouden. Softening behaviour of Al-Zn-Mg alloys due to welding. *Materials Science and Engineering A*, 266:198–204, 1999.

[94] E. Seib, M. Koçak, A. Motarjemi, H. Assler, and H.-J. Schmidt. Fracture assessment of laser beam welded Al-alloys. In *Juniot EUROMAT 2002, poster presentation*, 2002.

[95] R. Braun, C. Dalle-Donne, and G. Staniek. Laser beam welding and friction stir welding of 6013-T6 aluminium alloy sheet. *Mat.-wiss u. Werkstofftech.*, 31:1017–1026, 2000.

[96] M. Koçak, G. Çam, S. Riekehr, F. Torster, and J. F. dos Santos. Microtensile Test Technique for Weldments. *IIW-Doc. SC X-F-079-98*, 1998.

[97] H. Liu, H. Fujii, M. Maeda, and K. Nogi. Rupture locations of friction stir welded joints of AA2017-T351 and AA6061-T6 aluminum alloys. *Transactions-JWRI*, 32(1):151–154, 2003.

[98] H. Liu, H. Fujii, M. Maeda, and K. Nogi. Friction stir welding characteristics of two aluminum alloys. *Transactions Nonferrous Met. Soc. China*, 13(5):1108–1111, 2003.

[99] R. Braun, G. Roth, and J. Arnold. Nd:YAG laser beam welding of 6013 aluminium alloy sheet using different filler powders. *Materials Science Forum*, 396:1691–1696, 2002.

[100] J. X. Zhang, Y.W. Shi, and M. J. Tu. Studies on the fracture mechanics parameters of weldment with mechanical heterogeneity. *Engineering Fracture Mechanics*, 34(5):1041–1050, 1989.

[101] M. Koçak, J. Knaack, and K.-H. Schawalbe. Fracture behaviour of the undermatched weld joints. In M. M. Salama, H. C. Rhee, J. G. Williams, and S. Liu, editors, *The Ninth International Conference of Offshore Mechanics and Arctic Engineering*, pages 453–459, 1990.

[102] M. Koçak, B. Petrovski, and K.-H. Schawalbe. Fracture aspects of the under- and overmatched weld joints. In J. Milne, editor, *Engineering design in welded constructions*, pages 241–249, 1992.

[103] A. G. Vovnyanko and A. I. Semenec. Residual strength of integrally stiffened structures of extruded panels of D16thT alloy and its modifications. *Fiziko-chimiceskaya mechanika materialov*, 2:88–92, 1983. (in Russian).

[104] National Aerospace Laboratory NLR. *Residual strength of damage tolerant Aluminum-Lithium sheet materials*, 1992. NLR-TP-92439.

[105] WelAir. Development of Short Distance WELding Concepts for AIRframes. AST3-CT-2003-502832.

[106] ARAMIS. Optical deformation analysis. http://www.gom.com.

[107] S. P. Timoshenko and J. N. Goodier. *Theory of Elasticity.* McGraw Hill, third edition, 1970.

[108] N. E. Dowling. *Mechanical Behaviour of Materials.* Prentice Hall, 2nd edition, 1999.

[109] ABAQUS. *User's manual, Version 5.8.* Hibbitt, Karlson and Sorensen, Inc., 1998.

[110] R. D. Young, M. Rouse, D. R. Ambur, and J. H. Starnes, Jr. Residual Strength Pressure Tests and Nonlinear Analyses of Stringer- and Frame-Stiffened Aluminum Fuselage Panels with Longitudinal Cracks. In *Proceedings of the FAA-NASA Symposium on the Continued Airworthiness of Aircraft Structures*, pages 408–426, 1997. DOT/FAA/AR-92/2.

[111] I. S. Raju. Calculation of strain-energy release rates with higher order and singular finite elements. *Engineering Fracture Mechanics*, 28(3):251–274, 1987.

[112] M. M. Abdel Wahab and G. de Roeck. A finite element solution for elliptical cracks using the ICCI method. *Engineering Fracture Mechanics*, 53(4):519–526, 1996.

[113] G. de Roeck and M. M. Abdel Wahab. Strain energy release rate formulae for 3D finite element. *Engineering Fracture Mechanics*, 50(4):569–580, 1995.

[114] T. Swift. Development of fail-safe features of the DC-10. In *Damage Tolerance of Metallic Structures: Analysis Methods and Application, ASTM STP 486*, pages 164–214, 1971.

[115] T. Swift. Damage Tolerance in Pressurized Fuselages. In *New materials and fatigue resistant aircraft design, June 10-12, Ottawa, ICAF*, pages 1–77, 1987.

[116] E. Seib and H. Assler. K-factor for riveted 2-stringer panel. unpublished results.

[117] J. C. Gerdeen. A critical evaluation of plastic behaviour data and a united definition of plastic loads for pressure components. In *WRC–Welding Research Council, Bulletin 254*, 1979.

[118] P. G. Hodge, Jr. *Plastic Analysis of Structures.* McGraw-Hill, New York, 1959.

[119] P. S. Symonds. *Handbook of Engineering Mechanics.* McGraw-Hill, New York, 1962.

[120] Y.-J. Kim and K.-H. Schwalbe. Mismatch effect on plastic yield loads in idealised weldments, I. Weld centre cracks. *Engineering Fracture Mechanics*, 68:163–182, 2001.

[121] Y.-J. Kim and K.-H. Schwalbe. Mismatch effect on plastic yield loads in idealised weldments, II. Heat affected zone cracks. *Engineering Fracture Mechanics*, 68:183–199, 2001.

[122] M. Muscat, D. Mackenzie, and R. Hamilton. A work criterion for plastic collapse. *International Journal of Pressure Vessels and Piping*, 80:49–58, 2003.

[123] A. G. Miller. Review of Limit Loads of Structures Containing Defects. *International Journal of Pressure Vessels and Piping*, 32:197–327, 1988.

[124] T. Swift. The effects of fastener flexibility and stiffener geometry on the stress intensity in stiffened cracked sheet. In *Prospects of fracture mechanics*, pages 419–436, 1974.

A Appendix

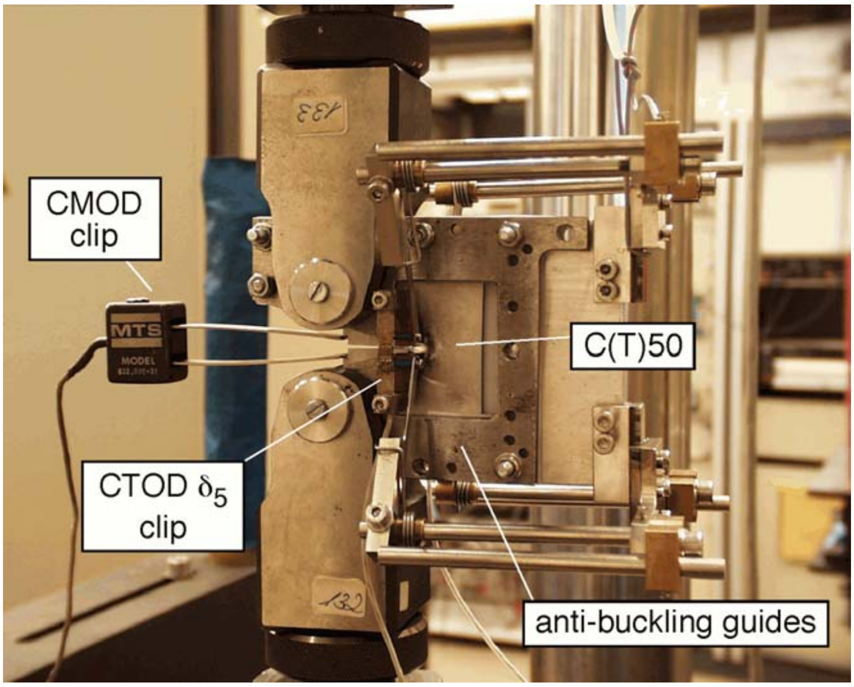

Figure A.1: Machine setup and instrumented C(T)50 specimen.

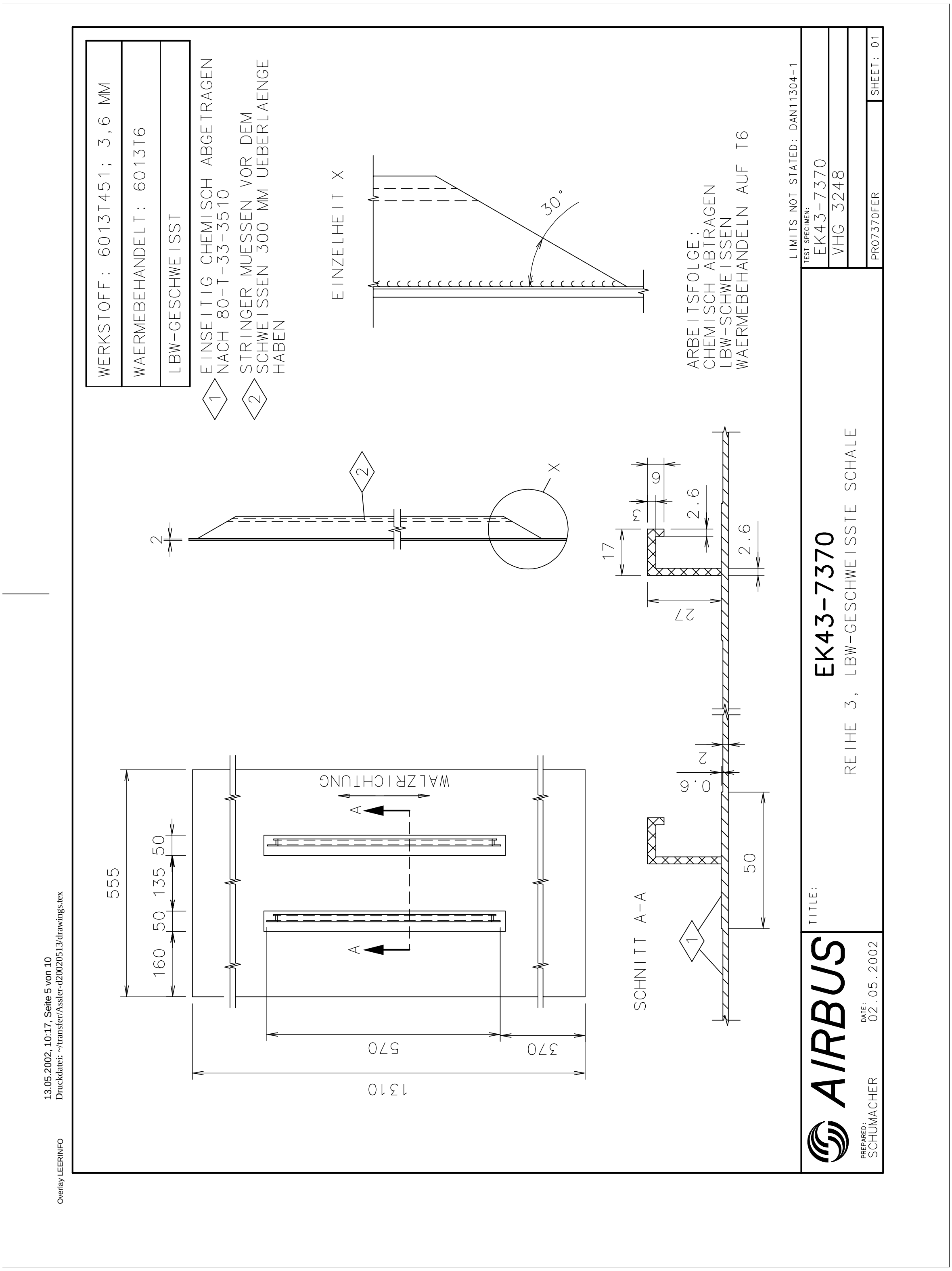

Figure A.2: Drawing of a 2-stringer panel.

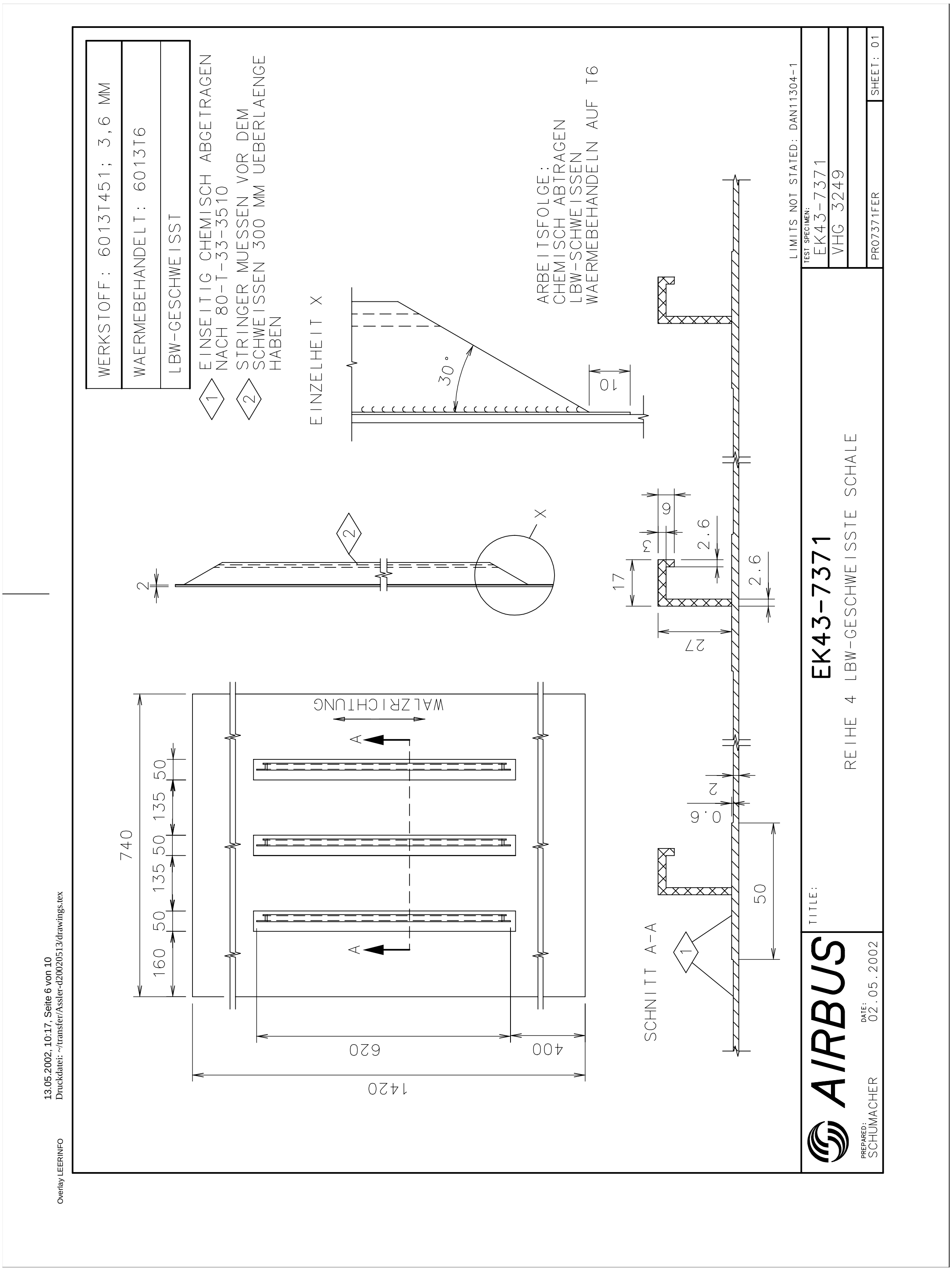

Figure A.3: Drawing of a 3-stringer panel.

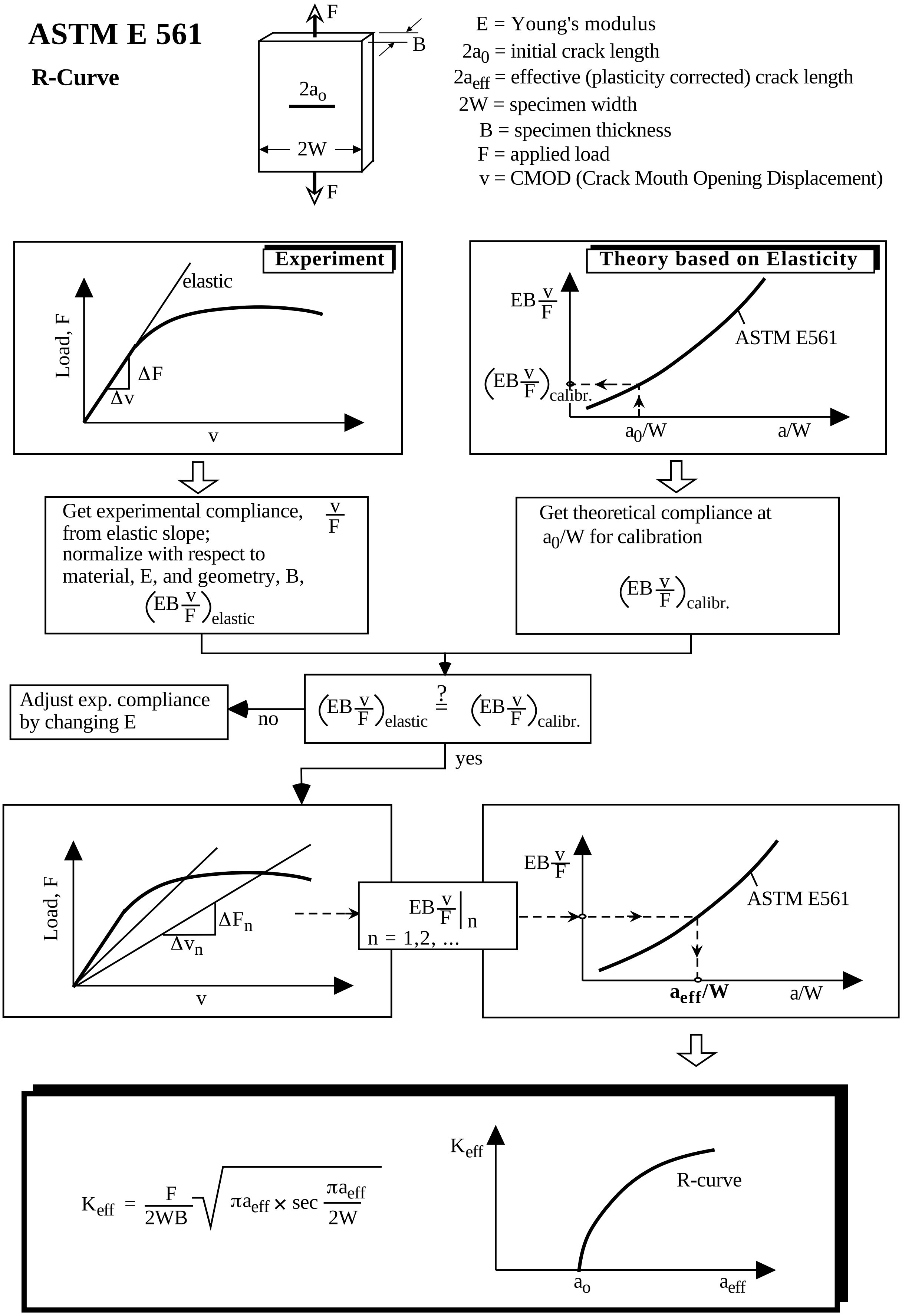

Figure A.4: Determination of the R-curve according to the compliance method of the ASTM E561 standard [16].

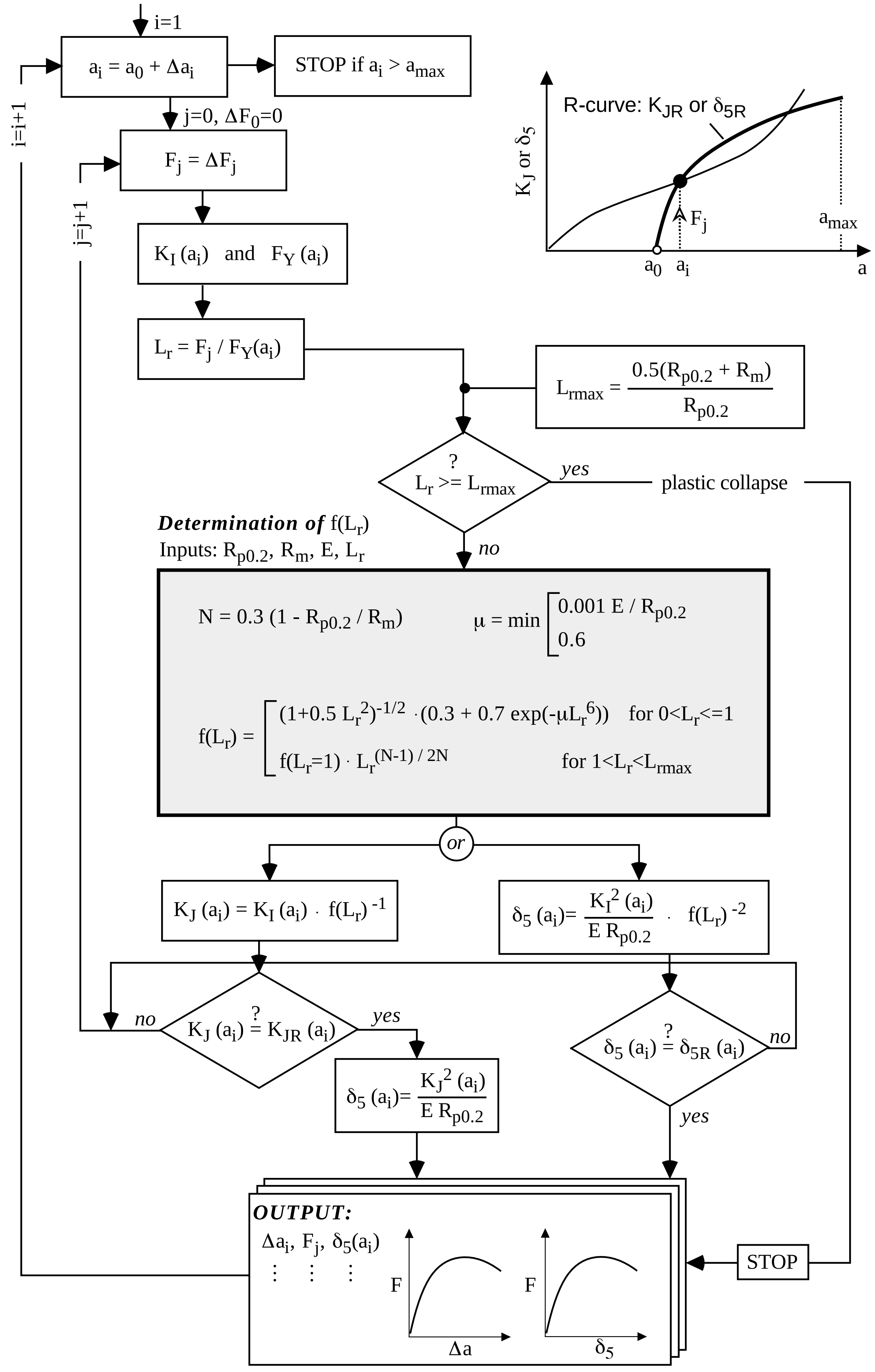

Figure A.5: Flow chart of SINTAP Level 1 used for the residual strength prediction of base material M(T) panels and also stiffened panels based on the skin failure criterion.

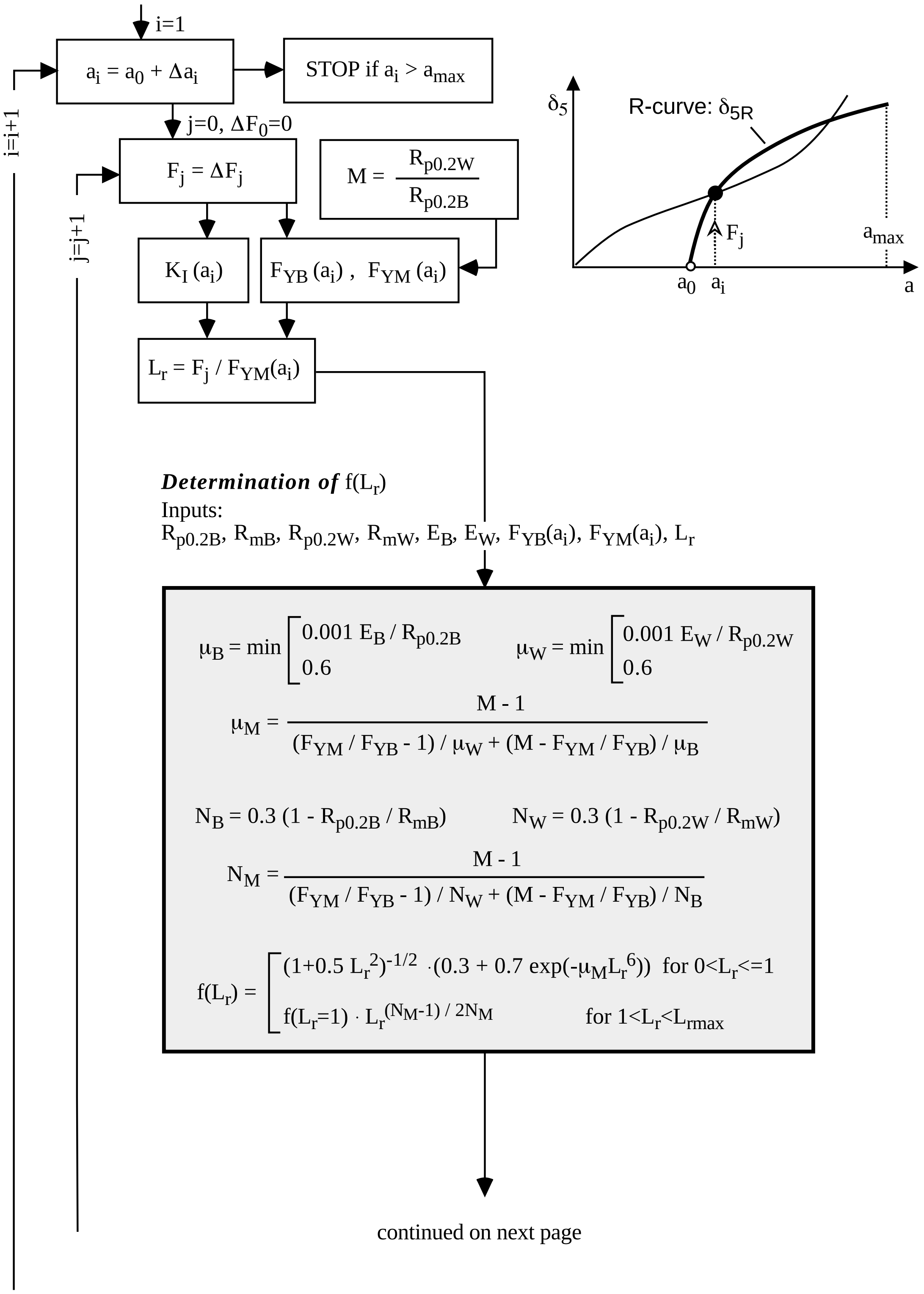

Figure A.6: Flow chart of SINTAP Level 2 (strength mismatch level) used for the residual strength prediction of LBW and FSW M(T) panels.

continued from previous page

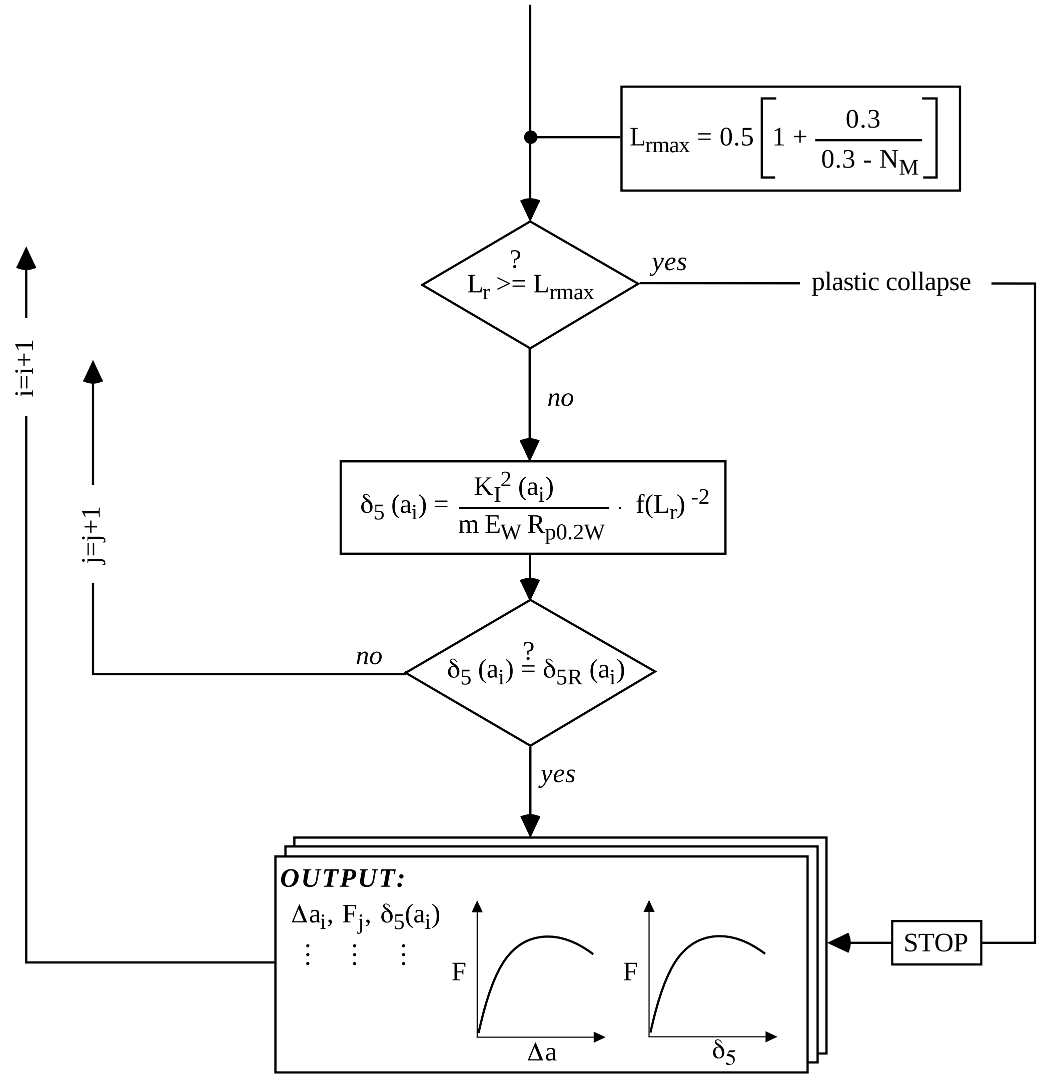

Fig. A.6 continued.

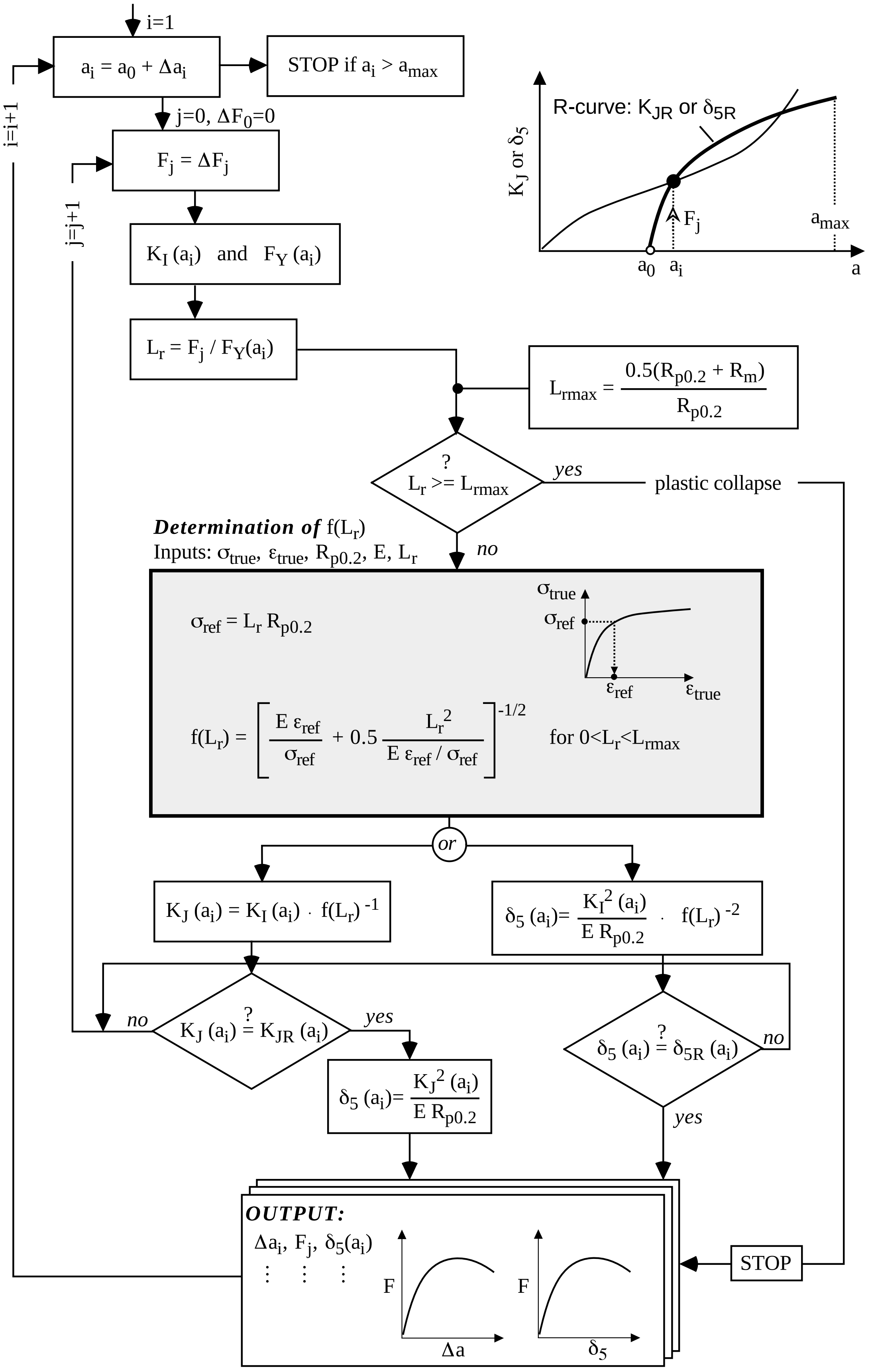

Figure A.7: Flow chart of SINTAP Level 3 used for the residual strength prediction of base material M(T) panels and also stiffened panels based on the skin failure criterion.

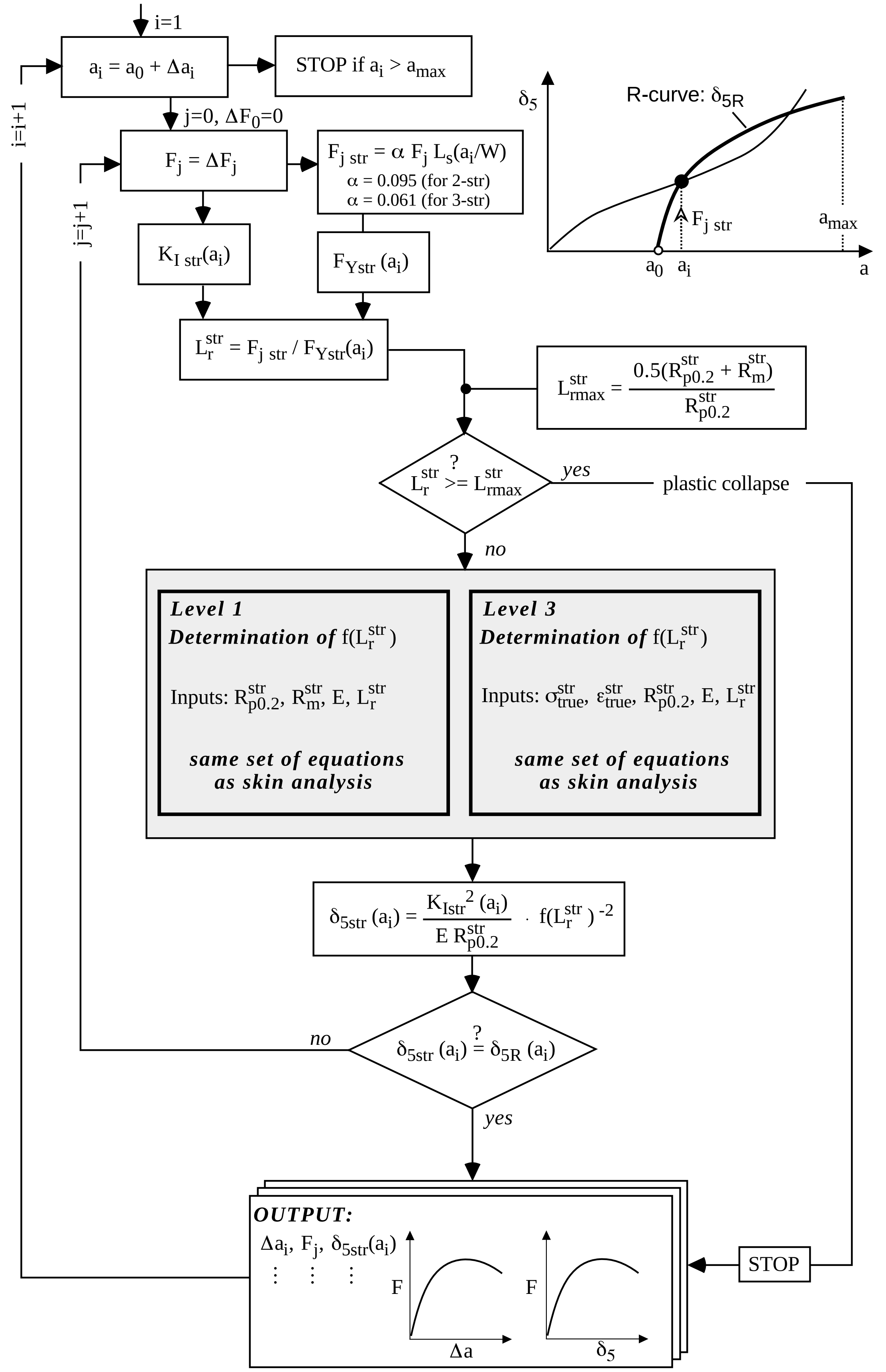

Figure A.8: Flow chart of SINTAP Level 1 and 3 used for the residual strength prediction of stiffened panels based on the stringer failure criterion.

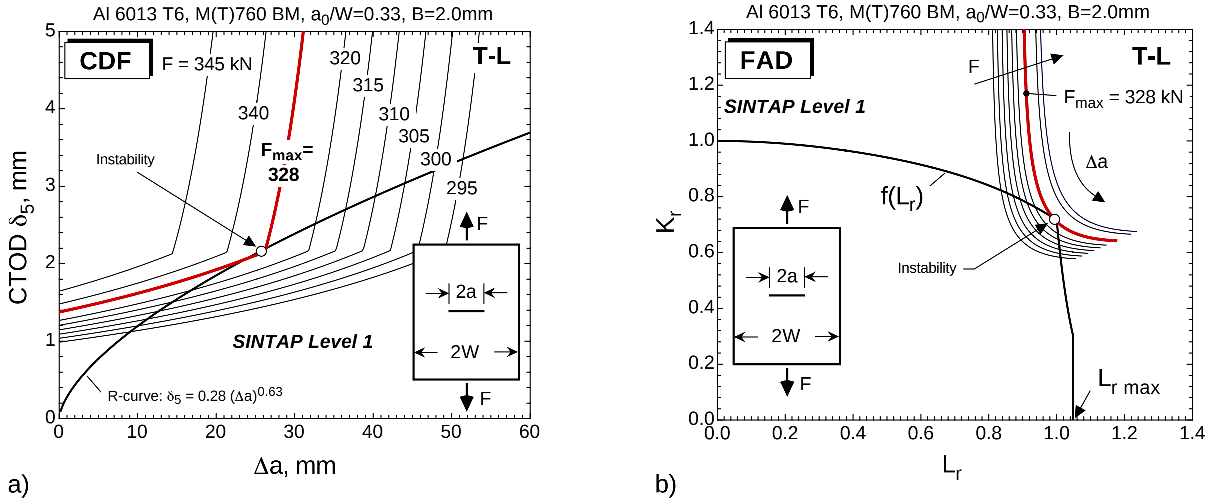

a) b)

Figure A.9: Residual strength prediction of the base material (T-L orientation) panel using a) CDF and b) FAD approaches of the SINTAP procedure. Analysis Level 1 is based on the CTOD δ_5 R-curve showing the equivalence of the two methods. Crack driving forces in the FAD approach are calculated for the same loads as in the CDF approach.

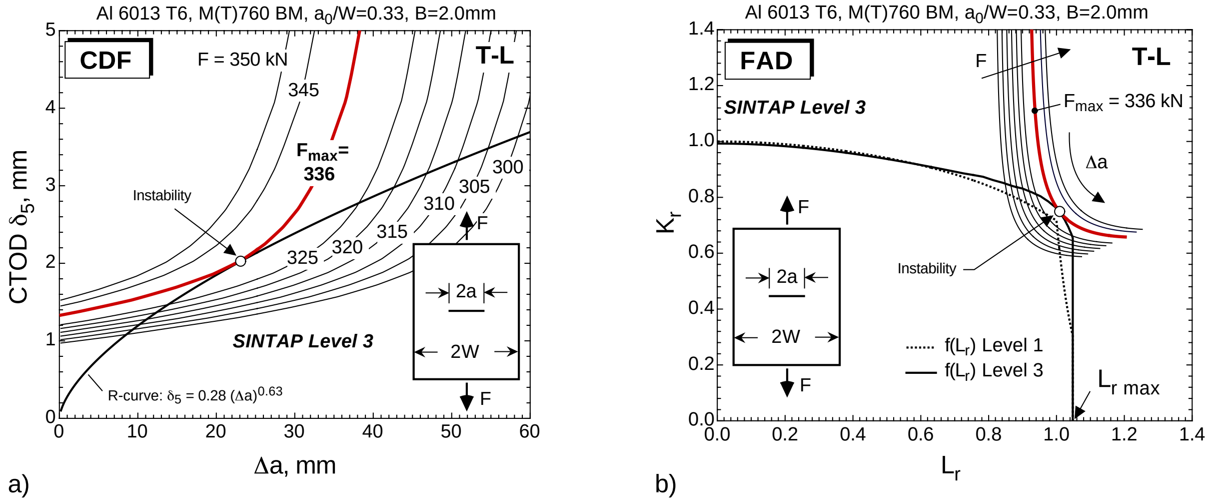

a) b)

Figure A.10: Residual strength prediction of the base material (T-L orientation) panel using a) CDF and b) FAD approaches of the SINTAP procedure. Analysis Level 3 is based on the CTOD δ_5 R-curve showing the equivalence of the two methods. Crack driving forces in the FAD approach are calculated for the same loads as in the CDF approach.

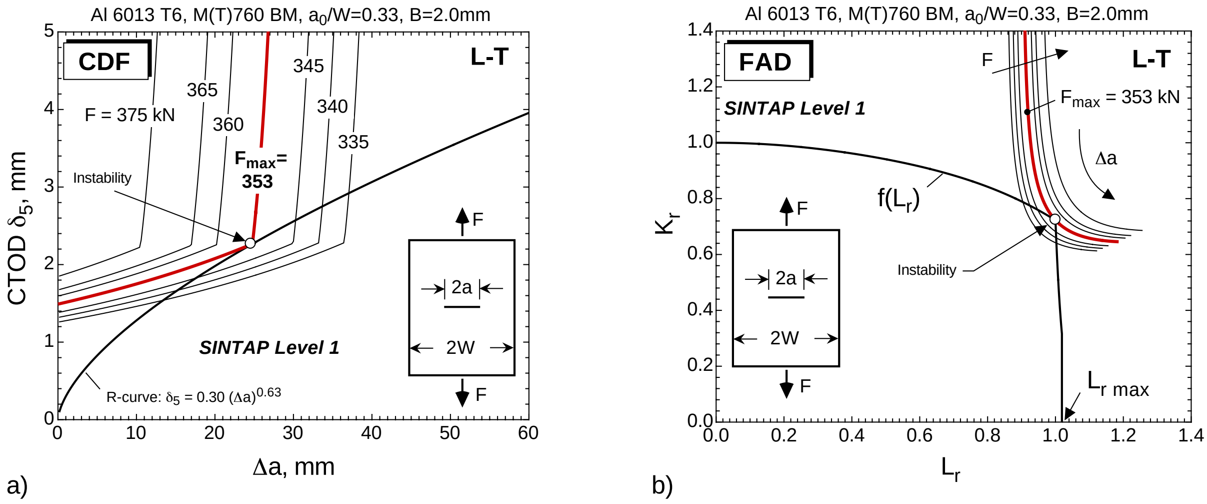

Figure A.11: Residual strength prediction of the base material (L-T orientation) panel using a) CDF and b) FAD approaches of the SINTAP procedure. Analysis Level 1 is based on the CTOD δ_5 R-curve showing the equivalence of the two methods. Crack driving forces in the FAD approach are calculated for the same loads as in the CDF approach.

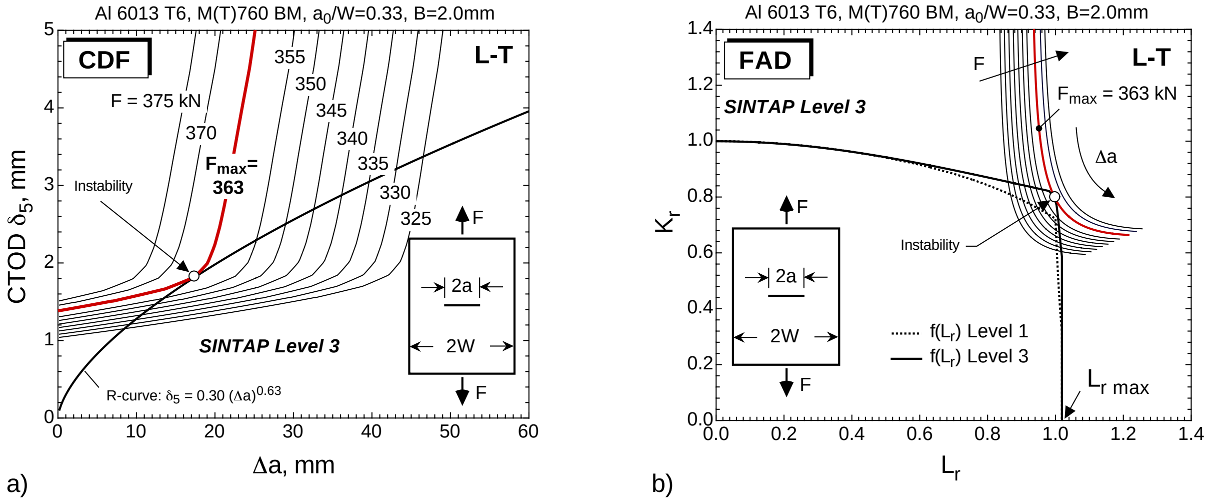

Figure A.12: Residual strength prediction of the base material (L-T orientation) panel using a) CDF and b) FAD approaches of the SINTAP procedure. Analysis Level 3 is based on the CTOD δ_5 R-curve showing the equivalence of the two methods. Crack driving forces in the FAD approach are calculated for the same loads as in the CDF approach.